Journal of
Mechanics of
Materials and Structures

msp

JOURNAL OF MECHANICS OF MATERIALS AND STRUCTURES

msp.org/jomms

Founded by Charles R. Steele and Marie-Louise Steele

Cover photo: Mando Gomez, www.mandolux.com

B-SPLINES COLLOCATION FOR PLATE BENDING EIGENANALYSIS

CHRISTOPHER G. PROVATIDIS

Following the recent encouraging findings in the area of 2-D acoustics, this paper investigates the performance of a B-spline collocation method in the extraction of natural frequencies (eigenvalue analysis) of thin plates in bending. Numerical formulation and associated results refer to uniformly discretized rectangular and circular plates, for which closed-form analytical or approximate solutions are available in the literature. The computational results show that the proposed B-spline collocation method is of higher quality than the previously known cubic B-splines Galerkin–Ritz formulation; both of them converge more rapidly to the accurate solution than what the conventional finite element method does for the same mesh density.

1. Introduction

Engineering analysis of arbitrarily shaped or arbitrarily loaded structures is usually performed using the well-known finite element method (FEM) [Bathe 1996]. Particularly in mechanical engineering, where the structural components generally consist of free shaped boundaries produced by a CAD system, it is more convenient to deal with their B-splines representation [de Boor 1972; Farin et al. 2002; Piegl and Tiller 1995]. In addition to a CAD model, computational engineering analysis (CAE) can be performed on the basis of either B-splines [Höllig 2003] or NURBS [Cottrell et al. 2009]. For a detailed review on the CAD/CAE integration, the interested reader may consult [Provatidis 2013].

B-splines based finite elements have been extensively used in the finite element praxis. In more detail, structural engineering applications cover static, dynamic and stability analyses [Peng-Cheng et al. 1987; Akhras and Li 2011]; an older survey is [Grigorenko and Kryukov 1995]. A great number of papers on B-splines finite element models applied to plates and shells have been published in the last twenty years. These include isotropic [Antes 1974; Gupta et al. 1991; Fan and Luah 1995], orthotropic [Cheng and Dade 1990], cross- and angle-ply multilayered laminated [Patlashenko and Weller 1995; Dawe and Wang 1995; Kolli and Chandrashekhara 1997; Reddy and Palaninathan 1999; Park et al. 2008; Kapoor and Kapania 2012; Golmakani and Mehrabian 2014], functional graded materials (FGM) [Valizadeh et al. 2013; Tran et al. 2013] and shell [Echter et al. 2013] structures, among others. A tendency of the last few years is to combine B-splines with wavelet ideas [Han et al. 2007; Zhang et al. 2010; Li and Chen 2014].

Despite the aforementioned progress, it has been reported that the computer effort required to estimate the matrices of these CAD-based macroelements (in potential and structural problems) is relatively high [Provatidis 2004; 2012]. As a remedy to this shortcoming, in 2005 the author proposed preserving the global CAD-based interpolation but substituting the Galerkin–Ritz formulation (which needs domain integration to estimate the mass and stiffness matrices) by a global collocation scheme [Provatidis 2006,

p. 6704]. Similar numerical results were later reported for the particular case of a (NURBS-based) isogeometric analysis [Hughes et al. 2010].

So far, the above idea of global collocation has been successfully applied to the static analysis of 2-D structures [Provatidis 2008b; 2009; Provatidis and Ioannou 2010], eigenvalue analysis of 1-D elastic rods [Provatidis 2008a], as well as the eigenanalysis of 2-D acoustic cavities [Provatidis 2014] and 2-D elastic structures [Filippatos 2010]. Later, isogeometric collocation methods were proposed [Auricchio et al. 2010]. Nevertheless, an application of this idea to thin plate bending is still missing.

Within this context, this paper preserves the aforementioned idea of approximating the deflection $w(x, y)$ within the plate through a B-splines tensor product but replaces the Galerkin–Ritz computational procedure with a global collocation method (GCM), thus avoiding domain integration. The cost of this facility is the increase of the polynomial degree from $p = 3$ to higher values ($p \geq 5$). The proposed methodology is successfully tested in a square plate (simply supported, clamped), as well as in a clamped circular plate.

2. Governing equations and numerical solution

The partial differential equation of motion for a plate in bending is given by

$$D\nabla^4 w(x, y, t) + \rho h \frac{\partial^2 w(x, y, t)}{\partial t^2} = f(x, y, t), \tag{1}$$

where D is the flexural rigidity, ρ is the mass density, h is the plate thickness, and f is the loading towards the z-direction.

Following [Antes 1974; Höllig 2003], the deflection is expanded into a B-splines tensor product of the form

$$w(x, y; t) = \sum_{i=1}^{n} \sum_{j=1}^{m} N_{i,p_n}(x) \cdot N_{j,p_m}(y) \cdot a_{ij}(t), \quad i = 1, \ldots, n; \ j = 1, \ldots, m, \tag{2}$$

where $N_{i,p_n}(x)$ and $N_{j,p_m}(y)$ are the basis functions in the x- and y-direction, respectively. The aforementioned basis functions (B-splines) are *piecewise* polynomials of p_n-th and p_m-th degree, respectively, and are characterized by compact support [Piegl and Tiller 1995]. Further details are given in Section 3.1.

It is noted that the integers n and m in (2) represent the number of *control* points in the x- and y-direction, respectively, whereas for the degrees of the corresponding polynomials, $p_n < n$ and $p_m < m$ (see (8) below).

According to the *global collocation method* [Provatidis 2008a; 2008b; 2009; Provatidis and Ioannou 2010; Filippatos 2010], a certain number of n_c collocation points (x_c, y_c) are chosen, at which the governing equation is satisfied as follows:

$$D \cdot \nabla^4 \left[\sum_{i=1}^{n} \sum_{j=1}^{m} N_{i,p_n}(x_c) \cdot N_{j,p_m}(y_c) \right] \cdot a_{ij}(t) + \rho h \cdot \sum_{i=1}^{n} \sum_{j=1}^{m} N_{i,p_n}(x_c) \cdot N_{j,p_m}(y_c) \cdot \ddot{a}_{ij}(t) = f(t). \tag{3}$$

Setting

$$k_{c,ij} = D \cdot \nabla^4 [N_{i,p_n}(x_c) \cdot N_{j,p_m}(y_c)] \tag{4}$$

and

$$m_{c,ij} = \rho h \cdot [N_{i,p_n}(x_c) \cdot N_{j,p_m}(y_c)], \tag{5}$$

(3) obtains the matrix form

$$[M] \cdot \{\ddot{a}(t)\} + [K] \cdot \{a(t)\} = \{f(t)\}. \tag{6}$$

In this way, mass and stiffness matrices of dimensions $n_c \times (nm)$ are produced.

In the general case, unlike the finite element method, the aforementioned matrices are not square before the boundary conditions are imposed. Imposing the prescribed values (flexural displacements or slopes) along the contour of the plate, we have to proceed so as to derive square matrices at the end. To this purpose, the proper choice of collocation points is demanded.

3. Global approximation

3.1. *One-dimensional B-spline approximation.* For the sake of completeness, in the following text, de Boor's procedure is briefly exposed.

For a given polynomial degree p, the construction of a B-spline along a straight line segment is based on a nondecreasing sequence of $q + 1$ *breakpoints* $(x_0, x_1, \ldots, x_{q-1}, x_q)$, i.e., the two ends (x_0, x_q) as well as $(q - 1)$ internal breakpoints $(x_1, \ldots, x_{q-1})$. Assuming a certain multiplicity for the inner knots, say μ, they compose the so-called *knot vector*,

$$V = \left\{ \underbrace{x_0, \ldots, x_0}_{p+1}, \underbrace{x_1, \cdots, x_1}_{\mu}, \ldots, \underbrace{x_{q-1}, \cdots, x_{q-1}}_{\mu}, \underbrace{x_q, \ldots, x_q}_{p+1} \right\}$$
$$= \{v_0, v_1, \ldots, v_{\mu(q-1)+2p+1}\}. \tag{7}$$

The following facts are well known:

(1) The above $\mu(q - 1) + 2(p + 1)$ elements in the vector V are associated to

$$n_{\text{CTRL}} = \mu(q - 1) + (p + 1) \tag{8}$$

control points [de Boor 1972; Farin et al. 2002; Piegl and Tiller 1995].

(2) The basis functions, $N_{i,p}(x)$, have the partition of unity property,

$$\sum_{j=0}^{q} N_{j,p}(x) = 1. \tag{9}$$

For a straight side (e.g., AB in the real domain Ω), the control points belong to the side while for a curved side they do not, except for the first (P_0) and last (P_n). In other words, the end segments of the polygon $P_0 P_1 \ldots P_{n-1} P_n$ (called the *generator*) are tangent to the curved side AB at end nodes P_0 and P_n. Details can be found elsewhere, for example, in [Farin et al. 2002].

The i-th B-spline function of p-degree, denoted by $N_{i,p}(x)$, is defined as follows (see for example

[Piegl and Tiller 1995, p. 50]):

$$N_{i,0}(x) = \begin{cases} 1, & \text{if } v_i \leq x < v_{i+1}, \\ 0, & \text{otherwise}, \end{cases} \tag{10}$$

$$N_{i,p}(x) = \frac{x - v_i}{v_{i+p} - v_i} N_{i,p-1}(x) + \frac{v_{i+p+1} - x}{v_{i+p+1} - v_{i+1}} N_{i+1,p-1}(x). \tag{11}$$

Similarly, the first derivative of $N_{i,p}(x)$ can be effectively calculated by the recursion [Piegl and Tiller 1995, p. 59]

$$N'_{i,p}(x) = \frac{p}{v_{i+p} - v_i} N_{i,p-1}(x) - \frac{p}{v_{i+p+1} - v_{i+1}} N_{i+1,p-1}(x), \tag{12}$$

whereas similar recursive expressions can be obtained for higher derivatives.

3.2. *Two-dimensional B-spline approximation: tensor product.* Let us consider a mapping from the real xy-domain (ABCD) to the reference $\xi\eta$-square (A′B′C′D′) in which $0 \leq \xi, \eta \leq 1$. The axis origin is chosen at the corner A (resp. A′), whereas the normalized axes ξ and η lie on the sides A′B′ and A′D′, respectively. Without loss of generality, the sides (AB, CD) and (A′B′, C′D′) as well as (B′C′, D′A′) and (BC, DA) are uniformly divided into n_ξ and n_η segments, respectively, thus introducing a mesh of $(n_\xi + 1) \times (n_\eta + 1)$ *breakpoints* (Figure 1).

Although the below illustrated B-spline macroelement reminds us of the classical Lagrangian type element [Bathe 1996, pp. 344, 456], it highly differs from it for the following reasons. Based on the aforementioned uniformly distributed breakpoints ($\xi = 0, \xi_1, \ldots, 1$; $\eta = 0, \eta_1, \ldots, 1$), each of the first two opposite sides AB and CD (parallel to x-axis) are described through n control points fulfilling the formula

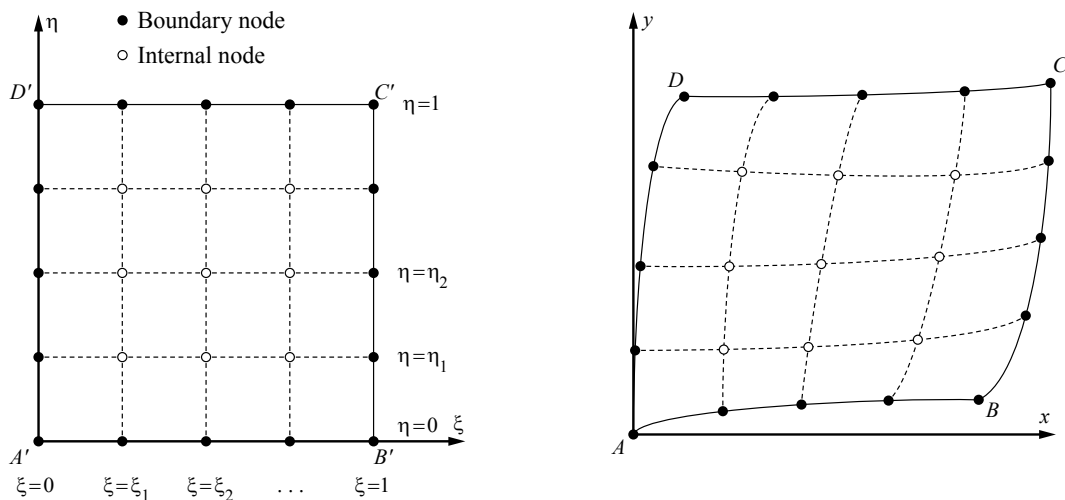$$n = \mu(n_\xi - 1) + (p_n + 1), \tag{13}$$

Figure 1. Uniformly arranged breakpoints of a B-splines plate-bending macroelement in the normalized, left, and the real domain, right (only the breakpoints are shown).
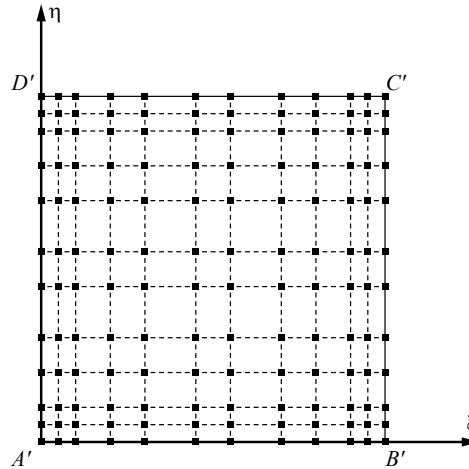
Figure 2. True position of the $\bar{q} = n \times m = 12 \times 12$ control points that correspond to the uniformly distributed breakpoints shown in Figure 1, left (number of segments $n_\xi = n_\eta = 4$; polynomial degree: $p = 5$).

while the other two opposite sides BC and DA (parallel to y-axis) are described through m control points

$$m = \mu(n_\eta - 1) + (p_m + 1). \tag{14}$$

Concerning the normalized (reference) element shown in Figure 1, left, the n control points belong to the straight line A′B′ and another set of n control points belong to the straight line D′C′. Similarly, the m control points belong to the straight line B′C′ and another set of m control points belong to the straight line A′D′. In contrast, in the real domain (let us consider, for example, the side AB: Figure 1, right) the *first* and *last* control points *coincide* with the *corner* points A and B respectively (ends of curve AB); however, the other control points may or may not belong to the curve AB (they may be found inside or outside the domain ABCD).

Returning to the normalized reference element (Figure 2), the mesh required for the B-spline representation of the patch geometry consists of $\bar{q} = nm$ control points, produced as the tensor product of n by m ones.

Each of the aforementioned control points, say the I-th, is associated with one global shape function given by

$$\phi_{I,\text{B-splines}}(\xi, \eta) = N_{i,p_n}(\xi) \cdot N_{j,p_m}(\eta), \quad \begin{cases} I = 1, \ldots, \bar{q} \equiv n \times m, \\ i = 1, \ldots, n; \ \ j = 1, \ldots, m. \end{cases} \tag{15}$$

Although the values of p_n and p_m may be different from one another, henceforth we take the same polynomial degree, that is $p_n = p_m = p$.

3.3. _Collocation points._ In order to determine the proper number of collocation points in each direction, it is necessary to assign values first to the polynomial degree p and then to the multiplicity of inner knots μ. It is well known that for every value of μ, the solution $w(x, y)$ is characterized by $C^{p-\mu}$-continuity.

According to (13), the number of control points towards a certain direction, say the ξ-direction, in which n_ξ subdivisions exist is $n = \mu(n_\xi - 1) + (p + 1)$. The four boundary conditions (for example, two fixed ends) reduce the number of total degrees of freedom by four, and therefore the remaining unknown coefficients will be $(n - 4)$. If within each of the n_ξ segments (defined between any two successive breakpoints) a number of c collocation points are considered, one should obtain so many equations at the c corresponding collocation points as the number of the unknowns, that is: $cn_\xi = n - 4$, whence

$$c = (n - 4)/n_\xi. \tag{16}$$

Substituting (13) into (16), one finally obtains

$$c = \mu + (p - \mu - 3)/n_\xi. \tag{17}$$

Since c must be an integer, we select the nominator in the second adding term of (17) to vanish, whence the multiplicity is given by

$$\mu = p - 3, \tag{18}$$

whence the number of collocation points in ξ-direction will be

$$c = p - 3. \tag{19}$$

Since the partial differential equation (1) is of fourth order, the minimum acceptable polynomial degree is $p = 5$, for which *double* knots ($\mu = 2$) and also $c = 2$ collocation points per direction are needed. Following previous studies in 1-D elliptic problems [de Boor and Swartz 1973], in the case of $p = 5$ the position of the collocation points within any cell of neighboring breakpoints was taken to be identical with those integration points used in a usual 2×2 Gaussian quadrature scheme.

In general, for every $p > 5$, the knot vector is built using $\mu = p - 3$ multiple inner knots, see (7), whereas a Gaussian quadrature scheme of $c \times c = (p - 3) \times (p - 3)$ collocation points per cell is adopted.

Remark. Due to (18), the above choice ($p - \mu = 3$) ensures a numerical solution characterized by C^3-continuity. This means that the deflection w, slope w', bending moment EIw'', and shear force EIw''' are continuous at all inner breakpoints.

Except for the above-mentioned Gaussian points, as also reported in 2-D acoustics (see [Provatidis 2014]), other sets of collocation points such as Demko and Greville ones can be used as well. Nevertheless, despite the global character of these abscissae, no significant influence on the numerical solution has been noticed so far (see Figure 5).

3.4. *Isoparametric approximations.* Tensor products of B-splines are based on the following series expansion ($\phi_j = \phi_{I,\text{B-splines}}$):

$$x(\xi, \eta) = \sum_{j=1}^{\bar{q}} \phi_j(\xi, \eta) \cdot x_j, \quad y(\xi, \eta) = \sum_{j=1}^{\bar{q}} \phi_j(\xi, \eta) \cdot y_j, \quad w(\xi, \eta) = \sum_{j=1}^{\bar{q}} \phi_j(\xi, \eta) \cdot a_j, \tag{20}$$

where a_j are generalized coefficients and *not* the nodal values of deflection w at the $\bar{q}$ control points. Only at the very ends of the boundary the extreme control points ($\boldsymbol{P}_0$ and $\boldsymbol{P}_n$) coincide with the corresponding ends of polygon curves (generator).

4. Imposition of Neumann boundary conditions

In contrast to the Dirichlet boundary conditions (b.c.), i.e., $w = 0$, which are imposed merely by deleting the columns that correspond to the restricted degree of freedom (DOF), the Neumann b.c. require a special treatment. In order to demonstrate the procedure, it is more instructive to deal with a clamped beam, and then extend the methodology to a real 2-D plate.

Within this context, let us assume a beam AB of length L, which is clamped at its left end (namely A) whereas the other end (namely B) is free to vibrate. The beam is discretized by B-splines using a number of breakpoints (like those arranged along the edge A′B′ of the square of Figure 2), which correspond to n control points. These control points are associated to the following generalized coefficients: $a_0 = w_0 = w(0)$, $a_1, \ldots, a_{n-1}$, $a_n = w_n = w(L)$. It is efficient to apply the local support property, according to which the basis function $N_{i,p}(x) = 0$ if x is outside the knot interval $[x_i, x_{i+p+1})$. After having constructed the matrices (K, M), which initially are of size $n_c \times n$, the following boundary conditions have to be considered.

Fixed point A:

$$w(0) = N_0(0)a_0 = 0 \tag{21a}$$

and

$$w'(0) = N_0'(0)a_0 + N_1'(0)a_1 = 0. \tag{21b}$$

Since $N_0(0) = 1 \neq 0$, (21a) implies

$$a_0 = 0. \tag{21c}$$

Substituting (21c) into (21b) by virtue of $N_1' \neq (0)$ gives

$$a_1 = 0. \tag{21d}$$

Therefore, the first and second columns of the matrices (K, M) should be deleted, because their elements are multiplied by the null values of the two restrained DOF at the end A (i.e., $a_0 = a_1 = 0$). Therefore, the number of the so far remaining columns (and the associated coefficients a_i) becomes $n - 2$.

Furthermore, concerning the load-free end B, the zero values of the bending moment $w''(L) = 0$ and the shear force $w'''(L) = 0$ have to be imposed. This is easily accomplished by taking into consideration the local support property for the control point B at $x = L$:

$$w''(L) = N_{n-2}''(L)a_{n-2} + N_{n-1}''(L)a_{n-1} + N_n''(L)a_n, \tag{21e}$$

$$w'''(L) = N_{n-3}'''(L)a_{n-3} + N_{n-2}'''(L)a_{n-2} + N_{n-1}'''(L)a_{n-1} + N_n'''(L)a_n. \tag{21f}$$

Equations (21e) and (21f) induce two linear dependencies between the remaining $(n - 2)$ generalized coefficients of the vector a. As a result, the final size of the matrices will be $n_c \times (n - 4)$, and (16)–(19) ensure that $(K_{\text{final}}, M_{\text{final}})$ will be square.

For a uniform arrangement of the breakpoints, and for any polynomial degree p, after some symbolic manipulation it is found that $N_{n-2}''(L) = N_n''(L) = -2N_{n-1}''(L)$; therefore (21e) implies

$$a_{n-1} = \tfrac{1}{2}(a_{n-2} + a_n). \tag{21g}$$

Substituting (21g) into (21f) and then solving for a_n gives

$$a_n = \gamma a_{n-3} + \delta a_{n-2}, \tag{21h}$$

where

$$\gamma = -\frac{N_{n-3}'''(L)}{\frac{1}{2}N_{n-1}'''(L) + N_n'''(L)}, \qquad \delta = -\frac{N_{n-2}'''(L) + \frac{1}{2}N_{n-1}'''(L)}{\frac{1}{2}N_{n-1}'''(L) + N_n'''(L)}. \tag{21i}$$

For each collocation point, by virtue of (21g) and (21h), the expression $\sum_{j=1}^{n} k_{ij} a_j$ is finally written as

$$\sum_{j=1}^{n} k_{ij} a_j = \ldots + k_{i,n-4} a_{n-4} + \underbrace{\left(k_{i,n-3} + \tfrac{1}{2}\gamma k_{i,n-1} + \gamma k_{i,n} \right)}_{\hat{k}_{i,n-3}} a_{n-3} + \underbrace{\left(k_{i,n-2} + \tfrac{1}{2}(1+\delta)k_{i,n-1} + \delta k_{i,n} \right)}_{\hat{k}_{i,n-2}} a_{n-2}. \tag{22}$$

Equation (22) dictates the algorithm which has to be followed for imposing the natural b.c. at the free end B. In brief, the last two columns of the initial matrices (K, M) should be deleted, but before performing this task a linear combination of their elements should be added to the initial $(n-3)$-th and $(n-2)$-th columns according to (22).

As an example, in the particular case of Bézier (Bernstein) polynomials $B_{i,n}(x) = \binom{n}{i} x^i (1-x)^{n-1}$, which is the simplest B-spline in the interval [0, 1], it is trivial to prove that

$$B_{n-3,n}'''(1) = -\alpha, \; B_{n-2,n}'''(1) = 3\alpha, \; B_{n-1,n}'''(1) = -3\alpha, \; B_{n,n}'''(1) = \alpha, \quad \text{with } \alpha = n(n-1)(n-2), \tag{23a}$$

$$B_{n-3,n}''(1) = 0, \quad B_{n-2,n}''(1) = \beta, \quad B_{n-1,n}''(1) = -2\beta, \; B_{n,n}''(1) = \beta, \quad \text{with } \beta = n(n-1), \tag{23b}$$

$$B_{n-3,n}'(1) = 0, \quad B_{n-2,n}'(1) = 0, \quad B_{n-1,n}'(1) = -n, \quad B_{n,n}'(1) = n; \tag{23c}$$

hence, $\gamma = -2$ and $\delta = 3$.

Let us now leave beams and return to real plates. In the case of a *clamped* plate, those columns of matrices (M, K) that correspond to the two layers of control points, which are the closest ones to the boundary, should be deleted. The explanation is the same as that for the clamped point A of the above-mentioned cantilever beam (i.e., by virtue of (21c) and (21d), perpendicularly to the boundary).

In the particular case of a *simply supported* plate, first all columns that correspond to the outermost control points will be deleted. Second, since the normal moment vanishes ($M_n = 0$), the current situation is very similar to (21e), and the concept of (22) can be applied as is.

In the general case of a 2-D plate with arbitrary boundary conditions, the above procedure is generalized as follows. In compact form, the imposition of Neumann b.c. can be written in the form

$$[A_{22} \; A_{2i}] \begin{Bmatrix} a_2 \\ a_i \end{Bmatrix} = \{\mathbb{0}\}, \tag{24}$$

where the elements of the matrices A_{22} and A_{2i} include second and third directional derivatives of the basis functions. The vector a_2 refers to the generalized coefficients that are related to the control points on the Neumann boundary, whereas the vector a_i refers to inner ones.

In the free vibration problem, (6) can be written as

$$[M_{c2} \; M_{ci}] \begin{Bmatrix} \ddot{a}_2 \\ \ddot{a}_i \end{Bmatrix} + [K_{c2} \; K_{ci}] \begin{Bmatrix} a_2 \\ a_i \end{Bmatrix} = \{\mathbb{0}\}. \tag{25}$$

Solving (24) in $\boldsymbol{a}_2$ and then substituting into (25), one finally obtains the standard expression

$$\bar{\boldsymbol{M}}\ddot{\boldsymbol{a}}_i + \bar{\boldsymbol{K}}\boldsymbol{a}_i = \mathbb{0} \tag{26}$$

where

$$\bar{\boldsymbol{M}} = \boldsymbol{M}_{ci} - \boldsymbol{M}_{c2}(\boldsymbol{A}_{22})^{-1}\boldsymbol{A}_{2i}, \qquad \bar{\boldsymbol{K}} = \boldsymbol{K}_{ci} - \boldsymbol{K}_{c2}(\boldsymbol{A}_{22})^{-1}\boldsymbol{A}_{2i}. \tag{27}$$

5. Handling the curved boundaries

The proposed method is based on isoparametric considerations. Therefore the tensor product, which describes the flexure of the plate according to (2), is considered to describe the curved geometry as well. As usual, natural coordinates (ξ, η) normalized in the interval $[0, 1]$ have to be considered.

In general, the analyst has to choose the four corner points (i.e., A, B, C and D, shown in Figure 1, right) on the real curvilinear boundary of the plate, and then define the number and the position of the breakpoints along the four curvilinear parts AB, BC, CD and DA on the boundary, as well as the polynomial degree p. Every collocation point corresponds to a specific pair (ξ, η), which is known in advance.

For the arbitrary curved plate with given collocation points, while the mass matrix continues to be described by the simple product of (5), the fourth-order operator of a shape function (i.e., $\nabla^4 N(x, y) = \partial^4 N/\partial x^4 + 2\,\partial^4 N/\partial x^2\partial y^2 + \partial^4 N/\partial y^4$) is more difficult to compute. Concretely, the computation of the stiffness matrix demands the transformation of $\nabla^4 N(x, y)$ in ξ- and η-coordinates, as outlined in the Appendix.

6. Numerical results

The proposed theory is thoroughly evaluated in two benchmark problems that concern a square thin plate of dimensions $a \times a$ under two different boundary conditions. In addition, at the end of this section, the applicability of the proposed method is shown for a circular plate as well. The first problem refers to a simply supported square plate (SS) whereas the second to a clamped (CL) one. In both cases the numerical solution is compared with:

(1) The previous *cubic B-splines Galerkin–Ritz formulation* [Antes 1974] implemented with a standard 4×4 Gaussian quadrature scheme in an in-house computer code, and

(2) the conventional *finite element method* (FEM) using element SHELL63 of ANSYS version 14.5 on a uniform mesh that coincides with the uniform mesh of breakpoints utilized in the global collocation solution.

(3) The *exact solution*, which is given as [Leissa 1973]

$$f_{ij}[\text{Hz}] = \frac{\lambda_{ij}^2}{2\pi a^2}\left[\frac{Eh^2}{12\rho(1-v^2)}\right]^{1/2}; \quad i = 1, 2, 3\ldots; \; j = 1, 2, 3\ldots, \tag{28}$$

where i and j are the numbers of half-waves in mode shape along x and y axis, respectively, and λ_{ij}^2 is a parameter that depends on the ratio (a/b) of the length over the width of the plate as well as on the type of boundary conditions according to Table 1.

Concerning the proposed global collocation method, we remind that, for a polynomial degree $p = 5$, 6 or 7, then 2×2, 3×3 or 4×4 collocation points per cell (of breakpoints) are chosen, respectively.

type of	λ_{ij}^2 (mode)					
boundary conditions	1	2	3	4	5	6
simply supported [Leissa 1973]	$2\pi^2$ (1, 1)	$5\pi^2$ (2, 1)	$5\pi^2$ (1, 2)	$8\pi^2$ (2, 2)	$10\pi^2$ (3, 1)	$10\pi^2$ (1, 3)
fully clamped [Wieners 1997, p. 38]	35.9852 (1, 1)	73.3938 (2, 1)	73.3938 (1, 2)	108.2165 (2, 2)	131.5808 (3, 1)	132.2048 (1, 3)

Table 1. The values of parameter λ_{ij}^2 and the numbers (i, j) of half-waves for a square plate in bending.

The computational results are presented in the form of errors (in percent, %) of the eigenvalue, $\omega_{ij}^2 = (2\pi f_{ij})^2$:

$$\text{Error}(\%) = \frac{\|\omega_{\text{calculated}}^2 - \omega_{\text{exact}}^2\|}{\omega_{\text{exact}}^2} \times 100. \qquad (29)$$

Example 1 (Simply supported rectangular plate). Depending on the polynomial degree, the results illustrated in Figure 3 show an excellent convergence in terms of mesh density. It is noted that when $p = 5$ (not shown), the global collocation method converges somewhat slower than the FEM solution. In contrast, Figure 3 shows that when $p = 6$ or 7 the numerical solution becomes extremely accurate even when treating the entire plate as a unique cell.

Example 2 (Clamped rectangular plate). Similar results were found in this example as well (see Figure 4). It is noted that the exact solution was taken according to Wieners [1997], who presents more decimal digits than Leissa [1973].

Finally, we show how the particular choice of collocation points affects the solution. Let the knot vector, see (7), be written as $V = \{v_1, \ldots, v_{n+p+1}\}$, where n is the number of control points. Except for the above-mentioned Gaussian points, more sets were determined as follows:

(1) "Demko" abscissae were determined on the basis of "p-2" degree. We used the MATLAB command *chbpnt(knotsx(4:length(knotsx)-3),k-2)*. This way leads to the same number of collocation points as obtained using Gaussian points. It is noted that neither the first abscissa is zero nor the last one is equal to the unit.

(2) "Greville-1" abscissae were again determined on the basis of "p-2" degree. The first four knots were not considered.

(3) "Greville-2" abscissae were now determined on the basis of "p" degree. The first three knots were not considered, and all produced abscissae were used.

Concerning the two first sets (i.e., Demko and Greville-1), it is noted that unlike the second order problems (see [Auricchio et al. 2010; Provatidis 2014]), neither the first abscissa is zero nor the last one is equal to the unit.

The performance of the above-mentioned abscissae as collocation points is shown in Figure 5. One may observe that while for $p = 6$ the Gaussian points are competitive with Demko's abscissae, in contrast
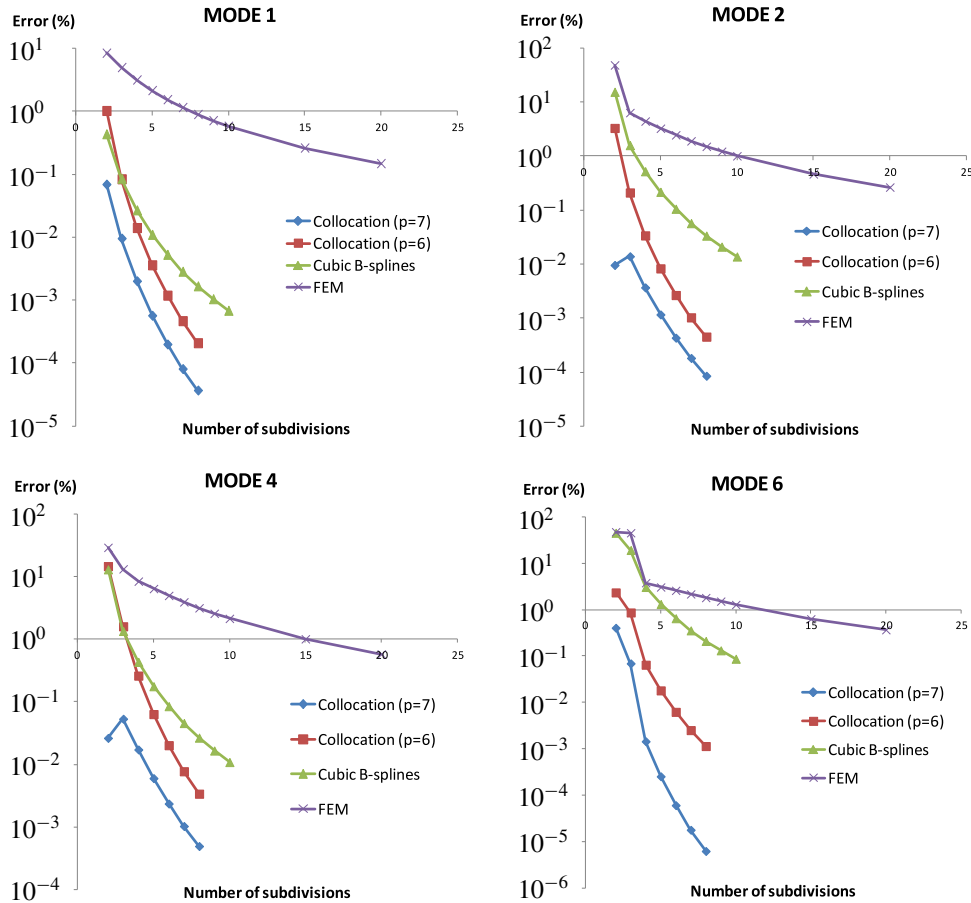
Figure 3. Convergence quality of the first calculated eigenvalues for a simply supported square plate.

to $p = 7$, these are rather superior. Between the two Greville-type abscissae, Greville-2 (based on p-th degree) is superior.

Example 3 (Circular clamped plate). A circular clamped plate of radius $R = 1$ was analyzed and the proposed collocation method was successfully compared with the exact solution [Zhou et al. 2011]. Table 2 presents the numerical results when the collocation points are taken at the location of the Gaussian points. One may observe the excellent and rapid convergence towards the exact solution. It is noted that the minor error that appears at the first natural frequency is probably due to the insufficient number of digital points that literature presents, a matter that has been extensively discussed in [Zhou et al. 2011]. Moreover, the number of equations is shown at the bottom of Table 2.

Concerning conventional plate finite elements (structured mesh using three different types from AN-SYS library), the convergence rate is very slow and the error of the first natural eigenfrequency is considerably greater than that of the proposed collocation method (Table 2), as clearly shown in Table 3.
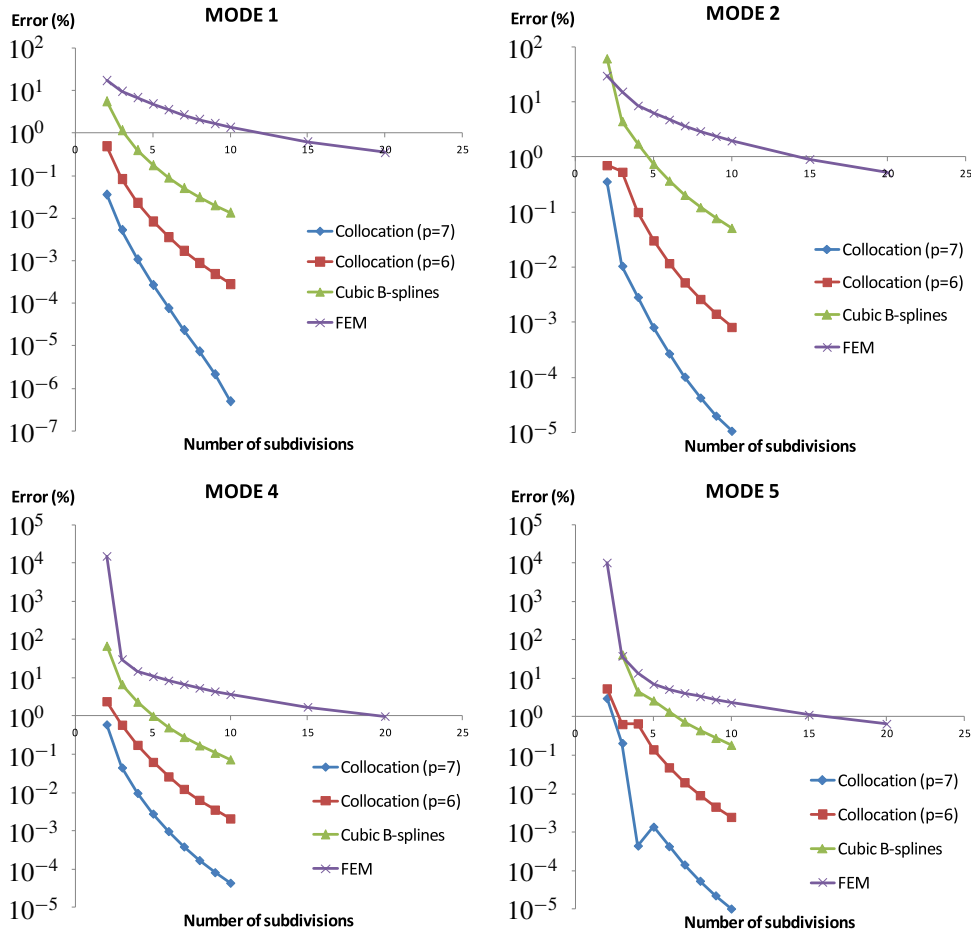
Figure 4. Convergence quality of the first calculated eigenvalues for a clamped square plate.

Regarding the other nine modes, the error is practically maintained at the same level with the first one, thus they are not shown.

7. Discussion

As previously reported in the case of 2-D acoustics [Provatidis 2014], the accuracy of the proposed B-splines collocation method in plate-bending eigenvalue analysis is again excellent. An interesting finding is that in the first two examples (square plate) of this study, the proposed global collocation method converges from lower to higher values, exactly as the FEM (ANSYS) solution behaves. It is noted that similar results with ANSYS (of slightly lower quality) were obtained using an in-house code that implemented the shape functions of the well-known MZC 12-DOF finite element [Melosh 1963] in conjunction with a consistent mass formulation. Therefore, the quality of the general purpose commercial software (one of the most reliable worldwide) or the particular choice of the SHELL63 is not to be

Figure 5. Influence of each particular set of collocation points on the first two eigenvalues for a clamped square plate.

blamed. The superiority of the proposed method is mainly due to the high polynomial degree of the flexural approximation.

Tables 2 and 3 show that for the circular clamped plate, the pattern of convergence is not as clear as it was for the square one, whereas even the three ANSYS types of elements tested also have different convergence patterns, although they converge to very similar values.
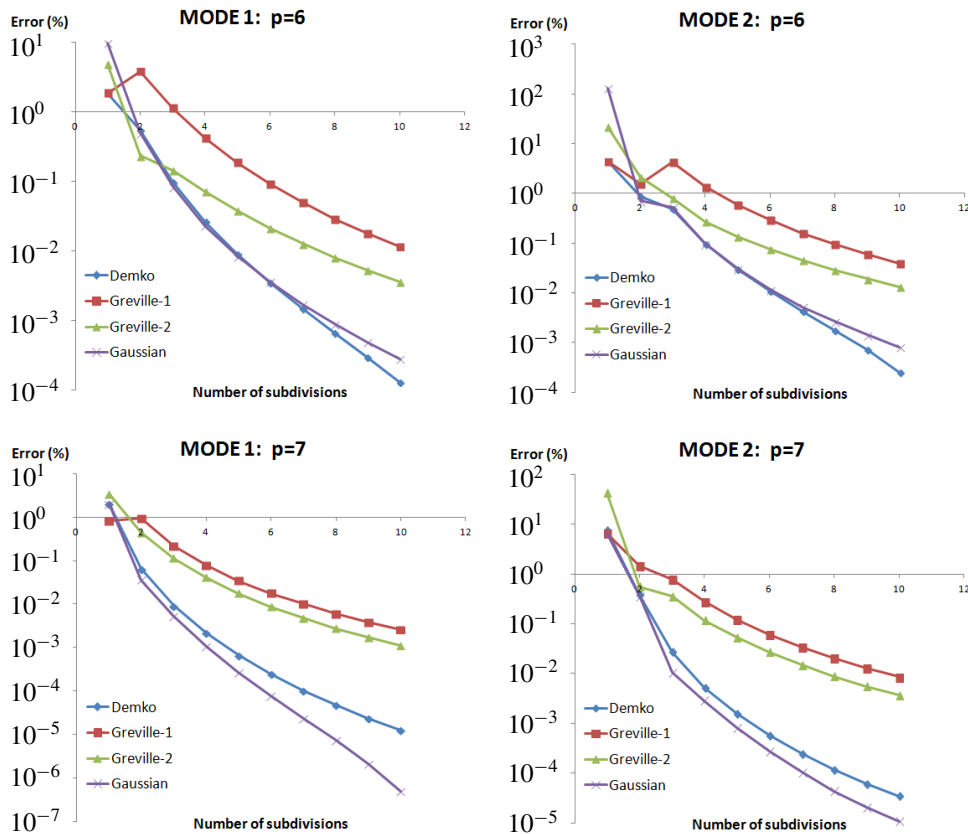
The above-mentioned procedure leads to excellent results but is strictly related to the proposed number of collocation points according to (16)–(19). In principle, an alternative could be to use a Lagrange multiplier scheme according to which the boundary condition at the Neumann part of the boundary is properly added to the equation related to the fulfillment of the partial differential equation. However, the accuracy of this procedure is out of the scope of this paper. For an analog to in-plane elasticity, the interested reader is referred to the Appendix of [Provatidis 2017].

Although this paper is restricted to B-spline collocation, which is a special case of the so-called *global collocation methods* (GCM), a generalization is possible. In more detail, it is worthy to mention that the high polynomial degree in the B-splines representation and the closely related high accuracy in the obtained numerical results characterize all other CAD-based formulations as well. Specifically, B-splines approximation is chronologically the fourth main "station" in CAD history [Provatidis 2014].

mode	λ_{ij}^2	$p = 6$				$p = 7$			
		number of knot spans				number of knot spans			
		2	3	4	6	1	2	3	4
1	10.2158	0.91	−0.03	0.03	0.03	7.17	−0.02	0.04	0.03
2	21.2604	1.31	0.50	−0.03	0.01	−8.04	−0.23	−0.01	0.01
3	21.2604	1.33	0.52	−0.01	0.02	−8.02	−0.22	0.00	0.03
4	34.8770	−7.55	−0.07	−0.14	0.02	−21.83	−0.89	−0.03	−0.02
5	34.8770	4.32	0.96	0.62	0.02	277.49	3.34	0.03	0.02
6	39.7711	−6.96	−0.00	0.62	0.02	262.93	3.31	0.04	−0.02
7	51.0306	−1.49	0.74	0.32	0.01	217.25	1.91	−0.00	0.00
8	51.0306	−1.48	0.74	0.32	0.01	217.27	1.91	−0.00	0.00
9	60.8287	3.93	1.83	0.19	−0.03	191.31	2.25	−0.25	0.02
number of equations		36	81	144	324	16	64	144	256

Table 2. Errors (in %) of the calculated natural frequencies for a clamped circular plate of unit radius. Natural frequencies were calculated using the proposed B-splines collocation method based on the Gaussian points, for piecewise polynomial degrees $p = 6$ and 7. For the exact parameter λ_{ij}^2, see (28).

element type (ANSYS)	number of circumferential uniform segments per quarter of the circle ($n_\xi = n_\eta$)			
	8	16	32	64
SHELL43	6.55	4.13	3.57	3.43
SHELL63	2.44	3.14	3.34	3.39
SHELL181	10.02	4.97	3.77	3.47
number of unrestrained nodal points	49	225	961	3969
number of equations	147	675	2883	11907

Table 3. Errors (in %) of the calculated first natural frequency for a clamped circular plate of unit radius. This demonstrates the quality of the calculated first natural frequency using several types of finite elements (ANSYS library). Value for the exact parameter λ_{ij}^2, see (28), is 10.2158. For the number of equations, all equations have unrestrained bending DOF, excepting the membrane behavior.

Taking the mid-1960s as a starting point, the five consecutive stations in CAD approximation theory are (see, for example, [Farin et al. 2002]):

 (1) Coons interpolation (in 1967),

 (2) Gordon transfinite interpolation (in 1970),

 (3) Bézier curves,

(4) B-splines and

(5) NURBS.

In general, and independently on the governing partial differential equation, the boundary value or the eigenvalue problem can be solved using one of the aforementioned five CAD-based approximations, and one of the basic computational methods: Ritz–Galerkin, boundary element and collocation, among others. These fifteen combinations increase by a factor equal to two when considering triangular patches (Barnhill's approximation: one more CAD-station) in addition to the quadrilateral ones.

Let us examine the above-mentioned four interpolations, one-by-one:

(1) Concerning the *boundary-only* Coons interpolation (first CAD-station), the GCM is not applicable at all. The reason is due to the elimination of all boundary DOF, a matter discussed in detail elsewhere [Provatidis 2014]. In contrast, the same interpolation performs well in the static plate analysis in conjunction with the Ritz–Galerkin formulation [Provatidis and Angelidis 2014].

(2) Although numerical results were not presented, the GCM performs well in conjunction with the *transfinite* interpolation (second CAD-station). Similarly, transfinite interpolation performs well in conjunction with the Ritz–Galerkin formulation [Provatidis 2008c]. This is due to the existence of internal nodes that raise the accuracy of the approximation.

(3) Although not mentioned so far, the numerical results of this paper include the Bézier interpolation (third CAD-station) as well. This happens because when using one subdivision of each side (shown by the left extreme points in Figures 3 and 4), B-spline degenerates to Bernstein polynomials.

(4) B-splines collocation performed well (see Figures 3 and 4). Similarly, when B-splines approximation is applied in conjunction with the Ritz–Galerkin formulation (not presented), the quality of the numerical solution is high, as summarized in [Höllig 2003].

8. Conclusions

It was shown that the proposed global collocation method has excellent performance in the eigenvalue analysis of simply supported and clamped plates. For a specified number of uniformly arranged break-points, the procedure is more accurate than the conventional finite element method as well as the cubic B-splines Galerkin–Ritz formulation. Although results were presented for only the eigenvalue problem, the static analysis shows a similar behavior. When the structure is of complex shape, it is suggested to subdivide it into large macroelements of regular shape and apply compatibility and equilibrium conditions along the interfaces. A similar behavior is anticipated for shell structures.

Appendix: The biharmonic function in the (ξ, η)-space

For each collocation point $P(\xi, \eta)$, which is known in the unit square of a reference (ξ, η)-plane, the proposed method needs to handle the Cartesian coordinates in the form $x(\xi, \eta)$ and $y(\xi, \eta)$. Since the global shape functions $N(x, y)$, which appear in (3), are tensor products of univariate basis functions (here, B-splines) that are known in the (ξ, η)-space, the biharmonic operator

$$\nabla^4 N(x, y) = \frac{\partial^4 N(x, y)}{\partial x^4} + 2\frac{\partial^4 N(x, y)}{\partial x^2 \partial y^2} + \frac{\partial^4 N(x, y)}{\partial y^4}, \tag{A.1}$$

has to be transformed from x and y into ξ and η.

This is accomplished first by calculating the Jacobian matrix $\boldsymbol{J} = \left[\begin{smallmatrix} \partial x/\partial \xi & \partial y/\partial \xi \\ \partial x/\partial \eta & \partial y/\partial \eta \end{smallmatrix}\right]$ at the collocation point $P(x(\xi, \eta), y(\xi, \eta))$. Then, by numerical inversion, the four terms of its inverse $\boldsymbol{J}^{-1}$ are found:

$$\boldsymbol{J}^{-1} = \begin{bmatrix} \dfrac{\partial \xi}{\partial x} & \dfrac{\partial \eta}{\partial x} \\ \dfrac{\partial \xi}{\partial y} & \dfrac{\partial \eta}{\partial y} \end{bmatrix}. \tag{A.2}$$

Second, every term that appears in (A.1) is processed in a systematic way as follows. The chain rule is successively applied on an arbitrary continuous and differentiable function $F(x, y)$, whence the following three principal formulas are derived:

$$\frac{\partial^2 F}{\partial x^2} = \frac{\partial^2 F}{\partial \xi^2} \left(\frac{\partial \xi}{\partial x}\right)^2 + 2\frac{\partial^2 F}{\partial \xi \partial \eta} \frac{\partial \xi}{\partial x} \frac{\partial \eta}{\partial x} + \frac{\partial^2 F}{\partial \eta^2} \left(\frac{\partial \eta}{\partial x}\right)^2 + \frac{\partial F}{\partial \xi} \frac{\partial^2 \xi}{\partial x^2} + \frac{\partial F}{\partial \eta} \frac{\partial^2 \eta}{\partial x^2}, \tag{A.3}$$

$$\frac{\partial^2 F}{\partial x \partial y} = \frac{\partial^2 F}{\partial \xi^2} \frac{\partial \xi}{\partial x} \frac{\partial \xi}{\partial y} + \frac{\partial^2 F}{\partial \xi \partial \eta} \left(\frac{\partial \xi}{\partial x} \frac{\partial \eta}{\partial y} + \frac{\partial \xi}{\partial y} \frac{\partial \eta}{\partial x}\right) + \frac{\partial^2 F}{\partial \eta^2} \frac{\partial \eta}{\partial x} \frac{\partial \eta}{\partial y} + \frac{\partial F}{\partial \xi} \frac{\partial^2 \xi}{\partial x \partial y} + \frac{\partial F}{\partial \eta} \frac{\partial^2 \eta}{\partial x \partial y}, \tag{A.4}$$

$$\frac{\partial^2 F}{\partial y^2} = \frac{\partial^2 F}{\partial \xi^2} \left(\frac{\partial \xi}{\partial y}\right)^2 + 2\frac{\partial^2 F}{\partial \xi \partial \eta} \frac{\partial \xi}{\partial y} \frac{\partial \eta}{\partial y} + \frac{\partial^2 F}{\partial \eta^2} \left(\frac{\partial \eta}{\partial y}\right)^2 + \frac{\partial F}{\partial \xi} \frac{\partial^2 \xi}{\partial y^2} + \frac{\partial F}{\partial \eta} \frac{\partial^2 \eta}{\partial y^2}. \tag{A.5}$$

It is noted that (A.3) and (A.5) have previously assisted the implementation of the collocation method in potential (Laplace and Poisson) type problems [Provatidis 2009].

As a third step in the above equations (A.3), (A.4), and (A.5), the arbitrary function F is replaced by the shape function N, thus respectively yielding

$$\frac{\partial^2 N}{\partial x^2} = \frac{\partial^2 N}{\partial \xi^2} \left(\frac{\partial \xi}{\partial x}\right)^2 + 2\frac{\partial^2 N}{\partial \xi \partial \eta} \frac{\partial \xi}{\partial x} \frac{\partial \eta}{\partial x} + \frac{\partial^2 N}{\partial \eta^2} \left(\frac{\partial \eta}{\partial x}\right)^2 + \frac{\partial N}{\partial \xi} \frac{\partial^2 \xi}{\partial x^2} + \frac{\partial N}{\partial \eta} \frac{\partial^2 \eta}{\partial x^2}, \tag{A.6}$$

$$\frac{\partial^2 N}{\partial x \partial y} = \frac{\partial^2 N}{\partial \xi^2} \frac{\partial \xi}{\partial x} \frac{\partial \xi}{\partial y} + \frac{\partial^2 N}{\partial \xi \partial \eta} \left(\frac{\partial \xi}{\partial x} \frac{\partial \eta}{\partial y} + \frac{\partial \xi}{\partial y} \frac{\partial \eta}{\partial x}\right) + \frac{\partial^2 N}{\partial \eta^2} \frac{\partial \eta}{\partial x} \frac{\partial \eta}{\partial y} + \frac{\partial N}{\partial \xi} \frac{\partial^2 \xi}{\partial x \partial y} + \frac{\partial N}{\partial \eta} \frac{\partial^2 \eta}{\partial x \partial y}, \tag{A.7}$$

$$\frac{\partial^2 N}{\partial y^2} = \frac{\partial^2 N}{\partial \xi^2} \left(\frac{\partial \xi}{\partial y}\right)^2 + 2\frac{\partial^2 N}{\partial \xi \partial \eta} \frac{\partial \xi}{\partial y} \frac{\partial \eta}{\partial y} + \frac{\partial^2 N}{\partial \eta^2} \left(\frac{\partial \eta}{\partial y}\right)^2 + \frac{\partial N}{\partial \xi} \frac{\partial^2 \xi}{\partial y^2} + \frac{\partial N}{\partial \eta} \frac{\partial^2 \eta}{\partial y^2}. \tag{A.8}$$

As a fourth step, the function F in (A.3) is replaced by $\partial^2 N/\partial x^2$ in the form of (A.6); in this way the term $\partial^4 N/\partial x^4$ is produced. Similarly, the function F in (A.4) is replaced by $\partial^2 N/\partial x \partial y$ in the form of (A.7), thus the term $\partial^4 N/\partial x^2 \partial y^2$ is produced. Finally, the function F in (A.5) is replaced by $\partial^2 N/\partial y^2$ in the form of (A.8), thus the final desired term $\partial^4 N/\partial y^4$ is produced.

Since each of (A.3) to (A.5) consists of five terms, the above procedure leads to $5 \times 5 = 25$ fundamental terms. But since all the aforementioned 25 fundamental terms are partial derivatives of rather complicated terms, which are multiples of up to three secondary functions, the further procedure is highly facilitated by systematically adopting the following identity (generalized chain rule):

$$\frac{\partial^2}{\partial \xi \partial \eta}(f \cdot g \cdot h) = \frac{\partial^2 f}{\partial \xi \partial \eta} \cdot g \cdot h + f \cdot \frac{\partial^2 g}{\partial \xi \partial \eta} \cdot h + f \cdot g \cdot \frac{\partial^2 h}{\partial \xi \partial \eta}$$
$$+ \left(\frac{\partial f}{\partial \eta} \cdot \frac{\partial g}{\partial \xi} + \frac{\partial f}{\partial \xi} \cdot \frac{\partial g}{\partial \eta}\right) \cdot h + \left(\frac{\partial f}{\partial \eta} \cdot \frac{\partial h}{\partial \xi} + \frac{\partial f}{\partial \xi} \cdot \frac{\partial h}{\partial \eta}\right) \cdot g + \left(\frac{\partial g}{\partial \eta} \cdot \frac{\partial h}{\partial \xi} + \frac{\partial g}{\partial \xi} \cdot \frac{\partial h}{\partial \eta}\right) \cdot f. \tag{A.9}$$

Obviously, (A.9) covers all necessary cases. For example, when dealing with $\partial^2/\partial\xi^2(fgh)$, one can easily consider that $\eta = \xi$. Also, when dealing with any partial derivative of (fg), one can easily apply (A.9) and taking $h = 1$.

Following the above procedure, rather lengthy expressions are derived. For example, the final result for the first term of (A.1) is given by

$$
\begin{aligned}
\frac{\partial^4 N}{\partial x^4} = & \frac{\partial^4 N}{\partial \xi^4}\cdot\left(\frac{\partial\xi}{\partial x}\right)^4 + \frac{\partial^4 N}{\partial\eta^4}\cdot\left(\frac{\partial\eta}{\partial x}\right)^4 + \frac{\partial^4 N}{\partial\xi^3\partial\eta}\cdot\left[4\left(\frac{\partial\xi}{\partial x}\right)^3\left(\frac{\partial\eta}{\partial x}\right)\right] + \frac{\partial^4 N}{\partial\xi^2\partial\eta^2}\cdot\left[6\left(\frac{\partial\xi}{\partial x}\right)^2\left(\frac{\partial\eta}{\partial x}\right)^2\right] \\
& + \frac{\partial^4 N}{\partial\xi\partial\eta^3}\cdot\left[4\left(\frac{\partial\xi}{\partial x}\right)\left(\frac{\partial\eta}{\partial x}\right)^3\right] + \frac{\partial^3 N}{\partial\xi^3}\cdot\left[6\left(\frac{\partial\xi}{\partial x}\right)^2\left(\frac{\partial^2\xi}{\partial x^2}\right)\right] + \frac{\partial^3 N}{\partial\eta^3}\cdot\left[6\left(\frac{\partial\eta}{\partial x}\right)^2\left(\frac{\partial^2\eta}{\partial x^2}\right)\right] \\
& + \frac{\partial^3 N}{\partial\xi^2\partial\eta}\cdot\left[12\left(\frac{\partial\xi}{\partial x}\right)\left(\frac{\partial\eta}{\partial x}\right)\left(\frac{\partial^2\xi}{\partial x^2}\right) + 6\left(\frac{\partial\xi}{\partial x}\right)^2\left(\frac{\partial^2\eta}{\partial x^2}\right)\right] \\
& + \frac{\partial^3 N}{\partial\xi\partial\eta^2}\cdot\left[12\left(\frac{\partial\xi}{\partial x}\right)\left(\frac{\partial\eta}{\partial x}\right)\left(\frac{\partial^2\eta}{\partial x^2}\right) + 6\left(\frac{\partial\eta}{\partial x}\right)^2\left(\frac{\partial^2\xi}{\partial x^2}\right)\right] \\
& + \frac{\partial^2 N}{\partial\xi^2}\cdot\left[4\left(\frac{\partial\xi}{\partial x}\right)\left(\frac{\partial^3\xi}{\partial x^3}\right) + 3\left(\frac{\partial^2\xi}{\partial x^2}\right)^2\right] + \frac{\partial^2 N}{\partial\eta^2}\cdot\left[4\left(\frac{\partial\eta}{\partial x}\right)\left(\frac{\partial^3\eta}{\partial x^3}\right) + 3\left(\frac{\partial^2\eta}{\partial x^2}\right)^2\right] \\
& + \frac{\partial^2 N}{\partial\xi\partial\eta}\cdot\left[4\left(\frac{\partial\xi}{\partial x}\right)\left(\frac{\partial^3\eta}{\partial x^3}\right) + 4\left(\frac{\partial\eta}{\partial x}\right)\left(\frac{\partial^3\xi}{\partial x^3}\right) + 6\left(\frac{\partial^2\xi}{\partial x^2}\right)\left(\frac{\partial^2\eta}{\partial x^2}\right)\right] \\
& + \frac{\partial N}{\partial\xi}\cdot\left(\frac{\partial^4\xi}{\partial x^4}\right) + \frac{\partial N}{\partial\eta}\cdot\left(\frac{\partial^4\eta}{\partial x^4}\right).
\end{aligned}
\tag{A.10}
$$

One may observe that the right part of (A.10) includes all partial derivatives of the shape function N, starting from the fourth derivative, $\partial^4 N/\partial\xi^4$, and finishing with the first one, $\partial N/\partial\eta$.

References

[Akhras and Li 2011] G. Akhras and W. Li, "Stability and free vibration analysis of thick piezoelectric composite plates using spline finite strip method", *Int. J. Mech. Sci.* **53**:8 (2011), 575–584.

[Antes 1974] H. Antes, "Bicubic fundamental splines in plate bending", *Int. J. Numer. Methods Eng.* **8**:3 (1974), 503–511.

[Auricchio et al. 2010] F. Auricchio, L. Beirão da Veiga, T. J. R. Hughes, A. Reali, and G. Sangalli, "Isogeometric collocation methods", *Math. Models Methods Appl. Sci.* **20**:11 (2010), 2075–2107.

[Bathe 1996] K. J. Bathe, *Finite element procedures*, Prentice-Hall, New Jersey, 1996.

[de Boor 1972] C. de Boor, "On calculating with *B*-splines", *J. Approx. Theory* **6**:1 (1972), 50–62.

[de Boor and Swartz 1973] C. de Boor and B. Swartz, "Collocation at Gaussian points", *SIAM J. Numer. Anal.* **10**:4 (1973), 582–606.

[Cheng and Dade 1990] S. P. Cheng and C. Dade, "Dynamic analysis of stiffened plates and shells using spline gauss collocation method", *Comput. Struct.* **36**:4 (1990), 623–629.

[Cottrell et al. 2009] J. A. Cottrell, T. J. R. Hughes, and Y. Bazilevs, *Isogeometric analysis: towards integration of CAD and FEA*, Wiley, Chichester, England, 2009.

[Dawe and Wang 1995] D. J. Dawe and S. Wang, "Spline finite strip analysis of the buckling and vibration of rectangular composite laminated plates", *Int. J. Mech. Sci.* **37**:6 (1995), 645–667.

[Echter et al. 2013] R. Echter, B. Oesterle, and M. Bischoff, "A hierarchic family of isogeometric shell finite elements", *Comput. Methods Appl. Mech. Eng.* **254** (2013), 170–180.

[Fan and Luah 1995] S. C. Fan and M. H. Luah, "Free vibration analysis of arbitrary thin shell structures by using spline finite element", *J. Sound Vib.* **179**:5 (1995), 763–776.

[Farin et al. 2002] G. Farin, J. Hoschek, and M.-S. Kim (editors), *Handbook of computer aided geometric design*, Elsevier, Amsterdam, 2002.

[Filippatos 2010] A. Filippatos, *Extraction of eigenfrequencies in acoustic cavities and elastic structures using the global collocation method*, Diploma work, National Technical University of Athens, 2010, available at http://users.ntua.gr/cprovat/yliko/Filippatos_Diploma_Thesis.pdf. In Greek.

[Golmakani and Mehrabian 2014] M. E. Golmakani and M. Mehrabian, "Nonlinear bending analysis of ring-stiffened circular and annular general angle-ply laminated plates with various boundary conditions", *Mech. Res. Commun.* **59** (2014), 42–50.

[Grigorenko and Kryukov 1995] Y. M. Grigorenko and N. N. Kryukov, "Solution of problems in the theory of plates and shells using spline functions (survey)", *Prikl. Mekh.* **31**:6 (1995), 3–27. In Russian; translated in *Internat. Appl. Mech.* **31**:6 (1995), 413–434.

[Gupta et al. 1991] A. Gupta, J. Kiusalaas, and M. Saraph, "Cubic B-spline for finite element analysis of axisymmetric shells", *Comput. Struct.* **38**:4 (1991), 463–468.

[Han et al. 2007] J.-G. Han, W.-X. Ren, and Y. Huang, "A wavelet-based stochastic finite element method of thin plate bending", *Appl. Math. Model.* **31**:2 (2007), 181–193.

[Höllig 2003] K. Höllig, *Finite element methods with B-splines*, Frontiers in Applied Mathematics **26**, Society for Industrial and Applied Mathematics, Philadelphia, 2003.

[Hughes et al. 2010] T. J. R. Hughes, A. Reali, and G. Sangalli, "Efficient quadrature for NURBS-based isogeometric analysis", *Comput. Methods Appl. Mech. Eng.* **199**:5–8 (2010), 301–313.

[Kapoor and Kapania 2012] H. Kapoor and R. K. Kapania, "Geometrically nonlinear NURBS isogeometric finite element analysis of laminated composite plates", *Compos. Struct.* **94**:12 (2012), 3434–3447.

[Kolli and Chandrashekhara 1997] M. Kolli and K. Chandrashekhara, "Non-linear static and dynamic analysis of stiffened laminated plates", *Int. J. Non-Linear Mech.* **32**:1 (1997), 89–101.

[Leissa 1973] A. W. Leissa, "The free vibration of rectangular plates", *J. Sound Vib.* **31**:3 (1973), 257–293.

[Li and Chen 2014] B. Li and X. Chen, "Wavelet-based numerical analysis: a review and classification", *Finite Elem. Anal. Des.* **81** (2014), 14–31.

[Melosh 1963] R. J. Melosh, "Basis for derivation of matrices for the direct stiffness method", *AIAA J.* **1**:7 (1963), 1631–1637.

[Park et al. 2008] T. Park, S.-Y. Lee, J. W. Seo, and G. Z. Voyiadjis, "Structural dynamic behavior of skew sandwich plates with laminated composite faces", *Compos. B Eng.* **39**:2 (2008), 316–326.

[Patlashenko and Weller 1995] I. Patlashenko and T. Weller, "Two-dimensional spline collocation method for nonlinear analysis of laminated panels", *Comput. Struct.* **57**:1 (1995), 131–139.

[Peng-Cheng et al. 1987] S. Peng-Cheng, H. Dade, and W. Zongmu, "Static, vibration and stability analysis of stiffened plates using B spline functions", *Comput. Struct.* **27**:1 (1987), 73–78.

[Piegl and Tiller 1995] L. Piegl and W. Tiller, *The NURBS Book*, Springer, Berlin, 1995.

[Provatidis 2004] C. G. Provatidis, "Coons-patch macroelements in two-dimensional eigenvalue and scalar wave propagation problems", *Comput. Struct.* **82**:4–5 (2004), 383–395.

[Provatidis 2006] C. G. Provatidis, "Transient elastodynamic analysis of two-dimensional structures using Coons-patch macroelements", *Int. J. Solids Struct.* **43**:22–23 (2006), 6688–6706.

[Provatidis 2008a] C. G. Provatidis, "Free vibration analysis of elastic rods using global collocation", *Arch. Appl. Mech.* **78**:4 (2008), 241–250.

[Provatidis 2008b] C. G. Provatidis, "Global collocation method for 2-D rectangular domains", *J. Mech. Mater. Struct.* **3**:1 (2008), 185–194.

[Provatidis 2008c] C. G. Provatidis, "Plate bending analysis using transfinite interpolation", in *6th GRACM International Congress on Computational Mechanics* (Thessaloniki, 2008), edited by D. Talaslidis et al., Sofia Publishers, Thessaloniki, 2008. CD version published by VK-4M Civil Engineering Software Company, Athens.

[Provatidis 2009] C. G. Provatidis, "Integration-free Coons macroelements for the solution of 2D Poisson problems", *Int. J. Numer. Methods Eng.* **77**:4 (2009), 536–557.

[Provatidis 2012] C. G. Provatidis, "Two-dimensional elastostatic analysis using Coons–Gordon interpolation", *Meccanica (Milano)* **47**:4 (2012), 951–967.

[Provatidis 2013] C. G. Provatidis, "A review on attempts towards CAD/CAE integration using macroelements", *Comput. Res.* **1**:3 (2013), 61–84.

[Provatidis 2014] C. G. Provatidis, "B-splines collocation eigenanalysis of 2D acoustic problems", *J. Mech. Mater. Struct.* **9**:3 (2014), 259–285.

[Provatidis 2017] C. G. Provatidis, "CAD-based collocation eigenanalysis of 2-D elastic structures", *Comput. Struct.* **182** (2017), 55–73.

[Provatidis and Angelidis 2014] C. G. Provatidis and D. I. Angelidis, "Performance of Coons' macroelements in plate bending analysis", *Int. J. Comput. Methods Eng. Sci. Mech.* **15**:2 (2014), 110–125.

[Provatidis and Ioannou 2010] C. G. Provatidis and K. S. Ioannou, "Static analysis of two-dimensional elastic structures using global collocation", *Arch. Appl. Mech.* **80**:4 (2010), 389–400.

[Reddy and Palaninathan 1999] A. R. K. Reddy and R. Palaninathan, "Free vibration of skew laminates", *Comput. Struct.* **70**:4 (1999), 415–423.

[Tran et al. 2013] L. V. Tran, A. J. M. Ferreira, and H. Nguyen-Xuan, "Isogeometric analysis of functionally graded plates using higher-order shear deformation theory", *Compos. B Eng.* **51** (2013), 368–383.

[Valizadeh et al. 2013] N. Valizadeh, S. Natarajan, O. A. Gonzalez-Estrada, T. Rabczuk, T. Q. Bui, and S. P. A. Bordas, "NURBS-based finite element analysis of functionally graded plates: static bending, vibration, buckling and flutter", *Compos. Struct.* **99** (2013), 309–326.

[Wieners 1997] C. Wieners, "Bounds for the *N* lowest eigenvalues of fourth-order boundary value problems", *Computing* **59**:1 (1997), 29–41.

[Zhang et al. 2010] X. Zhang, X. Chen, X. Wang, and Z. He, "Multivariable finite elements based on B-spline wavelet on the interval for thin plate static and vibration analysis", *Finite Elem. Anal. Des.* **46**:5 (2010), 416–427.

[Zhou et al. 2011] Z. H. Zhou, K. W. Wong, X. S. Xu, and A. Y. T. Leung, "Natural vibration of circular and annular thin plates by Hamiltonian approach", *J. Sound Vib.* **330**:5 (2011), 1005–1017.

CHRISTOPHER G. PROVATIDIS: cprovat@central.ntua.gr
School of Mechanical Engineering, National Technical University of Athens, Heroon Polytechniou 9, Zografou Campus, 15780 Athens, Greece

■
■msp

SHEAR CAPACITY
OF T-SHAPED DIAPHRAGM-THROUGH JOINTS
OF CFST COLUMNS

BIN RONG, RUI LIU, RUOYU ZHANG, SHUAI LIU AND APOSTOLOS FAFITIS

Diaphragm-through joints between rectangular concrete-filled steel tubular (CFST) columns and steel beams have been widely used in engineering design. In order to investigate the shear capacity of T-shaped diaphragm-through joints, three such joints were tested under seismic cyclic loading. The test results showed that the main contributors to the shear capacity of the joint are the core concrete and the steel tube. However, the flanges of the steel tube have little effect on the shear capacity. In addition, based on the principle of deformation coordination, a calculation method of shear force-deformation skeleton curve for T-shaped diaphragm-through joints is proposed. The theoretical predictions of the method are well fitted with the experimental results.

1. Introduction

In recent years, concrete-filled steel tubular (CFST) columns have been widely used in practical applications due to their benefits of excellent mechanical behavior and pleasing architectural advantages over conventional columns, particularly in terms of their high strength-to-weight ratio, high flexural stiffness, and aesthetic appearance. Beam to column joints are the main components that transmit loads in the whole structure. Diaphragm-through joints between rectangular CFST columns and steel H-shaped beams have concise form, a clear force transmission mechanism and are easy to install. Thus the diaphragm-through joint has become increasingly popular in high-rise buildings.

A large amount of experimental research and number of theoretical analyses have been conducted on the diaphragm-through joints between CFST columns and steel H-shaped beams [Zhang et al. 2012; Sheet et al. 2013; Qin et al. 2014]. The calculation formula in the AIJ specification [AIJ 1987] proposed by the Architectural Institute of Japan took into account the shear capacity of both the steel tube and the core concrete. The formula was derived directly by superposing the shear capacity of steel and concrete. Fujimoto [2000], Fukumoto and Morita [2005] conducted a series of experiments on the panel zone of internal-diaphragm joints and diaphragm-through joints between CFST columns and steel beams. They proposed the constrained compression truss model of the concrete core. Based on the superposition of shear force-deformation relations for the steel tube and concrete core, a practical calculation method was provided as a trilinear model with a yield strength and an ultimate strength for the panel zone. Lu and Yu [2000] conducted an experiment on five internal-diaphragm joints. The researchers also proposed a formula for the prediction of the yield strength of the joint by superposing the yield strength of each member in the joint, which is derived from the yield line theory. Wu, Chung, Tsai, Lu, and Huang [Wu et al. 2006] conducted a series of cyclic loading experiments on bidirectional bolted beams to CFST

column connections. They established a mechanical model to derive theoretical equations for calculating the stiffness, the yielding shear capacity and the ultimate shear capacity of the panel zone. Nie, Qin, and Cai [Nie et al. 2008] conducted a series of cyclic loading experiments on three types of connections inside the frame. Based on the experimental studies, the researchers proposed a calculation method of shear force-deformation skeleton curves by superposition.

Liu et al. [Liu et al. 2014] compared three main calculation methods for the shear capacity of joints between CFST columns and steel beams. The theoretical results were verified with test data. It was found that the applicability of the calculation methods was different between interior and exterior joints. The yield load of exterior joints was significantly nonconservative and the ultimate loads presented scattered results for the existent specimens. The number of exterior joint specimens was small. So further research is needed to develop procedures for accurate assessment of the panel zone shear capacity for exterior joints.

In order to investigate the shear capacity of exterior diaphragm-through joints, three T-shaped joints were tested under seismic cyclic loading in this study. The specimens were designed based on the principle of "strong members and weak joints" to ensure the shear failure in the panel zone of joints. Based on the test results, a nonlinear shear force-deformation model is proposed for the panel zone of exterior diaphragm-through joints between CFST columns and steel beams. This model is verified by experimental results based on various parameters.

2. Experimental design

2.1. *Specimen design.* Three full-sized T-shaped specimens have been designed to investigate the shear capacity of exterior diaphragm-through joints subjected to seismic cyclic loading. Under seismic actions, story drift occurs in the structure, and the inflection points of beam and column are assumed to occur at the mid-point. The panel zone of the joint is the center of the specimens, and the midpoints of the columns and beams are the boundaries of the specimens. In this T-shaped substructure, three hinges are used to simulate the upper, lower, left or right inflection points to perform the simulation. In order to evaluate the shear capacity of the panel zone, the specimens were designed to be "strong members and weak joints" to ensure the shear failure in the panel zone. This was achieved by making the thickness of the steel tube wall of the panel zone thinner than the ones used in practical engineering.

The thickness of the steel tube wall of the panel zone and diaphragm-through, and the strength of concrete in steel tube are changed for comparison. The dimensions of each specimen are listed in Table 1. Details of panel zone are shown in Figure 1.

Specimen	Column Section (mm)	Beam Section (mm)	Column Section in Panel Zone (mm)	Thickness of Diaphragm (mm)	Concrete
TDTC-1			$200 \times 200 \times 6$	16	C30
TDTC-2	$200 \times 200 \times 12$	H$250 \times 200 \times 8 \times 12$	$200 \times 200 \times 6$	14	C40
TDTC-3			$200 \times 200 \times 8$	14	C30

Table 1. Dimensions of specimens.
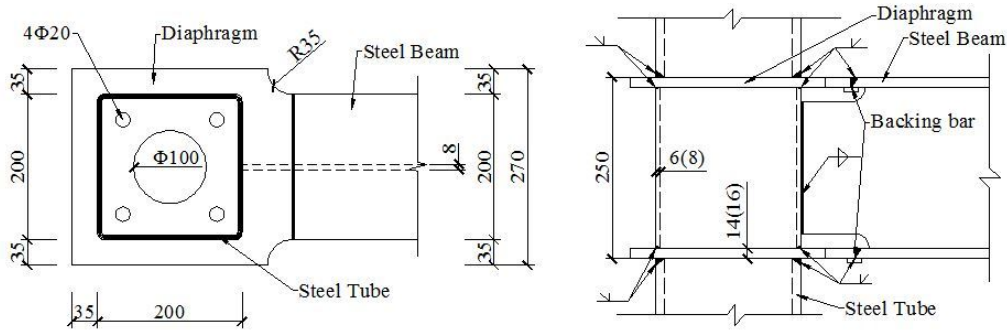
Figure 1. Details of panel zone

Thickness of steel (mm)	f_y(N/mm^2)	f_u(N/mm^2)
6	268.9	387.9
8	249.6	373.1
12	313.8	439.8
14	252.2	414.6
16	250.1	407.3

Table 2. Material properties of steel (f_y is the yield strength and f_u is the tensile strength).

The steel tubes of the specimens were made of cold-formed square steel tube. The beams of the specimens were made of H-shaped steel. The steel tubes were discontinuous at the position of diaphragms, and the diaphragms went through the steel tubes. All the steel components of the joint connected to each other by full penetration butt welds with backing bars. They were processed and welded together in the factory in advance. Then the steel tube was filled with concrete. The specimens were transported to the laboratory after the curing of concrete was completed in the factory.

The strength grade of steel of all the specimens was Q235B. According to the "metallic materials at room temperature tensile test method" (GB/T228-2002), standard tensile pieces of steel from steel tubes and beams of the specimens were cut. The dimension of the tension bar was 180 mm × 40 mm. The material properties of the steel were tested on the universal testing machine, as shown in Figure 2. The stress-strain curves of all thicknesses of steel are shown in Figure 3. The material properties of the steel are listed in Table 2. The grades of concrete in the steel tubes were C30 and C40. According to the "concrete strength inspection and evaluation standards" (GB/T50107-2010), standard concrete test cubes were made when concrete was cast into steel tubes. The dimension of the concrete cubes was 150 mm × 150 mm × 150 mm. The concrete cubes were cured under the same conditions with specimens for 28 days. Compression strength of the concrete cubes was tested on the electrohydraulic universal testing machine, as shown in Figure 2. The stress-strain curves of the two grades of concrete are shown in Figure 3. The material properties of the concrete are listed in Table 3.
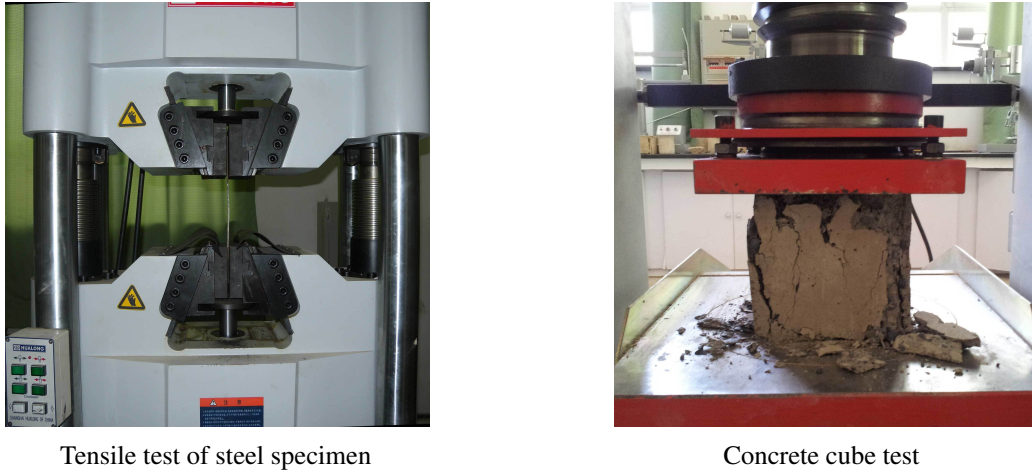
Tensile test of steel specimen   Concrete cube test

Figure 2. Material property test.

Stress-strain curves of steel   Stress-strain curves of concrete
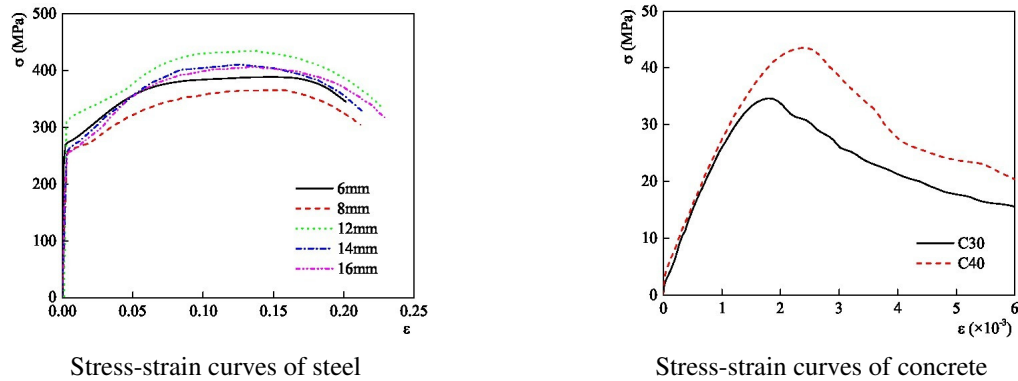
Figure 3. Stress-strain curves of material test results.

Grade of concrete	f_{cu}(N/mm^2)	f_c'(N/mm^2)
C30	34.63	27.36
C40	43.55	34.40

Table 3. Grade of concrete (f_{cu} is the cube compressive strength of concrete and f_c' is the cylinder compressive strength of concrete).

2.2. *Test setup and loading procedure.*

There are two kinds of common loading methods in the joint test, which are loading at the column end and loading at the beam end, respectively. When the research would be affected by the second order effects of gravity on the displacement of the column under horizontal load, the loading at the column end method should be adopted. Since the mechanical properties in the

Schematic drawing of test setup   Photo of test setup

Figure 4. Test setup.

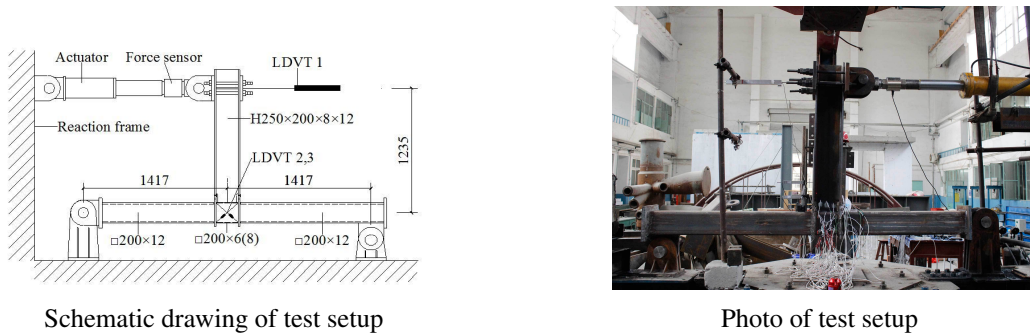panel zone of the joint will not be influenced by the second order effect of gravity, the beam end loading scheme was adopted in this study. Figure 4 shows the schematic drawing and the photo of the test setup. The T-shaped specimens were placed horizontally on the testing frame first. To simulate the inflection points of the columns and the beams, the T-shaped specimens were fixed on the testing frame by three hinged supports. The displacement of three directions was constrained at the bottom of the column. The top of the column was restricted by the displacement in two directions. The displacement in the direction of the column axis was relaxed, which was achieved by the long hole of the hinged support.

Before the actual experiment, the specimens were preloaded to ensure good contact with the test device. The relationship between load and deformation was stable. The entire test device was reliable. Furthermore, observation equipment worked properly. During the experiment, the horizontal cyclic load at the beam end was controlled by a force-displacement hybrid control loading system. That is, force-control was used before the yielding of the specimen. Displacement-control was employed after the yielding of the specimen. Stepwise force load was applied to the beam end and repeated one time at each step before yielding. After that, the specimen would be controlled by a multiple of the horizontal displacement of the beam end when specimens yielded. This was repeated three times for each step. During the loading process, in order to get the stable deformation data of the joint, the experimental data were collected after keeping the load for 5 minutes per level. The controlled displacement in the loading process was measured by LVDT1 (Linear Variable Differential Transformer), which was placed at the end of the beam corresponding to the location of a horizontal actuator. In addition, the diagonal displacement of the shear panels was measured by LVDT2 and LVDT3, as shown in Figure 4. The measured data were collected by the computer automatically.

2.3. *Observations.* For the specimen TDTC-1, the thickness of diaphragm was 16 mm. Before yielding, the load-displacement curve was linear. At the load of 139 kN, the joint yielded, while the deformation of the panel zone was so insignificant that no major phenomenon was observed. Beyond this point, the loading continued to increase with the displacement control method. The applied displacements were equal to multiples of yield displacement at the beam end, and the slope of the load-displacement curve became smaller. Local buckling occurred in the steel tube webs of the panel zone during the second cycle in one time of yield displacement. With the increasing displacement of the beam end, the horizontal load kept increasing. The internal force of the specimen was redistributed. The beam flanges began to bear more load transferred from the beam end. Then some local buckling took place on the beam flanges,
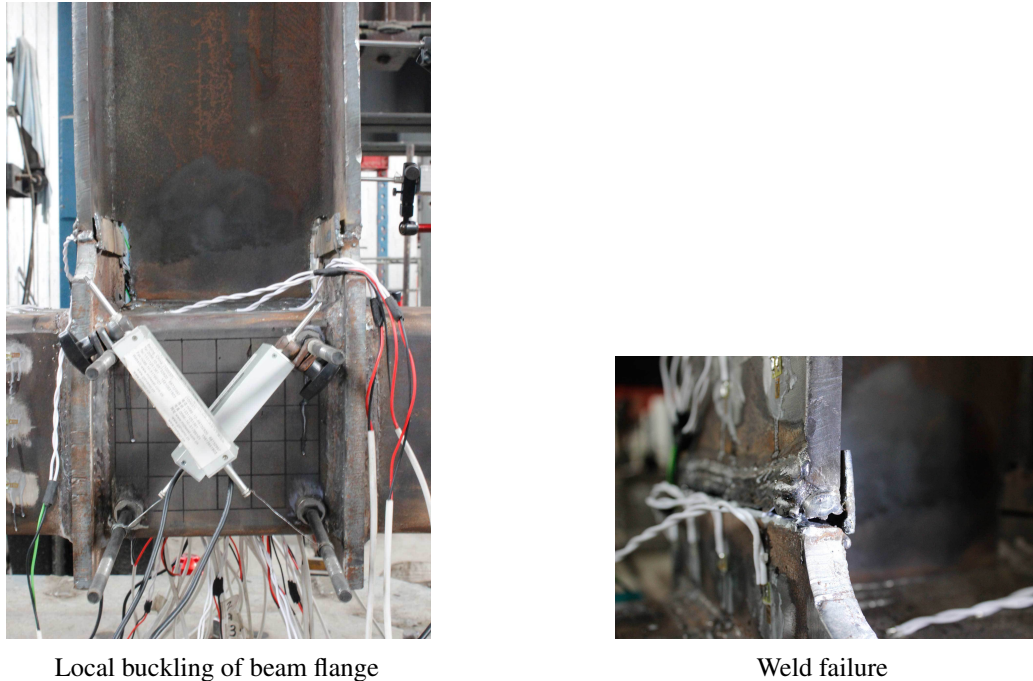
Local buckling of beam flange   Weld failure

Figure 5. Experimental phenomena of TDTC-1.

as shown in Figure 5. As the load increased, the weld between the steel beam and diaphragm started to fail, as shown in Figure 5. The load reached its peak value of 185.2 kN, corresponding to 50.2 mm displacement. The specimen was then unloaded and the test was terminated. It can be seen that the column web of panel zone bulged outward at the end of the test.

For the specimen of TDTC-2, the grade of filled concrete was C40. At the load of 138 kN, the panel zone yielded and the slope of load-displacement curve became smaller. Then the loading entered into the displacement control stage. TDTC-2 reached its maximum capacity of 199 kN and the corresponding displacement value was 61.1 mm. At four times the yield displacement, some local buckling on the column web of the panel zone became obvious. With the cyclic load at the beam end, the bulging outward of the column web along the two diagonals took place alternately with a characteristic sound. After that, the bearing capacity decreased slowly. At five times the yield displacement, a crack appeared near the weld on the tensile side of the diaphragm. At six times the yield displacement, the crack in diaphragm became bigger, as shown in Figure 6; the bulge outward of column web is shown in Figure 6. The load at the beam end dropped to 163 kN, smaller than 85% of the maximum load, and the test was terminated.

For the specimen of TDTC-3, the thickness of the steel tube in the panel zone was 8 mm. At the load of 160 kN, the panel zone yielded. The rectangular panel zone started to become rhombus at two times of yield displacement. There was a clear deflection of the steel beam due to the deformation of the panel zone, as shown in Figure 7. After the yielding of the panel zone, the internal force of the specimen was redistributed and the beam flanges began to bear more load transferred from the beam end. The TDTC-3 reached its maximum value of 179.3 kN with the corresponding displacement of 37.8 mm. At
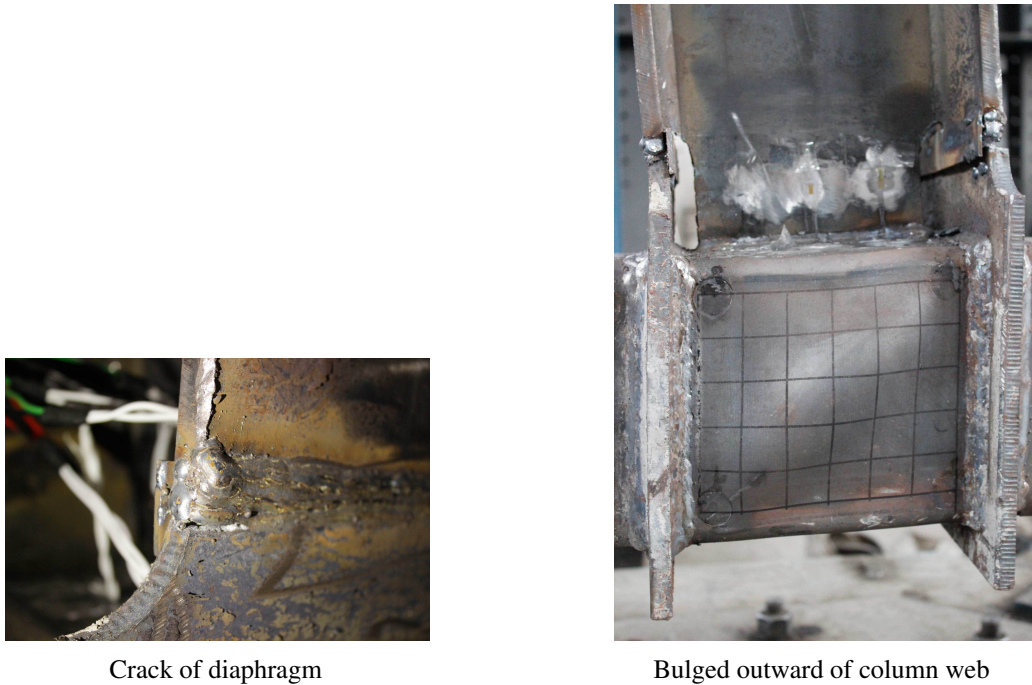
Crack of diaphragm   Bulged outward of column web

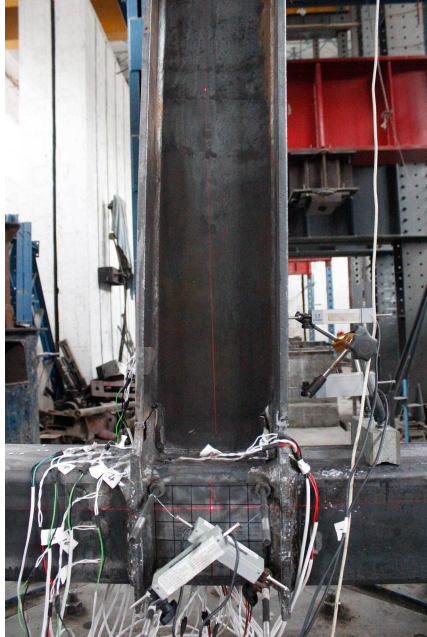**Figure 6.** Experimental phenomena of TDTC-2.

the same time, the weld between the steel beam and diaphragm failed, as shown in Figure 7. The test was terminated.

3. Slitting test of concrete

The steel tube walls at the panel zone of TDTC-2 and TDTC-3 were removed to examine the failure mode of the concrete core of the CFST columns. The distribution of the concrete cracks of TDTC-3 after the panel zone yielded is shown in Figure 8. The severe deformation of the concrete core in the column of TDTC-2 is shown in Figure 8. Under the cyclic load at the beam end, the corner of the panel zone was subjected to tension and pressure transformed from the moment, which was transferred from the beam end and column end. It can be seen from Figure 8 that diagonal cracks appeared and concrete diagonal compression struts formed. According to the test results, it can be found that the width of the diagonal compression strut is about 1/3 of the diagonal length of panel zone.

4. Discussion of test results

4.1. *Relationships between the shear forces and deformations of panel zone.* Shear force-deformation hysteretic curves and skeleton curves of three specimens are shown in Figures 9–11. In these figures, Q is the shear force and γ is the shear deformation of the panel zone. The shape of hysteretic curves of all specimens is smooth and full, which indicates that the specimens have a sound ductile behavior with large energy absorption. The strength decreases gradually after it reaches the maximum point. The slopes of the loading curves of the joints decrease with the increase of the cyclic load. However, the slopes of

Deflection of steel beam

Weld failure

Figure 7. Experimental phenomena of TDTC-3.

Concrete cracks in early stage

Concrete compression strut crushed

Figure 8. Concrete at panel zone.

the unloading curves are almost unchanged, which indicates bigger loading stiffness degradation and smaller unloading stiffness degradation.

The skeleton curves of hysteretic relations, which are obtained through connecting the displacement peaks of all cycles, are shown in Figures 9–11. All the skeleton curves are S-shaped, which indicates that all the specimens have elastic, yielding and hardening stages during the test. In the elastic stage of the joints, shear force-deformation curves are almost straight up. The steel tubes and the concrete are all
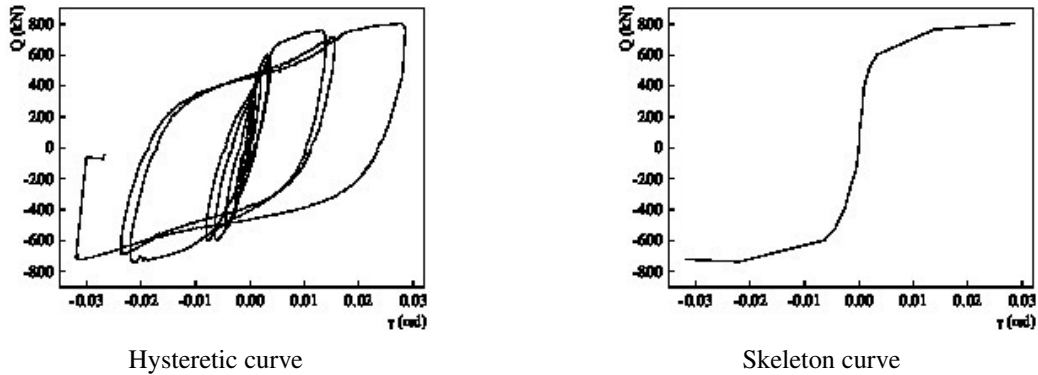
| Hysteretic curve | Skeleton curve |

Figure 9. Shear force-deformation of TDTC-1.

in the elastic stage. There are no cracks in the concrete core and the steel tube walls. The concrete and the steel tubes are bonded together effectively. The steel tubes and the concrete can be regarded as an integral part of this stage. The shear stiffness is bigger due to the cooperative working mechanism and deformation joints. In the yielding stage of the joints, the shear deformation increases with the increasing load. The concrete cracks and the web of the steel tube yields. The concrete is separated from the steel tube walls. The slope of shear force-deformation curves declines. Then the web of steel tube enters the hardening phase until it buckles.

After the web of steel tube buckles, the shear resistance of the concrete compression strut increases gradually due to the confinement provided by the steel tube and upper and lower diaphragms. Thus the joints exhibit good ductility. For TDTC-1 and TDTC-3, after the shear yield of the panel zone, the internal forces of the specimen are redistributed, and the beam flanges began to bear more load transferred from beam end. This will lead to the premature failure of the weld between the steel beam and diaphragm. Therefore, the development of shear deformation of the panel zone is insufficient after yielding. The energy dissipation capacity of the panel zone is not fully developed.

The yield shear capacity of specimens is presented in Table 4. From the figures combined with the data of Table 4, it can be seen that the yield shear capacity of TDTC-1 is significantly smaller than that of TDTC-2 and TDTC-3, which indicates that the influence of diaphragm thickness on the shear capacity of the joints is smaller than that of the steel tube wall thickness and the concrete strength. The comparison of TDTC-2 and TDTC-3 demonstrates that the influence of the thickness of steel tube on the shear capacity of the joint is larger.

4.2. *Comparison of test results and existing calculation results.* In order to evaluate the applicability of the existing calculation methods for the exterior diaphragm-through joints, the results obtained through existing calculation methods are compared with the test results. Three main methods for computing the panel zone shear capacity of composite CFST connections are briefly reproduced here.

4.2.1. *Calculation method in* [AIJ 1987]. The formula of the method incorporated in AIJ specification is shown in (1). It is derived directly by superposing the shear capacity of the concrete core and the steel tube, where V_c is the volume of the concrete core, f_{JS} is the concrete compression strength (in MPa), β_J is the coefficient for column cross sections, V_s is the volume of the web of the steel tube, and f_y is
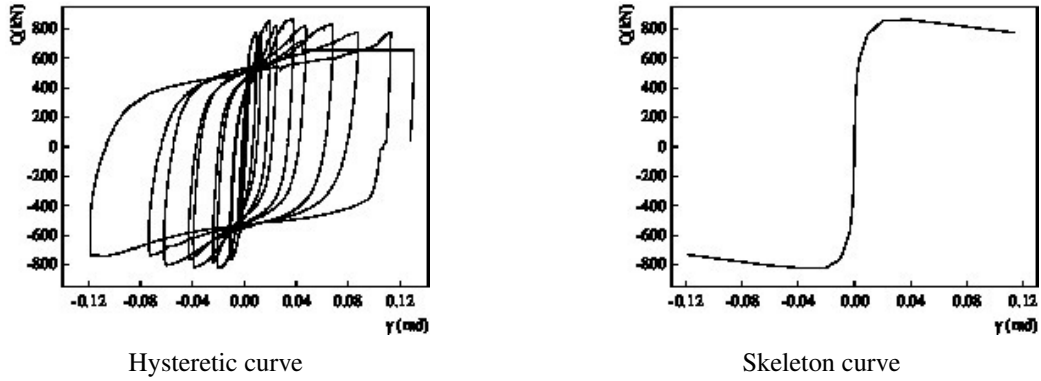
Hysteretic curve   Skeleton curve

Figure 10. Shear force-deformation of TDTC-2.

Hysteretic curve   Skeleton curve
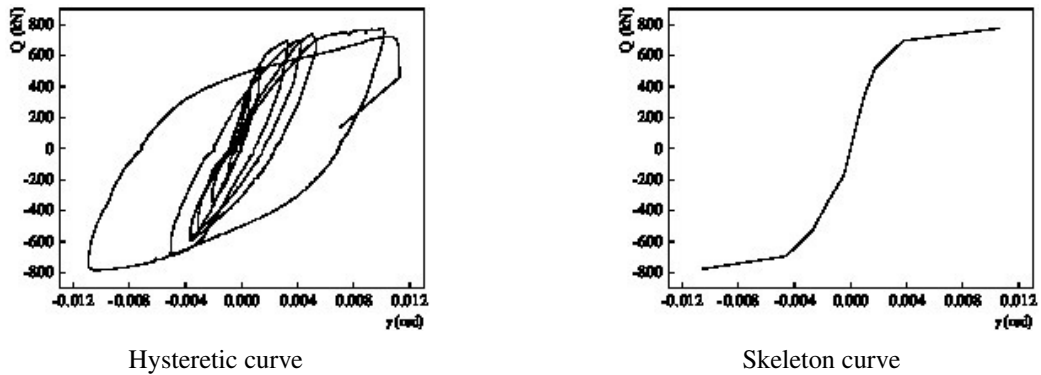
Figure 11. Shear force-deformation of TDTC-3.

the yield tensile strength of the web of steel tube (in MPa).

$$Q = V_c F_{JS} \beta_J + \frac{1.2}{\sqrt{3}} V_s f_y. \tag{1}$$

4.2.2. *Calculation method proposed by Lu Xilin (2000).* The formula of Lu's method [Lu and Yu 2000] for computing composite panel zone strength is shown in (2), where N_y is the shear capacity of the weld or tube web in the corner, h_c is the width of the cross-section of the concrete core, M_{pw} is the moment of the tube web, M_{pj} is the moment of the inner diaphragm, N_{cv} is the compressive strength of the concrete constrained compression truss, and H_b is the height of the steel beam:

$$Q = \left(2 N_y h_c + 4 M_{pw} + 4 M_{pj} + N_{cv} h_c/2\right) \big/ H_b. \tag{2}$$

4.2.3. *Calculation method proposed by Fukumoto and Morita (2005).* The formula of Fukumoto's method [Fujimoto et al. 2000] for computing composite panel zone strength is shown in (3), where V_{sy} is the contribution of the shear capacity of the steel tube, V_{cu} is the contribution of the concrete core which is

Figure 12. General yield point method.

derived from a constrained compression truss model, and β is the ratio of the shear yield load to shear ultimate load of the 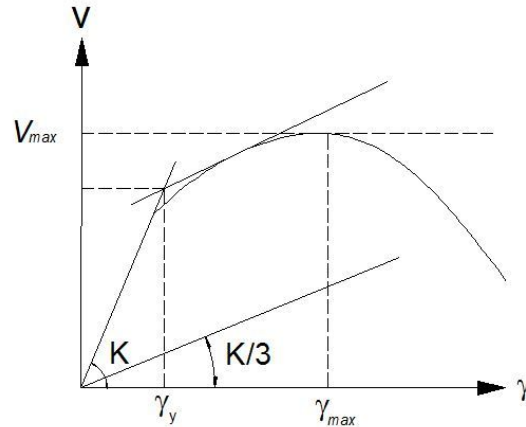concrete core. The shear capacity of the joint is obtained by directly superposing of the contribution of the steel tube and concrete core:

$$Q = V_{sy} + \beta V_{cu}. \tag{3}$$

The comparison of the test results and the existing calculation results of the three T-shaped diaphragm-through joints are shown in Table 4. The yield shear capacity can be obtained by the general yield point method [Park et al. 2010], as shown in Figure 12. The yield point is the intersection point of the two lines, whose slopes are the initial stiffness (K) of the specimen and one-third of the specimen $(K/3)$.

It can be seen from Table 4 that the shear capacity of the panel zone increases with the increase of the thickness of the steel tube and the concrete grade. The thickness of diaphragm-through has little influence on the shear capacity of the panel zone. The ratios of the test results and results calculated by AIJ, Lu Xilin, and Fukumoto range from 0.79 to 0.91, 0.70 to 0.77, and 0.97 to 1.17, respectively. They cannot reflect the shear capacity of T-shaped diaphragm-through joints accurately. That is to say, these calculation methods for calculating the shear capacity of panel zone are not suitable for T-shaped diaphragm-through joints. Thus, it is necessary to develop a new shear force-deformation model to estimate the shear capacity of T-shaped diaphragm-through joints accurately.

5. Models for shear force-deformation

5.1. *Shear force-deformation of steel tube flange.* The rectangular steel tube consists of column flanges and webs. When the beam end is subjected to the horizontal load, shear force is generated in the panel zone. This shear force causes shear deformation at the column web, and flexural deformation at the column flanges, as shown in Figure 13. The shear stiffness and shear capacity of the panel zone are influenced by the shear behavior of the webs and the flexural behavior of the flanges. The shear force

Specimen	Test result	AIJ		Lui Xilin		Fukumoto	
	Q_e	Q_y	Q_y/Q_e	Q_y	Q_y/Q_e	Q_e	Q_y/Q_e
TDTC-1	580.65	680.67	0.85	776.53	0.75	529.68	1.09
TDTC-2	638.62	701.78	0.91	828.68	0.77	547.48	1.17
TDTC-3	601.88	763.66	0.79	876.83	0.70	617.39	0.97
Average			0.85		0.74		1.08
Standard deviation			0.049		0.029		0.082

Table 4. Comparison of test and existing calculation results, where Q_e is the shear capacity of the test result and Q_y is the shear capacity calculated with the existing method.

affected by the flexural behavior of the column flanges (V_f) is

$$V_f = K_f \gamma_f, \tag{4}$$

$$K_f = 2 \times \frac{12 E_s I}{h_b - 2t_{bf}}, \tag{5}$$

where γ_f is shear strain of the column flanges when it's deformed, E_s is the Young's modulus of steel, h_b is the depth of the H-shaped beam, t_{bf} is the thickness of the diaphragm-through, b_c is the width of the column, t_c is the thickness of the beam flange, K_f is the shear stiffness of the two column flanges due to flexural deformation and $I = b_c t_c^3/12$ is the moment of inertia of the column flange.

When the column flanges reach the yielding point, the shear capacity (V_{fy}) is

$$V_{fy} = \frac{4 M_{fy}}{h_b - t_{bf}}, \tag{6}$$

where $M_{fy} = b_c t_c^2 f_y/6$ is the yield flexural strength of the column flanges, and f_y is the yielding tensile stress of the steel. The corresponding shear strain (γ_{fy}) is

$$\gamma_{fy} = \frac{V_{fy}}{K_f}. \tag{7}$$

5.2. *Shear force-deformation of steel tube web.* The shear force contributed by the shear behavior of the column webs (V_w) is

$$V_w = K_w \gamma_w, \tag{8}$$

where the shear stiffness of column webs before yielding (K_{w1}) is

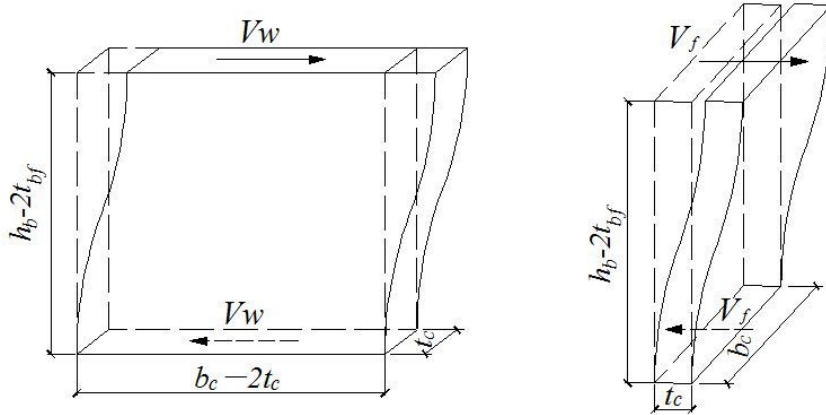$$K_{w1} = 2 A_w G_s = 2(b_c - t_c) t_c G_s. \tag{9}$$

Figure 13. Schematic diagram for deformation of steel tube

When the column webs yield, the strength of the two column webs (V_{wy}) is

$$V_{wy} = 2A_w f_{yv}. \tag{10}$$

The corresponding shear strain of column web (γ_{wy}) is

$$\gamma_{wy} = \kappa \frac{V_{wy}}{K_{wl}} = \kappa \frac{2A_w f_{yv}}{2A_w G_s} = \kappa \frac{f_{yv}}{G_s}, \tag{11}$$

where A_w is the web area of steel tube in the panel zone, $G_s = 79\,GP_a$ is the shear modulus for the steel tube and κ is the section coefficient for shear deformation. After reaching the yielding point, the shear stress-strain curve extends continuously at smaller stiffness until the strain is four times the yielding strain due to strain hardening of the material and restraint of the surrounding components [Krawinkler 1978]. Hence, the shear stiffness of the two column webs after yield is

$$K_{w2} = \left(\frac{\beta - 1}{3} \right) K_{w1}, \tag{12}$$

where β is the strain hardening factor, which is the ratio of the ultimate tensile stress to the yield tensile stress.

When the external loads increase continuously, the stress of the column webs subsequently reaches the ultimate point and the strength (V_{wu}) is

$$V_{wu} = 2t_c(b_c - 2t_c)\frac{f_u}{\sqrt{3}}, \tag{13}$$

where f_u is the ultimate tensile stress of the steel.

The corresponding shear strain of column web (γ_{wu}) is

$$\gamma_{wu} = \frac{V_{wu} - V_{wy}}{K_{w2}}. \tag{14}$$

5.3. *Shear force-deformation of concrete.* For diaphragm-through joints, the concrete compression strut mechanism is activated by the restricting effect of the through-diaphragms and the steel tube wall on
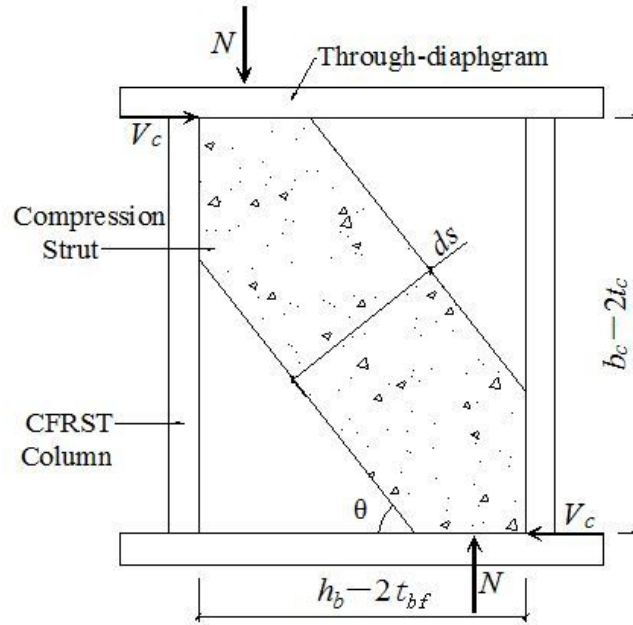
Figure 14. Schematic diagram for concrete compression strut.

the adjacent concrete. The schematic diagram for the concrete compression strut is shown in Figure 14. Based on the analysis in slitting tests of concrete, the concrete compression strut is along the diagonal direction of the panel zone. It is assumed that the width of the compression strut d_s is about 1/3 length of the panel zone diagonal:

$$d_s = \frac{1}{3}\sqrt{(b_c - 2t_c)^2 + (h_b - 2t_{bf})^2}. \tag{15}$$

The angle between the compression strut and the longitudinal beam axis θ is calculated as follows:

$$\theta = \tan^{-1}\frac{b_c - 2t_c}{h_b - 2t_{bf}}. \tag{16}$$

The shear force contributed by the concrete compression strut (V_c) is

$$V_c = f(b_c - 2t_c)\cos\theta, \tag{17}$$

where f is the compression stress of the concrete compression strut.

The stress-strain model for uniaxial and confined concrete under compression, proposed by Samani and Attard [2012], is utilized for the concrete in steel tube columns. This stress-strain model predicts the behavior of normal strength concrete, as well as high strength concrete accounting for the size effects. The complete stress-strain curve is divided into two regions: ascending and descending branches. For the ascending branch,

$$\frac{f}{f_0} = \frac{A \cdot X + B \cdot X^2}{1 + (A - 2)X + (B + 1)X^2}, \quad \text{where } X = \frac{\epsilon}{\epsilon_0} \text{ and } 0 \leq \epsilon \leq \epsilon_0,\ 0 \leq f \leq f_0. \tag{18}$$

The characteristic values A and B are

$$A = \frac{E_c \epsilon_0}{f_0} \quad \text{and} \quad B = \frac{(A-1)^2}{0.55} - 1. \tag{19}$$

For the softening descending branch, a power function is used on the condition that the stress-strain curve passes through a point on the softening branch, here taken as the so-called inflection point. The proposed post-peak softening function is

$$\frac{f}{f_0} = \frac{f_r}{f_0} + \left(1 - \frac{f_r}{f_0}\right)\left(\frac{f_{ic}}{f_c}\right)^{\left(\frac{\epsilon - \epsilon_0}{\epsilon_i - \epsilon_0}\right)^2}. \tag{20}$$

The inflection point strain ratio is

$$\frac{\epsilon_i}{\epsilon_0} = \left(\frac{f_r}{f_0}\right)\left(1.26 + \frac{2.89}{\sqrt{f_c'}}\right) + \left(1 - \frac{f_r}{f_0}\right)\left(\frac{\epsilon_{ic}}{\epsilon_c}\right). \tag{21}$$

In the above equations, f_0 is the compression strength of confined concrete, ϵ_0 is the corresponding stain, E_c is the secant modulus of concrete, f_r is the residual stress, f_{ic} is the stress level at the inflection point on descending branch of confined concrete, ϵ_{ic} is the corresponding strain and f_c' is the uniaxial compression strength of concrete. Details of the procedure to compute these parameters are described by Samani and Attard [2012].

Actually, compression stress is in one direction diagonally while there is tensile stress acting in the perpendicular direction. This effect should be considered by means of the concrete softening parameter β [Parra-Montesinos and Wight 2001]. The effect of transverse tensile strains on the softening parameter β is a function of the ratio k_{tc} given by $\beta = 1/(0.85 + 0.27k_{tc})$, where k_{tc} is related to the principle tensile and compression strains, with $k_{tc} = -\epsilon_t/\epsilon_c$.

When the concrete core is subjected to the resultant pressure along the diagonal direction, it will deform as Figure 15 shows. According to the relationship between each dimension in the figure, the shear deformation of concrete γ_c can be obtained by the law of cosines through the compression strain ϵ:

$$\gamma_c = \frac{(b_c - 2t_c)^2 + (h_b - 2t_{bf})^2}{(b_c - 2t_c)(h_b - 2t_{bf})} \epsilon. \tag{22}$$

Therefore, the relationship of shear force and deformation for concrete in the panel zone can be determined.

5.4. *Models for shear force-deformation of the panel zone.* According to the principle of coordination of shear deformation, the shear force-deformation model of the diaphragm-through joints can be obtained through the superposition of models for the steel tube and concrete, given by (23).

$$V_j = V_f + V_w + V_c \tag{23}$$

5.5. *Comparison of test and theoretical results.* The accuracy of the proposed model to predict the shear force-deformation of T-shaped diaphragm-through joints is evaluated by comparing the predicted versus experimental results, as shown in Figure 16. As these figures show, the proposed model closely predicts the behavior of the joints for all levels of the shear force-deformation curve.
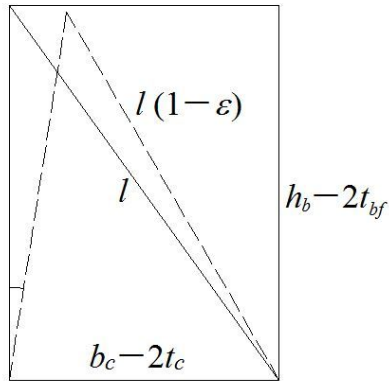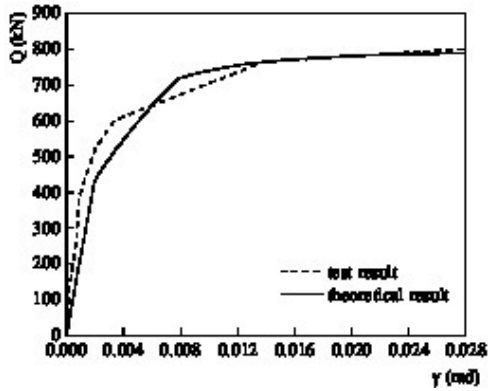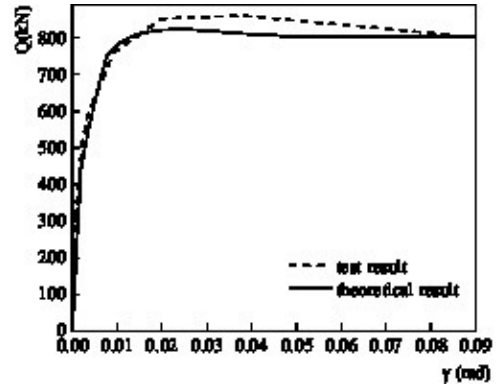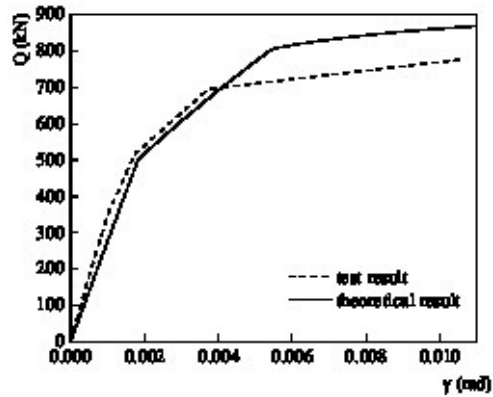
Figure 15. Deformation of concrete core.

TDTC-1

TDTC-2

TDTC-3

Figure 16. Predicted versus experimental shear force-deformation curves.

Specimen	Q_e	Q_y	Q_y/Q_e
TDTC-1	580.65	609.46	0.953
TDTC-2	638.62	661.54	0.965
TDTC-3	601.88	653.13	0.922

Table 5. Comparison of experimental and theoretical results, where Q_e is the shear capacity of the test result and Q_y is the shear capacity calculated with proposed method.

The predicted results of yield shear capacity for T-shaped diaphragm joints obtained through the proposed model are compared with the experimental results, as shown in Table 5. It can be seen that the theoretical results are in good agreement with the experimental data, the deviation of the prediction results is less than 10%. Because of the premature failure of the weld between the steel beam and diaphragm, the experimental result of TDTC-3 is significantly smaller than the predicted value. The shear force-deformation model proposed in this paper is a valuable tool for predicting the shear capacity of T-shaped diaphragm-through joints.

6. Conclusions

Three T-shaped diaphragm-through joints were tested under seismic cyclic loading to investigate the shear capacity of T-shaped diaphragm-through joints between rectangular CFST columns and H-shaped steel beams. Based on the test results, the following main conclusions are obtained:

- The shear capacity of the T-shaped diaphragm-through joint is contributed by the concrete core and the steel tube, which is composed of webs and flanges. The flanges of the steel tube have little effect on the shear capacity of the joint.

- From the slitting test of the concrete, it is apparent that the concrete compression strut is along the panel zone diagonal direction, and the width of the compression strut is about 1/3 length of the panel zone diagonal.

A model for the shear force-deformation skeleton curve for T-shaped diaphragm-through joints is proposed. The model is developed by superposition of models for steel tubes and the concrete cores based on the principle of deformation coordination. The predictions of the proposed model are in good agreement with the test results.

Acknowledgments

References

[AIJ 1987] *AIJ standard for structural calculation of steel reinforced concrete structures*, Architectural Institute of Japan, 1987. In Japanese.

[Fujimoto et al. 2000] T. Fujimoto, E. Inai, H. Tokinoya, M. Kai, K. Mori, O. Mori, and I. Nishiyama, "Behavior of beam-to-column connection of CFT column system under seismic force", pp. 557–564 in *Composite and hybrid structures: proceedings of the Sixth ASCCS International Conference on Steel-Concrete Composite Structures* (Los Angeles, 2000), edited by Y. Xiao and S. Mahin, University of Southern California, Los Angeles, 2000.

[Fukumoto and Morita 2005] T. Fukumoto and K. Morita, "Elastoplastic behavior of panel zone in steel beam-to-concrete filled steel tube column moment connections", *J. Struct. Eng. (ASCE)* **131**:12 (2005), 1841–1853.

[Krawinkler 1978] H. Krawinkler, "Shear in beam-column joints in seismic design of steel frames", *Eng. J.* **15**:3 (1978), 82–91.

[Liu et al. 2014] X. Liu, M. Tao, J. Fan, and J. Hajjar, "Comparative study of design procedures for CFST-to-steel girder panel zone shear strength", *J. Constr. Steel Res.* **94** (2014), 114–121.

[Lu and Yu 2000] X. Lu and Y. Yu, "Experimental study on the seismic behavior in the connection between CFRT column and steel beam", *Struct. Eng. Mech.* **9**:4 (2000), 365–374.

[Nie et al. 2008] J. Nie, K. Qin, and C. Cai, "Seismic behavior of connections composed of CFSSTCs and steel-concrete composite beams—experimental study", *J. Constr. Steel Res.* **64**:10 (2008), 1178–1191.

[Park et al. 2010] S. Park, S. Choi, Y. Kim, Y. Park, and J. Kim, "Hysteresis behavior of concrete filled square steel tube column-to-beam partially restrained composite connections", *J. Constr. Steel Res.* **66**:7 (2010), 943–953.

[Parra-Montesinos and Wight 2001] G. Parra-Montesinos and J. Wight, "Modeling shear behavior of hybrid RCS beam-column connections", *J. Struct. Eng. (ASCE)* **127**:1 (2001), 3–11.

[Qin et al. 2014] Y. Qin, Z. Chen, and B. Rong, "Component-based mechanical models for axially-loaded through-diaphragm connections to concrete-filled RHS columns", *J. Constr. Steel Res.* **102** (2014), 150–163.

[Samani and Attard 2012] A. Samani and M. Attard, "A stress-strain model for uniaxial and confined concrete under compression", *Eng. Struct.* **41** (2012), 335–349.

[Sheet et al. 2013] I. Sheet, Gunasekaran, U., and G. MacRae, "Experimental investigation of CFT column to steel beam connections under cyclic loading", *J. Constr. Steel Res.* **86** (2013), 167–182.

[Wu et al. 2006] L.-Y. Wu, L.-L. Chung, S.-F. Tsai, C.-F. Lu, and G.-L. Huang, "Seismic behavior of bidirectional bolted connections for CFT columns and H-beams", *Eng. Struct.* **29**:3 (2006), 395–407.

[Zhang et al. 2012] D. Zhang, S. Gao, and J. Gong, "Seismic behavior of steel beam to circular CFST column assemblies with external diaphragms", *J. Constr. Steel Res.* **76** (2012), 155–166.

BIN RONG: tjerobin@126.com
Key Laboratory of Coast Civil Structure Safety, Department of Civil Engineering, Tianjin University, Tianjin, 300072, China

RUI LIU: liurui5919@163.com
Department of Civil Engineering, Tianjin University, Tianjin, 300072, China
zryu@163.com

RUOYU ZHANG: zryu@163.com
School of Civil Engineering, Tianjin University, Weijin Road 92, Tianjin, 300072, China

SHUAI LIU: lao_xs@163.com
Department of Civil Engineering, Tianjin University, Tianjin, 300072, China

APOSTOLOS FAFITIS: fafitis@asu.edu
Department of Civil and Environmental Engineering, Arizona State University, Tempe, AZ 85287, United States

∎msp

POLARIZATION APPROXIMATIONS FOR ELASTIC MODULI
OF ISOTROPIC MULTICOMPONENT MATERIALS

Duc Chinh Pham, Nguyen Quyet Tran and Anh Binh Tran

Polarization approximations (PA) are proposed for the macroscopic elastic moduli of d-dimensional ($d = 2$ or 3) isotropic multicomponent materials. Specifically we use Hashin–Shtrikman-type polarization trial fields, which were constructed earlier from the minimum energy principles to bound the effective moduli of the composites, as the approximate solutions to the field equations. The approximations contain free reference parameters, which can be found analytically, numerically, or experimentally, from the reference effective moduli at dilute and/or finite volume proportions of the component materials. In the basic one-point reference parameter version, the approximations should obey Hashin–Shtrikman (HS) bounds for all the ranges of the volume proportions of the component materials. In the refined versions involving variable reference parameters to improve the accuracy of the scheme, the approximations satisfy HS bounds over the ranges of components' volume proportions between the extreme reference points. We provide numerous numerically and experimentally based examples to illustrate the applications of the proposed approach.

1. Introduction

Many natural and industrial materials are multicomponent with complex and irregular microstructure. Often only limited definite qualitative information about the composites, e.g., the properties and volume proportions of the component materials, is available. Still, the measured macroscopic moduli of many practical composites appear relatively definite (with small variation), and that encourages us to construct simple estimations of the moduli for practical uses. A mathematically rigorous approach to the problem is to construct the upper and lower bounds of the effective moduli using variational formulations [Hashin and Shtrikman 1963; Walpole 1966; Willis 1977; Pham 1993; 2012; 2014; Milton 2002; Torquato 2002]. Narrowing the bounds requires multipoint correlation information about the microgeometries of the composites that is difficult to collect and incorporate into the construction of the bounds. Alternatively, effective medium approximation (EMA) schemes have been developed for practical estimates of composites' macroscopic moduli [Mori and Tanaka 1973; Christensen 1979; Norris 1989; Mura 1987; Phan-Thien and Pham 2000; Torquato 2002; Nogales and Böhm 2008; Klusemann et al. 2012; Franciosi et al. 2011; Mogilevskaya et al. 2012; Kushch et al. 2013; Sevostianov and Kachanov 2014] (among many others). Many classical EMAs, such as the self-consistent, Mori–Tanaka, differential ones are based on the dilute solutions for the inhomogeneities of some idealistic forms suspended in an infinite matrix (the Eshelby problem [1957]) and are then developed into the forms that can predict the effective moduli of the composites over a range of volume proportions of the inhomogeneities. All EMAs converge at the dilute limit of the inclusions but diverge from each other at large volume proportions of the included

phases. To get better approximations, additional information about a particular composite, such as the effective moduli at some inclusions' volume proportion points, if available, should be included into an EMA. In this work we propose novel polarization approximations which can offer that flexibility. The idea was first introduced in our work [Tran and Pham 2015] for practical uniaxial circular fiber composites. We constructed certain polarization approximations for the effective elastic transverse (two-dimensional) bulk and shear moduli, among other moduli, of the transverse-isotropic composites, with numerical illustrations. In this work we generalize the idea as follows: polarization approximations are derived for the elastic bulk and shear moduli of isotropic three-dimensional composites and given in convenient forms valid for those in general d dimensions. General forms of the inhomogeneities (not just the circular one), with both numerical and experimental references from various composites, are considered. To improve the approximations, variable reference parameter for the approximation is proposed to take into account more information about a composite.

In Section 2, the polarization trial fields that were constructed earlier from the minimum energy principles to bound the effective elastic moduli will be used to derive the polarization approximations. Those approximations depend on certain free reference parameters. Those free (generally variable) parameters are determined analytically, numerically, or experimentally, using certain reference macroscopic moduli in subsequent sections, which are then followed by the conclusion (Section 6).

2. Polarization approximations

Let us consider a representative volume element (RVE) V in d-dimensional Euclidean space ($d = 2, 3$) of a macroscopically isotropic multicomponent. The material consists of n isotropic components occupying regions $V_\alpha \subset V$ of volumes v_α and having elastic moduli K_α and μ_α ($\alpha = 1, \ldots, n$ and the volume of V is assumed to be unity). The effective elastic moduli $\boldsymbol{C}^{\text{eff}} = \boldsymbol{T}(K^{\text{eff}}, \mu^{\text{eff}})$ of the isotropic composite may be defined via the minimum energy principle [Pham 1993; 2012; 2014]

$$\boldsymbol{\varepsilon}^0 : \boldsymbol{C}^{\text{eff}} : \boldsymbol{\varepsilon}^0 = \inf_{\langle \boldsymbol{\varepsilon} \rangle = \boldsymbol{\varepsilon}^0} \int_V \boldsymbol{\varepsilon}(\boldsymbol{x}) : \boldsymbol{C}(\boldsymbol{x}) : \boldsymbol{\varepsilon}(\boldsymbol{x}) \, d\boldsymbol{x}, \tag{1}$$

for all macroscopic constant strain tensors $\boldsymbol{\varepsilon}^0$, where $\boldsymbol{C}(\boldsymbol{x})$ is the fourth-rank stiffness tensor, $\boldsymbol{T}$ is the isotropic fourth-rank tensor with components

$$T_{ijkl}(K, \mu) = K\delta_{ij}\delta_{kl} + \mu\left(\delta_{ik}\delta_{jl} + \delta_{il}\delta_{jk} - \frac{2}{d}\delta_{ij}\delta_{kl}\right), \tag{2}$$

the trial compatible strain field is expressed through the displacement field $\boldsymbol{u}(\boldsymbol{x})$ as

$$\boldsymbol{\varepsilon}(\boldsymbol{x}) = \tfrac{1}{2}[\nabla\boldsymbol{u}(\boldsymbol{x}) + (\nabla\boldsymbol{u})^T(\boldsymbol{x})], \tag{3}$$

and $\langle \cdot \rangle$ means the volume average on V.

The effective elastic moduli may also be defined via the minimum complementary energy principle [Pham 1993; 2012; 2014]

$$\boldsymbol{\sigma}^0 : (\boldsymbol{C}^{\text{eff}})^{-1} : \boldsymbol{\sigma}^0 = \inf_{\langle \boldsymbol{\sigma} \rangle = \boldsymbol{\sigma}^0} \int_V \boldsymbol{\sigma}(\boldsymbol{x}) : \boldsymbol{C}^{-1}(\boldsymbol{x}) : \boldsymbol{\sigma}(\boldsymbol{x}) \, d\boldsymbol{x}, \tag{4}$$

for all macroscopic constant stress tensors $\boldsymbol{\sigma}^0$, where the trial stress field $\boldsymbol{\sigma}(\boldsymbol{x})$ should satisfy equilibrium equations in V

$$\nabla \cdot \boldsymbol{\sigma}(\boldsymbol{x}) = \boldsymbol{0}. \tag{5}$$

Note that the two-dimensional bulk modulus K here in the two-dimensional Cartesian coordinates $\{x_1, x_2\}$ is defined by $\sigma_{11} + \sigma_{22} = 2K(\varepsilon_{11} + \varepsilon_{22})$. Hence, it is related to the usual three-dimensional bulk modulus designated specifically here as $\widetilde{K}$: $K = \widetilde{K} + \mu/3$ in the plane strain case and $K = 9\widetilde{K}\mu/(3\bar{K} + 4\mu)$ in the plane stress case.

We consider the 3D case in the following equations, from (6) to (10). To find the upper correlation bounds on K^{eff} and μ^{eff} for isotropic three-dimensional composites, instead of directly optimizing the energy expression of the complex problem (1), we [Pham 1993; 2014] have optimized a "principal part" of it and came to a Hashin–Shtrikman-type polarization trial strain field

$$\varepsilon_{ij} = \varepsilon_{ij}^0 + \frac{3K_0 + \mu_0}{\mu_0(3K_0 + 4\mu_0)} \sum_{\alpha=1}^{n} p_{kl}^{\alpha} \psi_{,ijkl}^{\alpha} - \frac{1}{2\mu_0} \sum_{\alpha=1}^{n} (p_{mi}^{\alpha} \varphi_{,jm}^{\alpha} + p_{mj}^{\alpha} \varphi_{,im}^{\alpha}), \tag{6}$$

where K_0 and μ_0 are some free positive parameters (called the elastic moduli of a reference material in Hashin–Shtrikman approach); indices after a comma designate differentiation with respect to the corresponding Cartesian coordinates; conventional summation on repeated indices (from 1 to 3) is assumed; p_{kl}^{α} are the components of the second-order tensor $\boldsymbol{p}^{\alpha}$, which is referred to as the polarization field in the Hashin–Shtrikman (HS) approach

$$\boldsymbol{p}^{\alpha} = \left\{ \boldsymbol{I} - (\boldsymbol{C}^{\alpha} + \boldsymbol{C}^*)^{-1} : \left[\sum_{\beta=1}^{n} v_{\beta} (\boldsymbol{C}^{\beta} + \boldsymbol{C}^*)^{-1} \right]^{-1} \right\} : (\boldsymbol{C}^0 + \boldsymbol{C}^*) : \boldsymbol{\varepsilon}^0,$$

$$\boldsymbol{C}^0 = \boldsymbol{T}(K_0, \mu_0), \qquad \boldsymbol{I} = \boldsymbol{T}\left(\tfrac{1}{3}, \tfrac{1}{2}\right), \quad \boldsymbol{C}^{\alpha} = \boldsymbol{T}(K_{\alpha}, \mu_{\alpha}), \tag{7}$$

$$\boldsymbol{C}^* = \boldsymbol{T}(K_*, \mu_*), \quad K_* = \tfrac{4}{3}\mu_0, \qquad \mu_* = \mu_0 \frac{9K_0 + 8\mu_0}{6K_0 + 12\mu_0};$$

$\varphi^{\alpha}(\boldsymbol{x})$ and $\psi^{\alpha}(\boldsymbol{x})$ are harmonic and biharmonic potentials originated from the expression of the Green function for the 3D elastic infinite medium (which satisfy equations $\nabla^2 \varphi^{\alpha}(\boldsymbol{x}) = \nabla^4 \psi^{\alpha}(\boldsymbol{x}) = \delta_{\alpha\beta}$ for $\boldsymbol{x} \in V_{\beta}$, where $\delta_{\alpha\beta}$ is the usual Kronecker delta). Since the phases are assumed to be distributed isotropically in the material space, one has [Walpole 1966; Christensen 1979; Pham 1993]

$$\langle \varphi_{,ij}^{\beta} \rangle_{\alpha} = \frac{1}{v_{\alpha}} \int_{V_{\alpha}} \varphi_{,ij}^{\beta} \, d\boldsymbol{x} = \tfrac{1}{3} \delta_{ij} \delta_{\alpha\beta},$$

$$\langle \psi_{,ijkl}^{\beta} \rangle_{\alpha} = \frac{1}{v_{\alpha}} \int_{V_{\alpha}} \psi_{,ijkl}^{\beta} \, d\boldsymbol{x} = \tfrac{1}{15} (\delta_{ij} \delta_{kl} + \delta_{il} \delta_{jk} + \delta_{ik} \delta_{jl}) \delta_{\alpha\beta}, \tag{8}$$

where $\langle \cdot \rangle_{\alpha} = (1/v_{\alpha}) \int_{V_{\alpha}} \cdot \, d\boldsymbol{x}$ designates the volume average on V_{α}, while $\langle \cdot \rangle = \int_{V} \cdot \, d\boldsymbol{x}$ is the volume average on the whole representative volume element V.

In Pham's [1993; 2014] upper-bound approach, the upper correlation bounds on K^{eff} and μ^{eff} obtained from (1) with the trial field (6)–(7) contain the three-point correlation information about the microgeometry of a composite, and K_0 and μ_0 should be chosen to minimize the upper bounds. K_0 and μ_0 should lie within the extreme values of K_{α} and μ_{α}. The trial field of formal type (6) has also been obtained by [Walpole 1966; Willis 1977; Christensen 1979], using other approaches.

On the other side, to find the lower correlation bounds on the effective moduli, instead of directly optimizing the complementary energy expression of (4), [Pham 1993; 2014] optimized a "principal part" of it and obtained the polarization trial stress field

$$\boldsymbol{\sigma}(\boldsymbol{x}) = \boldsymbol{\sigma}^0 - \boldsymbol{C}^0 : [\boldsymbol{\varepsilon}'(\boldsymbol{x}) + \boldsymbol{q}(\boldsymbol{x})], \quad \hat{\boldsymbol{q}}^\alpha = \boldsymbol{C}^0 : \boldsymbol{q}^\alpha,$$

$$\varepsilon'_{ij}(\boldsymbol{x}) = \frac{3K_0 + \mu_0}{\mu_0(3K_0 + 4\mu_0)} \sum_{\alpha=1}^n \hat{q}^\alpha_{kl} \psi^\alpha_{,ijkl} - \frac{1}{2\mu_0} \sum_{\alpha=1}^n (\hat{q}^\alpha_{mi} \varphi^\alpha_{,jm} + \hat{q}^\alpha_{mj} \varphi^\alpha_{,im}),$$

$$\boldsymbol{q}^\alpha = \left\{ \boldsymbol{I} - [(\boldsymbol{C}^\alpha)^{-1} + (\boldsymbol{C}^*)^{-1}]^{-1} : \left[\sum_{\beta=1}^n v_\beta [(\boldsymbol{C}^\beta)^{-1} + (\boldsymbol{C}^*)^{-1}]^{-1} \right]^{-1} \right\} : [(\boldsymbol{C}^0)^{-1} + (\boldsymbol{C}^*)^{-1}] : \boldsymbol{\sigma}^0,$$

(9)

where $\boldsymbol{q}(\boldsymbol{x}) = \boldsymbol{q}^\alpha$ when $\boldsymbol{x} \in V_\alpha$; other notations are similar to those in (7) and (8). In the lower-bound approach, K_0 and μ_0 should be chosen to maximize the lower bounds on K^{eff} and μ^{eff} obtained from (4) with the trial field (9). K_0 and μ_0 should lie within the extreme values of K_α and μ_α.

Extracting the correlation information on a particular composite's microgeometry needed for the three-point correlation bounds in [Pham 1993] is costly. To avoid this, we directly use the "optimal" polarization trial fields (6) or (9) as the approximate solution fields on the RVE to construct the polarization approximations for the effective elastic moduli. Following the approach of [Tran and Pham 2015] in the two-dimensional case, one may use the polarization strain field (6)–(7), with (8), for our three-dimensional composites to find

$$K^{\text{eff}} = \frac{\langle \sigma_{ii} \rangle}{3 \langle \varepsilon_{ii} \rangle} = \frac{\sum_{\alpha=1}^n v_\alpha \langle \sigma_{ii} \rangle_\alpha}{3 \sum_{\alpha=1}^n v_\alpha \langle \varepsilon_{ii} \rangle_\alpha} = \frac{\sum_{\alpha=1}^n v_\alpha 3 K_\alpha \langle \varepsilon_{ii} \rangle_\alpha}{3 \sum_{\alpha=1}^n v_\alpha \langle \varepsilon_{ii} \rangle_\alpha}$$

$$= \frac{1}{\varepsilon^0_{ii}} \left(3 \sum_{\alpha=1}^n \frac{v_\alpha K_\alpha}{K_\alpha + K_*} \left(\sum_{\beta=1}^n \frac{v_\beta}{K_\beta + K_*} \right)^{-1} \varepsilon^0_{ii} \right) = \left(\sum_{\alpha=1}^n \frac{v_\alpha}{K_\alpha + K_*} \right)^{-1} - K_*. \quad (10)$$

Alternatively, instead of (6), one may use the polarization stress field (9) as the approximate field to find the approximation identical to (10). This is quite interesting, as the upper and lower bounds found in [Pham 1993] do not coincide. Indeed, the approximate fields (6) and (9) found from the upper- and lower-bound approaches without submitting to the minimum energy principles still cannot provide the precise information of whether they would help approximate the exact effective bulk modulus from above or below. They themselves only give some rough approximations involving some free parameters. Combining the two-dimensional case of [Tran and Pham 2015] and the three-dimensional case here, the estimation can be given in the general form (in d-dimensional space with $d = 2, 3$)

$$K^{\text{eff}} = P_K^{(n)}(K_*) = \left(\sum_{\alpha=1}^n \frac{v_\alpha}{K_\alpha + K_*} \right)^{-1} - K_*, \quad K_*(\mu_0) = \frac{2(d-1)}{d} \mu_0. \quad (11)$$

The estimation (11) has a feature that the property function $P_K^{(n)}(K_*)$ is a positive monotonously increasing function with respect to the positive parameter K_*, and it falls within HS bounds

$$P_K^{(n)}(K_{* \min}) \le K^{\text{eff}} \le P_K^{(n)}(K_{* \max}),$$

$$K_{* \min} = K_*(\mu_{\min}), \quad \mu_{\min} = \min\{\mu_1, \dots, \mu_n\},$$

$$K_{* \max} = K_*(\mu_{\max}), \quad \mu_{\max} = \max\{\mu_1, \dots, \mu_n\},$$

(12)

where $K_*(\mu_0)$ is defined in (11), when

$$K_{*\min} \leq K_* \leq K_{*\max}, \tag{13}$$

and vice versa.

The remaining free parameter K_* of the estimation (11) should be determined from a reference macroscopic bulk modulus of the composite at certain reference volume proportions v_α of the component materials. Should the reference macroscopic bulk modulus at some reference volume proportions of the components satisfy HS bounds, the respective reference parameter K_* would fall inside the interval bounded by $K_{*\min}$ and $K_{*\max}$. Then with that particular value K_* the estimation (11) shall obey HS bounds over all the volume proportions v_α of the component materials. Equation (11) shall be formally referred to as the polarization approximation (PA) for the effective elastic bulk modulus of the isotropic n-component material in the d-dimensional space.

Similarly, to find the approximation for the effective elastic shear modulus μ^{eff}, we again use the polarization strain field (6) to obtain

$$
\begin{aligned}
\mu^{\mathrm{eff}} &= \frac{\langle \sigma_{12} \rangle}{2 \langle \varepsilon_{12} \rangle} = \frac{\sum_{\alpha=1}^n v_\alpha 2 \mu_\alpha \langle \varepsilon_{12} \rangle_\alpha}{2 \sum_{\alpha=1}^n v_\alpha \langle \varepsilon_{12} \rangle_\alpha} \\
&= \frac{1}{\varepsilon_{12}^0} \left(\sum_{\alpha=1}^n \frac{2 v_\alpha \mu_\alpha}{\mu_\alpha + \mu_*} \left(\sum_{\beta=1}^n \frac{v_\beta}{\mu_\beta + \mu_*} \right)^{-1} \varepsilon_{12}^0 \right) = \left(\sum_{\alpha=1}^n \frac{v_\alpha}{\mu_\alpha + \mu_*} \right)^{-1} - \mu_*. \tag{14}
\end{aligned}
$$

Alternatively, the same estimation (14) can also be obtained starting from the polarization stress field (9).

Combining the two-dimensional case of [Tran and Pham 2015] and the three-dimensional case here, generally, in d-dimensional space ($d = 2, 3$), the estimation for μ^{eff} can be given in the form

$$
\begin{aligned}
\mu^{\mathrm{eff}} &= P_\mu^{(n)}(\mu_*) = \left(\sum_{\alpha=1}^n \frac{v_\alpha}{\mu_\alpha + \mu_*} \right)^{-1} - \mu_*, \\
\mu_*(K_0, \mu_0) &= \mu_0 \frac{d^2 K_0 + 2(d+1)(d-2)\mu_0}{2 d K_0 + 4 d \mu_0},
\end{aligned} \tag{15}
$$

which falls inside HS bounds

$$
\begin{aligned}
P_\mu^{(n)}(\mu_{*\min}) &\leq \mu^{\mathrm{eff}} \leq P_\mu^{(n)}(\mu_{*\max}), \\
\mu_{*\min} &= \mu_*(K_{\min}, \mu_{\min}), \quad K_{\min} = \min\{K_1, \ldots, K_n\}, \\
\mu_{*\max} &= \mu_*(K_{\max}, \mu_{\max}), \quad K_{\max} = \max\{K_1, \ldots, K_n\},
\end{aligned} \tag{16}
$$

where $\mu_*(K_0, \mu_0)$ is defined in (15) and $\mu_{\min}$ and $\mu_{\max}$ are defined in (12), when

$$\mu_{*\min} \leq \mu_* \leq \mu_{*\max}. \tag{17}$$

Similarly as in the case of the bulk modulus, the remaining free parameter μ_* of estimation (15) should be determined from a reference macroscopic shear modulus of the composite at certain reference volume proportions v_α of the component materials. Should the reference macroscopic shear modulus at some reference volume proportions of the components satisfy HS bounds, the respective reference parameter μ_* would fall inside the interval bounded by $\mu_{*\min}$ and $\mu_{*\max}$. Then with that particular

value μ_* the estimation (15) shall obey HS bounds over all the volume proportions v_α of the component materials. Equation (15) shall be referred to as the PA for the effective elastic shear modulus of the isotropic n-component material in d-dimensional space.

3. Reference at dilute suspension of the inclusions

Many EMAs are based on analytical Eshelby theoretical dilute solution results for an ellipsoidal inclusion suspended in an infinite matrix. So firstly, we construct a polarization approximation using the dilute solution reference. Let us consider the n-component matrix composite that is composed of the matrix component with $v_1 = v_M$, $K_1 = K_M$, and $\mu_1 = \mu_M$ and the inclusion components with v_α, K_α, and μ_α ($\alpha = 2, \ldots, n$). We may take the reference model for the composite as that at dilute suspensions of the same-geometry inclusions with the moduli K_α and μ_α and volume fractions tv_α ($\alpha = 2, \ldots, n$ and $t \ll 1$) in the matrix of moduli K_M and μ_M. Let the respective dilute solution results have the forms

$$K^{\text{eff}} = K_M + \sum_{\alpha=2}^{n} tv_\alpha(K_\alpha - K_M)D_{K\alpha}(K_\alpha, \mu_\alpha, K_M, \mu_M), \quad t \ll 1, \tag{18}$$

$$\mu^{\text{eff}} = \mu_M + \sum_{\alpha=2}^{n} tv_\alpha(\mu_\alpha - \mu_M)D_{\mu\alpha}(K_\alpha, \mu_\alpha, K_M, \mu_M), \quad t \ll 1, \tag{19}$$

where $D_{K\alpha}$ and $D_{\mu\alpha}$ are inclusion functions depending on the α-inclusion component's geometry; their values can be found analytically, numerically, or even experimentally. At that dilute limit, our polarization approximations (11) and (15) have the respective asymptotic expressions

$$K^{\text{eff}} = K_M + \sum_{\alpha=2}^{n} tv_\alpha(K_\alpha - K_M)\frac{K_M + K_*}{K_\alpha + K_*}, \quad t \ll 1, \tag{20}$$

$$\mu^{\text{eff}} = \mu_M + \sum_{\alpha=2}^{n} tv_\alpha(\mu_\alpha - \mu_M)\frac{\mu_M + \mu_*}{\mu_\alpha + \mu_*}, \quad t \ll 1. \tag{21}$$

Equalizing (18) with (20) and (19) with (21), respectively, one obtains the equations determining the reference parameters K_* and μ_* separately:

$$\sum_{\alpha=2}^{n} v_\alpha(K_\alpha - K_M)\left[\frac{K_M + K_*}{K_\alpha + K_*} - D_{K\alpha}(K_\alpha, \mu_\alpha, K_M, \mu_M)\right] = 0, \tag{22}$$

$$\sum_{\alpha=2}^{n} v_\alpha(\mu_\alpha - \mu_M)\left[\frac{\mu_M + \mu_*}{\mu_\alpha + \mu_*} - D_{\mu\alpha}(K_\alpha, \mu_\alpha, K_M, \mu_M)\right] = 0. \tag{23}$$

Equation (11), with K_* determined from (22), and (15), with μ_* determined from (23), are our polarization approximations for the effective moduli of the matrix composite, using the dilute solution result reference (denoted further as PA0).

In the two-component case, with inclusion functions $D_K = D_K(K_I, \mu_I, K_M, \mu_M)$ and $D_\mu = D_\mu(K_I, \mu_I, K_M, \mu_M)$, (22) and (23) are solved explicitly:

$$K_* = \frac{D_K(K_I, \mu_I, K_M, \mu_M)K_I - K_M}{1 - D_K(K_I, \mu_I, K_M, \mu_M)}, \tag{24}$$

$$\mu_* = \frac{D_\mu(K_I, \mu_I, K_M, \mu_M)\mu_I - \mu_M}{1 - D_\mu(K_I, \mu_I, K_M, \mu_M)}. \tag{25}$$

Analytical expressions of the inclusion-associated functions $D_K(K_I, \mu_I, K_M, \mu_M)$ and $D_\mu(K_I, \mu_I, K_M, \mu_M)$ for 3D ellipsoidal and 2D elliptic inclusions have been constructed by Eshelby. They can be given in the form [Mura 1987; Torquato 2002]

$$D_K = \frac{1}{d}D^0_{iijj}, \qquad D_\mu = \frac{d}{d^2 + d - 2}\left(D^0_{ijij} - \frac{1}{d}D^0_{iijj}\right), \tag{26}$$

where

$$\mathbf{D}^0 = [\mathbf{I} + \mathbf{P} : \mathbf{C}_M^{-1} : (\mathbf{C}_I - \mathbf{C}_M)]^{-1}, \quad \mathbf{C}_I = \mathbf{T}(K_I, \mu_I), \ \mathbf{C}_M = \mathbf{T}(K_M, \mu_M) \tag{27}$$

and $\mathbf{P}$ is the fourth-rank Eshelby tensor. Particular expressions of the components of the tensors in two- and three-dimensional spaces are given in [Mura 1987].

The expressions of the inclusion-associated functions $D_K(K_I, \mu_I, K_M, \mu_M)$ and $D_\mu = D_\mu(K_I, \mu_I, K_M, \mu_M)$ for spherical (or circular) inclusions in general d-dimensional space are simply

$$D_K = \frac{K_M + K_{*M}}{K_I + K_{*M}}, \quad K_{*M} = K_*(\mu_M), \tag{28}$$

$$D_\mu = \frac{\mu_M + \mu_{*M}}{\mu_I + \mu_{*M}}, \quad \mu_{*M} = \mu_*(K_M, \mu_M), \tag{29}$$

where $K_*(\mu_0)$ and $\mu_*(K_0, \mu_0)$ are defined in (11) and (15), respectively. Then the solution of (20) with (28) and that of (21) with (29) should be $K_* = K_{*M}$ and $\mu_* = \mu_{*M}$, respectively (correspondingly, $K_0 = K_M$ and $\mu_0 = \mu_M$). Thus, we obtain the polarization approximation using the dilute solution result reference (PA0) for the n-component matrix composites with spherical inclusions in general d-dimensional space:

$$K^{\mathrm{eff}} = P_K^{(n)}(K_{*M}), \qquad \mu^{\mathrm{eff}} = P_\mu^{(n)}(\mu_{*M}), \tag{30}$$

which coincide with the Maxwell and Mori–Tanaka approximations [Torquato 2002] in that specific case.

Later we shall apply, among others, PA0 from (20)–(27) to matrix composites with noncircular inclusions. It appears that the results of PA0 for the two-component matrix composites with elliptic inclusions also coincide with those of the Mori–Tanaka approximation (as in the case of Figure 3). However, they generally differ for n-component matrix composites if $n \geq 3$ (as in the three-component case of Figure 4), except for the specific pure spherical-circular inclusion composites (30). That is expected, since the Mori–Tanaka approximation for three-component composites may violate Hashin–Shtrikman bounds [Norris 1989], while our polarization approximations, including PA0, by their construction, always obey the bounds.

4. Reference at finite volume proportions of the component materials

The reference parameters K_* and μ_* can be found from the dilute suspension results for the inclusions as was done in the previous section. Otherwise, the reference parameters can be determined, once the respective reference macroscopic moduli of a composite are available numerically or experimentally at any finite volume proportions of the component materials, for the approximations (11) and (15) to fit those reference macroscopic moduli. The resulting polarization approximations are called PA1.

For numerical illustrations, we consider some simple two-dimensional hexagonal-symmetry periodic microstructures, which have macroscopically isotropic elastic moduli, in Figures 1–4. Highly accurate numerical boundary element results used in Figure 1 have been taken from [Eischen and Torquato 1993], where $K_1 = K_M = 1$, $\mu_1 = \mu_M = 0.3$, $K_2 = K_I = 67.5$, and $\mu_2 = \mu_I = 40.5$. Standard periodic boundary conditions with finite element realizations have been used in Figures 2–4. Three periodic cells are indicated at the top of Figures 1–4.

For two-component composites of Figures 2–3, we take $K_1 = K_M = 1$, $\mu_1 = \mu_M = 0.4$, $K_2 = K_I = 20$, and $\mu_2 = \mu_I = 12$ (K_M is normalized to be unity). Figures 1 and 2 involve circular-inclusion composites, while the elliptic inclusions of Figures 3 and 4 have the aspect ratio $a_1 : a_2 = 2$.

In Figures 1–3 we compare graphics of effective elastic moduli of the respective two-component
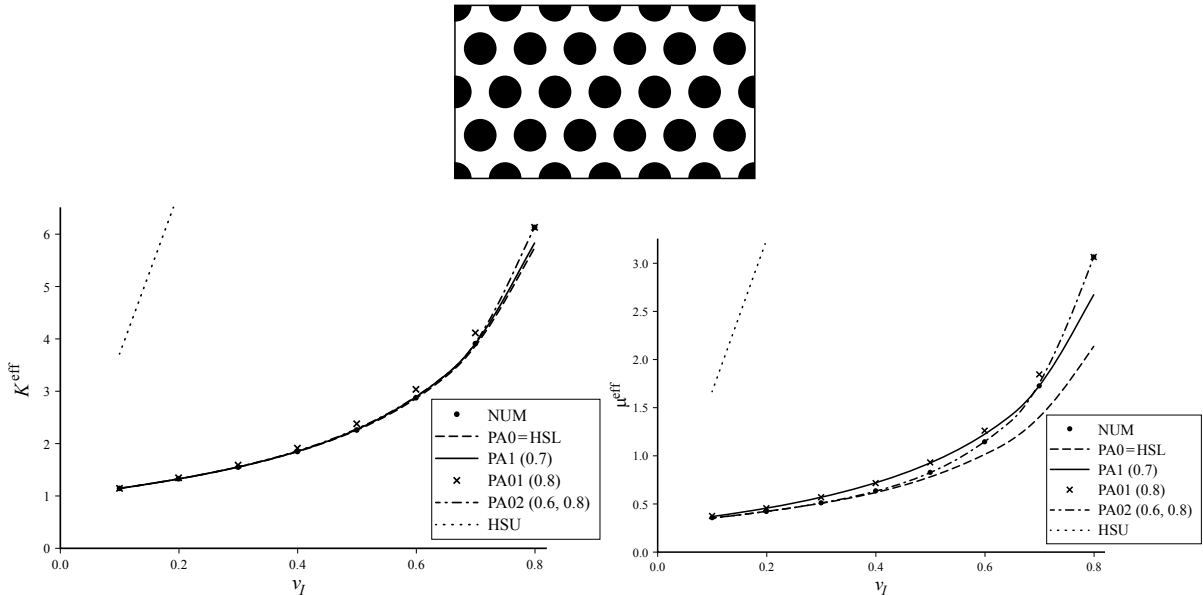
Figure 1. Effective elastic moduli of a 2D periodic circular-inclusion composite at a range of inclusion volumes v_I, with $K_M = 1$, $\mu_M = 0.3$, $K_I = 135$, and $\mu_I = 81$: numerical results (NUM) are compared with HS upper (HSU) and lower (HSL) bounds and polarization approximations PA0 using dilute solution reference, PA1(0.7) using the reference at $v_I = 0.7$, PA02(0.6, 0.8) using dilute solution reference and two references at $v_{I1} = 0.6$ and $v_{I2} = 0.8$, and PA01(0.8) using dilute solution reference and the reference at $v_I = 0.8$. Top: microstructure. Left: bulk modulus. Right: shear modulus.

Figure 2. The moduli of another 2D periodic circular-inclusion composite (the data and notation as in Figure 1): FE are compared with HSU and HSL, PA0, PA1(0.5), PA02(0.5, 0.6), and PA01(0.6). Top: microstructure. Left: bulk modulus. Right: shear modulus.

composites calculated numerically (NUM or FE) with the Hashin–Shtrikman upper (HSU) and lower (HSL) bounds and our polarization approximations PA0, using the dilute suspension reference results, and PA1, using the reference at some finite vol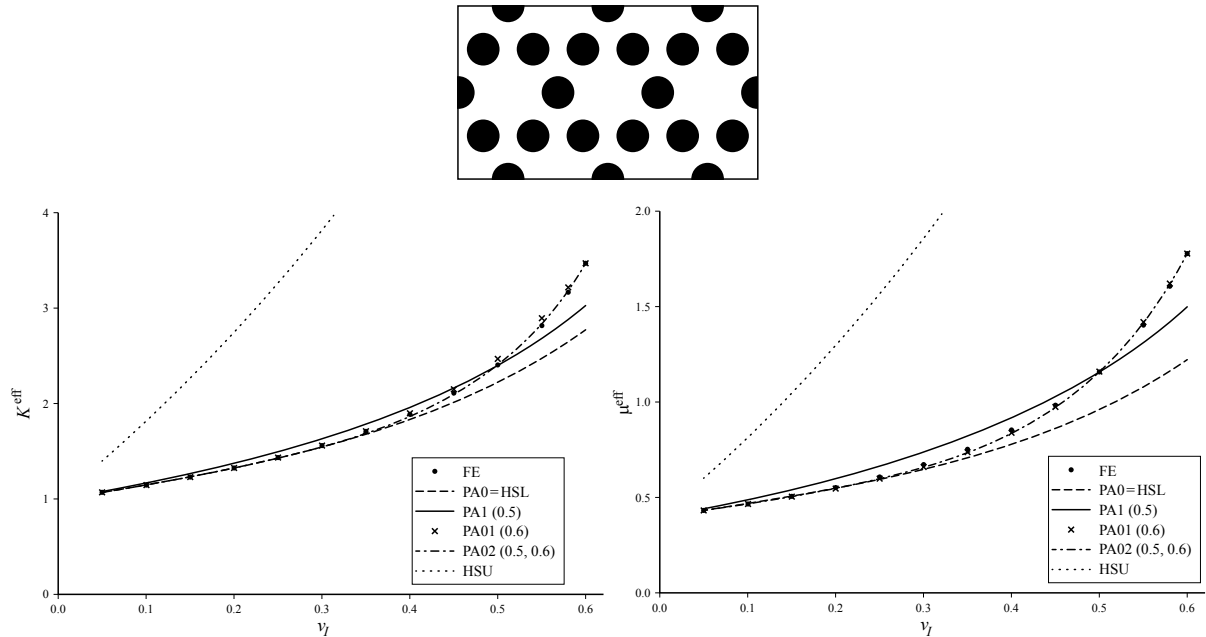ume proportions of the inclusion component, over large ranges of the inclusion phase $v_1 = v_I$. PA1(0.7), for example, indicates PA1 using the reference at $v_I = v_I^{\mathrm{ref}} = 0.7$.

In Figures 1 and 2 with circular inclusions, PA0 coincides with HSL, Maxwell, and Mori–Tanaka approximations, as noted in the previous section. However, PA0 using the dilute elliptic-inclusion reference results from (22)–(23) and (26)–(27) in Figure 3 (as well as PA0 of Figure 4) differs from HS bounds.

One may observe that all PA0 and PA1 fall within HS bounds as expected. PA1, using the reference at finite volume proportion of the included phases, approximates the numerical results better than PA0, using the dilute suspension reference results, over certain finite volume ranges of the included phases (especially near the reference points). The results also reveal that, for the two-component matrix composites, PA0 seems to give lower estimates of the effective moduli, while PA1 provides lower estimates at $v_I > v_I^{\mathrm{ref}}$ and upper estimates at $v_I < v_I^{\mathrm{ref}}$ if the inclusion phase is stiffer than the matrix phase and vice versa if the matrix phase is stiffer (we do not show the respective graphs in the case that the matrix phase is stiffer, because the differences between the curves NUM, FE, HSU, PA0, and PA1 are much less significant there, and we do not want to overload the paper with additional figures).

Our approximations apply to general multicomponent materials. In Figure 4 a three-component composite is considered. Again $K_1 = K_M = 1$ and $\mu_1 = \mu_M = 0.4$, and we take $K_2 = 10$ and $\mu_2 = 6$

(dark elliptic inclusions) and $K_3 = 0.2$ and $\mu_3 = 0.1$ (gray circular inclusions). FE, HSU, HSL, PA0, and PA1 results are compared in Figure 4 over a range of volume proportions of the included phases $v_I = v_2 + v_3$ (presume $v_2 = v_3$).

Experimentally measured values of the macroscopic elastic moduli of a composite at certain volume fractions of the component materials can also serve as the reference moduli for our polarization approximation for the composite over all the ranges of volume fractions of the component materials. Experimental data on the compressibility (elastic bulk modulus) of the porous glass over a range of porosity v_I reported in [Walsh et al. 1965] is displayed in Figure 5. The elastic moduli of the glass are $K_M = 46.3\,\text{GPa}$ and $\mu_M = 30.5\,\text{GPa}$. PA1 for the macroscopic bulk modulus corresponding to an experimental reference point and the HS upper bound are given in the figure for comparisons (HS lower bound is identically zero in this case). The notation PA1(6) denotes PA1 corresponding to the experimental reference point 6 in the graph.

Experimental data on the macroscopic elastic Young's modulus E^{eff} and Poisson's ratio v^{eff} of a particulate-filled glassy polymer [Smith 1976] is displayed in Figure 6, top row. The elastic constants of the polymer matrix are $E_M = 3.01\,\text{GPa}$ and $v_M = 0.394$, while those for the glass are $E_I = 76\,\text{GPa}$ and $v_I = 0.23$. The relations between the 3D elastic constants E, v, K, and μ are

$$K = \frac{E}{3(1-2v)}, \quad \mu = \frac{E}{2(1+v)}, \quad E = \frac{9K\mu}{3K+\mu}, \quad v = \frac{3K-2\mu}{6K+2\mu}. \tag{31}$$

Figure 6 shows PAs for the macroscopic elastic constants corresponding to various experimental reference points and HS bounds.
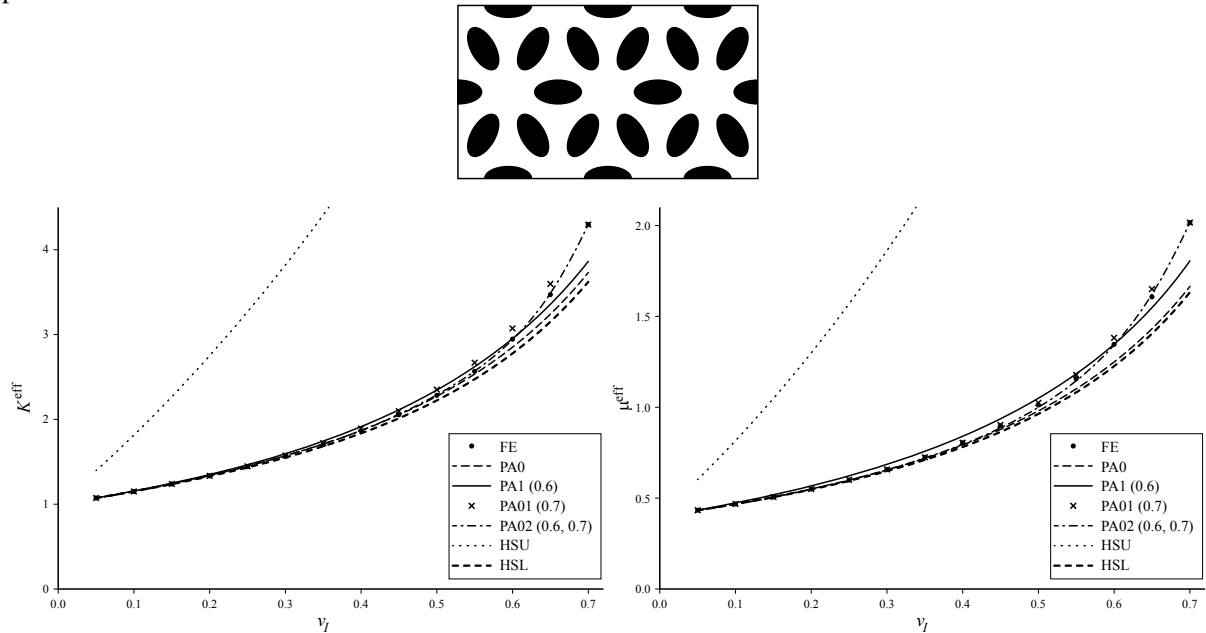
Figure 3. The moduli of a 2D periodic elliptic-inclusion composite (the data and notation as in Figure 1), and the aspect ratio of the ellipses is 2: FE are compared with HS bounds, PA0, PA1(0.6), PA02(0.6, 0.7), and PA01(0.7). Top: microstructure. Left: bulk modulus. Right: shear modulus.
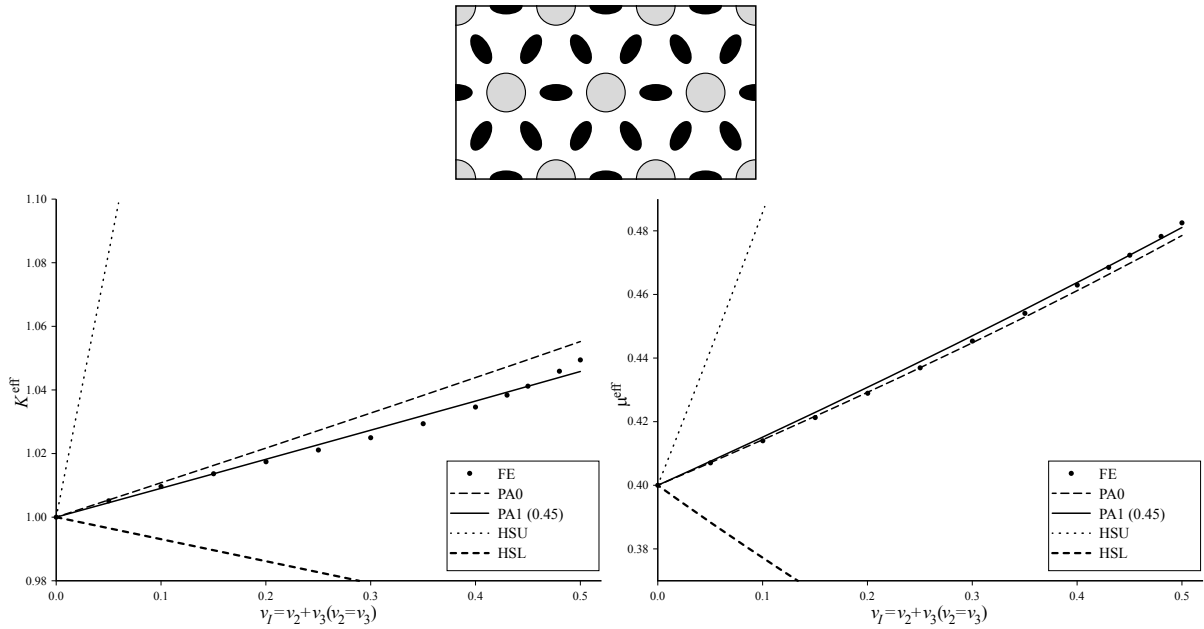
Figure 4. The moduli of a 2D three-component periodic elliptic-circular-inclusion composite at a range of inclusion volumes $v_I = v_2 + v_3$, $v_2 = v_3$, with $K_1 = K_M = 1$ and $\mu_1 = \mu_M = 0.4$ and $K_2 = 10$ and $\mu_2 = 6$ (dark elliptic inclusions) or $K_3 = 0.2$ and $\mu_3 = 0.1$ (gray circular inclusions), and the aspect ratio of the ellipses is 2: FE are compared with HS bounds, PA0, and PA1(0.45). Top: microstructure. Left: bulk modulus. Right: shear modulus.
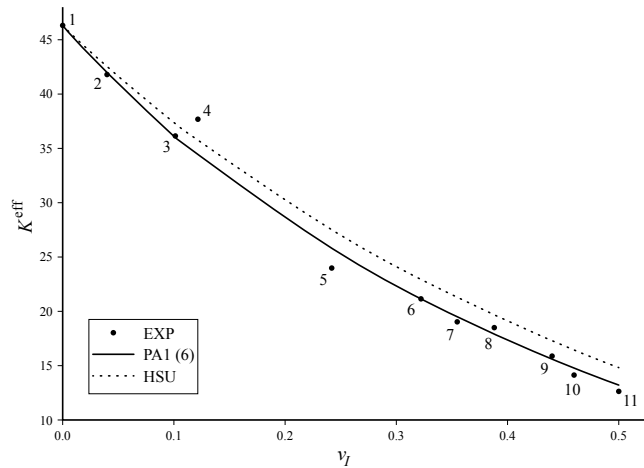
Figure 5. Macroscopic elastic bulk modulus of a porous glass over a range of porosity v_I; the elastic moduli of the glass are $K_M = 46.3$ GPa and $\mu_M = 30.5$ GPa. Experimental data (EXP) are compared with HSU (HSL is identically zero) and PA1(6) using the reference at the reference experimental point 6.
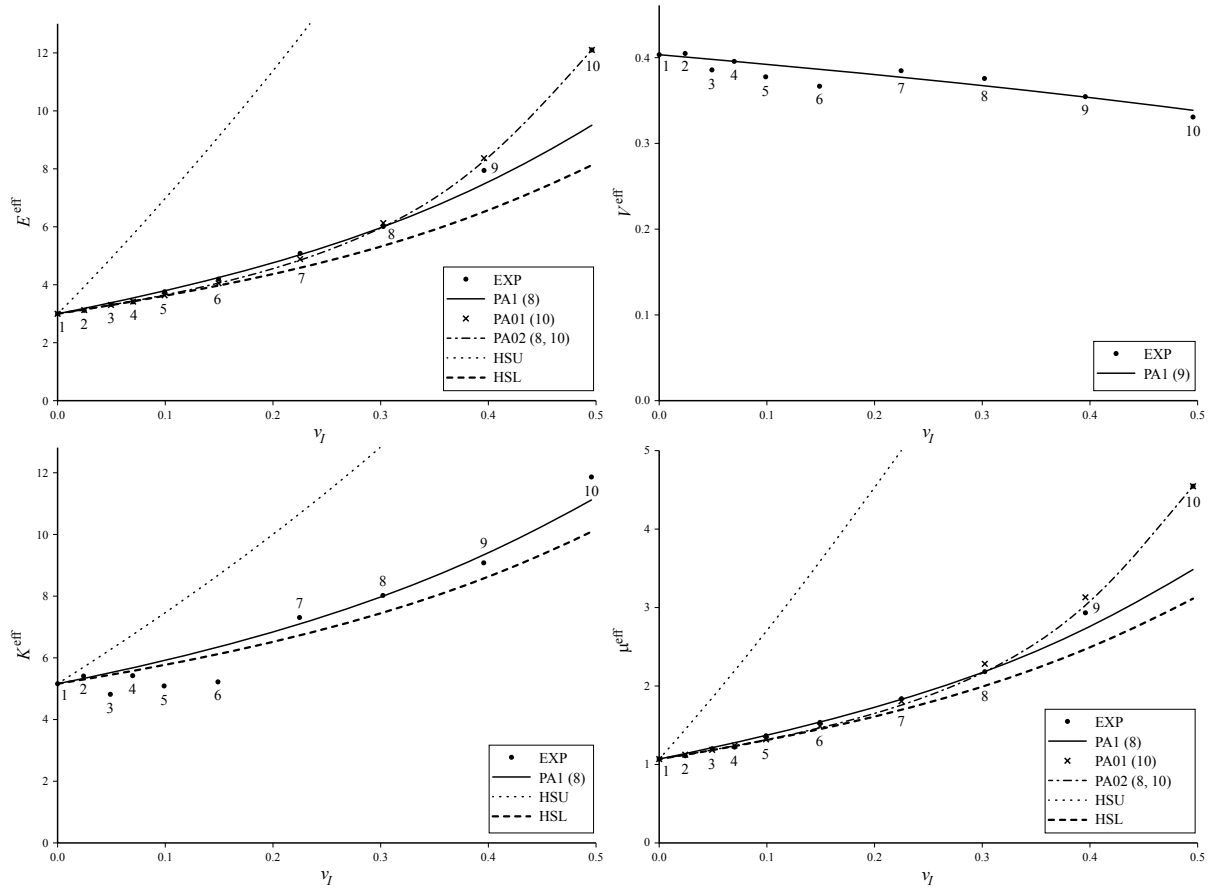
Figure 6. Macroscopic elastic constants of a particulate-filled glassy polymer over a range of inclusion volumes v_I; the elastic constants of the polymer matrix are $E_M = 3.01$ GPa and $v_M = 0.394$, while those for the glass are $E_I = 76$ GPa and $v_I = 0.23$. Experimental data (EXP) are compared with HS bounds, PA1, PA02, and PA01 using the references at the indicated reference experimental points. Top left: Young's modulus. Top right: Poisson's ratio. Bottom left: bulk modulus. Bottom right: shear modulus.

With a one-point reference parameter reflecting the feature of the microgeometry of a particular composite, as with many other EMAs, the polarization approximations PA0 and PA1 have inevitable limitations. For high-contrast-component-property composites, at finite volume proportions of the inclusions, the approximations yield good results only near the reference point and the results become poorer with increasing distance from the reference point. Even so, they should obey HS bounds over all the ranges of component proportions, once the reference model satisfies HS bounds at the reference point.

5. Multipoint polarization approximations

By assuming K_* and μ_* are functions of volume proportions of the component materials, we are able to use more reference points to obtain better approximations of the effective moduli. The variable reference

parameters K_* and μ_* should lie within the intervals (13) and (17), respectively, for the approximations to obey HS bounds.

Further, in the remaining part of this paper, we shall restrict ourselves to two-component materials and assume the variable reference parameters K_* and μ_* of the polarization approximations (11) and (15), respectively, to be of the form

$$K_* = \overline{K}_*(c + av_2^b), \qquad b > 0, \tag{32}$$

$$\mu_* = \overline{\mu}_*(c' + a'v_2^{b'}), \quad b' > 0, \tag{33}$$

where $\overline{K}_*$ and $\overline{\mu}_*$ are some fixed values of elastic moduli dimension; three dimensionless parameters a, b, c or a', b', c' should be found from appropriate available references. Presume we have three numerical or experimental reference values of the effective elasticity $K^{\mathrm{eff}} = K^{\mathrm{eff}}_{\mathrm{ref}\,1}, K^{\mathrm{eff}}_{\mathrm{ref}\,2}, K^{\mathrm{eff}}_{\mathrm{ref}\,3}$ and $\mu^{\mathrm{eff}} = \mu^{\mathrm{eff}}_{\mathrm{ref}\,1}, \mu^{\mathrm{eff}}_{\mathrm{ref}\,2}, \mu^{\mathrm{eff}}_{\mathrm{ref}\,3}$ at the volume proportions $v_2 = v_{21}, v_{22}, v_{23}$, respectively. Solving (11) in the two-component case, one finds

$$K_*^{\mathrm{ref}} = \frac{K^{\mathrm{eff}}_{\mathrm{ref}}(v_1 K_2 + v_2 K_1) - K_1 K_2}{v_1 K_1 + v_2 K_2 - K^{\mathrm{eff}}_{\mathrm{ref}}} \tag{34}$$

and the respective values of the reference parameter $K^{\mathrm{ref}}_{*1}, K^{\mathrm{ref}}_{*2}, K^{\mathrm{ref}}_{*3}$ corresponding to $K^{\mathrm{eff}}_{\mathrm{ref}\,1}, K^{\mathrm{eff}}_{\mathrm{ref}\,2}, K^{\mathrm{eff}}_{\mathrm{ref}\,3}$. Now with (32) one derives three dimensionless equations for three dimensionless parameters a, b, c:

$$(c + av_{21}^b) = k_1, \qquad (c + av_{22}^b) = k_2, \qquad (c + av_{23}^b) = k_3, \tag{35}$$

where

$$k_1 = K^{\mathrm{ref}}_{*1}/\overline{K}_*, \qquad k_2 = K^{\mathrm{ref}}_{*2}/\overline{K}_*, \qquad k_3 = K^{\mathrm{ref}}_{*3}/\overline{K}_*. \tag{36}$$

Equation (35) leads to the unique equation determining b

$$\frac{v_{21}^b - v_{22}^b}{v_{21}^b - v_{23}^b} = \frac{k_1 - k_2}{k_1 - k_3}, \tag{37}$$

and explicit expressions for a and c

$$a = \frac{k_1 - k_2}{v_{21}^b - v_{22}^b}, \qquad c = k_1 - av_{21}^b. \tag{38}$$

The polarization approximations (11) and (32) for K^{eff} with the parameters a, b, c determined from (37)–(38) shall be referred to as three-point polarization approximation PA3. Since K_* in (32) is a monotonous function of v_2, if the reference macroscopic moduli $K^{\mathrm{eff}}_{\mathrm{ref}\,1}, K^{\mathrm{eff}}_{\mathrm{ref}\,2}, K^{\mathrm{eff}}_{\mathrm{ref}\,3}$ satisfy HS bounds, the approximations (11) and (38) also obey HS bounds, at least, over the range $\min\{v_{21}, v_{22}, v_{23}\} \le v_2 \le \max\{v_{21}, v_{22}, v_{23}\}$. Independently, a similar three-point polarization approximation for μ^{eff} from (15) and (33) is obtained. The respective equations (34)–(38) keep the same forms, except that one has to substitute notations μ, a', b', c' for K, a, b, c.

In the case of two-component matrix composites, with the notation $v_1 = v_M$, $K_1 = K_M$, $\mu_1 = \mu_M$, and $v_2 = v_I$, $K_2 = K_I$, $\mu_2 = \mu_I$, if dilute solution results (18)–(19) are available, one can use them to find c and c' independently as was done in Section 3 and suggest simpler two-point polarization approximations

(11) for K^{eff} and (15) for μ^{eff} with variable reference parameters involving just two free parameters a and b (and a' and b'):

$$K_* = \bar{K}_*(1 + a v_2^b), \quad \bar{K}_* = \frac{D_K K_I - K_M}{1 - D_K}, \tag{39}$$

$$\mu_* = \bar{\mu}_*(1 + a' v_2^{b'}), \quad \bar{\mu}_* = \frac{D_\mu \mu_I - \mu_M}{1 - D_\mu}, \tag{40}$$

where D_K and D_μ are the functions from the dilute solution results (27)–(28) which have the expressions (26)–(27) for ellipsoidal (elliptic) inclusion cases. Now one needs just two reference equations determining a and b:

$$1 + a v_{21}^b = k_1, \qquad 1 + a v_{22}^b = k_2. \tag{41}$$

Equation (41) can be solved explicitly to give

$$b = \log_{v_{21}/v_{22}} \frac{k_1 - 1}{k_2 - 1} = \ln \frac{k_1 - 1}{k_2 - 1} \Big/ \ln \frac{v_{21}}{v_{22}}, \quad a = \frac{k_1 - 1}{v_{21}^b}. \tag{42}$$

Polarization approximations (11), (39), (41), and (42) using the dilute solution reference and two references at $v_2 = v_{21}$, v_{22} is referred to as PA02. Independently, a similar polarization approximation PA02 for μ^{eff} from (15) and (40) is obtained. The respective equations (41)–(42) keep the same forms, with the only change being the substitution of the notations μ, a', b', c' for K, a, b, c. One observes that the approximations obey HS bounds, at least, over the range $0 \le v_2 \le \max\{v_{21}, v_{22}\}$.

Graphs of PA02 from (11), (15), (39)–(42), and (26) for the suspension of elliptic inclusions of the configuration of Figure 3, top, using the dilute solution result and two numerical references at $v_{I1} = 0.6$ and $v_{I2} = 0.7$, are presented with $a = 27.6$ and $b = 9.75$ (Figure 3, left) and $a' = 8.17$ and $b' = 6.11$ (Figure 3, right). One can observe that PA02 fits well with the numerical data.

In the case of composites with sphere-like (circular-like) inclusions, D_K and D_μ have simple expressions (28)–(29), and $\bar{K}_* = K_*(\mu_M)$ and $\bar{\mu}_* = \mu_*(K_M, \mu_M)$ in (39) and (40). Applications of PA02 are presented with numerical references at $v_{I1} = 0.6$ and $v_{I2} = 0.8$ and $a = 3.17$ and $b = 9.43$ (Figure 1, left) and $a' = 3.18$ and $b' = 3.60$ (Figure 1, right). Similarly PA02 is given with numerical references at $v_{I1} = 0.5$ and $v_{I2} = 0.6$ and $a = 32.5$ and $b = 5.72$ (Figure 2, left) and $a' = 19$ and $b' = 4.08$ (Figure 2, right). PA02 with experimental references at the experimental points 8 and 10 are shown with $a = 10.5$ and $b = 2.34$ (Figure 6, top left) and $a' = 12.5$ and $b' = 2.9$ (Figure 6, bottom right). In all the cases, PA02 fits the numerical or experimental data much better than PA0 or PA1, as expected.

If only one numerical or experimental value of the effective moduli of the matrix composite at a finite volume proportion point $v_2 = v_I = v_{I1}$ is available for reference (in addition to the dilute solution one), one has to fix an additional parameter, for instance b or b', and obtains just one equation (the first one of (41)) which determines the remaining parameter a or a', according to the second equation of (42). The resulted approximation is called PA01. It should obey HS bounds, at least, over the range $0 \le v_I \le v_{I1}$.

PA01 with $b = b' = 4$ is projected using numerical reference at $v_{I1} = 0.6$ and $a = 13.5$ (Figure 2, left) or $a' = 18.2$ (Figure 2, right) and at $v_{I1} = 0.7$ and $a = 3.55$ (Figure 3, left) or $a' = 3.85$ (Figure 3, right). PA01 with $b = b' = 2$ is applied using numerical reference at $v_{I1} = 0.8$ and $a = 0.606$ (Figure 1, left) and $a' = 0.227$ (Figure 1, right) and with experimental reference at the experimental point 10 and $a = 8.31$ (Figure 6, top left) or $a' = 6.68$ (Figure 6, bottom right). Though b and b' for PA01 in those

figures are chosen to be not quite close to the respective b and b' for PA02, the approximations appear relatively good.

6. Conclusion

Unlike other EMAs (such as the self-consistent, differential, Maxwell, and Mori–Tanaka ones), which are constructed from the field equations, our PAs are based on the approximate field solutions which come from minimum energy principles. The "optimal" polarization trial fields constructed earlier to bound the effective elastic moduli of isotropic multicomponent materials have been implemented to derive the PAs for the moduli in three and generally d dimensions. The approximations are separate functions for the effective bulk and shear moduli and contain, in addition to the moduli and volume proportions of the components, certain free parameters, which should be determined from some reference effective moduli at certain volume proportions of the component materials analytically, numerically, or experimentally. Specifically, PA0 using the dilute solution reference (similar to other EMAs) as well as PA1 using the reference at a component's finite volume proportion point should obey HS bounds over all the ranges of volume proportions of the component materials. Refined approximations with variable reference parameters incorporating more available information about a particular composite should improve the accuracy of the estimations. Specifically, PA02 using dilute solution reference and two references at components' finite volume proportion points and PA01 using dilute solution reference and one reference at a component's finite volume proportion point can yield good approximations. The approximations satisfy HS bounds, at least, over the volume proportion range between the extreme reference points.

Acknowledgment

References

[Christensen 1979] R. M. Christensen, *Mechanics of composite materials*, Wiley, New York, 1979.

[Eischen and Torquato 1993] J. W. Eischen and S. Torquato, "Determining elastic behavior of composites by the boundary element method", *J. Appl. Phys.* **74**:1 (1993), 159–170.

[Eshelby 1957] J. D. Eshelby, "The determination of the elastic field of an ellipsoidal inclusion, and related problems", *Proc. Roy. Soc. London. A* **241** (1957), 376–396.

[Franciosi et al. 2011] P. Franciosi, R. Brenner, and A. El Omri, "Effective property estimates for heterogeneous materials with cocontinuous phases", *J. Mech. Mater. Struct.* **6**:5 (2011), 729–763.

[Hashin and Shtrikman 1963] Z. Hashin and S. Shtrikman, "A variational approach to the theory of the elastic behaviour of multiphase materials", *J. Mech. Phys. Solids* **11**:2 (1963), 127–140.

[Klusemann et al. 2012] B. Klusemann, H. J. Böhm, and B. Svendsen, "Homogenization methods for multi-phase elastic composites with non-elliptical reinforcements: comparisons and benchmarks", *Eur. J. Mech. A* **34** (2012), 21–37.

[Kushch et al. 2013] V. I. Kushch, S. G. Mogilevskaya, H. K. Stolarski, and S. L. Crouch, "Evaluation of the effective elastic moduli of particulate composites based on Maxwell's concept of equivalent inhomogeneity: microstructure-induced anisotropy", *J. Mech. Mater. Struct.* **8**:5–7 (2013), 283–303.

[Milton 2002] G. W. Milton, *The theory of composites*, Cambridge Monographs on Applied and Computational Mathematics **6**, Cambridge University, 2002.

[Mogilevskaya et al. 2012] S. G. Mogilevskaya, H. K. Stolarski, and S. L. Crouch, "On Maxwell's concept of equivalent inhomogeneity: when do the interactions matter?", *J. Mech. Phys. Solids* **60**:3 (2012), 391–417.

[Mori and Tanaka 1973] T. Mori and K. Tanaka, "Average stress in matrix and average elastic energy of materials with misfitting inclusions", *Acta Metall.* **21**:5 (1973), 571–574.

[Mura 1987] T. Mura, *Micromechanics of defects in solids*, 2nd ed., Mechanics of Elastic and Inelastic Solids **3**, Kluwer, Dordrecht, 1987.

[Nogales and Böhm 2008] S. Nogales and H. J. Böhm, "Modeling of the thermal conductivity and thermomechanical behavior of diamond reinforced composites", *Int. J. Eng. Sci.* **46**:6 (2008), 606–619.

[Norris 1989] A. N. Norris, "An examination of the Mori–Tanaka effective medium approximation for multiphase composites", *ASME J. Appl. Mech.* **56**:1 (1989), 83–88.

[Pham 1993] D. C. Pham, "Bounds on the effective shear modulus of multiphase materials", *Int. J. Eng. Sci.* **31**:1 (1993), 11–17.

[Pham 2012] D. C. Pham, "Bounds on the elastic moduli of statistically isotropic multicomponent materials and random cell polycrystals", *Int. J. Solids Struct.* **49**:18 (2012), 2646–2659.

[Pham 2014] D. C. Pham, "Improved three-point correlation estimates for the effective elastic moduli of random orthorhombic crystals and multicomponent materials", *Philos. Mag. A* **94**:10 (2014), 1112–1131.

[Phan-Thien and Pham 2000] N. Phan-Thien and D. C. Pham, "Differential multiphase models for polydispersed spheroidal inclusions: thermal conductivity and effective viscosity", *Int. J. Eng. Sci.* **38**:1 (2000), 73–88.

[Sevostianov and Kachanov 2014] I. Sevostianov and M. Kachanov, "On some controversial issues in effective field approaches to the problem of the overall elastic properties", *Mech. Mater.* **69**:1 (2014), 93–105.

[Smith 1976] J. C. Smith, "Experimental values for the elastic constants of a particulate-filled glassy polymer", *J. Res. NBS A* **80A**:1 (1976), 45–49.

[Torquato 2002] S. Torquato, *Random heterogeneous materials: microstructure and macroscopic properties*, Interdisciplinary Applied Mathematics **16**, Springer, 2002.

[Tran and Pham 2015] A. B. Tran and D. C. Pham, "Polarization approximations for the macroscopic elastic constants of transversely isotropic multicomponent unidirectional fiber composites", *J. Compos. Mater.* **49**:30 (2015), 3765–3780.

[Walpole 1966] L. J. Walpole, "On bounds for the overall elastic moduli of inhomogeneous systems, I", *J. Mech. Phys. Solids* **14**:3 (1966), 151–162.

[Walsh et al. 1965] J. B. Walsh, W. F. Brace, and A. W. England, "Effect of porosity on compressibility of glass", *J. Am. Ceram. Soc.* **48**:12 (1965), 605–608.

[Willis 1977] J. R. Willis, "Bounds and self-consistent estimates for the overall properties of anisotropic composites", *J. Mech. Phys. Solids* **25**:3 (1977), 185–202.

DUC CHINH PHAM: pdchinh@imech.vast.vn
Institute of Mechanics, Vietnam Academy of Science and Technology, 264 Doi Can, Ba dinh, Hanoi, Vietnam

and

Graduate University of Science and Technology – VAST, 18 Hoang Quoc Viet, Hanoi, Vietnam

NGUYEN QUYET TRAN: tranquyetth@gmail.com
Department of Applied Mechanics, Hanoi University of Industry, 298 Cau Dien, Hanoi, Vietnam

and

Graduate University of Science and Technology – VAST, 18 Hoang Quoc Viet, Hanoi, Vietnam

ANH BINH TRAN: anh-binh.tran@nuce.edu.vn
Department of Applied Informatics in Construction, National University of Civil Engineering, 55 Giai phong, Hanoi, Vietnam

and

Graduate University of Science and Technology – VAST, 18 Hoang Quoc Viet, Hanoi, Vietnam

msp

A NONLINEAR MICROMECHANICAL MODEL FOR PROGRESSIVE DAMAGE OF VERTEBRAL TRABECULAR BONES

EYASS MASSARWA, JACOB ABOUDI, FABIO GALBUSERA,
HANS-JOACHIM WILKE AND RAMI HAJ-ALI

A new three-dimensional (3D) nonlinear micromechanical analysis is proposed to predict the overall mechanical response to damage evolution of the vertebral trabecular bone (VTB) highly porous microstructure. Towards that goal, a nonlinear micromechanical model, based on the 3D parametric high fidelity generalized method of cells (HFGMC) micromechanics, is extended to include progressive damage. The damage is initiated at the local subcell and its evolution is carried out using a strain-softening method. The nonlinear HFGMC behavior including damage evolution is first verified by examining its ability to predict the experimental nonlinear compression stress-strain response of printed polymeric VTB highly porous microstructure. Next, predicted HFGMC pre- and postultimate failure for native VTB representative unit cells (RUCs) harvested from different vertebrae of human cadavers (n = 10) are carried out. Some of the latter predictions were compared to reported values found in the literature. The proposed nonlinear HFGMC micromechanical model with evolving damage can predict the overall nonlinear behavior, including postultimate range.

1. Introduction

Osteoporosis is a bone disease state characterized by low bone strength and an increased fracture risk of the bone walls. Although osteoporosis affects the entire skeleton, osteoporotic fractures commonly occur in the spine vertebrae [Nevitt et al. 1999]. The vertebral bodies, primary structures located in the spine, bear the compressive loads. Vertebrae are composed of an internal highly porous trabecular bone core surrounded by a thin shell of dense material called cortical bone [Cowin 2001]. Studies have shown that the trabecular bone carries a substantial proportion of the compressive loads applied to the vertebral body [Rockoff et al. 1969]. The loss of trabecular bone density and strength throughout the osteoporotic process leads to failure of the entire vertebra. Maquer et al. [2015] showed that osteoporotic vertebral compression fractures strongly depend on bone volume fraction and trabecular bone microarchitecture.

Experimental studies with irreversible loading (overloading and damage) of the trabecular bone have been conducted. A reduction of the elastic moduli, strength and accumulation of residual deformations in the trabecular bone were the main consequences [Keaveny et al. 1994; 1999; Zysset 1994]. Another extensive experimental outcome demonstrated that for postyield behavior, the yield strains over a limited range of densities for human vertebral trabecular bones (VTBs) are independent of the apparent density and have reasonably constant values [Kopperdahl and Keaveny 1998]. Another important study by Fyhrie et al. [1994] microscopically examined the mechanisms of failure in human VTBs compressed by a large

---

deformation. Microscopic cracking as the result of shear stresses in the trabeculae, complete fractures of trabeculae occurring in those oriented transversely to the loading direction and residual compressive strain formation were the main observations of this study. Based on other experimental studies [Fyhrie and Schaffler 1994; Gibson and Ashby 1999; Hayes and Carter 1976], the load-displacement curves for VTB specimens can include a sequence of several responses:

(1) an initial linear undamaged region;

(2) a material nonlinear response including strain-softening caused by damage accumulation;

(3) ultimate load peak region;

(4) postpeak unloading with increased strain and displacement; and

(5) a region where with increased displacements, the load is increased with very small values.

Finite element models have been extensively used to study trabecular bone mechanical behavior due to the anatomical complexity of the trabecular bone and limited availability of cadaveric specimens. A previous study [Niebur et al. 2000] presented a nonlinear high-resolution finite element analysis framework to calibrate the effective elastic moduli, as well as tensile and compressive yield strains of the bovine tibia trabecular bone. In another study, based on a voxel-based finite element analysis combined with physical measurements of volume fraction, μCT reconstructions, uniaxial mechanical and nanoindentation tests of trabecular bone extracted from cadaveric proximal femurs was demonstrated [Chevalier et al. 2007]. More recently, Hamed and Jasiuk [2013] introduced a multiscale computational finite element model with dominant damage mechanisms to predict stiffness and bone strength at different structural scales by using cohesive interface elements. Harrison et al. [2013] also developed a 3D high-resolution model with fracture criteria and a large-deformation computational model predicting the full range of response including the pre- and postultimate stress state, referred to as "ultimate strength" by the authors. The damage and fracture processes were simulated at the local element by reducing the elastic modulus and removing the element, respectively. This analysis model has successfully predicted ultimate strength following the softening of the trabecular bone. In order to analyze human trabecular bone samples under compressive loading, an isotropic μCT finite element model coupled to a damage law was developed [Hambli 2013]. The element deletion technique was also adapted.

Goda et al. [2012] presented a micromechanical method to investigate the microstructural effects of the macroscopic mechanical properties of trabecular bones. A Cosserat anisotropic continuum model was modeled from the discrete homogenization of a quasiperiodical lattice model for the microstructural trabecular bone where the effective mechanical properties of the trabecular bone were directly related to the lattice microstructure and its elastic properties. In addition, the bone walls of the lattice were modeled as linear elastic Timoshenko thick beams. Recently, Goda and Ganghoffer [2015] introduced a three-dimensional model studying the multiaxial yield and failure response of trabecular bones and established criteria for brittle and ductile collapse based on micromechanical methods. In this study, the homogenization technique was used to create the plastic yield surfaces of two and three-dimensional bending-dominated periodic lattices which demonstrate the topology of trabecular bones. More recently, Goda et al. [2016] developed a numerical model to predict the effective properties of porous polymeric biomaterials. Finite element models based on an accurate three-dimensional solid model from μCT data were generated to quantify the effects of the porosity. In this study, the second gradient of deformation,

which is expressed as in couples stress continuum theories, was used to address the size dependency in porous structures.

The high fidelity generalized method of cells (HFGMC) is a micromechanical method used to analyze 2 and 3D multiphase composites. Global and local quadratic displacement fields (microvariables) within a discretized representative volume element (RVE) divided into subcells are applied. The mechanical formulation of the HFGMC is performed using traction and displacement continuity equations between the interfaces of the subcells as well as the average volume equilibrium applied in the subcells [Haj-Ali and Aboudi 2013, 2016]. The HFGMC method has been widely used for both linear and nonlinear applications in order to analyze the behavior of multiphase composites such as viscoelastic, viscoplastic, bond damage of fiber, smart composite materials and piezoresistive fiber-reinforced composites [Aboudi et al. 2013; Haj-Ali et al. 2014]. The HFGMC method with damage evolution effects has also been proposed [Haj-Ali and Aboudi 2009] using cohesive traction-separation between the subcells and cell extinction damage (CED) approaches.

In the present study, to predict the overall nonlinear mechanical response with evolving damage of VTB highly porous microstructures, a proposed nonlinear 3D parametric HFGMC with progressive damage is presented. Verification of the model is performed by comparing the nonlinear stress-strain predicted curve to one obtained from our own compression tests performed on a printed polymeric VTB-RUC microstructure as well as curves reported in the literature for native VTBs.

2. Methods

A nonlinear micromodeling framework based on the 3D parametric HFGMC micromechanical method was formulated to predict the nonlinear response including damage evolution of a VTB highly porous microstructure deformed under a uniaxial compression stress state [Haj-Ali and Aboudi 2013, 2016]. A nonlinear elastic power-law model and postfailure approach were used. Three-dimensional μCT HFGMC models were geometrically generated from scanned specimens. In addition, compression tests
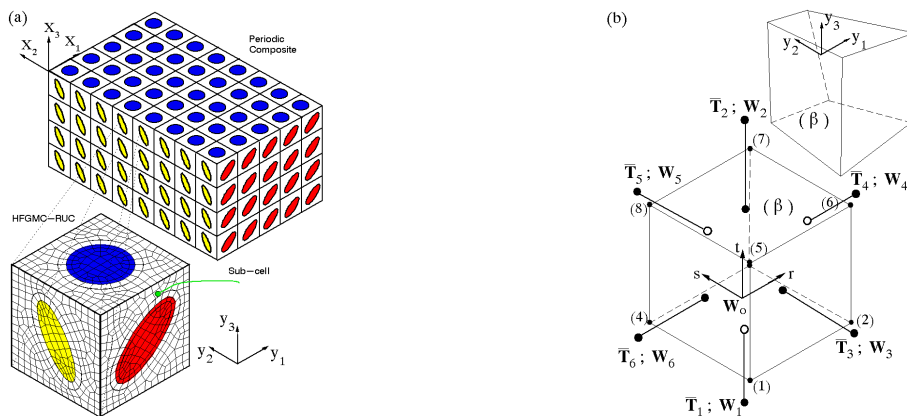

Figure 1. Schematic illustration of a triply periodic multiphase composite material in the global coordinate system with its HFGMC representative unit cell (RUC) comprising general hexahedral subcells defined with respect to its local coordinate system, (a). A general hexahedral subcell in its physical and parent coordinate systems, (b).

on 3D printed polymeric VTB-RUC microstructures were conducted to generate its stress-strain response and verify the ability of the nonlinear HFGMC model to predict nonlinear VTB behavior.

2.1. *Nonlinear HFGMC model.* We present herein the mechanical formulation of the nonlinear parametric HFGMC based on Haj-Ali and Aboudi's studies [2013; 2016]. The parametric HFGMC micromechanical method is based on the homogenization technique, in which a representative unit cell (RUC) of a triply periodic multiphase composite can be identified. A multiphase composite of a triply periodic microstructure defined with respect to the global coordinate system (X_1, X_2, X_3) is schematically described together with its parallelepiped RUC and defined with respect to the local material coordinate system (y_1, y_2, y_3) (Figure 1a). The RUC domain is discretized into a general assembly of hexahedral subcells representing different phase geometries. A general hexahedral subcell is mapped to a uniform parametric coordinate system (r, s, t) using a classical linear transformation (Figure 1b). The compact quadratic form of the increment of the displacement vector Δu in each subcell is defined by

$$\begin{aligned}
\Delta u = \Delta u^0 + \Delta W_0 &+ \tfrac{1}{2}(\Delta W_4 - \Delta W_6)r + \tfrac{1}{2}(\Delta W_5 - \Delta W_3)s + \tfrac{1}{2}(\Delta W_2 - \Delta W_1)t \\
&+ \tfrac{1}{4}(\Delta W_4 + \Delta W_6 - 2 \cdot \Delta W_0)(3r^2 + rs + rt - 1) \\
&+ \tfrac{1}{4}(\Delta W_3 + \Delta W_5 - 2 \cdot \Delta W_0)(3s^2 + rs + st - 1) \\
&+ \tfrac{1}{4}(\Delta W_1 + \Delta W_2 - 2 \cdot \Delta W_0)(3t^2 + rt + st - 1),
\end{aligned} \tag{1}$$

where the applied remote global increment of the displacement field is $\Delta u^0 \equiv \Delta \varepsilon^0 \cdot X$. Here, ε^0 is the applied remote second order strain tensor.

The components of vectors ΔW_k, $k = 1 \ldots 6$ and one additional internal displacement variable ΔW_0 are the increments of the fluctuating displacement microvariables. The strain vector

$$\varepsilon^T \equiv \{\varepsilon_{11}, \varepsilon_{22}, \varepsilon_{33}, 2\varepsilon_{23}, 2\varepsilon_{13}, 2\varepsilon_{12}\}$$

in a given subcell (β) is defined in an incremental form by

$$\Delta \varepsilon_{ij}^{(\beta)}(y(r, s)) = \Delta \varepsilon_{ij}^0 + \frac{1}{2}\left(\frac{\partial(\Delta u_i)}{\partial y_j} + \frac{\partial(\Delta u_j)}{\partial y_i} \right), \tag{2}$$

$$\Delta \varepsilon^{(\beta)} = \Delta \varepsilon^0 + A^{(\beta)} \Delta W^{(\beta)}, \tag{3}$$

where $A^{(\beta)}$ is the matrix relating to the incremental strain displacement microvariables. The nonzero components of this matrix are found in Haj-Ali and Aboudi's studies [2013; 2016]. The increment of the displacement microvariables vector $\Delta W^{(\beta)}$ of the subcell (β) includes 21 components.

For a general nonlinear material filling a subcell (β), the incremental form of its constitutive relationship is given by

$$\Delta \sigma^{(\beta)} = C^{t,(\beta)} : \Delta \varepsilon^{(\beta)}, \tag{4}$$

where $C^{t,(\beta)}$ is the proper instantaneous fourth-order tangential stiffness tensor that is computed based on the considered nonlinear material response within the subcell. The incremental stress and strain vectors of a subcell (β) are $\Delta \sigma^{(\beta)}$ and $\Delta \varepsilon^{(\beta)}$, respectively.

The incremental surface-average traction vector on face number k of the hexahedral subcell (β) is then obtained by the following equation:

$$\Delta \bar{T}^{(\beta_k)} = \tfrac{1}{4} N^{(\beta_k)} \Delta C^{t,(\beta)} [\Delta \varepsilon^0 + \bar{A}^{(\beta_k)} \Delta W^{(\beta)}], \tag{5}$$

where the $N^{(\beta_k)}$ matrix is defined by

$$N^{(\beta_k)} = \begin{bmatrix} n_1 & 0 & 0 & 0 & n_3 & n_2 \\ 0 & n_2 & 0 & n_3 & 0 & n_1 \\ 0 & 0 & n_3 & n_2 & n_1 & 0 \end{bmatrix}^{(\beta_k)}. \tag{6}$$

The (n_1, n_2, n_3) are the components of the normal vector to the k-th face of subcell (β). Matrix $\bar{A}^{(\beta_k)}$ is computed as

$$\bar{A}^{(\beta_k)} = \int_{-1}^{1} \int_{-1}^{1} A^{(\beta)} \, dr \, ds. \tag{7}$$

Next, we impose traction and displacement interfacial continuity conditions within the inner subcells:

$$\begin{aligned} \Delta \bar{T}^{(\beta_k)} &= \Delta \bar{T}^{(\gamma_m)}, \\ \Delta W_k^{(\beta)} &= \Delta W_m^{(\gamma)}. \end{aligned} \tag{8}$$

This is done using the incremental surface-average microvariables. In addition, equilibrium equations of each subcell are applied in an incremental volumetric average form:

$$\int_V \nabla \cdot (\Delta \sigma) \, dV = \sum_{k=1}^{6} A_k \Delta \bar{T}^{(\beta_k)} = 0. \tag{9}$$

Here, (β_k) denotes the k-th face of subcell (β), (γ_m) is the neighboring m-th face of subcell (γ), v_β is the volume of subcell (β) and A_k is the area of the k-th face.

The total number of unknown incremental displacement microvariables in the RUC is $21 \times N_c$, where N_c is the total number of subcells (each one having 21 displacement microvariables). The number of continuity equations for incremental displacements is $3 \times 3N_c$ (for each subcell there are only three independent interfaces). The number of incremental traction continuity equations is also $3 \times 3N_c$. The incremental volume average equilibrium equations in (9) present an additional $3N_c$ equations.

The assembly of the derived $21N_c$ HFGMC governing equations of the RUC can be symbolically expressed by

$$[\Delta R] \equiv \begin{bmatrix} \Delta T^{(+)} - \Delta T^{(-)} \\ \Delta W^{(+)} - \Delta W^{(-)} \\ \int_V \nabla \cdot (\Delta \sigma) \, dV \end{bmatrix} = 0, \quad \{D\} \equiv \begin{Bmatrix} D_T \\ 0 \\ 0 \end{Bmatrix}, \tag{10}$$

where $[\Delta R]$ is the incremental residual matrix expressing the incremental form of the displacement continuity, traction continuity and subcells' equilibrium, respectively.

The 21 unknown incremental displacement microvariables for each subcell (β) are obtained by solving the system of linear equation resulting from the linearized incremental form of (10). In general, the

governing incremental equations can symbolically be written as

$$\{\Delta W\} = -[\partial(\Delta R)/\partial(\Delta W)]^{-1} \cdot \{D\} \cdot \{\Delta \bar{\varepsilon}^0\}. \tag{11}$$

Then, the above system is solved for a given incremental remote applied strain vector $\Delta \bar{\varepsilon}^0$ in order to obtain the incremental displacement microvariables of the subcells. Moreover, the incremental local strain vectors can be readily obtained using (3), leading in turn to the spatial distribution of the incremental stresses in the RUC. Further discussion of the solution approach for the above equation system and how to obtain the overall tangential stiffness matrix of a multiphase composite can be found in Haj-Ali and Aboudi's research [2013; 2016].

2.2. *Material nonlinearity.* A nonlinear elastic power-law model of the Ramberg–Osgood (R-O) strain-stress relationship is used to reflect the softening of the bone wall tissue material [Hambli 2013; Keaveny et al. 2003]. To this end, a nonlinear response of an isotropic and reversible material is modeled [Haj-Ali and Aboudi 2009; Haj-Ali and Kilic 2003; Khan and Huang 1995] using the general multiaxial form of the R-O representation as follows:

$$\varepsilon_{ij} = \varepsilon_{ij}^e + \varepsilon_{ij}^p = \left(\frac{1+v}{E} + \frac{3\alpha}{2E}\left(\frac{\sigma_e}{\sigma_0}\right)^{n-1}\right) \cdot s_{ij} + \frac{\sigma_{kk}}{9K}\delta_{ij}, \tag{12}$$

where the Young's modulus is E, Poisson's ratio is v, $K = E/[3(1-2v)]$ and α, σ_0, n are the material constants and ε_{ij} is the total strain tensor, ε_{ij}^e is the elastic strain components, ε_{ij}^p is the plastic strain components and σ_{ij}, s_{ij} are the stress and stress deviatoric tensors, respectively. Kronecker's delta tensor is δ_{ij} and σ_e is the equivalent stress as follows:

$$\sigma_e = \sqrt{\tfrac{3}{2} \cdot s_{ij} \cdot s_{ij}}. \tag{13}$$

To this end, the incremental strain-stress relationship in vector notation is

$$\Delta \boldsymbol{\varepsilon} = (S^e + \phi \cdot P + \alpha_t \cdot \phi \cdot \hat{s} \cdot \hat{s}^T)\Delta \boldsymbol{\sigma} = S_t \Delta \boldsymbol{\sigma}, \tag{14}$$

where the linear elastic compliance matrix for an isotropic material is $S^e(6 \times 6)$, $\hat{s}(6 \times 1)$ is the stress deviatoric vector and $S_t(6 \times 6)$ is the tangent compliance matrix. We also have:

$$\phi = \frac{3\alpha}{2E}\left(\frac{\sigma_e}{\sigma_0}\right)^{n-1},$$

$$\alpha_t = \tfrac{3}{2}(n-1) \cdot \frac{1}{\sigma_e^2},$$

$$P = \frac{1}{3}\begin{bmatrix} 2 & & & & & \\ -1 & 2 & & & \text{Symm.} & \\ -1 & -1 & 2 & & & \\ 0 & 0 & 0 & 6 & & \\ 0 & 0 & 0 & 0 & 6 & \\ 0 & 0 & 0 & 0 & 0 & 6 \end{bmatrix}. \tag{15}$$

To this end, the tangent stiffness matrix is derived by inverting the tangent compliance matrix. Once the stress vector is given, the corresponding stain vector and the tangent stiffness matrix can be computed

using (12). But when the strain vector is provided, it should initially determine the equivalent stress (σ_e) by iteratively solving the following scalar nonlinear polynomial equation using the Newton–Raphson method to obtain the corresponding stress vector and tangent stiffness matrix:

$$\phi \cdot \sigma_e + \frac{1}{2G} \cdot \sigma_e - \varepsilon_e = 0. \tag{16}$$

The shear modulus $G = E/[2(1+v)]$, where ε_e is defined as the equivalent strain and is related to the deviatoric strain tensor (e_{ij}) as follows:

$$\varepsilon_e = \sqrt{\tfrac{3}{2} \cdot e_{ij} \cdot e_{ij}}. \tag{17}$$

2.3. *Damage response.* An isotropic damage model for postfailure stiffness degradation is used. When failure is detected, the relevant subcell is extinct. This progressive damage model is coupled with the HFGMC micromechanical model at the subcell level. To this end, the following isotropic damage model is adopted and imposed:

$$\boldsymbol{\sigma}^{(\beta)} = (1 - D^{(\beta)})\boldsymbol{C}^{t,(\beta)} : \boldsymbol{\varepsilon}^{(\beta)}, \tag{18}$$

where the current associated subcell damage variable is $0 \le D^{(\beta)} \le 1$ and $\boldsymbol{C}^{t,(\beta)}, \boldsymbol{\sigma}^{(\beta)}, \boldsymbol{\varepsilon}^{(\beta)}$ are the instantaneous tangent stiffness matrix, stress vector and strain vector of subcell (β), respectively. Damage variable in a subcell is governed by the equivalent strain ε_e; see (17). A linear relationship between the subcell damage variable $D^{(\beta)}$ and the equivalent strain $\varepsilon_e^{(\beta)}$ is assumed as follows:

$$\begin{cases} D^{(\beta)} = 0 & \text{if } 0 < \varepsilon_e^{(\beta)} < \varepsilon_e^{(\beta),\text{initial}}, \\ D^{(\beta)} = \dfrac{1}{1-\eta}\left(1 - \dfrac{\varepsilon_e^{(\beta)}}{\varepsilon_e^{(\beta),\text{initial}}}\right) & \text{if } \varepsilon_e^{(\beta)} > \varepsilon_e^{(\beta),\text{initial}}, \\ D^{(\beta)} = 1 & \text{if } \varepsilon_f = \eta\varepsilon_e^{(\beta),\text{initial}}, \end{cases} \tag{19}$$

where the parameter η is used to relate the equivalent strain damage $\varepsilon_e^{(\beta),\text{initial}}$ to the final strain ε_f when the subcell is extinct (removed, no stiffness). Its limit values ($\eta = 1, \infty$) correspond to highly brittle and highly ductile states, respectively. Once the damage variable is initiated, a strain softening scheme is imposed whereby the stiffness of the subcell is degraded. Herein, damage initiates at the subcell once the failure is detected according to

$$\sigma_e^{(\beta)} \ge X, \tag{20}$$

where $\sigma_e^{(\beta)}$ is the equivalent stress at subcell (β) and X is a calibrated value denoting the effective strength value of the bone wall constituent.

2.4. *Nonlinear implementation.* To this end, an incremental solution algorithm using the 3D nonlinear parametric HFGMC, a nonlinear material model and a damage approach is developed. The numerical algorithm proceeds incrementally for a given number of increments n_{inc} as shown on the next page. Once given the history of total stress and strain vectors in the subcells (Step 2.1), the prior local tangent stiffness matrices of the subcells $\overline{\boldsymbol{C}}_{i-1}^{t,(\beta)}$ (Step 2.2) and the overall prior tangential stiffness matrix $\overline{\boldsymbol{C}}_{i-1}^{t}$ (Step 2.3), can be computed. Next, the current remote incremental average strain vector $\{\Delta\bar{\boldsymbol{\varepsilon}}^0\}_i = \{\Delta\bar{\varepsilon}_a, \Delta\bar{\varepsilon}_b\}_i$

Incremental solution algorithm

1 Initialize parameters: n_{inc}, $\boldsymbol{\sigma}_0^{(\beta)} = \{0\}$, $\boldsymbol{\varepsilon}_0^{(\beta)} = \{0\}$, $\Delta\bar{\varepsilon}_a$, X

2 WHILE $i \leq n_{\text{inc}}$ DO

  2.1 Recall prior total local stress $\boldsymbol{\sigma}_{i-1}^{(\beta)}$, strain $\boldsymbol{\varepsilon}_{i-1}^{(\beta)}$, and damage variable $D_{i-1}^{(\beta)}$.

  2.2 Compute prior tangent stiffness matrices $\boldsymbol{C}_{i-1}^{t,(\beta)}$.

  2.3 Compute prior global tangent stiffness matrix $\bar{\boldsymbol{C}}_{i-1}^{t}$.

  2.4 Using (21), get applied remote incremental average strain vector: $\{\Delta\bar{\boldsymbol{\varepsilon}}^0\}_i$

  2.5 Solve Eq. (11), $\{\Delta\boldsymbol{W}\}_i = -[\partial(\Delta\boldsymbol{R})/\partial(\Delta\boldsymbol{W})]_i^{-1} \cdot \{\boldsymbol{D}\}_i \cdot \{\Delta\bar{\boldsymbol{\varepsilon}}^0\}_i$, for the current incremental displacement microvariables.

  2.6 FOR $\beta = 1, 2, 3, \ldots, N_c$ DO

    2.6.1 Get current total local strain vector $\{\boldsymbol{\varepsilon}\}_i^{(\beta)} = \{\bar{\boldsymbol{\varepsilon}}^0\}_i + A_i^{(\beta)}\{\Delta\boldsymbol{W}\}_i^{(\beta)} + \{\boldsymbol{\varepsilon}\}_{i-1}^{(\beta)}$.

    2.6.2 Compute current tangent stiffness matrix $\boldsymbol{C}_i^{t,(\beta)}$.

    2.6.3 Using (18), perform constitutive calculations for total local stress vector $\{\boldsymbol{\sigma}\}_i^{(\beta)}$:

        IF $D_{i-1}^{(\beta)} \leq 1$ THEN

$$\{\boldsymbol{\sigma}\}_i^{(\beta)} = (1 - D_{i-1}^{(\beta)})\boldsymbol{C}_i^{t,(\beta)} : \{\boldsymbol{\varepsilon}\}_i^{(\beta)}$$

        ELSE

$$\{\boldsymbol{\sigma}_i^{(\beta)}\} = \{0\}, \ \boldsymbol{\varepsilon}_i^{(\beta)} = \{0\}, \ \text{subcell } (\beta) \text{ extinct}$$

    2.6.4 Using (13), compute current total equivalent stress $\sigma_e^{(\beta),i}$.

        IF $\sigma_e^{(\beta),i} \geq X$ and $D_{i-1}^{(\beta)} = 0$ THEN

            Using (17), compute total equivalent strain for damage initiation: $\varepsilon_e^{(\beta),\text{initial}}$

    2.6.5 Using (17), compute current total equivalent strain: $\varepsilon_e^{(\beta),i}$

    2.6.6 Using (19), update current damage variable: $D_i^{(\beta)}$

  2.7 Compute RUC current total stress and strain vectors:

$$\{\bar{\boldsymbol{\sigma}}\}_i = \frac{1}{V}\int_V \{\boldsymbol{\sigma}\}_i \, dV = \frac{1}{V}\sum_{\beta=1}^{N_c} v_\beta\{\boldsymbol{\sigma}\}_i^{(\beta)}, \quad \{\bar{\boldsymbol{\varepsilon}}\}_i = \frac{1}{V}\int_V \{\boldsymbol{\varepsilon}\}_i \, dV = \frac{1}{V}\sum_{\beta=1}^{N_c} v_\beta\{\boldsymbol{\varepsilon}\}_i^{(\beta)}.$$

Set $i = i + 1$.

---

for the RUC, deformed under a uniaxial stress state, is evaluated (Step 2.4) by solving the following linearized equation system:

$$\left\{\begin{array}{c} \Delta\bar{\sigma}_a \\ \hline 0 \\ 0 \\ 0 \\ 0 \\ 0 \end{array}\right\}_i = \left[\begin{array}{c|c} \bar{C}_{aa}^t & \{\bar{C}_{ab}^t\}_{1\times 5} \\ \hline \{\bar{C}_{ba}^t\}_{5\times 1} & [\bar{C}_{bb}^t]_{5\times 5} \end{array}\right]_{i-1} \cdot \left\{\begin{array}{c} \Delta\bar{\varepsilon}_a \\ \hline \{\Delta\bar{\boldsymbol{\varepsilon}}_b\}_{5\times 1} \end{array}\right\}_i,$$

$$\{\Delta\bar{\boldsymbol{\varepsilon}}_b\}_i = -[\bar{C}_{bb}^t]_{i-1}^{-1} \cdot \{\bar{C}_{ba}^t\}_{i-1} \cdot \Delta\bar{\varepsilon}_a,$$

$$\{\Delta\bar{\boldsymbol{\varepsilon}}^0\}_i = \{\Delta\bar{\varepsilon}_a, \Delta\bar{\boldsymbol{\varepsilon}}_b\}_i,$$

(21)

where $\Delta\bar{\boldsymbol{\varepsilon}}_a$ is a given average strain increment in the axial direction (11) of the RUC. In Step 2.5, the equation system (10) is established and solved with the current incremental $\{\Delta\bar{\boldsymbol{\varepsilon}}^0\}_i$ evaluating the current incremental microvariables $\{\Delta W\}_i$; see (11). Then, for all the subcells in the given RUC, the current total local strain vector (Step 2.6.1), tangent stiffness matrix (Step 2.6.2) and stress vector (Step 2.6.3) are evaluated. Subsequently in Step 2.6.4, the equivalent stress is computed and compared with the calibrated value denoting the effective strength value of the bone wall constituent. Once the equivalent stress is greater than the calibrated effective strength value, the initial equivalent strain is computed and fixed. Next, the current total equivalent strain is computed (Step 2.6.5) and in Step 2.6.6, the current damage variable is updated according to the computed current total equivalent strain (19). The global stress and strain vectors are obtained in Step 2.7 and the algorithm proceeds to the next increment. It should be noted that there is no need to apply periodic boundary conditions in order to simulate the current axial loading which is directly imposed on the RUC. This special case yields zero average traction on the edges of the RUC. To that end, the microvariables at the edges are set to zero.

2.5. *Microcomputed tomography imaging.* Selected CT bone scans shown in Table 1 were acquired from a larger database originally reported by Wolfram et al. [2011] which included 104 (50 males, 54 females) fresh frozen human vertebrae (T1–L3) obtained from 32 donors (21–94y, median = 65) and stored at $-20°$ after harvest. Surrounding soft tissue was removed from the vertebrae, and the posterior structures were partially removed. Endplates were removed with a band saw. Subsequently, 251 cylindrical specimens (8 mm in diameter and 18–25 mm in height) were cored from the remaining slices by a custom-made core drill. Marrow was removed from the top and bottom of the cylinders using a pulsed waterjet (Braun Oral-B Professional Care 6500). The cylinders were submerged in water containing 0.9% sodium chloride and scanned in a μCT (μCT 40, SCANCO Medical AG) at a resolution of $12\,\mu\text{m}^3$.

2.6. *Damage analysis of vertebral trabecular bones.* 3D RUCs demonstrating the VTB highly porous microstructure were studied for nonlinear with damage response. Figure 3a represents a human vertebral body macroscale from which high resolution images of sequential and cylindrical cross sections of μCT scans were generated. By stacking the cross-sectional images, the original VTB microstructure can then be rebuilt as a 3D solid model (Figure 3b). The VTB-RUC has been arbitrarily selected with an approximate length of $l = w = h = 8.1 \pm 0.3$ mm. Then, the 3D solid model representing the bone walls (Figure 3c) and the marrow (soft fatty substances in the cavities of bones) domain (Figure 3d)

vertebral level	gender	age	vertebral level	gender	age
T11	F	43	T11	M	37
T12	F	43	T12	M	44
T12	F	46	T12	M	56
T11	F	60	T11	M	84
T12	F	60	L2	M	84
L3	F	80			

Table 1. Vertebrae scanned samples analyzed in this study reported in [Wolfram et al. 2011].
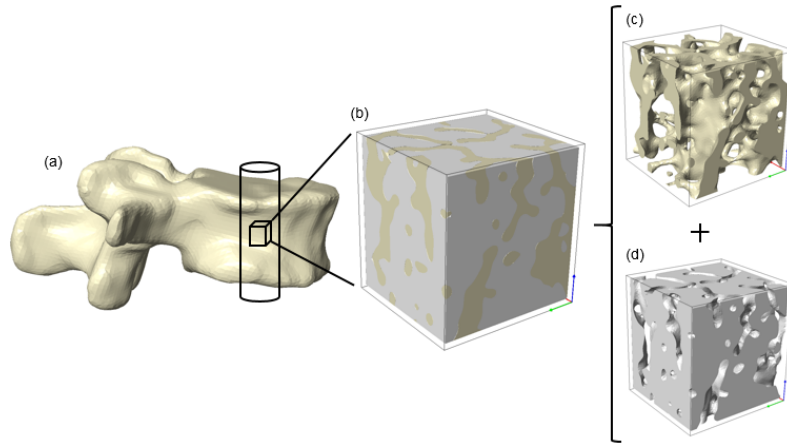
Figure 3. Human vertebral body (macroscale), (a); a VTB-RUC microstructure, (b); bone walls, (c), and marrow domain, (d).
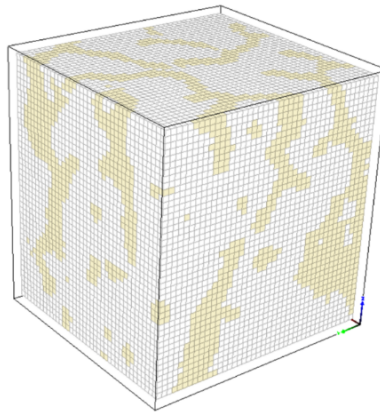
Figure 4. A 3D discretized of VTB-RUC.

were converted to approximately 72,000 equally shaped brick elements (subcells); see Figure 4. In situ material properties of each subcell representing bone wall were defined with the nonlinear R-O model with the material parameters found in Table 2, while subcells representing the marrow domain were set with very little stiffness. Then, the nonlinear with damage evolution response of the VTB-RUC was predicted using the incremental solution algorithm described above with a strain increment finite-size of $5 \cdot 10^{-4}$, presenting a sufficiently convergent criterion.

2.7. *Compression tests of printed polymeric VTB-RUC.* In order to generate the overall compression stress-strain response of a VTB-RUC manufactured from a polymeric material using a 3D-printer, compression tests were performed. The aim was to verify the ability of the calibrated nonlinear HFGMC to predict the tested response of a VTB-RUC behavior. Towards that goal, a 3D VTB-RUC solid model obtained from a μCT scan of a human cadaveric VTB (37 years old) was generated. Three printed polymeric VTB-RUC samples with a scale factor of 5:1 of the last 3D VTB-RUC with bottom and upper

parameters	notation	polymeric material	bone wall
elastic modulus	E (GPa)	2.56	11.00
Poisson ratio	v	0.35	0.3
material parameter	σ_0 (GPa)	0.060	0.110
material parameter	α	1	1
material parameter	n	5	5
strain-softening parameter	η	$1-\infty$	1.001
effective strength value	X (GPa)	0.060	0.110

Table 2. Material properties and model parameters for tested polymeric material and bone wall, calibrated and used in the analysis of the one-dimensional R-O relation: $\varepsilon = \sigma/E + \alpha(\sigma_0/E)(\sigma/\sigma_0)^n$.

caps were produced by a 3D printer. The volume fraction of the polymeric material in the VTB-RUC was 24.71%. In addition, three "dog-bone" specimens of the polymeric material were produced to measure the polymeric material response under tension. The experimental study was performed as follows: the "dog-bone" specimens were stretched using the Instron 5582 machine. Subsequently, compression tests were performed on the three polymeric 3D printed VTB-RUC samples. Initially, the VTB-RUC samples were cycled between two polished steel plates under reversed compression, three times nondestructively, between a 0 and 0.7% strain at a rate of 0.1 mm/min, followed by 10 minutes of relaxation. Subsequently, the samples were destructively compressed to a $\sim$3% strain at a rate of 0.1 mm/min (Figure 5a). The axial deformation (Figure 5b) was measured using the digital-image-correlation (DIC) method. The axial stress was defined as an instantaneous applied load divided by the cross-sectional area of the VTB-RUC. Strain was defined as an instantaneous deformation divided by the effective initial length between the steel plates. Subsequently, the measured results were compared with the nonlinear HFGMC model including a progressive damage analysis.
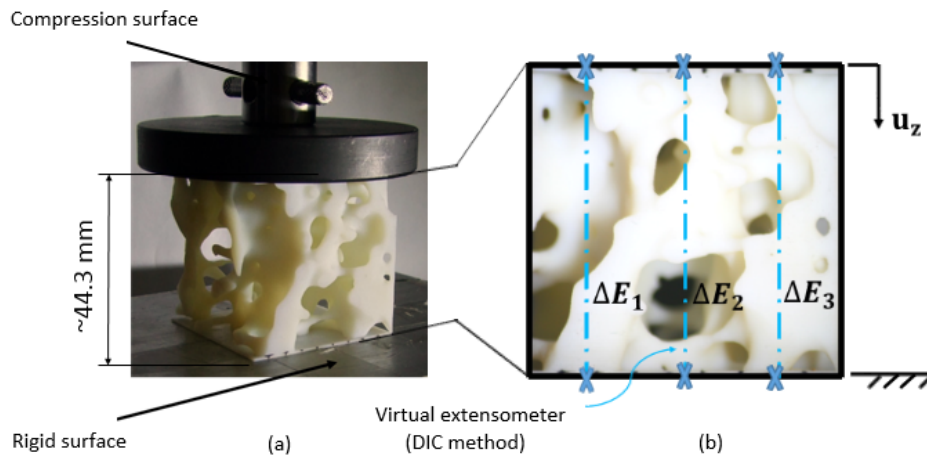

Figure 5. Experimental study: a compressed polymeric VTB-RUC highly porous microstructure, (a). An axial deformation gauge, (b).

3. Results and discussion

Figure 6 presents the experimental tension mechanical responses of the polymeric material used in this study. The material parameters of the R-O stress-strain relationship describing the nonlinear response of the polymeric material were calibrated (Table 2) and used in the analysis of the polymeric VTB-RUC samples to predict its nonlinear response with damage evolution.

The compression test results and the predicted HFGMC mechanical response with evolving damage of the polymeric VTB-RUC samples are shown in Figure 7. The effective strength value X of the polymeric material was calibrated at 0.06 GPa, while different values for the strain-softening parameter η were used to examine the ability to simulate energy dissipation rates. The above results provide an excellent agreement between the predicted and experimentally obtained nonlinear mechanical response of the polymeric VTB-RUC samples which began with an elastic region, followed by a nonlinear reversible response and continued with a nonlinear softening region caused by both the nonlinear elastic and damage. The experiments ceased after detecting the ultimate load. The predicted nonlinear response included postpeak strain-softening degradation behavior. This degradation was related to the strain-softening parameter η that controls the energy dissipation rate.

The predicted nonlinear with evolving damage responses of the available native VTB-RUCs compared with compression overloading tests available in the literature [Keaveny et al. 1999; Kopperdahl and Keaveny 1998] are shown in Figure 8. Bone volume fraction of the VTB-RUCs are also presented. The material parameters of the R-O constitutive relationship, effective strength value and parameter η were calibrated (Table 2) and used as the in situ nonlinear behavior of the bone wall phase in the VTB-RUCs.

The obtained mechanical responses were typical of the curves reported for the trabecular bone [Hayes and Carter 1976] and other natural and synthetic porous materials, such as cellular foams [Gibson and Ashby 1999]. Moreover, the predicted mechanical responses after the softening region presented another region of stiffening. When high compression closes the pores and cavities in the material, thus causing material stiffening, the consolidation region emerges [Gibson and Ashby 1999; Gibson et al. 2010].
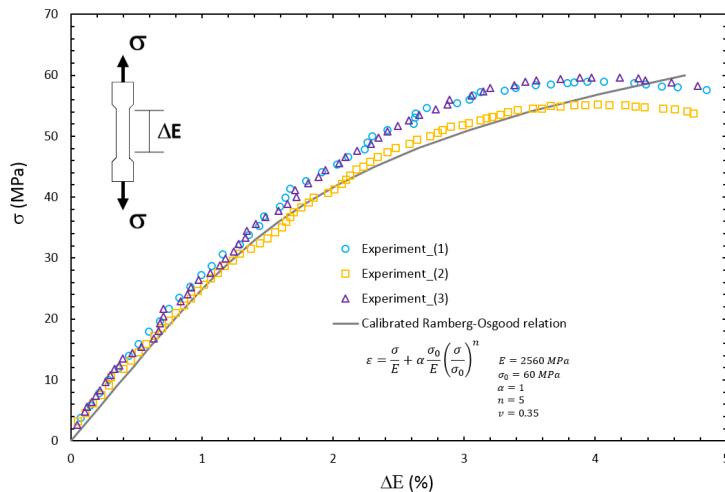
Figure 6. Mechanical response of the polymeric material used by the 3D printer.
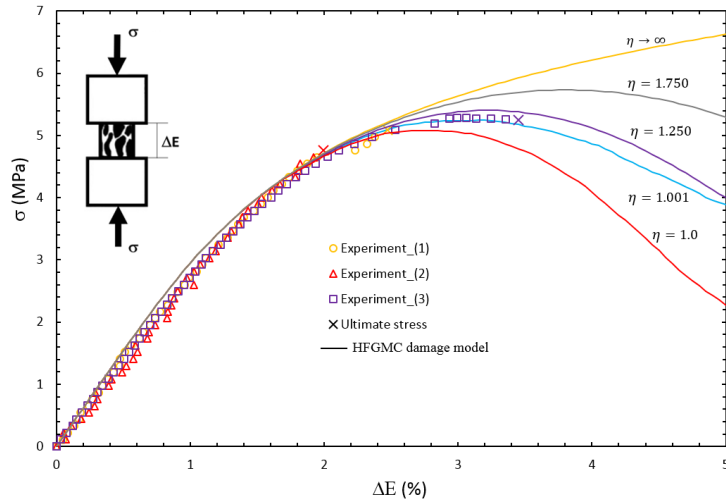
Figure 7. Experimental results of compressive loading and a predicted HFGMC mechanical responses with softening and evolving damage of a polymeric VTB-RUC highly porous microstructure.
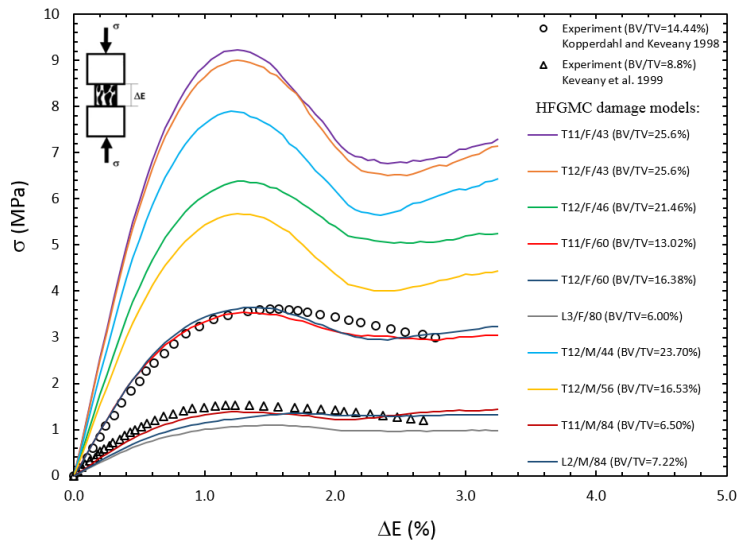
Figure 8. Predicted HFGMC mechanical responses vs. compression overloading tests of native VTBs available in the literature.

Figures 9 and 10 show the mechanical responses with yield points of the available native VTB-RUCs of the six VTB μCT scans of females and four scans of males with different vertebral levels (T11, T12, L3, and L4), respectively. The yield points were determined using a similar protocol proposed by Kopperdahl and Keaveny [1998]. In this study, the elastic modulus for each curve was computed based on all points up to 0.2% strain. The elastic slope was then used to construct 0.2% strain offset lines as shown in Figures 9 and 10. The intersections of the offset lines with the damage curves define the yield
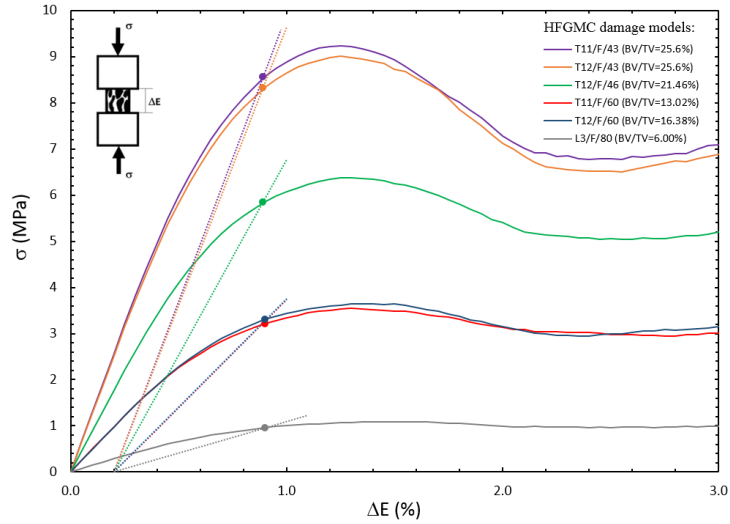
Figure 9. Predicted HFGMC mechanical responses for native female vertebral bones.
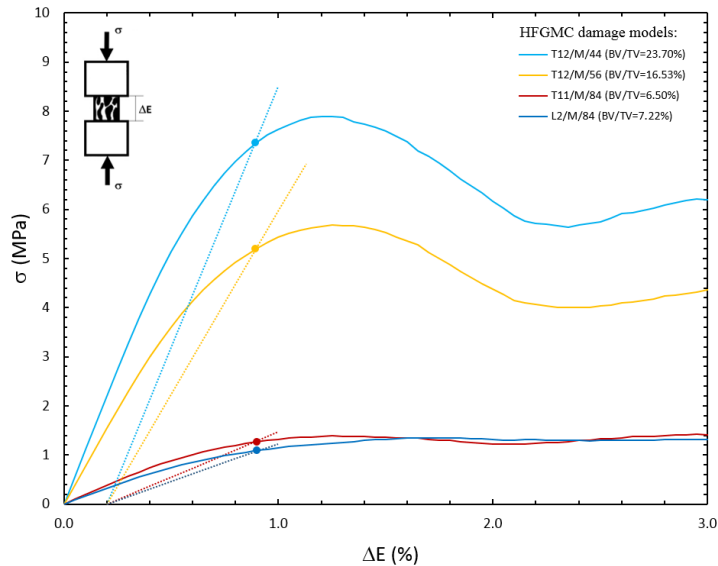
Figure 10. Predicted HFGMC mechanical responses for native male vertebral bones.

points. To this end, we present in Figures 11 and 12, respectively, the predicted yield stress and strain of the available native VTB-RUCs and compare these with the results found in the literature [Kopperdahl and Keaveny 1998]. Unlike the yield stresses for human VTBs, which demonstrated strong correlations with the bone volume fraction (BV/TV), the results of the yield strains were significantly independent of BV/TV. The above results strongly correspond with the previous outcomes indicating that for over-yielding behavior, the yield strains are independent of the apparent density and have reasonably constant values [Kopperdahl and Keaveny 1998]. Studies examining the independency of the compressive yield
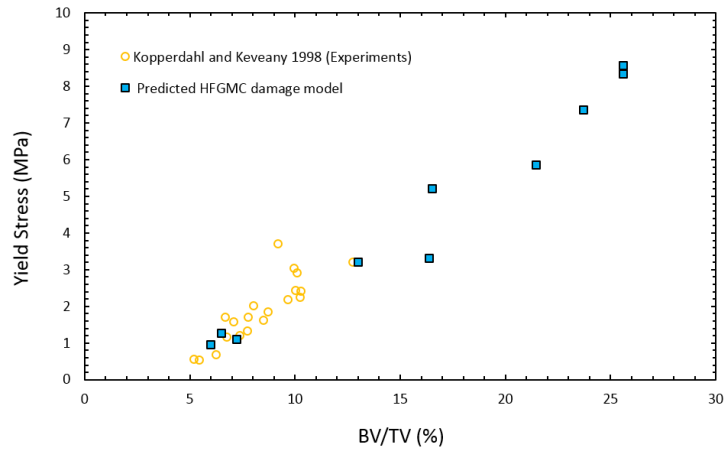
Figure 11. Predicted HFGMC yield stress vs. bone volume fraction of native VTBs.
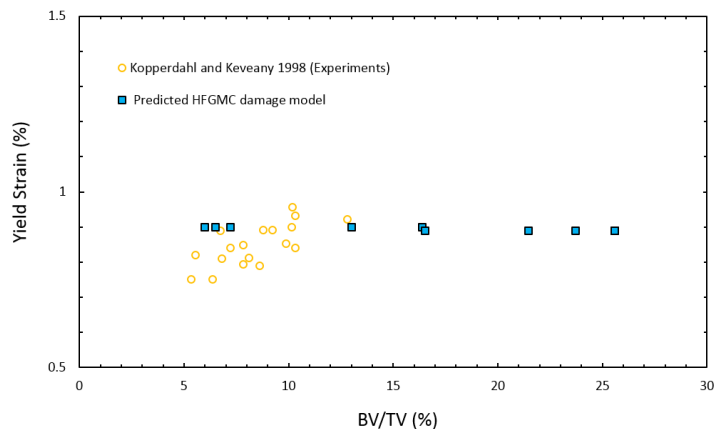
Figure 12. Predicted HFGMC yield strain vs. bone volume fraction of native VTBs.

strains to bone volume fractions have suggested that the failure of the highly porous trabecular bone microstructure is based on the strain [Gibson et al. 2010; Turner 1989].

4. Limitations

There are several limitations to the proposed approach seeking to generate a VTB nonlinear mechanical response. The first limitation is related to the acquisition accuracy of the μCT images. The relative Hounsfield Units (HUs) are associated with the full range of bone density all the way through the marrow medium. Thus, a threshold is used to determine whether a voxel is considered a bone wall or void. Therefore, we assumed that the μCT scans can represent the VTB microstructure and its porosity. The accuracy of these scans is a challenging problem, leading to errors in computing the microstructure and its bone volume fraction. Ultimately, this error in the RUC geometry can influence the computed mechanical response. Secondly, random bone variations and end fixtures may result in several errors and variation measurements resulting from in-vitro bone compression tests. These errors can be associated

with end-artifacts in the platen compression tests for trabecular bones [Keaveny et al. 1997]. Despite such limitations, we have adopted the same mechanical testing for the current polymeric VTB-RUC samples representing the microstructure of the VTB. Thirdly, periodic conditions of traction and displacement that may be imposed on the edges of the RUC can affect the predicted nonlinear behavior. In the current HFGMC model, the last periodic conditions were not applied. Fourthly, the porous media representing the marrow phase of the VTB was modeled with very little stiffness which might cause errors, especially for large cavities. Fifthly, small increments have to be used in the current nonlinear HFGMC incremental solution algorithm, which may be computationally expensive. A correction-algorithm suited for the micromechanical formulation can be developed to enhance computational efficiency. Sixthly, because of the limited availability of the experimental study for native human VTBs, it was difficult to calibrate the strain-softening parameter η that controls the energy dissipation rate of the native human VTB microstructure. More experimental and anisotropic damage modeling is needed to further develop the proposed progressive damage and better tailor it to different failure modes, such as local microbuckling and combined shear-compression modes, among others. The current damage parameter is isotropic with one damage parameter combining all these modes. Seventhly, this study concentrated on the compression analysis of the VTBs which mostly feature VTB failure; therefore, the characterization of tension-compression asymmetry [Kopperdahl and Keaveny 1998] is not investigated herein. Finally, the softening postpeak behavior will always be affected by mesh size unless a nonlocal interpolated solution variable and failure criteria are applied.

5. Conclusions

The parametric HFGMC micromechanics has been extended to include progressive damage of a highly porous microstructure such as VTB. The 3D nonlinear micromechanical modeling approach can predict the compression response of tested highly porous polymeric RUC. The proposed nonlinear HFGMC progressive damage micromodel was used to simulate compression failure of native VTB microstructures. Good predictive ability was shown for the compression yield stresses and strains compared to results reported in the literature. The proposed HFGMC VTB micromechanical damage analysis can be employed in future multiscale FE models of the macroscale vertebral bodies.

Acknowledgements

References

[Aboudi et al. 2013] J. Aboudi, S. M. Arnold, and B. A. Bednarcyk, *Micromechanics of composite materials: a generalized multiscale analysis approach*, 1st ed., Elsevier, Oxford, 2013.

[Chevalier et al. 2007] Y. Chevalier, D. Pahr, H. Allmer, M. Charlebois, and P. Zysset, "Validation of a voxel-based FE method for prediction of the uniaxial apparent modulus of human trabecular bone using macroscopic mechanical tests and nanoindentation", *J. Biomech.* **40**:15 (2007), 3333–3340.

[Cowin 2001] S. C. Cowin, *Bone mechanics handbook*, 2nd ed., Taylor & Francis, 2001.

[Fyhrie and Schaffler 1994] D. P. Fyhrie and M. B. Schaffler, "Failure mechanisms in human vertebral cancellous bone", *Bone* **15**:1 (1994), 105–109.

[Gibson and Ashby 1999] L. J. Gibson and M. F. Ashby, *Cellular solids: structure and properties*, 2nd ed., Cambridge University Press, 1999.

[Gibson et al. 2010] L. J. Gibson, M. F. Ashby, and B. A. Harley, *Cellular materials in nature and medicine*, Cambridge University Press, 2010.

[Goda and Ganghoffer 2015] I. Goda and J.-F. Ganghoffer, "3D plastic collapse and brittle fracture surface models of trabecular bone from asymptotic homogenization method", *Int. J. Eng. Sci.* **87** (2015), 58–82.

[Goda et al. 2012] I. Goda, M. Assidi, S. Belouettar, and J. F. Ganghoffer, "A micropolar anisotropic constitutive model of cancellous bone from discrete homogenization", *J. Mech. Behav. Biomed. Mater.* **16** (2012), 87–108.

[Goda et al. 2016] I. Goda, R. Rahouadj, J.-F. Ganghoffer, H. Kerdjoudj, and L. Siad, "3D couple-stress moduli of porous polymeric biomaterials using μCT image stack and FE characterization", *Int. J. Eng. Sci.* **100** (2016), 25–44.

[Haj-Ali and Aboudi 2009] R. Haj-Ali and J. Aboudi, "Nonlinear micromechanical formulation of the high fidelity generalized method of cells", *Int. J. Solids Struct.* **46** (2009), 2577–2592.

[Haj-Ali and Aboudi 2013] R. Haj-Ali and J. Aboudi, "A new and general formulation of the parametric HFGMC micromechanical method for two and three-dimensional multi-phase composites", *Int. J. Solids Struct.* **50** (2013), 907–919.

[Haj-Ali and Aboudi 2016] R. Haj-Ali and J. Aboudi, "Integrated microplane model with the HFGMC micromechanics for nonlinear analysis of composite materials with evolving damage", *Int. J. Solids Struct.* **90** (2016), 129–143.

[Haj-Ali and Kilic 2003] R. Haj-Ali and H. Kilic, "Nonlinear constitutive models for pultruded FRP composites", *Mech. Mater.* **35**:8 (2003), 791–801.

[Haj-Ali et al. 2014] R. Haj-Ali, H. Zemer, R. El-Hajjar, and J. Aboudi, "Piezoresistive fiber-reinforced composites: A coupled nonlinear micromechanical–microelectrical modeling approach", *Int. J. Solids Struct.* **51**:2 (2014), 491–503.

[Hambli 2013] R. Hambli, "Micro-CT finite element model and experimental validation of trabecular bone damage and fracture", *Bone* **56**:2 (2013), 363–374.

[Hamed and Jasiuk 2013] E. Hamed and I. Jasiuk, "Multiscale damage and strength of lamellar bone modeled by cohesive finite elements", *J. Mech. Behav. Biomed. Mater.* **28** (2013), 94–110.

[Harrison et al. 2013] N. M. Harrison, P. McDonnell, L. Mullins, N. Wilson, D. O'Mahoney, and P. E. McHugh, "Failure modelling of trabecular bone using a non-linear combined damage and fracture voxel finite element approach", *Biomech. Model. Mechanobiol.* **12** (2013), 225–241.

[Hayes and Carter 1976] W. C. Hayes and D. R. Carter, "Postyield behavior of subchondral trabecular bone", *J. Biomed. Mater. Res. A* **10**:4 (1976), 537–544.

[Keaveny et al. 1994] T. M. Keaveny, E. F. Wachtel, X. E. Guo, and W. C. Hayes, "Mechanical behavior of damaged trabecular bone", *J. Biomech.* **27**:11 (1994), 1309–18.

[Keaveny et al. 1997] T. M. Keaveny, E. F. Morgan, and O. C. Oscar, *Bone mechanics*, edited by M. Kuts, McGraw-Hill, 1997.

[Keaveny et al. 1999] T. M. Keaveny, E. F. Wachtel, and D. L. Kopperdahl, "Mechanical behavior of human trabecular bone after overloading", *J. Orthop. Res.* **17**:3 (1999), 346–353.

[Keaveny et al. 2003] T. M. Keaveny, T. P. Pinilla, R. P. Crawford, D. L. Kopperdahl, and A. Lou, "Systematic and random errors in compression testing of trabecular bone", *J. Orthop. Res.* **15**:1 (2003), 101–110.

[Khan and Huang 1995] A. S. Khan and S. Huang, *Continuum Theory of Plasticity*, Wiley, New York, 1995.

[Kopperdahl and Keaveny 1998] D. L. Kopperdahl and T. M. Keaveny, "Yield strain behavior of trabecular bone", *J. Biomech.* **31** (1998), 601–608.

[Maquer et al. 2015] G. Maquer, S. N. Musy, J. Wandel, T. Gross, and P. K. Zysset, "Bone volume fraction and fabric anisotropy are better determinants of trabecular bone stiffness than other morphological variables", *J. Bone Miner. Res.* **30**:6 (2015), 1000–1008.

[Nevitt et al. 1999] M. C. Nevitt, P. D. Ross, L. Palermo, T. Musliner, H. K. Genant, and D. E. Thompson, "Association of prevalent vertebral fractures, bone density, and alendronate treatment with incident vertebral fractures: effect of number and spinal location of fractures", *Bone* **25**:5 (1999), 613–619.

[Niebur et al. 2000] G. L. Niebur, M. J. Feldstein, J. C. Yuen, T. J. Chen, and T. M. Keaveny, "High-resolution finite element models with tissue strength asymmetry accurately predict failure of trabecular bone", *J. Biomech.* **33**:12 (2000), 1575–1583.

[Rockoff et al. 1969] S. D. Rockoff, E. Sweet, and J. Bleustein, "The relative contribution of trabecular and cortical bone to the strength of human lumbar vertebrae", *Calcif. Tissue Res.* **3**:1 (1969), 163–175.

[Turner 1989] C. H. Turner, "Yield behavior of bovine cancellous bone", *J. Biomech. Eng.* (*ASME*) **111**:3 (1989), 256–260.

[Wolfram et al. 2011] U. Wolfram, H.-J. Wilke, and P. K. Zysset, "Damage accumulation in vertebral trabecular bone depends on loading mode and direction", *J. Biomech.* **44**:6 (2011), 1164–1169.

[Zysset 1994] P. Zysset, *A constitutive law for trabecular bone*, École Polytechnique Fédérale de Lausanne, Lausanne, Switzerland, 1994.

EYASS MASSARWA: eyassmas@post.tau.ac.il
Faculty of Engineering, Tel-Aviv University, 69978 Tel-Aviv, Israel

JACOB ABOUDI: aboudi@eng.tau.ac.il
Faculty of Engineering, Tel-Aviv University, 69978 Tel-Aviv, Israel

FABIO GALBUSERA: fabio.galbusera@uni-ulm.de
Department of Spine Surgery III, IRCCS Galeazzi Orthopaedic Institute, Via Riccardo Galeazzi 4, 20161 Milan, Italy

HANS-JOACHIM WILKE: hans-joachim.wilke@uni-ulm.de
Institute for Orthopedic Research and Biomechanics, Ulm University, Helmholtzstrasse 14, D-89081 Ulm, Germany

RAMI HAJ-ALI: rami98@tau.ac.il
Faculty of Engineering, Tel-Aviv University, 69978 Tel-Aviv, Israel

msp

NONLOCAL PROBLEMS WITH LOCAL DIRICHLET AND NEUMANN BOUNDARY CONDITIONS

BURAK AKSOYLU AND FATIH CELIKER

We present novel governing operators in the theory of peridynamics (PD) which will allow the extension of PD to applications that require local boundary conditions (BC). Due to its nonlocal nature, the original PD governing operator uses nonlocal BC. The novel operators agree with the original PD operator in the bulk of the domain and simultaneously enforce local Dirichlet or Neumann BC. Our construction is straightforward and easily accessible. The main ingredients are antiperiodic and periodic extensions of kernel functions together with even and odd parts of functions. We also present governing operators that enforce antiperiodic and periodic BC and the corresponding compatibility conditions for the right-hand side function in a given operator equation. Finally, we present the basic idea in extending the 1D construction to 2D.

1. Introduction

We present novel governing operators in the theory of peridynamics (PD), a nonlocal extension of continuum mechanics developed by Silling [2000]. We consider problems in 1D and choose the domain $\Omega := [-1, 1]$. By suppressing the dependence of u on the time variable t, the original bond based PD governing operator is given as

$$\mathcal{L}_{\text{orig}} u(x) := \int_\Omega \widehat{C}(x' - x) u(x) \, dx' - \int_\Omega \widehat{C}(x' - x) u(x') \, dx', \quad x \in \Omega. \tag{1-1}$$

Due to its nonlocal nature, the operator $\mathcal{L}_{\text{orig}}$ uses nonlocal boundary conditions (BC); see [Silling 2000, p. 201]. We define the operator that is closely related to $\mathcal{L}_{\text{orig}}$ as

$$\mathcal{L} u(x) := c u(x) - \int_\Omega \widehat{C}(x' - x) u(x') \, dx', \quad x \in \Omega, \tag{1-2}$$

where $c := \int_\Omega C(x') \, dx'$. We will prove that the two operators agree in the bulk. As the main contribution, we present novel governing operators that agree with $\mathcal{L}$ in the bulk of Ω, and, at the same time, enforce local Dirichlet or Neumann BC.

Since PD is a nonlocal theory, one might expect only the appearance of nonlocal BC. Indeed, so far the concept of local BC does not apply to PD. Instead, external forces must be supplied through the loading force density [Silling 2000]. On the other hand, we demonstrate that the anticipation of local BC being incompatible with nonlocal operators is not quite correct. Hence, our novel operators present an alternative to nonlocal BC and we hope that the ability to enforce local BC will provide a remedy for

surface effects seen in PD; see [Madenci and Oterkus 2014, Chapters 4, 5, 7, and 12] and [Kilic 2008; Mitchell et al. 2015].

For $x, x' \in [-1, 1]$, it follows that $x' - x \in [-2, 2]$. Hence, in (1-1), the kernel function $C(x)$ needs to be extended from Ω to the domain of $\widehat{C}(x' - x)$, which is $\widehat{\Omega} := [-2, 2]$. The default extension is the zero extension defined by

$$\widehat{C}(x) := \begin{cases} 0 & \text{if } x \in [-2, -1), \\ C(x) & \text{if } x \in [-1, 1], \\ 0 & \text{if } x \in (1, 2]. \end{cases}$$

Furthermore, the kernel function $C(x)$ is assumed to be even. Namely, $C(-x) = C(x)$. An important first choice of $C(x)$ is the *canonical* kernel function $\chi_\delta(x)$ whose only role is the representation of the nonlocal neighborhood, called the *horizon*, by a characteristic function. More precisely, for $x \in \Omega$,

$$\chi_\delta(x) := \begin{cases} 1 & \text{if } x \in (-\delta, \delta), \\ 0 & \text{otherwise.} \end{cases} \tag{1-3}$$

The size of nonlocality is determined by δ and we assume $\delta < 1$. Since the horizon is constructed by $\chi_\delta(x)$, a kernel function used in practice is in the form

$$C(x) = \chi_\delta(x)\mu(x), \tag{1-4}$$

where $\mu(x) \in L^2(\Omega)$ is even.

We define the periodic and antiperiodic extensions of $C(x)$ from Ω to $\widehat{\Omega}$, respectively, as follows

$$\widehat{C}_{\mathrm{a}}(x) := \begin{cases} -C(x+2) & \text{if } x \in [-2, -1), \\ C(x) & \text{if } x \in [-1, 1], \\ -C(x-2) & \text{if } x \in (1, 2], \end{cases} \qquad \widehat{C}_{\mathrm{p}}(x) := \begin{cases} C(x+2) & \text{if } x \in [-2, -1), \\ C(x) & \text{if } x \in [-1, 1], \\ C(x-2) & \text{if } x \in (1, 2]. \end{cases} \tag{1-5}$$

Even for smooth $\mu(x)$, note that $\widehat{C}(x)$, $\widehat{C}_{\mathrm{a}}(x)$, and $\widehat{C}_{\mathrm{p}}(x)$ are not necessarily smooth; see Figure 1.

Throughout the paper, we assume that

$$u(x) \in L^2(\Omega) \cap C^1(\partial\Omega). \tag{1-6}$$

Even and odd parts of the function u are used in the novel governing operators. Here we provide their definitions. We denote the orthogonal projections that give the even and odd parts, respectively, of a function by $P_e, P_o : L^2(\Omega) \to L^2(\Omega)$, whose definitions are

$$P_e u(x) := \tfrac{1}{2}\big(u(x) + u(-x)\big), \quad P_o u(x) := \tfrac{1}{2}\big(u(x) - u(-x)\big). \tag{1-7}$$

Theorem 1.1 (Main Theorem). *Let $c = \int_\Omega C(x')\,\mathrm{d}x'$. The following operators $\mathcal{M}_{\mathrm{D}}$ and $\mathcal{M}_{\mathrm{N}}$ defined by*

$$(\mathcal{M}_{\mathrm{D}} - c)u(x) := -\int_\Omega \big[\widehat{C}_{\mathrm{a}}(x' - x)P_e u(x') + \widehat{C}_{\mathrm{p}}(x' - x)P_o u(x')\big]\,\mathrm{d}x',$$

$$(\mathcal{M}_{\mathrm{N}} - c)u(x) := -\int_\Omega \big[\widehat{C}_{\mathrm{p}}(x' - x)P_e u(x') + \widehat{C}_{\mathrm{a}}(x' - x)P_o u(x')\big]\,\mathrm{d}x'$$

agree with $\mathcal{L}u(x)$ in the bulk, i.e., for $x \in (-1 + \delta, 1 - \delta)$. Furthermore, the operators $\mathcal{M}_{\mathrm{D}}$ and $\mathcal{M}_{\mathrm{N}}$ enforce homogeneous Dirichlet and Neumann BC, respectively. More precisely, for $u(\pm 1) = 0$ and $u'(\pm 1) = 0$, we obtain $\mathcal{M}_{\mathrm{D}}u(\pm 1) = 0$ and $\mathcal{M}_{\mathrm{N}}u'(\pm 1) = 0$, respectively.

Related work and structure of the paper. In [Beyer et al. 2016], one of our major results was the finding that, in $\mathbb{R}$, the PD governing operator is a function of the governing operator of (local) classical elasticity. This result opened the path to the introduction of local boundary conditions into PD theory. Building on [Beyer et al. 2016], we generalized the results in $\mathbb{R}$ to bounded domains, a critical feature for all practical applications. In [Aksoylu et al. 2017b], we laid the theoretical foundations and in [Aksoylu et al. 2017a], we applied the foundations to prominent BC such as Dirichlet and Neumann, as well as presented numerical implementation of the corresponding wave propagation. We carried out numerical experiments by utilizing $\mathcal{M}_D$ and $\mathcal{M}_N$ as governing operators in the previously cited work. In [Aksoylu and Celiker 2016], we studied other related governing operators. In [Aksoylu et al. 2017c], we presented the extension of the novel operators to 2D. In [Aksoylu and Kaya 2017], we studied the condition numbers of the novel governing operators. Therein, we proved that the modifications made to the operator $\mathcal{L}_{\text{orig}}$ to obtain the novel operators are minor as far as the condition numbers are concerned.

The rest of the article is structured as follows. In Section 2, we present the main observation that leads to the construction of the novel operators that enforce Dirichlet and Neumann BC. In Section 3, we give the proof of the main theorem. In Section 4, we show how to obtain the operators that enforce antiperiodic and periodic BC by choosing suitable combinations of kernel functions. In Section 5, when an equation using the governing operators is solved, we show that the right-hand side function should satisfy the same the BC enforced by the governing operator. In Section 6, we provide the highlights of the extension from the 1D construction to 2D. We conclude in Section 7.

2. The main observation and the construction

Let us study the definition of $\widehat{C}_a(x)$ given in (1-5) by explicitly writing the expression of the kernel in (1-4) as follows:

$$\widehat{C}_a(x) = \begin{cases} -\chi_\delta(x+2)\mu(x+2), & x \in [-2,-1), \\ \chi_\delta(x)\mu(x), & x \in [-1,1], \\ -\chi_\delta(x-2)\mu(x-2), & x \in (1,2]. \end{cases}$$

Let us closely look at the first expression in the above definition of $\widehat{C}_a(x)$:

$$\widehat{C}_a(x)|_{x\in[-2,-1)} = -\chi_\delta(x+2)\mu(x+2). \tag{2-1}$$

The expression in (2-1) is equivalent to

$$\widehat{C}_a(x)|_{x\in[-2,-1)} = \begin{cases} -\mu(x+2) & \text{if } x+2 \in (-\delta,\delta) \text{ and } x \in [-2,-1), \\ 0 & \text{if } x+2 \notin (-\delta,\delta) \text{ and } x \in [-2,-1). \end{cases} \tag{2-2}$$

Due to the set equivalence

$$\{x : x+2 \in (-\delta,\delta) \text{ and } x \in [-2,-1)\} = \{x : x \in [-2-\delta,-2+\delta) \cap [-2,-1) = [-2,-2+\delta)\},$$

the expression in (2-2) reduces to

$$\widehat{C}_a(x)|_{x\in[-2,-1)} = \begin{cases} -\mu(x+2) & \text{if } x \in [-2,-2+\delta), \\ 0 & \text{if } x \in [-2+\delta,-1). \end{cases} \tag{2-3}$$

Plot of $\widehat{C}(x)$.

Plot of $\widehat{C}_{\mathrm{p}}(x)$.

Plot of $\widehat{C}_{\mathrm{a}}(x)$.

Plot of $C(x, x')$.

Plot of $C_{\mathrm{p}}(x, x')$.

Plot of $C_{\mathrm{a}}(x, x')$.

Contour plot of $C(x, x')$.

Contour plot of $C_{\mathrm{p}}(x, x')$.

Contour plot of nonnegative part of $C_{\mathrm{a}}(x, x')$.
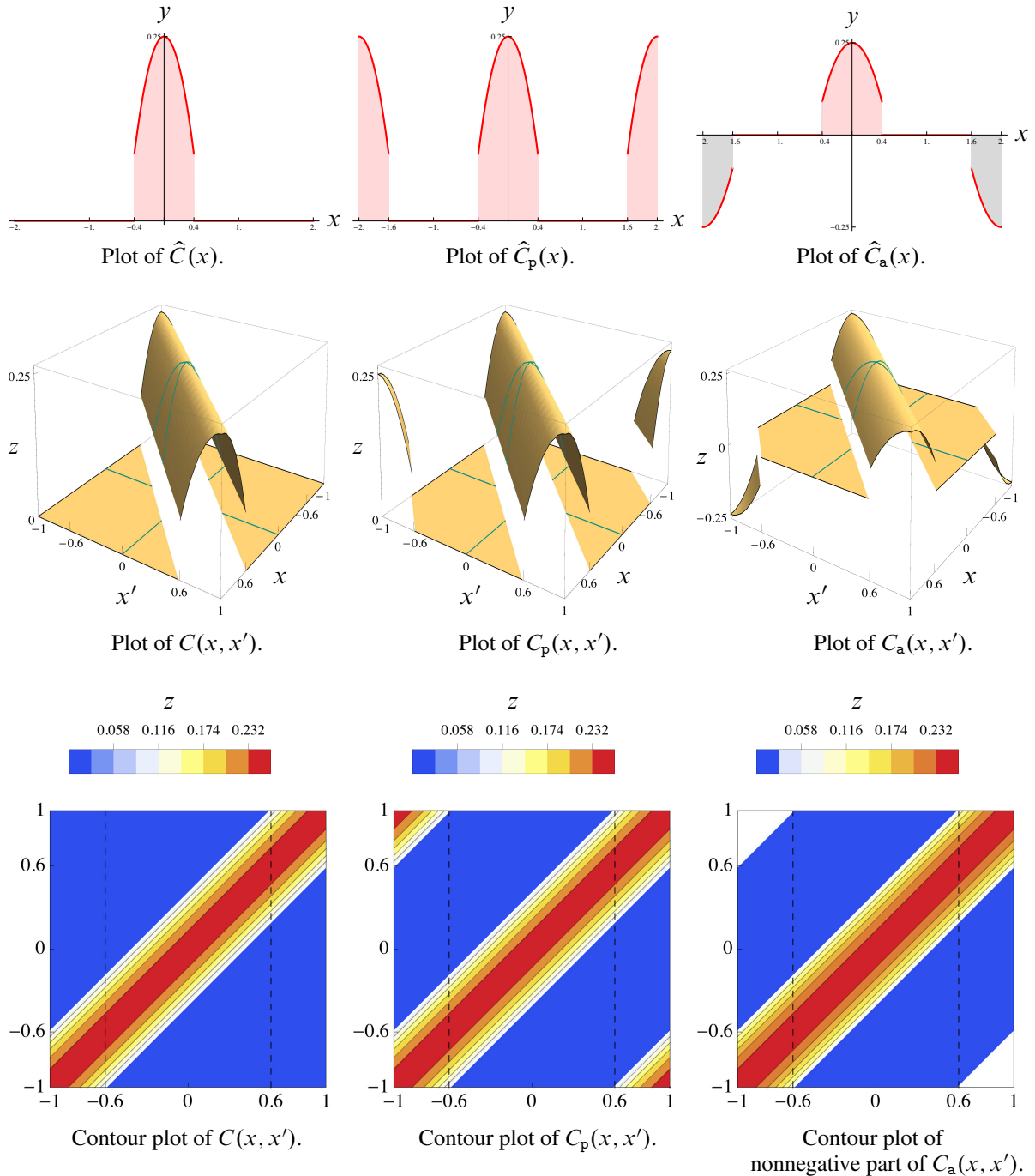
Figure 1. The kernel function $C(x) = \chi_\delta(x)\mu(x)$ with $\chi_\delta(x)$ given in (1-3), $\delta = 0.4$, and $\mu(x) = 0.25 - x^2$. The zero, periodic, and antiperiodic extensions of $C(x)$ are denoted by $\widehat{C}(x)$, $\widehat{C}_p(x)$, and $\widehat{C}_a(x)$, respectively. For plotting, we employ bivariate versions of $\widehat{C}(x' - x)$, $\widehat{C}_{\mathrm{p}}(x' - x)$, and $\widehat{C}_{\mathrm{a}}(x' - x)$ defined by $C(x, x') := \widehat{C}(x' - x)$, $C_{\mathrm{p}}(x, x') := \widehat{C}_{\mathrm{p}}(x' - x)$, and $C_{\mathrm{a}}(x, x') := \widehat{C}_{\mathrm{a}}(x' - x)$.

Similarly, for $x \in (1, 2]$, we have

$$\widehat{C}_{\mathrm{a}}(x)|_{x \in (1,2]} = \begin{cases} 0 & \text{if } x \in (1, 2 - \delta], \\ -\mu(x - 2) & \text{if } x \in (2 - \delta, 2]. \end{cases} \tag{2-4}$$

Combining (2-3) and (2-4), for $x \in [-2, 2]$, we obtain

$$\widehat{C}_{\mathrm{a}}(x) = \begin{cases} -\mu(x - 2) & \text{if } x \in [-2, -2 + \delta), \\ \mu(x) & \text{if } x \in (-\delta, \delta), \\ -\mu(x + 2) & \text{if } x \in (2 - \delta, 2], \\ 0 & \text{otherwise.} \end{cases} \tag{2-5}$$

Similarly, we obtain the following expression for the periodic extension:

$$\widehat{C}_{\mathrm{p}}(x) = \begin{cases} \mu(x - 2) & \text{if } x \in [-2, -2 + \delta), \\ \mu(x) & \text{if } x \in (-\delta, \delta), \\ \mu(x + 2) & \text{if } x \in (2 - \delta, 2], \\ 0 & \text{otherwise.} \end{cases} \tag{2-6}$$

Lemma 2.1. *Let the kernel function $C(x)$ be in the form*

$$C(x) = \chi_\delta(x)\mu(x),$$

where $\mu(x) \in L^2(\Omega)$ is even. Let $\widehat{C}(x)$, $\widehat{C}_{\mathrm{a}}(x)$, and $\widehat{C}_{\mathrm{p}}(x)$ denote the zero, antiperiodic, and periodic extensions of $C(x)$ to $\widehat{\Omega} := [-2, 2]$, respectively. Then,

$$\widehat{C}(x) = \widehat{C}_{\mathrm{a}}(x) = \widehat{C}_{\mathrm{p}}(x), \quad x \in (-2 + \delta, 2 - \delta). \tag{2-7}$$

Furthermore, we have the following agreement in the bulk. For $x \in (-1 + \delta, 1 - \delta)$,

$$\widehat{C}(x' - x) = \widehat{C}_{\mathrm{a}}(x' - x) = \widehat{C}_{\mathrm{p}}(x' - x), \quad x' \in [-1, 1]. \tag{2-8}$$

Proof. By the definition of the functions $\widehat{C}_{\mathrm{a}}(x)$ and $\widehat{C}_{\mathrm{p}}(x)$ in (2-5) and (2-6), respectively, they differ from $\widehat{C}(x)$ only on $[-2, -2 + \delta) \cup (2 - \delta, 2]$. Also, see Figure 1. Hence, $\widehat{C}(x)$, $\widehat{C}_{\mathrm{a}}(x)$, and $\widehat{C}_{\mathrm{p}}(x)$ coincide on $[-2 + \delta, 2 - \delta)$, i.e., (2-7) holds.

Since for x in the bulk, i.e., $x \in (-1 + \delta, 1 - \delta)$ and x' in the range of integration, i.e., $x' \in [-1, 1]$, we have $x' - x \in (-2 + \delta, 2 - \delta)$. From (2-7), we conclude (2-8). $\square$

Remark 2.2. The kernel $\widehat{C}(x) : [-2, 2] \to \mathbb{R}$ is a univariate function. The operator $\mathcal{L}_{\mathrm{orig}}$ utilizes $\widehat{C}(x' - x)$. In order to visualize (2-7), it is more useful to define bivariate versions of $\widehat{C}(x' - x)$, $\widehat{C}_{\mathrm{a}}(x' - x)$, and $\widehat{C}_{\mathrm{p}}(x' - x)$, respectively, as follows:

$$C, C_{\mathrm{a}}, C_{\mathrm{p}} : [-1, 1] \times [-1, 1] \to \mathbb{R}.$$

For brevity, with a slight abuse of notation, we represent the bivariate functions using the same name of the univariate function $C(\cdot)$, i.e., $C(x, x') := \widehat{C}(x' - x)$, $C_{\mathrm{a}}(x, x') := \widehat{C}_{\mathrm{a}}(x' - x)$, and $C_{\mathrm{p}}(x, x') := \widehat{C}_{\mathrm{p}}(x' - x)$. This notation is also used in Figure 1. Hence, analogous to (2-7), in the bulk (i.e., $x \in (-1 + \delta, 1 - \delta)$), kernel functions coincide

$$C(x, x') = C_{\mathrm{a}}(x, x') = C_{\mathrm{p}}(x, x'). \tag{2-9}$$

We first prove that the operators $\mathcal{L}$ and $\mathcal{L}_{\text{orig}}$ agree in the bulk.

Lemma 2.3. $\qquad\qquad\qquad \mathcal{L}u(x) = \mathcal{L}_{\text{orig}}u(x), \quad x \in (-1 + \delta, 1 - \delta).$

Proof. For x in the bulk, we have $(x - \delta, x + \delta) \cap \Omega = (x - \delta, x + \delta)$. Hence,

$$
\begin{aligned}
\int_\Omega \widehat{C}(x' - x) \, dx' &= \int_\Omega \widehat{\chi}_\delta(x' - x)\widehat{\mu}(x' - x) \, dx' \\
&= \int_{(x-\delta,x+\delta)\cap\Omega} \widehat{\mu}(x' - x) \, dx' \\
&= \int_{(x-\delta,x+\delta)} \widehat{\mu}(x' - x) \, dx' \\
&= \int_{(-\delta,\delta)} \mu(x') \, dx' \\
&= \int_\Omega \chi_\delta(x')\mu(x') \, dx' \\
&= \int_\Omega C(x') \, dx'.
\end{aligned}
$$

The result follows. $\square$

3. Dirichlet and Neumann BC, and differentiation under the integral sign

Imposing Neumann (also antiperiodic and periodic) BC requires differentiation. Thus, we present technical details regarding differentiation under the integral sign which are provided in Lemma 3.1. The proof of Lemma 3.1, which is omitted here, is by the Lebesgue dominated convergence theorem. Similarly, the limit in the definition of the Dirichlet BC can be interchanged with the integral, again by the Lebesgue dominated convergence theorem.

Lemma 3.1. *Suppose that the function* $k : \Omega_x \times \Omega_{x'} \to \mathbb{R}$ *satisfies the following conditions.*

 (1) *The function* $k(x, x')$ *is measurable with respect to* x' *for each* $x \in \Omega_x$.

 (2) *For almost every* $x' \in \Omega_{x'}$, *the derivative* $\partial k / \partial x(x, x')$ *exists for all* $x \in \Omega_x$.

 (3) *There is an integrable function* $\ell : \Omega_{x'} \to \mathbb{R}$ *such that* $|\partial k / \partial x(x, x')| \leq \ell(x')$ *for all* $x \in \Omega_x$.

Then,

$$
\frac{d}{dx} \int_{\Omega_{x'}} k(x, x') \, dx' = \int_{\Omega_{x'}} \frac{\partial k}{\partial x}(x, x') \, dx'.
$$

We use Lemma 3.1 to check if the operator $\mathcal{M}_{\text{N}}$ enforces homogeneous Neumann BC. First, we want to identify the integrand associated to $\mathcal{M}_{\text{N}}$. We start with writing P_e and P_o explicitly and utilizing a simple change of variable as follows:

$$
\begin{aligned}
(\mathcal{M}_{\text{N}} - c)u(x) &= -\int_\Omega \left[\widehat{C}_{\text{p}}(x' - x)\tfrac{1}{2}\big(u(x') + u(-x')\big) + \widehat{C}_{\text{a}}(x' - x)\tfrac{1}{2}\big(u(x') - u(-x')\big) \right] dx' \\
&= -\int_\Omega K_{\text{N}}(x, x')u(x') \, dx',
\end{aligned}
\tag{3-1}
$$

where

$$K_{\mathbb{N}}(x, x') := \tfrac{1}{2}\{[\widehat{C}_{\mathrm{a}}(x'-x) - \widehat{C}_{\mathrm{a}}(x'+x)] + [\widehat{C}_{\mathrm{p}}(x'-x) + \widehat{C}_{\mathrm{p}}(x'+x)]\}.$$

Analogous to the construction given in [Aksoylu et al. 2017a], we assume that $C(x) \in L^2(\Omega)$, and hence,

$$\widehat{C}(x), \ \widehat{C}_{\mathrm{a}}(x), \ \widehat{C}_{\mathrm{p}}(x) \in L^2(\widehat{\Omega}). \tag{3-2}$$

We are now in a position to determine the necessary conditions needed to apply Lemma 3.1. First, we set $\Omega_x = \Omega_{x'} = \Omega$ and

$$k(x, x') = K_{\mathbb{N}}(x, x')u(x').$$

Considering the jumps and the fact that the BC is enforced at the boundary, we assume that $\widehat{C}_{\mathrm{a}}(x)$ and $\widehat{C}_{\mathrm{p}}(x)$ are piecewise continuously differentiable in $\widehat{\Omega}$ and continuously differentiable functions up to $\partial\widehat{\Omega}$. Hence, the first two conditions of Lemma 3.1 are satisfied. To satisfy the third condition, we define

$$\ell(x') := \operatorname*{ess\,sup}_{x \in \Omega_x}\left|\frac{\partial K_{\mathbb{N}}}{\partial x}(x, x')\right| |u(x')|,$$

and assume that

$$\operatorname*{ess\,sup}_{x \in \Omega_x}\left|\frac{\partial K_{\mathbb{N}}}{\partial x}(x, x')\right| \in L^2(\Omega_{x'}). \tag{3-3}$$

The integrability of $\ell(x')$ is sufficient to satisfy the third condition. We could choose any $L^p(\Omega_{x'})$ space. We choose the space $L^2(\Omega_{x'})$ in (3-3) in order to align with the construction given in [Aksoylu et al. 2017a]. Since $u(x') \in L^2(\Omega_{x'})$, we obtain $\ell(x') \in L^2(\Omega_{x'})$.

We are now ready to prove our Main Theorem.

Proof of Theorem 1.1. We exploit (2-9) in constructing the governing operators that enforce Neumann and Dirichlet BCs by rewriting the $\mathcal{L}$ operator in the following way. For $x \in (-1+\delta, 1-\delta)$, we have

$$\begin{aligned}
(\mathcal{L}-c)u(x) &= -\int_{\Omega} \widehat{C}(x'-x)u(x')\,\mathrm{d}x' \\
&= -\int_{\Omega} \widehat{C}(x'-x)(P_e + P_o)u(x')\,\mathrm{d}x' \\
&= -\int_{\Omega} \left[\widehat{C}(x'-x)P_e u(x') + \widehat{C}(x'-x)P_o u(x')\right]\mathrm{d}x' \\
&= -\int_{\Omega} \left[\widehat{C}_{\mathrm{p}}(x'-x)P_e u(x') + \widehat{C}_{\mathrm{a}}(x'-x)P_o u(x')\right]\mathrm{d}x' \\
&= (\mathcal{M}_{\mathbb{N}}-c)u(x).
\end{aligned}$$

Similarly, for $x \in (-1+\delta, 1-\delta)$,

$$\begin{aligned}
(\mathcal{L}-c)u(x) &= -\int_{\Omega} \left[\widehat{C}(x'-x)P_e u(x') + \widehat{C}(x'-x)P_o u(x')\right]\mathrm{d}x' \\
&= -\int_{\Omega} \left[\widehat{C}_{\mathrm{a}}(x'-x)P_e u(x') + \widehat{C}_{\mathrm{p}}(x'-x)P_o u(x')\right]\mathrm{d}x' \\
&= (\mathcal{M}_{\mathbb{D}}-c)u(x).
\end{aligned}$$

Next, we show that $\mathcal{M}_\mathrm{N}$ and $\mathcal{M}_\mathrm{D}$ enforce homogeneous Neumann and Dirichlet BC, respectively.

The operator $\mathcal{M}_\mathrm{N}$: First we remove the points at which the derivative of $K_\mathrm{N}(x, x')$ does not exist from the set of integration. Note that such points form a set of measure zero, and hence, do not affect the value of the integral. We differentiate both sides of (3-1) and apply Lemma 3.1 to interchange the differentiation with the integral. We can differentiate the integrand $K_\mathrm{N}(x, x')$ in a piecewise fashion and obtain

$$\frac{\mathrm{d}}{\mathrm{d}x}[(\mathcal{M}_\mathrm{N} - c)u](x) = -\int_\Omega \frac{\partial K_\mathrm{N}}{\partial x}(x, x')u(x')\,\mathrm{d}x', \tag{3-4}$$

where

$$\frac{\partial K_\mathrm{N}}{\partial x}(x, x') = \tfrac{1}{2}\{[\widehat{C}_\mathrm{a}'(x' - x) - \widehat{C}_\mathrm{a}'(x' + x)] + [\widehat{C}_\mathrm{p}'(x' - x) + \widehat{C}_\mathrm{p}'(x' + x)]\}.$$

We check the boundary values by plugging $x = \pm 1$ in (3-4):

$$\frac{\mathrm{d}}{\mathrm{d}x}[(\mathcal{M}_\mathrm{N} - c)u](\pm 1) = -\int_\Omega \frac{\partial K_\mathrm{N}}{\partial x}(\pm 1, x')u(x')\,\mathrm{d}x'. \tag{3-5}$$

The functions $\widehat{C}_\mathrm{a}'$ and $\widehat{C}_\mathrm{p}'$ are 2-antiperiodic and 2-periodic because they are the derivatives of 2-antiperiodic and 2-periodic functions, respectively. Hence,

$$\widehat{C}_\mathrm{a}'(\pm 1 + x') = -\widehat{C}_\mathrm{a}'(\mp 1 + x') \quad \text{and} \quad \widehat{C}_\mathrm{p}'(\mp 1 + x') = \widehat{C}_\mathrm{p}'(\pm 1 + x'). \tag{3-6}$$

Hence, the integrand in (3-5) vanishes, i.e.,

$$\frac{\partial K_\mathrm{N}}{\partial x}(\pm 1, x') = 0.$$

Therefore, we arrive at

$$\frac{\mathrm{d}}{\mathrm{d}x}\mathcal{M}_\mathrm{N}u(\pm 1) = cu'(\pm 1). \tag{3-7}$$

Since we assume that u satisfies homogeneous Neumann BC, i.e., $u'(\pm 1) = 0$, we conclude that the operator $\mathcal{M}_\mathrm{N}$ enforces homogeneous Neumann BC as well.

The operator $\mathcal{M}_\mathrm{D}$: In order to check if the operator $\mathcal{M}_\mathrm{D}$ enforces homogeneous Dirichlet BC, we start again with writing P_e and P_o explicitly and utilizing a simple change of variables as follows:

$$(\mathcal{M}_\mathrm{D} - c)u(x) = -\int_\Omega \widehat{C}_\mathrm{a}(x' - x)\tfrac{1}{2}(u(x') + u(-x'))\,\mathrm{d}x' - \int_\Omega \widehat{C}_\mathrm{p}(x' - x)\tfrac{1}{2}(u(x') - u(-x'))\,\mathrm{d}x'$$

$$= -\int_\Omega K_\mathrm{D}(x, x')u(x')\,\mathrm{d}x',$$

where

$$K_\mathrm{D}(x, x') := \tfrac{1}{2}\{[\widehat{C}_\mathrm{a}(x' - x) + \widehat{C}_\mathrm{a}(x' + x)] + [\widehat{C}_\mathrm{p}(x' - x) - \widehat{C}_\mathrm{p}(x' + x)]\}. \tag{3-8}$$

By the Lebesgue dominated convergence theorem, the limit in the definition of the Dirichlet BC can be interchanged with the integral. Now, we check the boundary values by plugging $x = \pm 1$ in (3-8):

$$(\mathcal{M}_\mathrm{D} - c)u(\pm 1) = -\int_\Omega K_\mathrm{D}(\pm 1, x')u(x')\,\mathrm{d}x'. \tag{3-9}$$

Since $\widehat{C}_{\mathrm{a}}$ and $\widehat{C}_{\mathrm{p}}$ are 2-antiperiodic and 2-periodic, respectively, we have

$$\widehat{C}_{\mathrm{a}}(\mp 1 + x') = -\widehat{C}_{\mathrm{a}}(\pm 1 + x') \quad \text{and} \quad \widehat{C}_{\mathrm{p}}(\mp 1 + x') = \widehat{C}_{\mathrm{p}}(\pm 1 + x'). \tag{3-10}$$

Hence, the integrand in (3-9) vanishes, i.e., $K_{\mathrm{D}}(\pm 1, x') = 0$. Therefore, we arrive at

$$\mathcal{M}_{\mathrm{D}}u(\pm 1) = cu(\pm 1). \tag{3-11}$$

Since we assume that u satisfies homogeneous Dirichlet BC, i.e., $u(\pm 1) = 0$, we conclude that the operator $\mathcal{M}_{\mathrm{D}}$ enforces homogeneous Dirichlet BC as well. $\qquad\square$

Remark 3.2. We have defined $\mathcal{M}_{\mathrm{D}}$ and $\mathcal{M}_{\mathrm{N}}$ in a way that they are linear bounded operators. More precisely, $\mathcal{M}_{\mathrm{D}}, \mathcal{M}_{\mathrm{N}} \in L(X, X)$ where $X = L^2(\Omega) \cap C^1(\partial\Omega)$. For $\mathcal{M}_{\mathrm{D}}$, the choice of X can be relaxed as $L^2(\Omega) \cap C^0(\partial\Omega)$. This choice is implied when we study $\mathcal{M}_{\mathrm{D}}$. Boundedness of $\mathcal{M}_{\mathrm{D}}$ and $\mathcal{M}_{\mathrm{N}}$ follows from the choice of (1-6) and (3-2). In addition, since $\mathcal{M}_{\mathrm{D}}$ and $\mathcal{M}_{\mathrm{N}}$ are both integral operators, their self-adjointness follows easily from the fact that the corresponding kernels are symmetric (due to evenness of C), i.e., $K_{\mathrm{D}}(x, x') = K_{\mathrm{D}}(x', x)$ and $K_{\mathrm{N}}(x, x') = K_{\mathrm{N}}(x', x)$.

4. Other possible boundary conditions

The construction employed to satisfy local BC is based on the following decomposition of $u(x')$:

$$u(x') = P_e u(x') + P_o u(x'),$$

and the agreement of $\widehat{C}(x' - x)$ with $\widehat{C}_{\mathrm{a}}(x' - x)$ and $\widehat{C}_{\mathrm{p}}(x' - x)$ in the bulk; see (2-8). By replacing $\widehat{C}(x' - x)$ with either $\widehat{C}_{\mathrm{a}}(x' - x)$ or $\widehat{C}_{\mathrm{p}}(x' - x)$, we have the following four combinations for the integrand of $\mathcal{L}$:

$$\widehat{C}(x' - x)u(x') = \{\widehat{C}_{\mathrm{a}}(x' - x), \widehat{C}_{\mathrm{p}}(x' - x)\} P_e u(x') + \{\widehat{C}_{\mathrm{a}}(x' - x), \widehat{C}_{\mathrm{p}}(x' - x)\} P_o u(x').$$

Denoting the choice of $\widehat{C}_{\mathrm{a}}(x' - x)$ and $\widehat{C}_{\mathrm{p}}(x' - x)$ by $\mathtt{a}$ and $\mathtt{p}$, respectively, the combinations $\mathtt{ap}$ and $\mathtt{pa}$ give rise to Dirichlet and Neumann BC, respectively; see Theorem 1.1. Namely,

$$\text{Dirichlet (ap):} \quad \widehat{C}(x' - x)u(x') = \widehat{C}_{\mathrm{a}}(x' - x) P_e u(x') + \widehat{C}_{\mathrm{p}}(x' - x) P_o u(x'),$$
$$\text{Neumann (pa):} \quad \widehat{C}(x' - x)u(x') = \widehat{C}_{\mathrm{p}}(x' - x) P_e u(x') + \widehat{C}_{\mathrm{a}}(x' - x) P_o u(x').$$

We show that the combinations $\mathtt{aa}$ and $\mathtt{pp}$ give rise to antiperiodic and periodic BC, respectively. Namely,

$$\text{Antiperiodic (aa):} \quad \widehat{C}(x' - x)u(x') = \widehat{C}_{\mathrm{a}}(x' - x) P_e u(x') + \widehat{C}_{\mathrm{a}}(x' - x) P_o u(x') = \widehat{C}_{\mathrm{a}}(x' - x)u(x'),$$
$$\text{Periodic (pp):} \quad \widehat{C}(x' - x)u(x') = \widehat{C}_{\mathrm{p}}(x' - x) P_e u(x') + \widehat{C}_{\mathrm{p}}(x' - x) P_o u(x') = \widehat{C}_{\mathrm{p}}(x' - x)u(x').$$

Then, the operators $\mathcal{M}_{\mathrm{a}}$ and $\mathcal{M}_{\mathrm{p}}$ are defined by

$$(\mathcal{M}_{\mathrm{a}} - c)u(x) := -\int_\Omega \widehat{C}_{\mathrm{a}}(x' - x)u(x')\,\mathrm{d}x',$$
$$(\mathcal{M}_{\mathrm{p}} - c)u(x) := -\int_\Omega \widehat{C}_{\mathrm{p}}(x' - x)u(x')\,\mathrm{d}x'.$$

We recall the space of functions used to enforce antiperiodic and periodic BC, respectively [Aksoylu et al. 2017a]:

$$\{u \in L^2(\Omega) \cap C^1(\partial\Omega) : \lim_{x \to -1} u(x) = -\lim_{x \to 1} u(x), \quad \lim_{x \to -1} u'(x) = -\lim_{x \to 1} u'(x)\},$$

$$\{u \in L^2(\Omega) \cap C^1(\partial\Omega) : \lim_{x \to -1} u(x) = \lim_{x \to 1} u(x), \quad \lim_{x \to -1} u'(x) = \lim_{x \to 1} u'(x)\}.$$

Since $\widehat{C}_a$ and $\widehat{C}_a'$ are 2-antiperiodic and $\widehat{C}_p$ and $\widehat{C}_p'$ are 2-periodic, similar to (3-10) and (3-6), we have

$$\widehat{C}_a(-1 - x') = -\widehat{C}_a(1 - x'), \quad \widehat{C}_p(-1 - x') = \widehat{C}_p(1 - x'),$$

$$\widehat{C}_a'(-1 - x') = -\widehat{C}_a'(1 - x'), \quad \widehat{C}_p'(-1 - x') = \widehat{C}_p'(1 - x').$$

Consequently,

$$(\mathcal{M}_a - c)u(-1) = -(\mathcal{M}_a - c)u(1), \tag{4-1}$$

$$(\mathcal{M}_p - c)u(-1) = (\mathcal{M}_p - c)u(1). \tag{4-2}$$

In addition, by applying Lemma 3.1, we obtain

$$\frac{d}{dx}[(\mathcal{M}_a - c)u](-1) = -\frac{d}{dx}[(\mathcal{M}_a - c)u](1), \tag{4-3}$$

$$\frac{d}{dx}[(\mathcal{M}_p - c)u](-1) = \frac{d}{dx}[(\mathcal{M}_p - c)u](1). \tag{4-4}$$

These imply that the operators $\mathcal{M}_a$ and $\mathcal{M}_p$ enforce antiperiodic and periodic BC, respectively.

5. Compatibility conditions

When we solve an equation using the operators $\mathcal{M}_{BC}$ where $BC \in \{D, N, a, p\}$, i.e.,

$$\mathcal{M}_{BC} u = f_{BC},$$

we want to identify the conditions imposed on f_{BC}. Since the operator $\mathcal{M}_{BC}$ enforces the corresponding BC, we observe that the same BC is imposed on f_{BC}. To see this, we start by assuming that u satisfies the corresponding BC. Then, we choose f_{BC} from the same space to which u belongs, i.e.,

$$f_{BC} \in L^2(\Omega) \cap C^1(\partial\Omega).$$

From (4-1) and (4-2), respectively, we immediately see that

$$f_a(-1) = -f_a(1), \quad f_p(-1) = f_p(1).$$

From (4-3) and (4-4), respectively, we also get

$$f_a'(-1) = -f_a'(1), \quad f_p'(-1) = f_p'(1).$$

In addition, from (3-11) and (3-7), respectively, we obtain

$$f_D(\pm 1) = 0, \quad \frac{d f_N}{dx}(\pm 1) = 0.$$

6. The extension to a 2D problem

In this section, we present the extension of the present work to 2D problems. The main idea of this extension relies on our 1D construction but it is nontrivial. Its proof requires a significant amount of technical detail. Here, we provide only a small part of the results without proof.

We choose the domain in 2D to be $\Omega = [-1, 1] \times [-1, 1]$. There are various combinations of BC one can enforce. Here, we report only pure Dirichlet and pure Neumann BC, the 2D analogues of the ones presented in Theorem 1.1. The proofs, a comprehensive discussion, and numerical results are provided in [Aksoylu et al. 2017c].

In 2D, the governing operator in (1-1) takes the form

$$\mathcal{L}_{\text{orig}} u(x, y) := \iint\limits_{\Omega} \widehat{C}(x' - x, y' - y) u(x, y) \, dx \, dx' - \iint\limits_{\Omega} \widehat{C}(x' - x, y' - y) u(x', y') \, dx' \, dy'.$$

Similar to (1-2), we define the operator that is closely related to $\mathcal{L}_{\text{orig}}$ as

$$\mathcal{L} u(x, y) := c u(x, y) - \iint\limits_{\Omega} \widehat{C}(x' - x, y' - y) u(x', y') \, dx' \, dy', \quad (x, y) \in \Omega,$$

where $c = \iint\limits_{\Omega} C(x', y') \, dx' \, dy'$. The kernel function $C(x, y)$ is assumed to be even. Namely,

$$C(-x, -y) = C(x, y).$$

Similar to the 1D case, we choose the kernel function $C(x, y)$ to be the *canonical* kernel function $\chi_\delta(x, y)$, whose definition is given as follows. For $(x, y) \in \Omega$,

$$\chi_\delta(x, y) := \begin{cases} 1 & \text{if } (x, y) \in (-\delta, \delta) \times (-\delta, \delta), \\ 0 & \text{otherwise.} \end{cases}$$

The agreement of the operators $\mathcal{L}$ and $\mathcal{L}_{\text{orig}}$ in the 1D bulk shown in Lemma 2.1 carries over to the 2D bulk whose definition is given by

$$\text{bulk} = \big\{(x, y) \in \Omega : (x, y) \in (-1 + \delta, 1 - \delta) \times (-1 + \delta, 1 - \delta)\big\}.$$

Inspired by the projections that give the even and odd parts of a univariate function given in (1-7), we define the following operators that act on a bivariate function.

$$P_{e,x'}, P_{o,x'}, P_{e,y'}, P_{o,y'} : L^2(\Omega) \to L^2(\Omega),$$

whose definitions are

$$P_{e,x'} u(x', y') := \tfrac{1}{2}(u(x', y') + u(-x', y')), \qquad P_{o,x'} u(x', y') := \tfrac{1}{2}(u(x', y') - u(-x', y')), \quad (6\text{-}1)$$

$$P_{e,y'} u(x', y') := \tfrac{1}{2}(u(x', y') + u(x', -y')), \qquad P_{o,y'} u(x', y') := \tfrac{1}{2}(u(x', y') - u(x', -y')). \quad (6\text{-}2)$$

Each operator is an orthogonal projection and possesses the following decomposition property:

$$P_{e,x'} + P_{o,x'} = I_{x'}, \quad P_{e,y'} + P_{o,y'} = I_{y'}.$$

One can easily check that all four orthogonal projections in (6-1) and (6-2) commute with each other. We define the following new operators obtained from the products of these projections:

$$P_{e,x'} P_{e,y'} u(x', y') := \tfrac{1}{4}\{[u(x', y') + u(x', -y')] + [u(-x', y') + u(-x', -y')]\},$$

$$P_{e,x'} P_{o,y'} u(x', y') := \tfrac{1}{4}\{[u(x', y') - u(x', -y')] + [u(-x', y') - u(-x', -y')]\},$$

$$P_{o,x'} P_{o,y'} u(x', y') := \tfrac{1}{4}\{[u(x', y') - u(x', -y')] - [u(-x', y') - u(-x', -y')]\},$$

$$P_{o,x'} P_{e,y'} u(x', y') := \tfrac{1}{4}\{[u(x', y') + u(x', -y')] - [u(-x', y') + u(-x', -y')]\}.$$

These operators are also orthogonal projections and satisfy the following decomposition property:

$$P_{e,x'} P_{e,y'} + P_{e,x'} P_{o,y'} + P_{o,x'} P_{e,y'} + P_{o,x'} P_{o,y'} = I_{x',y'}.$$

They will be used in the definition of the operators $\mathcal{M}_D$ and $\mathcal{M}_N$.

Theorem 6.1 (Main Theorem in 2D). *Let $\Omega := [-1, 1] \times [-1, 1]$ and the kernel function be separable in the form*

$$C(x, y) = X(x)Y(y), \tag{6-3}$$

where X and Y are even functions. Then, the operators $\mathcal{M}_D$ and $\mathcal{M}_N$ defined by

$$(\mathcal{M}_D - c)u(x, y) :=$$
$$-\iint_{\Omega} \left[\widehat{X}_a(x' - x) P_{e,x'} + \widehat{X}_p(x' - x) P_{o,x'}\right]\left[\widehat{Y}_a(y' - y) P_{e,y'} + \widehat{Y}_p(y' - y) P_{o,y'}\right] u(x', y') \, dx' \, dy',$$

$$(\mathcal{M}_N - c)u(x, y) :=$$
$$-\iint_{\Omega} \left[\widehat{X}_p(x' - x) P_{e,x'} + \widehat{X}_a(x' - x) P_{o,x'}\right]\left[\widehat{Y}_p(y' - y) P_{e,y'} + \widehat{Y}_a(y' - y) P_{o,y'}\right] u(x', y') \, dx' \, dy',$$

agree with $\mathcal{L}u(x, y)$ in the bulk, i.e., for $(x, y) \in (-1 + \delta, 1 - \delta) \times (-1 + \delta, 1 - \delta)$. Furthermore, the operators $\mathcal{M}_D$ and $\mathcal{M}_N$ enforce pure Dirichlet and pure Neumann BC, respectively:

$$(\mathcal{M}_D - c)u(x, \pm 1) = (\mathcal{M}_D - c)u(\pm 1, y) = 0,$$

$$\frac{\partial}{\partial n}[(\mathcal{M}_N - c)u](x, \pm 1) = \frac{\partial}{\partial n}[(\mathcal{M}_N - c)u](\pm 1, y) = 0,$$

where n denotes the outward unit normal vector.

Remark 6.2. Although we assume a separable kernel function $C(x, y) = X(x)Y(y)$ as in (6-3), note that we do not impose a separability assumption on the solution $u(x, y)$.

Remark 6.3. In Theorem 6.1, the function u is scalar valued, which corresponds to the solution of a nonlocal diffusion problem. In higher dimensional PD problems, the function u is vector valued. The extension of our construction to such problems is the subject of ongoing work.

7. Conclusion

We presented novel governing operators $\mathcal{M}_D$ and $\mathcal{M}_N$ in the theory of PD constructed by the guiding principle that they agree with the original PD operator $\mathcal{L}_{orig}$ in the bulk, and, at the same time, enforce local Dirichlet or Neumann BC. We also presented the operators $\mathcal{M}_a$ and $\mathcal{M}_p$ that enforce local antiperiodic and periodic BC. In [Aksoylu et al. 2017d], we give an overview of local BC in general nonlocal problems. We believe that our contribution is an important step towards extending the applicability of PD to problems that require local BC such as contact, shear, and traction. For future research, we plan to investigate if our approach of enforcing local BC can be used to eliminate surface effects. Finally, we presented the extension of the 1D governing operators to 2D on rectangular domains. The generalization to 3D box domains is straightforward. The construction of the operators for general geometries remains an open problem and constitutes the subject of ongoing work.

References

[Aksoylu and Celiker 2016] B. Aksoylu and F. Celiker, "Comparison of nonlocal operators utilizing perturbation analysis", pp. 589–606 in *Numerical mathematics and advanced applications ENUMATH 2015*, edited by B. Karasözen et al., Lecture Notes in Computational Science and Engineering **112**, Springer, Cham, Switzerland, 2016.

[Aksoylu and Kaya 2017] B. Aksoylu and A. Kaya, "Conditioning analysis of nonlocal problems with local boundary conditions", 2017. Submitted.

[Aksoylu et al. 2017a] B. Aksoylu, H. R. Beyer, and F. Celiker, "Application and implementation of incorporating local boundary conditions into nonlocal problems", 2017. To appear in *Numer. Funct. Anal. Optim.*

[Aksoylu et al. 2017b] B. Aksoylu, H. R. Beyer, and F. Celiker, "Theoretical foundations of incorporating local boundary conditions into nonlocal problems", 2017. To appear in *Rep. Math. Phys.*

[Aksoylu et al. 2017c] B. Aksoylu, F. Celiker, and O. Kilicer, "Nonlocal operators with local boundary conditions in higher dimensions", 2017. Submitted.

[Aksoylu et al. 2017d] B. Aksoylu, F. Celiker, and O. Kilicer, "Nonlocal problems with local boundary conditions: an overview", 2017. Submitted.

[Beyer et al. 2016] H. R. Beyer, B. Aksoylu, and F. Celiker, "On a class of nonlocal wave equations from applications", *J. Math. Phys.* **57**:6 (2016), art. id. 062902, 28 pp.

[Kilic 2008] B. Kilic, *Peridynamic theory for progressive failure prediction in homogeneous and heterogeneous materials*, Ph.D. thesis, University of Arizona, 2008, available at http://hdl.handle.net/10150/193658.

[Madenci and Oterkus 2014] E. Madenci and E. Oterkus, *Peridynamic theory and its applications*, Springer, New York, 2014.

[Mitchell et al. 2015] J. Mitchell, S. Silling, and D. Littlewood, "A position-aware linear solid constitutive model for peridynamics", *J. Mech. Mater. Struct.* **10**:5 (2015), 539–557.

[Silling 2000] S. A. Silling, "Reformulation of elasticity theory for discontinuities and long-range forces", *J. Mech. Phys. Solids* **48**:1 (2000), 175–209.

BURAK AKSOYLU: burak@wayne.edu
Department of Mathematics, Wayne State University, 656 W. Kirby, Detroit, MI 48202, United States

FATIH CELIKER: celiker@wayne.edu
Department of Mathematics, Wayne State University, 656 W. Kirby, Detroit, MI 48202, United States

msp

OPTIMIZATION OF CHABOCHE KINEMATIC HARDENING PARAMETERS BY USING AN ALGEBRAIC METHOD BASED ON INTEGRAL EQUATIONS

LIU SHIJIE AND LIANG GUOZHU

The current work is devoted to optimizing the Chaboche kinematic hardening parameters via an algebraic method based on its integral equations, which is rarely investigated. An experimental test in strain range of ±0.8% for 304 stainless steel (304SS) is applied to demonstrate this method. Firstly, the first quarter tensile part, along with the Osgood–Ramberg equation, is used to estimate the initial parameters. Then, optimizations are conducted based on the first quarter tensile part for the first and the 150th cyclic test. Results indicate that:

  (i) the value of initial yielding stress has a significant effect on the simulation. The optimized initial yielding stress is roughly 181 MPa for 304SS, which corresponds to the test at strain range of ±0.8% with a frequency of 0.25 Hz.
 (ii) The experimental plastic strains in elastic loading/unloading segments in the proposed method are unreasonable in calculating the stresses and should be removed before conducting an optimization.

A list of symbols can be found on page 453.

1. Introduction

It is well-known that metallic materials exhibit a gradual fatigue life consumption phenomenon under a complicated cyclic loading. Indeed, the cyclic deformation, including ratcheting, of metallic structures has been extensively studied in the last few decades, as it plays a very important role in safety assessments and fatigue-life estimations.

Many experimental studies were conducted about mechanical behaviors subjected to cyclic loading [Prager 1956; Benham 1965; Kamaya and Kawakubo 2015]. Along with those experimental studies, many researchers have tried to develop appropriate constitutive models to better predict the response of metallic materials subjected to cyclic loading, especially the Bauchinger effect and the strain accumulation in unsymmetric uniaxial stress-controlled conditions. The first systematic literature in this regard is [Prager 1956], in which the author proposed a linear hardening model capable of capturing the Bauchinger effect; however, the model failed to simulate ratcheting strains in the presence of mean stress due to its constant plastic hardening modulus. For this reason, in [Armstrong and Frederick 1966], the authors modified Prager's hardening rule by adding a nonlinear recall term to propose the so-called Armstrong and Frederick hardening model. This new term could account for the fading memory effect of the plastic strain path observed in experiments by making a difference in the plastic hardening modulus between the forward and reverse parts in a typical unsymmetric stress cycle. Due to this initial work of Armstrong and Frederick, the idea of describing the evolution of kinematic hardening variables in terms of nonlinear differential equations has been followed in many other studies, such as [Chaboche

Keywords: Chaboche kinematic hardening, Ramberg–Osgood model, parameters optimization, integral equations.

et al. 1979; Chaboche 1991; 2008]. The Chaboche model is a decomposed nonlinear kinematic hardening model (CHK-M, where M is the total number of AF rules in the Chaboche kinematic hardening model), in which each of the backstress components plays a primary role in controlling the shape of σ-ε response at different ranges of strain. The CHK-M model is rate-independent and able to account for the Bauschinger effect. The advantage of this model is that it can be modified to solve for complex behaviors of the materials under various conditions. Besides the CHK-M model, many other evolution of kinematic hardening models have been proposed; see, e.g., [Ohno and Wang 1994; Voyiadjis and Basuroychowdhury 1998; Bari and Hassan 2000; Dafalias et al. 2008; Abdel-Karim 2010; Ahmadzadeh and Varvani-Farahani 2013; Jiang et al. 2013]. Note that the multimechanism model has attracted attention in the last twenty years. In [Velay et al. 2006], the authors proposed a nonunified elasto-plastic model for describing the TMF behavior of AISI L6. Two integration methods, explicit Runge–Kutta method and implicit θ method, of constitutive equations were developed for the numerical implementation of the 2-mechanisms -1 yield criterion (2M1C) model. Based on the modification of 2M1C model, a new version of the multimechanism model for plasticity was proposed in [Taleb and Cailletaud 2010] for considering the nonproportional effect of the loading and the strain memory phenomenon. In the previous work, the kinematic hardening parameters were identified by using optimization software included in the finite element method (FEM) code ZeBuLoN. The optimization algorithms in the software are shown in [Besson et al. 1998].

Among various constitutive models mentioned above, the CHK-M model was widely used [Abdel-Karim 2010; Jiang et al. 2009; Djimli et al. 2010]. As suggested in [Chaboche et al. 1979; Chaboche 1986], at least three AF rules should be incorporated in the model. Because of its simplicity and efficiency, this model was implemented into different kinds of finite element software (e.g., ABAQUS and ANSYS).

The CHK-M model has been applied for decades and the metal-related fatigue literature are numerous, for example, [Egner and Egner 2014; Pereira and Jesus 2011; Chaboche 1988; Jiang et al. 2009]. Indeed, higher accuracy of the predicted material cyclic mechanical behavior accompanies higher accuracy of fatigue life estimation. Consequently, in order to get an accurate description of fatigue material behavior and its properties [Chaboche et al. 2012; Djimli et al. 2010; Li et al. 2014], it is necessary to choose or develop a suitable constitutive model that will accurately describe its mechanical behavior of materials. While the identification of material parameters in various hardening models is always one of the principal difficulties to be handled prior to the fatigue life estimation, the parameters of CHK-M model can be identified by using the finite element method with the return-mapping algorithm through a trial-and-error approach. However, this method is difficult to implement, especially for practical applications, because the test data are mainly being used to validate the parameters, not to identify them (which is rather time consuming). In this case, an algebraic approach simulating the stress with the integral equations was developed to predict and optimize the CHK-M model parameters, which directly identifies the model parameters based on the test data. The current work is to determine the CHK-M model parameters in the cyclic experimental tests under strain-controlled conditions, but isotropic hardening/softening and ratcheting are not taken into account.

2. Optimization method of model parameters identification

There exist a lot of yield criteria for determining the yield condition, among which the von Mises criterion is widely used. The yield surface, regarding the plasticity criterion, of a purely kinematic hardening von

Mises material can be written as

$$f(\underset{\approx}{\sigma}, \underset{\approx}{X}) = \sqrt{\tfrac{3}{2}(\underset{\approx}{s} - \underset{\approx}{X}) : (\underset{\approx}{s} - \underset{\approx}{X})} - k = 0, \tag{1}$$

where the backstress tensor $\underset{\approx}{X}$ defines the current center of the yield surface in the stress space.

Actually, the Chaboche decomposed hardening model [Chaboche et al. 1979; Chaboche 1986] is an assembly of several AF rules, which can be expressed as

$$\mathrm{d}\underset{\approx}{X} = \sum_{i=1}^{M} \mathrm{d}\underset{\approx}{X}_i, \quad \mathrm{d}\underset{\approx}{X}_i = \tfrac{2}{3}C_i \mathrm{d}\underset{\approx}{\varepsilon}_p - \gamma_i \underset{\approx}{X}_i \mathrm{d}p, \quad \mathrm{d}p = \sqrt{\tfrac{2}{3}\mathrm{d}\underset{\approx}{\varepsilon}_p : \mathrm{d}\underset{\approx}{\varepsilon}_p}, \tag{2}$$

where M is the total number of decomposed AF rules utilized. The main reason for the superposition of several AF rules in the Chaboche model is to improve its accuracy at different ranges of strain; as stated in Section 1, the goal cannot be achieved using only one AF rule. Chaboche [1986] first used the superposition of three AF rules ($M = 3$) to simulate the three critical segments of monotonic stress-strain curves and this method is also adopted in the current study.

In the case of uniaxial loading, each of the decomposed rules takes the form

$$\mathrm{d}X_x = \sum_{i=1}^{M} \mathrm{d}X_{ix}, \quad \mathrm{d}X_{ix} = \tfrac{2}{3}C_i \mathrm{d}\varepsilon_{p,x} - \gamma_i X_{ix} |\mathrm{d}\varepsilon_{p,x}|, \tag{3}$$

where the subscript x stands for the direction of applied load. Now, it can be easily shown that the following equation holds between the uniaxial stress, the backstress, and the initial yielding stress:

$$\left| \sigma_x - \tfrac{3}{2}X_x \right| = k. \tag{4}$$

For simplicity, the subscript x was omitted for deducing the integral equation for (3) in uniaxial state. Furthermore, combining (3) and (4), the decomposed component equation in (3) will be $\mathrm{d}X_i = C_i \mathrm{d}\varepsilon_p - \gamma_i X_i |\mathrm{d}\varepsilon_p|$.

In the first quarter tensile part, $v = \text{sign } \dot{\varepsilon}_p = 1$ and starts from the initial virgin state ($\varepsilon_{p,0} = 0$, $X_{i,0} = 0$). Integrating (3), we have

$$X_{i,j} = \frac{C_i}{\gamma_i}[1 - \exp(\gamma_i \varepsilon_{p,j})] \quad (i = 1, 2, \ldots, M), \tag{5}$$

where the subscript j denotes the serial number of plastic strain used. In (5), for $\varepsilon_{p,j} \to \infty$, the stress asymptotically approaches a limit value C_i/γ_i. This means that the kinematic hardening process becomes saturated and the backstress cannot exceed $X_{i,\infty} = C_i/\gamma_i$.

If the loading direction is reversed at plastic strain ε_{p,N_1} and the corresponding backstress at ε_{p,N_1} is $X_{i,N_1} = X_{i,\infty}[1 - \exp(-\gamma_i \varepsilon_{p,N_1})]$, the subsequent evolution of backstress is given by

$$\begin{aligned} X_{i,j} &= -\frac{C_i}{\gamma_i} + \left(X_{i,N_1} + \frac{C_i}{\gamma_1} \right) \exp[\gamma_1(\varepsilon_{p,j} - \varepsilon_{p,N_1})] \\ &= -X_{i,\infty} + (X_{i,N_1} + X_{i,\infty}) \exp[\gamma_i(\varepsilon_{p,j} - \varepsilon_{p,N_1})]. \end{aligned} \tag{6}$$

Similarly denoting X_{i,N_2} and ε_{p,N_2} as the final values of $X_{i,j}$ and $\varepsilon_{p,j}$ for (6), the backstress at ε_{p,N_2} is

$$X_{i,N_2} = -X_{i,\infty} + (X_{i,N_1} + X_{i,\infty}) \exp[\gamma_i(\varepsilon_{p,N_2} - \varepsilon_{p,N_1})].$$

The evolution of the backstress from compression to tension is given as

$$
\begin{aligned}
X_{i,j} &= \frac{C_i}{\gamma_i} + \left(X_{i,N_2} - \frac{C_i}{\gamma_i}\right)\exp[-\gamma_i(\varepsilon_{p,j} - \varepsilon_{p,N_2})] \\
&= X_{i,\infty} + (X_{i,N_2} - X_{i,\infty})\exp[-\gamma_i(\varepsilon_{p,j} - \varepsilon_{p,N_2})].
\end{aligned}
\tag{7}
$$

By means of (7), the backstress from the compressive tip ε_{p,N_2} to the tensile endpoint ε_{p,N_3} can be calculated. Then, the backstress-strain response is determined with equations (5)–(7). Substituting the total backstress $X_j = \sum_{i=1}^{M} X_{i,j}$ into (4), the total simulated stress σ_j^{sim} can be identified. Thus, the simulated stresses can all be calculated with equations (4)–(7). It is convenient to obtain the backstress-strain curve because only algebraic calculations exist in the above-mentioned method.

It is difficult identifying a set of reasonable CHK-M model parameters when using the traditional trial-and-error method. The well-known L-M nonlinear least square algorithm is a good tool in determining optimal model parameters, especially for the nonlinear system employed in the current work.

In the optimization, the differences between the stress values from the numerical simulated stress σ_j^{sim} and experimental measured stress σ_j^{exp} are represented in the following objective function F:

$$
F = \tfrac{1}{2}\sum_{j=1}^{N}(\sigma_j^{\text{sim}} - \sigma_j^{\text{exp}})^2,
$$

where N is the total number of the data points used in the optimization. The optimum values can be determined when the objective function reaches the specified convergence criterion, which is set to $1 \cdot 10^{-6}$ in the current work. Referring to the rules suggested in [Bari and Hassan 2000], parameters C_1, C_2, and C_3 are all constrained within the range of 100 to $1 \cdot 10^8$. In addition, γ_1 and γ_2 are in the range of 1 to $1 \cdot 10^4$, and then the constraint interval for γ_3 is $[0.1, 6]$.

3. Study procedures

For the material 304SS, three groups of strain-controlled fatigue tests were performed at the material level, and the fatigue test at 0.8% strain amplitude was employed so as to identify the CHK-3 model parameters. Figure 1 is the detailed flow chart of the study procedures.

In Figure 1, the Ramberg–Osgood equation is applied to approximately represent the first quarter tensile part by using the L-M algorithm. After determining the parameters in the Ramberg–Osgood equation, the Chaboche kinematic hardening parameter C_i can be obtained by taking the derivative of the Ramberg–Osgood equation with plastic strain. Subsequently, the other relevant parameters γ_i can be predicted through allocating contribution percentages for every AF rule.

As indicated in [Dafalias et al. 2008], if the first quarter tensile segment includes a yield plateau that is significantly different from the hysteresis curve, then it is impossible to attempt to simulate all the curves by using one set of parameters. Conveniently, the first quarter tensile segment is used for estimating the initial parameters because $p = \varepsilon_p$ in the region and further optimizations can be performed to obtain more reasonable ones. Note that a reasonable initial yielding stress is beneficial for the stress-strain simulation. So the initial yielding stress and the hardening parameters for the first quarter tensile part was optimized in the current work. In order to verify the feasibility of these parameters for cyclic tests, the stress-strain response for the first cycle was simulated. Poor accuracy causes further optimization of
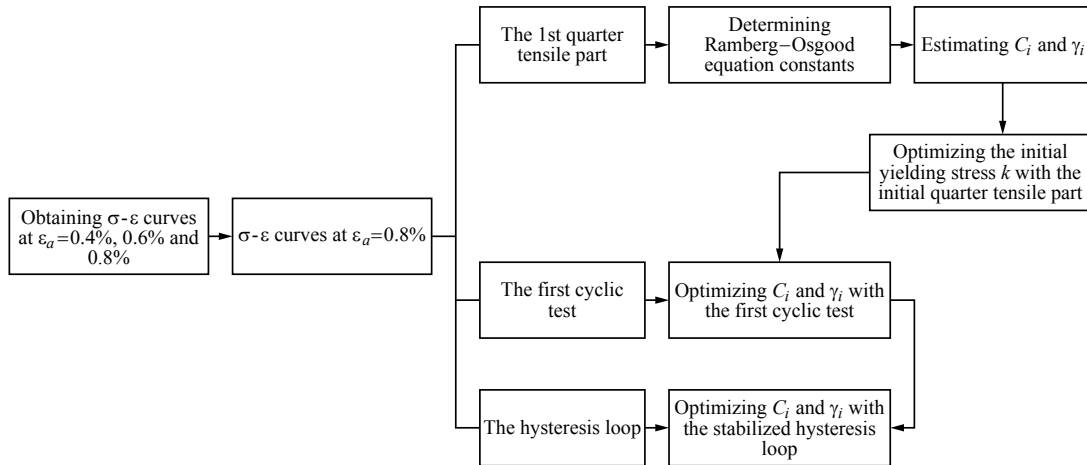
Figure 1. Study procedures of identifying CHK-3 model parameters.

parameters for the first cyclic test. Then, an investigation for the stabilized hysteresis loop was executed. As pointed out in previous literature [Bari and Hassan 2000; Ahmadzadeh and Varvani-Farahani 2013], the ratcheting parameter γ_3 in the third AF hardening rule should be constrained to a small range, such as [0.5, 10]. First, in order to verify the feasibility of the approach for the ratcheting simulation, the ratcheting parameter γ_3 was constrained within the interval from 0.1 to 6. Then, in order to improve the simulation accuracy for the stabilized hysteresis loop, the ratcheting parameter γ_3 was set to whatever the ratcheting strain is. Although the ratcheting issue was not included in the investigation, the ratcheting actually exists when using the parameters to perform a simulation.

4. Experimental testing

4.1. *Test specimen.* 304SS was chosen to verify the general method because it is cheap and it has extensive applications in industry. Table 1 shows the chemical composition of 304SS. In order to homogenize the 304SS material to obtain the expected mechanical properties, the steel ingots were forged into bars at 1160 °C. Then, an annealing treatment was performed by heating the bars up to 720 °C and cooling very slowly to room temperature. All experimental tests were conducted by using round-bar specimens. Figure 2 shows the test specimen.

4.2. *Test program.* Three groups of strain-controlled LCF tests were conducted, which were controlled by using the triangular waveform at a constant frequency of 0.25 Hz with a strain ratio $R_\varepsilon = -1$ and strain amplitude ε_a of 0.4%, 0.6%, and 0.8%. A 25 mm gauge extensometer was used for measuring and controlling the strain in the specimen and all tests were carried out according to the ASTM standard [ASTM

C	Si	Mn	P	S	C	Ni	Mo
≤ 0.08	≤ 1	≤ 2	≤ 0.045	≤ 0.03	> 17.03	> 8.01	> 0.02

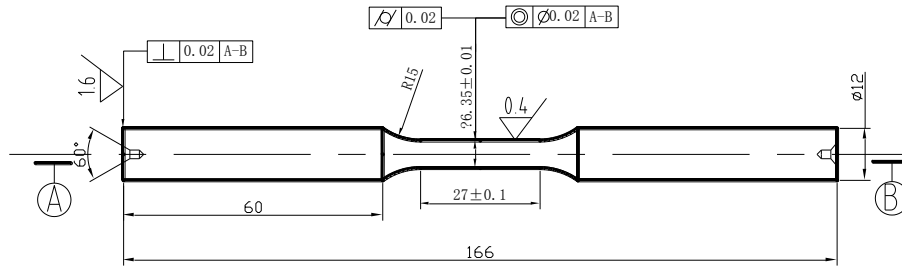**Table 1.** Chemical compositions of the 304 stainless steel (wt%).

Figure 2. Specimen geometry used for strain-controlled fatigue test.

E606/E606M 2012]. The experiments were conducted on multiple specimens; namely, each test was carried out at a constant strain amplitude until failure occurred at room temperature.

4.3. *Experimental results.* First, we should determine which hysteresis loop could be suitably used for this study. Typical cyclic tests at different strain amplitudes are shown in Figure 3, left. It can be seen from Figure 3, left, that the reasonable strain range for identifying the CHK-3 model parameters is ±0.8%, which ensures that the first and the second AF rules get stabilized within the strain limit, while the third one does not. Therefore, the experimental test at a strain range of ±0.8% was used to obtain the CHK-3 model parameters.

The Chaboche kinematic hardening model is closely related to the plasticity. So, determining the plastic stress-strain response becomes a critical step in identifying its parameters.

Conveniently, the initial tensile curve (the first quarter cycle), OA, was used to estimate the parameters. Equation (3) is readily dealt with because of the relationship $p = \varepsilon_p$ in this segment.

The aforementioned first cyclic test at strain amplitude of 0.8%, together with its plastic stress-strain curve is displayed in Figure 3, right. As shown in this figure, the Young's modulus E is taken as the slope of the initial linear region. After performing a regression analysis for segment OP, the Young's modulus E is approximately 183500 MPa with the correlation efficient of 0.99887.
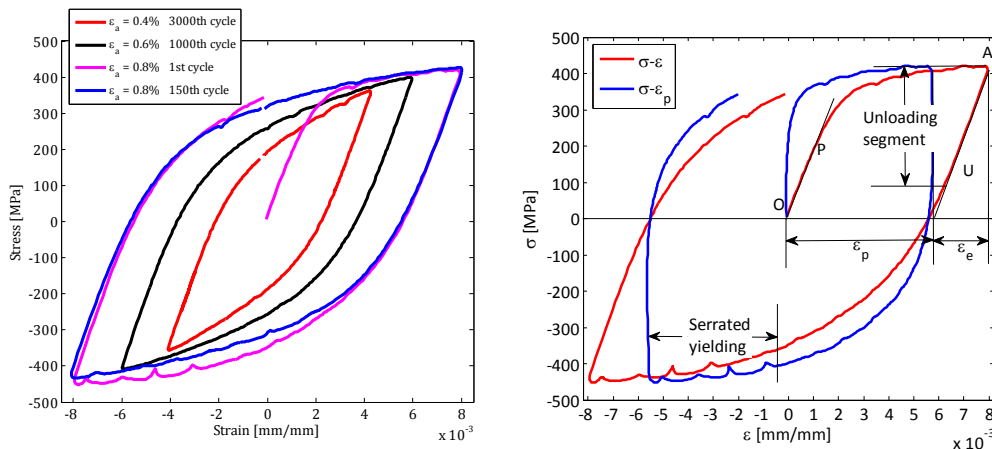

Figure 3. Left: LCF test results for 304 SS specimens. Right: The first cyclic test results at strain amplitude of 0.8%.

Some unreasonable problems exist, assuming all the plastic strain points are used to calculate the stress. The details are illustrated in the schematic diagram Figure 4. The Young's modulus E is the slope of the initial elastic loading segment OI. Theoretically, the plastic strain in OI is nearly equal to zero because of the relationship

$$\varepsilon_p = \varepsilon_T - \varepsilon_e = \varepsilon_T - \sigma/E = \varepsilon_T - \varepsilon_T = 0.$$

In addition, the test strain is portioned as

$$\varepsilon_T = \varepsilon_{th} + \varepsilon_{fl}.$$

In practice, the plastic strain in this region is not absolutely identical to zero due to the fluctuation. For example, the plastic strain in point B, ε_p^B, is negative because

$$\varepsilon_p^B = \varepsilon_T - \frac{\sigma_B}{E} = \varepsilon_T - \varepsilon_{th} = (\varepsilon_{th} + \varepsilon_{fl}) - \varepsilon_{th} = \varepsilon_{fl} < 0,$$

which leads to an unacceptable value when using (5) to simulate the backstress. This fact can be explained as follows:

$$X_{i,B} = \frac{C_i}{\gamma_i}[1 - \exp(\gamma_i \varepsilon_p^B)] < 0,$$

where $X_{i,B}$ is the backstress at point B. It is impossible that $X_{i,B}$ has a negative sign in the first quarter tensile part. Although the plastic strain in point A is positive, the simulated total stress at this point nearly equals the initial yielding stress, which will never approach the test stress. Therefore, points like A and B are called abnormal data in this investigation. In the elastic unloading part II-III, the ratio of ε_{fl} to ε_T is relatively small, which means the experimental plastic strain is very close to the theoretical. The theoretical plastic strain in II-III remains unchanged, as well-known. Thus, the simulated stress in II-III equals the stress at point II because such a small plastic strain fluctuation has little effect on
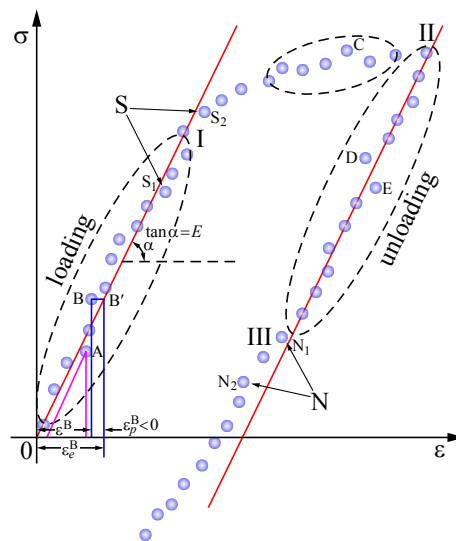

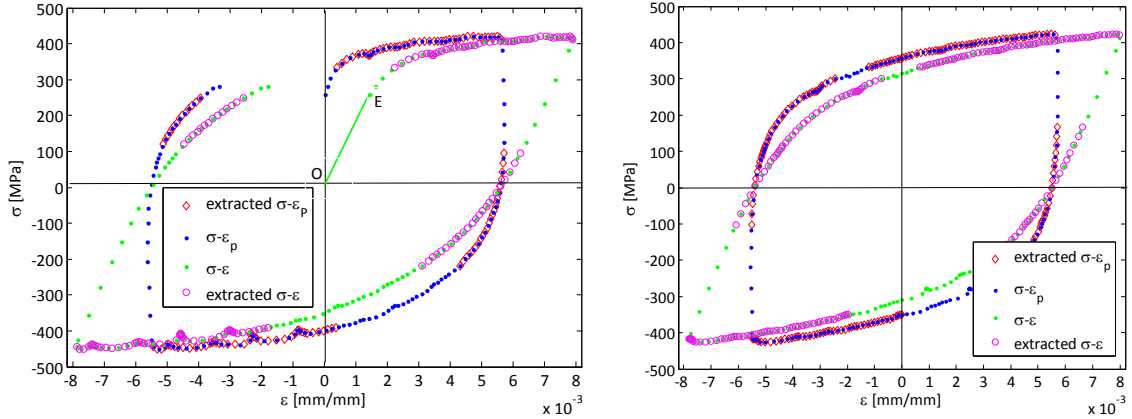**Figure 4.** Schematic diagram of the cyclic stress-strain test response.

Figure 5. The effective first (left) and 150th (right) cyclic test data used for optimization.

the simulation. However, the experimental stress in II-III is gradually decreasing. In all, the simulated stresses in the elastic loading/unloading segments are not appropriate for use in the proposed method. Note that although the plastic strain fluctuation occurs in I-II, the calculated stress is acceptable. This fact can be partly explained by the analysis for II-III, and the simulated stress has a good tendency toward the experimental in this region.

Fortunately, the L-M algorithm is excellent for identifying the model parameters by using the subsequence extracted from the original test data. So, the elastic segments are removed in the following optimization.

Figure 5 shows the effective test data used for optimization, which are extracted from the original first and the 150th cyclic test curves.

5. Estimation of the initial values for the model parameters

As discussed in Section 2, the CHK-M model is a superposition of different AF rules; namely, the total back stress is the summation of backstress components. The AF hardening rule follows a series of successive specific slopes which are defined by the derivatives of backstress plastic strain curve, and the slope of the curve of AF rule gradually approaches zero with increasing plastic strain. Thus, a certain AF rule in the CHK-M model has a primary role in a special strain range, which means the other rules have a slight effect on the shape of the σ-ε curve in this range. For example, provided that the shape of σ-ε curve in strain range $[0, 0.01\%]$ is determined by the first AF rule, the influence by other AF rules can be ignored. Similarly, the second AF rule influences the shape of the σ-ε curve in the strain range $[0.01\%, 0.03\%]$. As a result, we can differentiate the first quarter tensile curve with respect to the plastic strain at different strain points to estimate the parameters C_i.

In order to efficiently and conveniently calculate parameters C_i, the Ramberg–Osgood equation is applied for approximating the first quarter tensile curve:

$$\frac{\varepsilon_{\mathrm{T}}}{\varepsilon_0} = \frac{\sigma}{\sigma_0} + \left(\frac{\sigma}{\sigma_0}\right)^{n_0}. \tag{8}$$

The reason for using (8) to fit the first quarter tensile part is that the segment is similar to the mono-

tonic tensile curve. We use the following values for the Ramberg–Osgood constants of 304SS in the segment OA (strain amplitude of 0.8%):

$$n_0 = 5.3390, \quad \varepsilon_0 = 0.171\%, \quad \sigma_0 = 356 \text{MPa}.$$

In order to verify the feasibility of these constants, the simulated stress-strain relationship was obtained by using the Ramberg–Osgood equation and shown in Figure 6 together with the first cyclic experimental test curve.

As shown in Figure 6, there exists a slight deviation between the simulation and the experimental test, particularly at the knee part. This may be ascribed to the quick hardening behavior of 304SS. However, the simulated curve has a good tendency for the real stress-strain curve, so the Ramberg–Osgood curve can be applied to predict the initial values of CHK-3 model parameters.

After obtaining the Ramberg–Osgood constants, the relationship of $\varepsilon_0 = \sigma_0/E$ can be substituted into (8) to give

$$\frac{E\varepsilon_{\mathrm{T}}}{\sigma_0} = \frac{\sigma}{\sigma_0} + \left(\frac{\sigma}{\sigma_0}\right)^{n_0}, \tag{9}$$

which can then be differentiated with respect to ε_{T} to give

$$\frac{\mathrm{d}\sigma}{\mathrm{d}\varepsilon_{\mathrm{T}}} = \frac{\sigma_0}{\varepsilon_0(1 + n_0(\sigma/\sigma_0)^{n_0-1})}. \tag{10}$$

The calculation of $\mathrm{d}\sigma/\mathrm{d}\varepsilon_p$ is more complicated. First, $\mathrm{d}\sigma/\mathrm{d}\varepsilon_p$ must be changed into the form

$$\frac{\mathrm{d}\sigma}{\mathrm{d}\varepsilon_p} = \frac{\mathrm{d}\sigma}{\mathrm{d}\varepsilon_{\mathrm{T}}}\frac{\mathrm{d}\varepsilon_{\mathrm{T}}}{\mathrm{d}\varepsilon_p} = \frac{\mathrm{d}\sigma}{\mathrm{d}\varepsilon_{\mathrm{T}}}\frac{\mathrm{d}\varepsilon_{\mathrm{T}}/\mathrm{d}t}{\mathrm{d}\varepsilon_p/\mathrm{d}t} = \frac{\mathrm{d}\sigma}{\mathrm{d}\varepsilon_{\mathrm{T}}}\frac{1}{\dot{\varepsilon}_p}\dot{\varepsilon}_{\mathrm{T}}. \tag{11}$$

Using Hooke's law and the total strain relationship, $\mathrm{d}\varepsilon_p/\mathrm{d}t$ can be given as

$$\frac{\mathrm{d}\varepsilon_p}{\mathrm{d}t} = \frac{\mathrm{d}\varepsilon_{\mathrm{T}}}{\mathrm{d}t} - \frac{\mathrm{d}\sigma}{\mathrm{d}t}\frac{1}{E}. \tag{12}$$
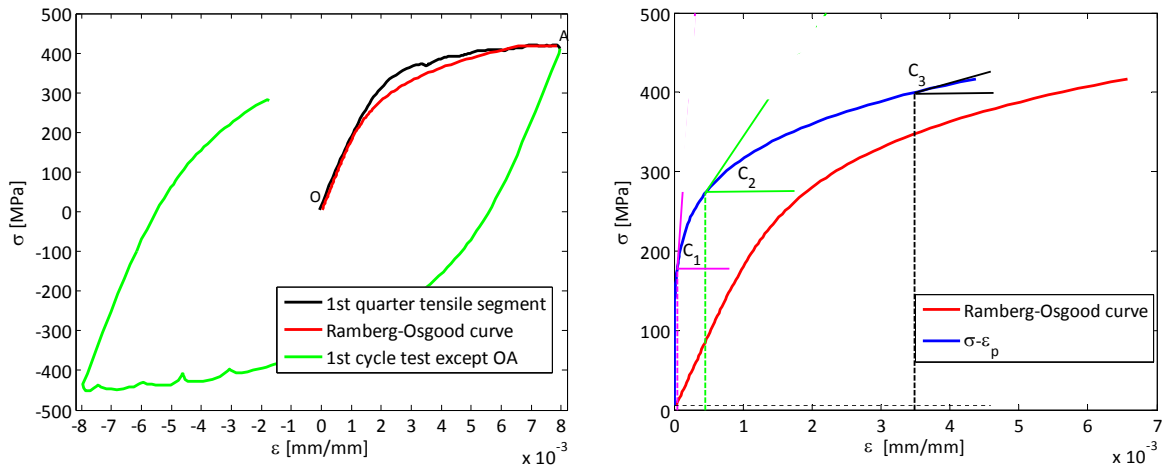

Figure 6. Left: comparison of the simulated Ramberg–Osgood curve and the first cyclic test curve. Right: The derivatives of the σ-ε_p curve at different points.

C_1	1249658.623	γ_1	42102.530
C_2	129813.037	γ_2	874.712
C_3	23817.112	γ_3	200.607

Table 2. Initial values of CHK-3 model parameters.

Then, (12) can be reformulated as

$$\frac{d\varepsilon_p}{dt} = \frac{d\varepsilon_T}{dt} - \frac{d\sigma}{dt}\frac{1}{E}\frac{d\varepsilon_T}{d\varepsilon_T} = \frac{d\varepsilon_T}{dt} - \frac{d\sigma}{d\varepsilon_T}\frac{1}{E}\frac{d\varepsilon_T}{dt} = \frac{d\varepsilon_T}{dt}\left(1 - \frac{d\sigma}{d\varepsilon_T}\frac{1}{E}\right). \tag{13}$$

So $\dot{\varepsilon}_p = \dot{\varepsilon}_T\big(1 - (d\sigma/d\varepsilon_T)(1/E)\big)$, which means $\dot{\varepsilon}_T/\dot{\varepsilon}_p = 1/\big(1 - (d\sigma/d\varepsilon_T)(1/E)\big)$.

The expression for $d\sigma/d\varepsilon_p$ can then be obtained expressed in terms of the derivative $d\sigma/d\varepsilon_T$ by substituting $\dot{\varepsilon}_T/\dot{\varepsilon}_p$ into (11):

$$\frac{d\sigma}{d\varepsilon_p} = \frac{d\sigma}{d\varepsilon_T}\frac{1}{1 - (1/E)(d\sigma/d\varepsilon_T)}. \tag{14}$$

Since the Young's modulus has been confirmed, the plastic stress-strain response can be determined with the relationship $\varepsilon_p = \varepsilon_T - \sigma/E$. Meanwhile, the slopes of the plastic stress-strain curve can also be given by (14). As a consequence, the tangent lines of the σ-ε_p curve can be identified, which are shown in Figure 6, right.

The AF rules contribution method, as described in [Rahman 2006], is applied for determining the parameters γ_i, which control the rate of the hardening modulus, which decreases with increasing plastic strain. In the tensile part, the total stress σ_x could be denoted by adding the summation of the backstresses of AF rules and the yield stress k, so the following relationship provides the reference for assigning the contribution fractions:

$$\frac{C_1}{\gamma_1} + \frac{C_2}{\gamma_2} + \left[\frac{C_3}{\gamma_3}\right] = \sigma_x - k. \tag{15}$$

Equation (15) indicates that the first and the second AF rule reach the saturated values before the testing strain attains its peak, while the third AF rule (embraced in a bracket) denotes that this component may not be up to its saturation value. The advantage of this strategy is that the first and the second AF rule respectively determine the shape of the initial and the knee part for the stress-strain curve; the third unsaturated AF rule controls the end part of the curve and the ratcheting strain evolution. Obviously, the right side of (15) can be readily determined. As a result, if the backstress contributions from each of the three AF rules in the left side of (15) can be determined, then the initial values of γ_1, γ_2, and γ_3 can be estimated. Following the data applied in [Rahman 2006], contribution fractions of 0.1, 0.5, and 0.3 are also applied for each of the three AF rules, respectively, in the current study.

Table 2 shows the initial values of CHK-3 model parameters estimated for the first quarter tensile part.

As illustrated above, the CHK-3 model parameters have been estimated successfully for the first quarter tensile segment, but in general, these parameters have poor accuracy for simulating the stabilized hysteresis loop, especially when the first quarter tensile segment includes a yield plateau. As depicted in Figure 3, right, one set of model parameters cannot be used to simultaneously simulate the first quarter tensile part and the hysteresis loops with high precision. Thus, the above model parameters can only be used as initial values for further optimization for the stabilized hysteresis loop.

6. Optimization of the model parameters

Two important factors, the kinematic hardening parameters and the initial yielding stress, have significant effects on the simulation. Based on the first quarter cycle, the initial yielding stress can be optimized with the CHK-3 model. It is well-known that the isotropic hardening rule will change the yield surface, which influences the shapes of the hysteresis loops. To identify the influence of the isotropic hardening on the model parameters, both the 150th cyclic test (the stabilized hysteresis loop) and the first cyclic test will be used for optimizing the CHK-3 model parameters, C_i, γ_i, and k.

6.1. *Optimization based on the first quarter tensile part.* The initial yielding stress definition, as pointed out by some authors [Facheris and Janssens 2014; Guijuan et al. 2014], has significant influence on the yield surface and the plastic flow directions. However, an exact definition for the yielding stress is not very clear at present. In [Abdel-Karim 2010], the author applied a smaller plastic strain offset (0.0025%) to determine the initial yielding stress. In the current work, the initial yielding stress (defined with a 0.02% plastic strain offset from the origin, where the initial yield stress is 232.251 MPa), serves as an initial value for optimization.

Because the CHK-3 model parameters will change with the alteration of the initial yielding stress, the following two steps are adopted in the optimization of the initial yielding stress:

(1) fixing C_i and γ_i to optimize k;

(2) fixing k to optimize C_i and γ_i.

Table 3 gives the optimal CHK-3 model parameters for the first quarter tensile curve. The optimized initial yielding stress is 181.392 MPa. Figure 7, left, shows the plastic stress strain response simulated by using the CHK-3 model with parameters before and after optimization. As a comparison, the first quarter tensile segment is also plotted in the figure.

Obviously, the simulated plastic stress-strain response produces a good agreement with the first tensile segment. In Figure 7, left, the calculated stress is always identical to zero when the plastic strain is substantially small and then it suddenly grows to the initial yielding stress k due to the large value of γ_1. This result proves that the aforementioned method is feasible.

6.2. *Optimization based on the first cyclic test.* In order to study the simulation capability of the initial values of the CHK-3 model parameters listed in Table 3 for the hysteresis loops, the cyclic plastic stress-strain response for the first cycle was calculated. Figure 7, right, shows the simulated plastic stress-strain response and the experimental test curve.

As illustrated in Figure 7, right, the shape of simulated plastic stress-strain response is remarkably different from the first cyclic test, especially at the transient portion. This can be attributed to the fact that the strain cycling leads to a decrease in the subsequent yielding stress when the first reverse occurs.

C_1	1444579.469	γ_1	21051.266
C_2	184230.879	γ_2	1749.424
C_3	22817.112	γ_3	278.154

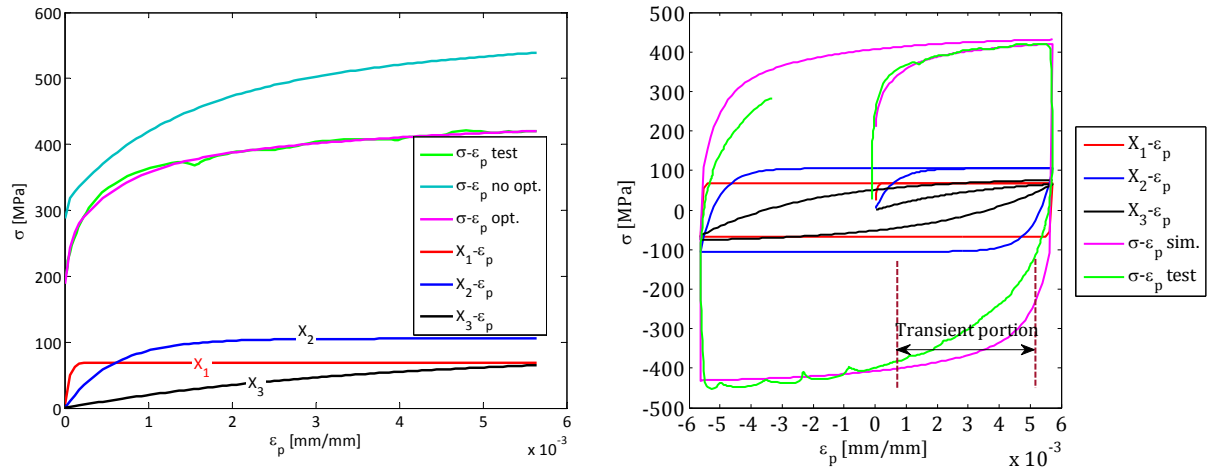**Table 3.** Optimum CHK-3 model parameters for the first quarter tensile curve.

Figure 7. Left: comparison of the first quarter tensile part and the plastic stress-strain response simulated with and without parameter optimization. Right: comparison of the first cyclic test and the simulated plastic stress-strain response.

Because the values in Table 3 are determined from the uniaxial tensile part, there inevitably exists an overestimation when using them to simulate the first cycle.

To reduce the overestimation, another optimization was conducted based on the initial values for the first cycle. The plastic strain used in equations (5)–(7) was calculated based on the effective data shown in Figure 5, left, and the initial yielding stress is set to 181 MPa. Table 4 shows the optimal values of the CHK-3 model parameters for the first cyclic test. The simulated σ-ε_p response as well as the first cyclic test curve is plotted in Figure 8, left.

As seen in that graph, the simulation is in a good agreement with the first cyclic test except at the first quarter tensile segment. This suggests that the first quarter tensile curve and the cyclic test curves may not possess the same set of kinematic parameters if they exhibit a significant difference in shape.
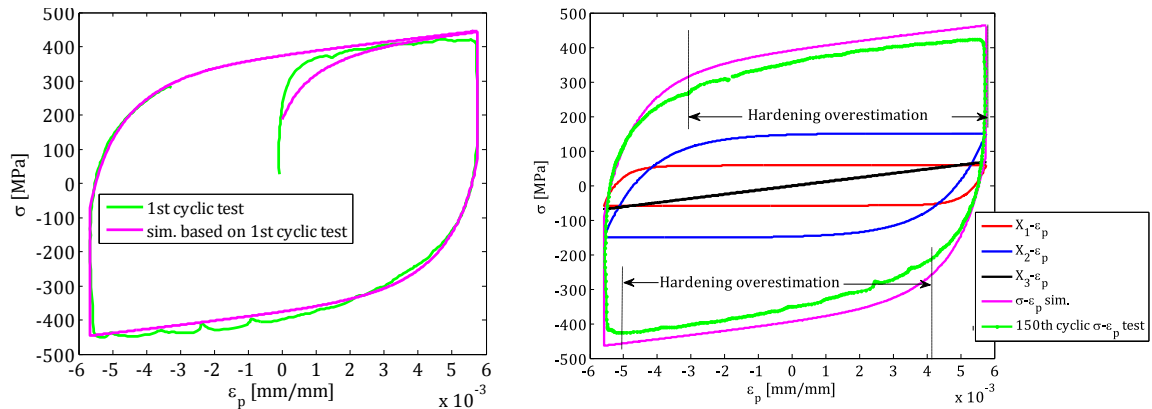

Figure 8. Left: comparison between the simulated σ-ε_p response and the first cyclic test. Right: comparison between the 150th cyclic test and σ-ε_p response simulated based on the parameters from Table 4.

The isotropic hardening could change the radius of the yield surface, causing the hysteresis loop to continuously change till it becomes the stabilized one. As a result, the kinematic hardening parameters will be different when respectively using the stable and unstable hysteresis loops to perform the parameter's optimization. To investigate these differences, a further optimization was executed with the stabilized hysteresis loop (the 150th cyclic test curve).

6.3. *Optimization based on the stabilized hysteresis loop.* The model parameters shown in Table 4 were used to simulate the stress-strain response for the stabilized hysteresis loop (the 150th cycle). Figure 8, right, gives the experimental σ-ε_p curve for the stabilized hysteresis loop and the σ-ε_p response simulated using the CHK-3 model with parameters listed in Table 4.

As shown in Figure 8, right, the simulated σ-ε_p curve exhibits a poor agreement with the 150th cyclic test. Qualitatively, the hardening overestimation in Figure 8, right, may be caused by the isotropic hardening. As analyzed in Section 6.2, the hysteresis loop continuously changes till it becomes a stabilized one due to the isotropic hardening effect. Consequently, the values of CHK-3 model parameters determined in Section 6.2 are not suitable for the stabilized hysteresis loop. Note that the cyclic softening occurs in the test. It is well-known, however, that 304SS should exhibit cyclic hardening under cyclic loading. The abnormal phenomenon may be ascribed to the high experimental frequency because an additional test at a frequency of 0.1 Hz exhibits the cyclic hardening effect; the additional test is displayed in Figure 9, left.

We thus draw the significant conclusion that the cyclic hardening behavior is rate-dependent. However, the method developed in this paper is feasible whatever the real material cyclic behavior.

C_1	122733.002	γ_1	3121.596
C_2	18641.186	γ_2	785.931
C_3	12127.629	γ_3	5.563

C_1	165362.400	γ_1	2372.604
C_2	80140.956	γ_2	834.633
C_3	18322.853	γ_3	0.111

Table 4. Optimal results of the CHK-3 model parameters for the first (left) and 150th (right) cyclic tests.
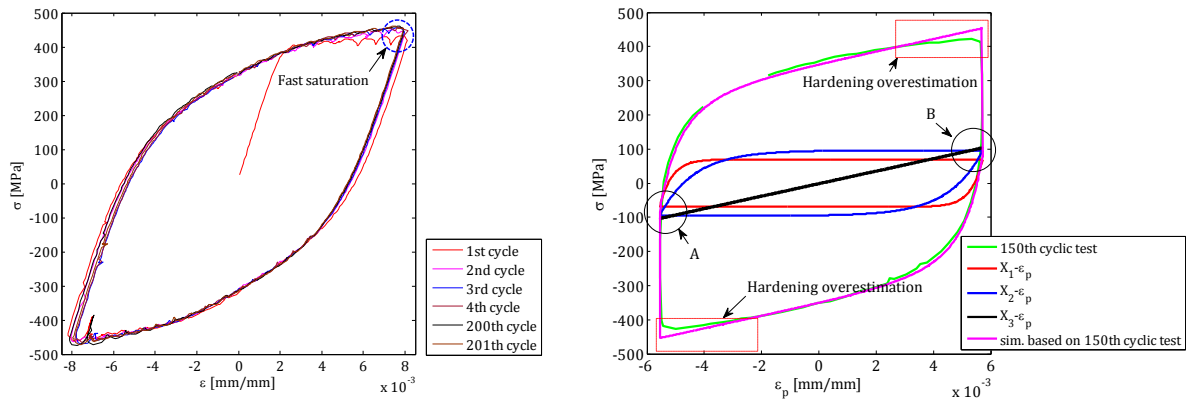

Figure 9. Left: stress-strain response at the strain-controlled test with test frequency of 0.1 Hz. Right: comparison between the 150th cyclic test and σ-ε_p response simulated based on the parameters from Table 4, right.

C_1	46318.993	γ_1	1501.795
C_2	80426.735	γ_2	1501.940
C_3	42612.671	γ_3	219.000

Table 5. CHK-3 model parameters optimized by fixing $\gamma_3 = 219$.

In the following optimization, the ratcheting parameter γ_3 was constrained to the range of 0.1 to 6 so as to meet the requirement for ratcheting simulation. Indeed, the reasonable value for γ_3 should be adjusted according to the ratcheting test, which has a slight effect on the hysteresis loop simulation. Table 4 also gives the optimized CHK-3 model parameters for the 150th experimental response.

Figure 9, right, shows the σ-ε_p response simulated with the CHK-3 model parameters from Table 4, right. For comparison, the 150th cyclic test curve is also plotted. We see that the simulation is in good agreement with experiments except at the regions near the peak of tension and the valley of compression. The fact is that the first and the second AF rule reach their saturated values before the relative plastic strain increases to a certain value, but the third AF rule does not. Thus, the hardening overestimation was closely associated with the third AF hardening rule.

The ratcheting parameter γ_3 has a significant effect on the ratcheting. As such, a reasonable value for γ_3 should be verified by the ratcheting test. In this investigation, we just want to verify the effect of γ_3 on the hysteresis loop. Accordingly, the reasonable ratcheting parameter for 304SS was not considered in a further optimization. Next, a special consideration for γ_3 was taken for obtaining a better simulation for the stabilized hysteresis loop.

As shown in Figure 9, right, hardening overestimation is ascribed to the fact that there exists a slow increasing/decreasing tendency in the third AF hardening rule. So, a larger value of γ_3 should be applied to increase its changing rate. To lower the effect of the third AF hardening rule on the hardening overestimation, a trial value of $\gamma_3 = 219$ was applied for an in-depth optimization.

The optimized values are given in Table 5. Figure 10 gives the σ-ε_p result calculated using the CHK-3
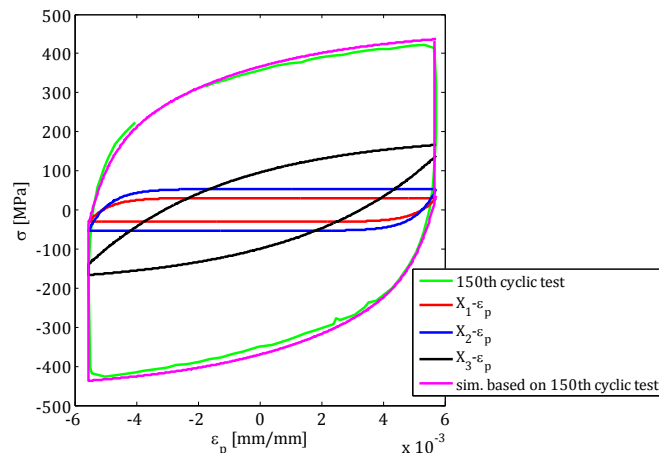

Figure 10. Comparison between the 150th cyclic test and σ-ε_p response simulated based on the parameters from Table 5.

model with the parameters given in Table 5. The 150th cyclic test is also plotted in the figure.

By comparing Figure 9, right, with Figure 10, we find that the simulation accuracy has been greatly improved by fixing the value of $\gamma_3 = 219$ to perform a new parameter optimization. As a consequence, the ratcheting parameter γ_3 actually has an effect on the hysteresis loop. Generally, however, a small change of γ_3 is enough to simulate the ratcheting evolution. Thus, the value of γ_3 for ratcheting is always assigned to a small value. The ratcheting parameter γ_3 in this work is not appropriate for ratcheting simulation, because a reasonable γ_3 should be verified through a further ratcheting test [Bari and Hassan 2000; Facheris and Janssens 2014]. Qualitatively, however, the parameters shown in Table 4, right, will be recommended for the ratcheting simulation, although they lead to a hardening overestimation.

7. Conclusions

The current work is devoted to identifying the CHK-3 model parameters with an algebraic calculation method based on its integral equations. The experimental test at strain range of $\pm 0.8\%$ was selected for optimizing the CHK-3 model parameters. The main conclusions for this paper are these:

(1) One same set of CHK-3 model parameters cannot ensure a same high precision when they are used simultaneously to simulate the stress-strain responses for both the first quarter tensile segment and the stabilized hysteresis loop.

(2) It is recommended removing the elastic loading/unloading segments from the experimental stress-strain curves before conducting an optimization of CHK-3 mode parameters.

(3) The initial yielding stress definition should be treated carefully for obtaining a good simulation. In this work, 232.251 MPa corresponding to 0.02% plastic strain offset was taken as the initial yielding stress, but after optimization, the reasonable initial yielding stress became around 181 MPa.

(4) The optimization procedure proposed can be applied generally to identify the CHK-3 model parameters for other similar metallic materials.

List of symbols

LCF	low cyclic fatigue
AF rule	Armstrong and Frederick kinematic hardening rule
LM algorithm	Levenberg–Marquardt algorithm
304SS	304 stainless steel
X_i	the i-th kinematic hardening rule
$C_i\ \gamma_i$	the ith Chaboche kinematic hardening parameters
E	Young's modulus
p	accumulated plastic strain
$\mathrm{d}p$	accumulated plastic strain rate
$\underset{\approx}{\varepsilon}_{\mathrm{T}}$	total strain tensor
$\dot{\underset{\approx}{\varepsilon}}_{\mathrm{T}}$	total strain rate
$\underset{\approx}{\varepsilon}_{p}$	plastic strain tensor
$\underset{\approx}{\varepsilon}_{px}$	plastic x-axial strain

$\dot{\underset{\approx}{\varepsilon}}_p$	plastic strain rate
$\underset{\approx}{\varepsilon}_e$	elastic strain tensor
$\underset{\approx}{\varepsilon}_a$	strain amplitude
$\underset{\approx}{X}$	backstress tensor
$\underset{\approx}{S}$	deviatoric stress tensor
k	initial yielding stress
σ_x	x-axial stress
X_x	x-axial backstress
$\sigma_0\ \varepsilon_0\ n_0$	Ramberg–Osgood constants
σ_i^{sim}	the i-th simulated stress
σ_i^{exp}	the i-th experimental stress
$\varepsilon_{\mathrm{th}}$	theoretical strain
$\varepsilon_{\mathrm{fl}}$	fluctuating strain

Acknowledgments

References

[Abdel-Karim 2010] M. Abdel-Karim, "An evaluation for several kinematic hardening rules on prediction of multiaxial stress-controlled ratcheting", *Int. J. Plast.* **26**:5 (2010), 711–730.

[Ahmadzadeh and Varvani-Farahani 2013] G. Ahmadzadeh and A. Varvani-Farahani, "Ratcheting assessment of materials based on the modified Armstrong–Frederick hardening rule at various uniaxial stress levels", *Fatigue Fract. Eng. Mater. Struct.* **36** (2013), 1232–1245.

[Armstrong and Frederick 1966] P. Armstrong and C. Frederick, "A mathematical representation of the multiaxial Bauscinger effect", CEGB Report RD/B/N731, 1966. Reproduced in *Materials at High Temperatures* **24**:1 (2007), 11–26.

[ASTM E606/E606M 2012] "Standard test method for strain-controlled fatigue testing", ASTM Standard E606/E606M, ASTM International, 2012.

[Bari and Hassan 2000] S. Bari and T. Hassan, "Anatomy of coupled constitutive models for ratcheting simulation", *Int. J. Plast.* **16** (2000), 381–409.

[Benham 1965] P. Benham, "Some observations on the cyclic strain-induced creep in mild steel at room temperature", *Int. J. Mech. Sci.* **7**:2 (1965), 81–86.

[Besson et al. 1998] J. Besson, R. Leriche, R. Foerch, and G. Cailletaud, "Object-oriented programming applied to the finite element method, II: Application to material behaviors", *Rev. Européenne Élém. Finis* **7**:5 (1998), 567–588.

[Chaboche 1986] J. Chaboche, "Time-independent constitutive theories for cyclic plasticity", *Int. J. Plast.* **2**:2 (1986), 149–188.

[Chaboche 1988] J. Chaboche, "Continuum damage mechanics, I: General concepts", *J. Appl. Mech.* (*ASME*) **55**:1 (1988), 55–64.

[Chaboche 1991] J. Chaboche, "On some modifications of kinematic hardening to improve the description of ratcheting effects", *Int. J. Plast.* **7**:7 (1991), 661–678.

[Chaboche 2008] J. Chaboche, "A review of some plasticity and viscoplasticity constitutive theories", *Int. J. Plast.* **24**:10 (2008), 1642–1693.

[Chaboche et al. 1979] J. Chaboche, K. Dang Van, and G. Cordier, "Modelization of the strain memory effect on the cyclic hardening of 316 stainless steel", art. id. L11/3 in *Transactions the 5th International Conference on Structural Mechanics in Reactor Technology* (Berlin, 1979), North-Holland, Amsterdam, 1979.

[Chaboche et al. 2012] J. Chaboche, P. Kanouté, and F. Azzouz, "Cyclic inelastic constitutive equations and their impact on the fatigue life predictions", *Int. J. Plast.* **35** (2012), 44–66.

[Dafalias et al. 2008] Y. Dafalias, K. Kourousis, and G. Saridis, "Multiplicative AF kinematic hardening in plasticity", *Int. J. Solids Struct.* **45**:10 (2008), 2861–2880.

[Djimli et al. 2010] L. Djimli, L. Taleb, and S. Meziani, "The role of the experimental data base used to identify material parameters in predicting the cyclic plastic response of an austenitic steel", *Int. J. Press. Vessels Pip.* **87**:4 (2010), 177–186.

[Egner and Egner 2014] H. Egner and W. Egner, "Modeling of a tempered martensitic hot work tool steel behavior in the presence of thermo-viscoplastic coupling", *Int. J. Plast.* **57** (2014), 77–91.

[Facheris and Janssens 2014] G. Facheris and K. Janssens, "An internal variable dependent constitutive cyclic plastic material description including ratcheting calibrated for AISI 316L", *Comput. Mater. Sci.* **87** (2014), 160–171.

[Guijuan et al. 2014] H. Guijuan, Z. Keshi, and M. Zhili, "Numerical analysis on subsequent yield surfaces and plastic flow direction of 45 steel by Chaboche model", *J. Guangxi Univ. Nat. Sci. Ed.* **39** (2014), 171–179. In Chinese.

[Jiang et al. 2009] Y. Jiang, W. Ott, C. Baum, M. Vormwald, and H. Nowack, "Fatigue life predictions by integrating EVICD fatigue damage model and an advanced cyclic plasticity theory", *Int. J. Plast.* **25**:5 (2009), 780–801.

[Jiang et al. 2013] X. Jiang, Y. Zhu, J. Hong, Y. Zhang, and Q. Kan, "Constitutive model for time-dependent ratcheting of SS304 stainless steel: simulation and its finite element analysis", *J. Méc. Théor. Appl.* **51**:1 (2013), 63–73.

[Kamaya and Kawakubo 2015] M. Kamaya and M. Kawakubo, "Loading sequence effect on fatigue life of type 316 stainless steel", *Int. J. Fatigue* **81** (2015), 10–20.

[Li et al. 2014] J. Li, C. Li, Y. Qiao, and Z. Zhang, "Fatigue life prediction for some metallic materials under constant amplitude multiaxial loading", *Int. J. Fatigue* **68** (2014), 10–23.

[Ohno and Wang 1994] N. Ohno and J. Wang, "Kinematic hardening rules for simulation of ratchetting behavior", *Eur. J. Mech. A Solids* **13**:4 (1994), 519–531.

[Pereira and Jesus 2011] H. Pereira and A. Jesus, "Fatigue modeling of a notched geometry under spectrum block loading supported on elastoplastic FEA", *Procedia Eng.* **10** (2011), 1354–1359.

[Prager 1956] W. Prager, "A new method of analyzing stresses and strains in work hardening plastic solids", *J. Appl. Mech. (ASME)* **23** (1956), 493–496.

[Rahman 2006] S. Rahman, *Finite element analysis and related numerical schemes for ratcheting simulation*, Ph.D. thesis, North California State University, 2006, available at http://www.lib.ncsu.edu/resolver/1840.16/5967.

[Taleb and Cailletaud 2010] L. Taleb and G. Cailletaud, "An updated version of the multimechanism model for cyclic plasticity", *Int. J. Plast.* **26**:6 (2010), 859–874.

[Velay et al. 2006] V. Velay, G. Bernhart, and L. Penazzi, "Cyclic behavior modeling of a tempered martensitic hot work tool steel", *Int. J. Plast.* **22**:3 (2006), 459–496.

[Voyiadjis and Basuroychowdhury 1998] G. Voyiadjis and I. Basuroychowdhury, "A plasticity model for multiaxial cyclic loading and ratcheting", *Acta Mech.* **126**:1 (1998), 19–35.

LIU SHIJIE: shi.jieliu@163.com
School of Astronautics, Beihang University (Beijing University of Aeronautics and Astronautics),
Xueyuan Road 37#, Haidian district, Beijing, Beijing, 100191, China

LIANG GUOZHU: lgz@buaa.edu.cn
School of Astronautics, Beihang University (Beijing University of Aeronautics and Astronautics),
Xueyuan Road 37#, Haidian district, Beijing, Beijing, 100191, China

msp

INTERFACIAL WAVES IN AN A/B/A PIEZOELECTRIC STRUCTURE WITH ELECTRO-MECHANICAL IMPERFECT INTERFACES

M. A. REYES, J. A. OTERO AND R. PÉREZ-ÁLVAREZ

We study the propagation of shear horizontal (SH) waves in the interfaces of an A/B/A piezoelectric structure with an electrical and mechanical imperfect contact, being modeled by means of a capacitor and a spring, respectively. The analytical dispersion relations are obtained and some limit cases are analyzed in detail, predicting the existence of interface waves. Based on numerical calculations, it can be shown that the electrical and mechanical imperfections strongly influence the dispersion curves.

1. Introduction

The possibility of an elastic shear surface wave being guided by the free surface of a piezoelectric crystal with 6 mm hexagonal symmetry has been studied in [Bleustein 1968].

Maerfeld and Tournois [1971] found that these kinds of waves can also be guided by the interface in perfect contact between two semi-infinite media, where at least one of these is a piezoelectric medium. Moreover, a shear horizontal (SH) wave propagating along an interface between a piezoelectric half-space and piezomagnetic half-space was investigated in [Soh and Liu 2006]. In [Fan et al. 2006b], imperfection was considered by means of a discontinuity of the displacement (spring model). An exact solution for antiplane waves in a ceramic half-space including an imperfectly bonded layer was obtained in [Fan et al. 2006a]. In [Chen et al. 2008], an exact solution for antiplane waves in a 6 mm crystal between two piezoceramic half-spaces with imperfect interface bonding was obtained. Furthermore, the effect of an electric field gradient on the SH interface waves was investigated in [Yang and Yang 2009]. The SH surface waves propagating in a layered piezoelectric half-space with an imperfectly bonded interface were studied in [Liu et al. 2010]. In [Sun et al. 2011], the SH wave propagation was studied in a cylindrical PE/PM structure with an imperfect interface and two exact dispersion relations were obtained. Dispersion relations of SH waves in an A/B/A heterostructure (which has different magnetic, electric and elastic properties with imperfect bonding at the surfaces) taking 6 mm hexagonal symmetry into account have been studied in great detail by Otero et al. [2011], giving some dispersion curves for different A/B/A heterostructures with magneto-electro-elastic properties and showing how strongly the behavior of these curves depends on the spring constant material parameter k_u (GPa/m). In [Otero et al. 2012], propagation of SH waves between the interfaces of two piezoelectric materials with electro-mechanical imperfect contacts modeled by means of a spring and a capacitor and the corresponding dispersion relations for the imperfect contact was presented.

Several works have been presented in order to study the effects of interface bonding on acoustic wave generation in elastic bodies using piezoelectric transducers driven electrically, as in [Li et al. 2013].

A coupling model for interfacial imperfection is proposed in [Li et al. 2015a] in order to characterize the imperfect interface in a bilayered multiferroic cylinder, and in [Li et al. 2016a] the SH wave propagation at the interface in a bilayered multiferroic is considered. In [Li and Jin 2015], the shear-lag interface model is used to simulate the effect of an imperfect interface on SH wave propagation in a piezoelectric composite structure. Trying to generalize the interfacial imperfection coupling model, Li et al. [2015b] introduced a new model to describe the magneto-electro-mechanical imperfect interfacial region in a multiferroic composite consisting of an FE layer and another FM layer. Xiong et al. [2015] proposed an interfacial sliding prevention/promotion model in order to consider the effect of interfacial normal stress on interfacial sliding and Li et al. [2015c; 2016b] proposed a generalization of the spring model while including intercoupling effects. Some authors, like Kakar [2015], have investigated the existence of SH waves in a fiber-reinforced layer placed over a heterogeneous elastic half-space. Kong et al. [2016] studied the propagation of SH waves in the layered structure consisting of a transversely isotropic FGPM layer and a PMN-0.29PT substrate that is being poled along [011]c, finding that the dispersion characteristics of the SH waves are dominated by the cut orientation of the PE substrate.

In the present work, different to the work of Otero et al. [2011], we consider the existence of two imperfections at the interfaces on an A/B/A piezoelectric structure: electrical and mechanical. The presence of electrical and mechanical imperfections are modeled by means of a capacitor and a spring, respectively. The capacity of the capacitor is the measure of the electrical imperfection.

This paper is organized as follows: in Section 2 the equations governing the SH wave propagating in piezoelectric materials with 6 mm hexagonal symmetry and the constitutive relations are presented. Section 3 is dedicated to the general formulation of the main problem, considering two types of imperfections at the interfaces. Symmetric and antisymmetric solutions are obtained for a specific system. Section 4 is devoted to calculating the dispersion relations, and some limiting cases are analyzed. These results are in agreement with known results from the literature. In Section 5 some numerical examples are shown and analyzed. Finally, in Section 6 some conclusions are presented.

2. Governing equations for the SH mode

A system of two coupled partial differential equations with two unknowns: the z component of the elastic displacement u_z and the in-plane electric potential φ, describe SH waves in this type of material; that is,

$$c\nabla^2 u + e\nabla^2\varphi = \rho\frac{\partial^2 u}{\partial t^2}, \qquad (2\text{-}1)$$

$$e\nabla^2 u - \varepsilon\nabla^2\varphi = 0, \qquad (2\text{-}2)$$

where $\nabla^2 \equiv \partial^2/\partial x^2 + \partial^2/\partial y^2$ and $u \equiv u_z$. Here, $c \equiv c_{44}$, $e \equiv e_{15}$, $\varepsilon \equiv \varepsilon_{11}$ are the elastic, piezoelectric, and dielectric permittivity coefficients, respectively. For the case of SH waves, both components u_x and u_y are equal to zero. Equations (2-1)–(2-2), which depend only on (x, y, t), describe the motion of a SH wave in a homogeneous material. Firstly, we have to rewrite (2-1)–(2-2) using an auxiliary potential function ϕ defined by

$$\phi = \varphi - \frac{e}{\varepsilon}u. \qquad (2\text{-}3)$$

Then, (2-1) can be written as

$$\left(\nabla^2 - \frac{1}{\bar{v}^2}\frac{\partial^2}{\partial t^2}\right)u = 0, \tag{2-4}$$

where $\bar{v} = \sqrt{\bar{c}/\rho}$ is the bulk shear wave speed within the piezoelectric and $\bar{c} = c + e^2/\varepsilon$ is the electro-elastically stiffened constant. Secondly, (2-2) can be written as

$$\nabla^2\phi = 0. \tag{2-5}$$

3. SH waves in piezoelectrics

Consider a piezoelectric material with 6 mm hexagonal symmetry exhibiting polarization in the z-axis direction of an xyz Cartesian coordinate system and the xy plane is an isotropy plane. The planes $y = \pm\frac{1}{2}d$ are the interfaces. The spaces $y < -\frac{1}{2}d$ and $y > \frac{1}{2}d$ are occupied by a piezoelectric of type A and the region enclosed in the interval $[-\frac{1}{2}d, \frac{1}{2}d]$ by a piezoelectric of type B, as shown in Figure 1.

We want to find u and ϕ describing SH waves propagating along the positive x axis that satisfy (2-4) and (2-5) at each interface of the piezoelectric structure. We are really interested in finding confined modes, which is why the functions u and ϕ in media A should vanish as y goes to $\pm\infty$. This in turn implies that at these interfaces the solutions of (2-4) and (2-5) must be of the form

$$u_s = e^{i(\xi x - \omega t)}\begin{cases} U_A e^{\eta_A y} & \text{if } y < -\frac{1}{2}d, \\ U_B \cos(\eta_B y) & \text{if } |y| \leq \frac{1}{2}d, \\ U_A e^{-\eta_A y} & \text{if } y > \frac{1}{2}d, \end{cases} \tag{3-1}$$

for the symmetric modes in y, and

$$u_{as} = e^{i(\xi x - \omega t)}\begin{cases} U_{A1} e^{\eta_A y} & \text{if } y < -\frac{1}{2}d, \\ U_{B1} \sin(\eta_B y) & \text{if } |y| \leq \frac{1}{2}d, \\ -U_{A1} e^{-\eta_A y} & \text{if } y > \frac{1}{2}d, \end{cases} \tag{3-2}$$

for the antisymmetric modes in y, where U_A, U_B, U_{A1}, and U_{B1} are undetermined constants. Here, ω, ξ, and η are the frequency, the x-component of the wave vector, and the y-component of the wave vector,
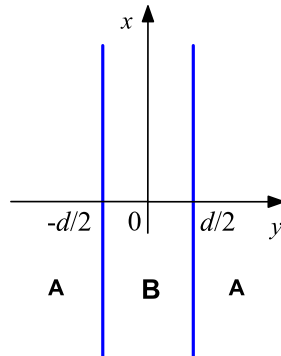

Figure 1. Scheme of a piezoelectric structure A/B/A.

respectively, which are related to each other through the expressions

$$
\begin{aligned}
\eta_A &= \xi \sqrt{(1 - v^2/\bar{v}_A^2)} > 0, \quad |y| \geq \tfrac{1}{2}d, \\
\eta_B &= \xi \sqrt{(v^2/\bar{v}_B^2 - 1)} > 0, \quad |y| \leq \tfrac{1}{2}d,
\end{aligned}
\tag{3-3}
$$

where $v = \omega/\xi$ is the phase velocity. Using the above considerations, we obtain

$$
\phi_s = e^{i(\xi x - \omega t)}
\begin{cases}
\Phi_A e^{\xi y} & \text{if } y < -\tfrac{1}{2}d, \\
\Phi_B \cosh(\xi y) & \text{if } |y| \leq \tfrac{1}{2}d, \\
\Phi_A e^{-\xi y} & \text{if } y > \tfrac{1}{2}d,
\end{cases}
\tag{3-4}
$$

for the symmetric modes in y, and

$$
\phi_{as} = e^{i(\xi x - \omega t)}
\begin{cases}
\Phi_{A1} e^{\xi y} & \text{if } y < -\tfrac{1}{2}d, \\
\Phi_{B1} \sinh(\xi y) & \text{if } |y| \leq \tfrac{1}{2}d, \\
-\Phi_{A1} e^{-\xi y} & \text{if } y > \tfrac{1}{2}d,
\end{cases}
\tag{3-5}
$$

for the antisymmetric modes in y, where Φ_A, Φ_B, Φ_{A1}, and Φ_{B1} are undetermined constants.

4. Dispersion relations

Now, the stress component $T \equiv T_{zy}$ and the electric displacement $D \equiv D_y$ are related to u and ϕ by

$$
T = c \frac{\partial u}{\partial y} + e \frac{\partial \varphi}{\partial y}, \quad D = e \frac{\partial u}{\partial y} - \varepsilon \frac{\partial \varphi}{\partial y}.
\tag{4-1}
$$

It is convenient to express (4-1) using the potential function ϕ, which leads to the following expressions:

$$
T = \bar{c} \frac{\partial u}{\partial y} + e \frac{\partial \phi}{\partial y}, \quad D = -\varepsilon \frac{\partial \phi}{\partial y}.
\tag{4-2}
$$

Substituting (3-1) and (3-4) into (2-3), the symmetric parts of the electric potential are written as

$$
\varphi_s = e^{i(\xi x - \omega t)}
\begin{cases}
e_A/\varepsilon_A U_A e^{\eta_A y} + \Phi_A e^{\xi y} & \text{if } y < -\tfrac{1}{2}d, \\
e_B/\varepsilon_B U_B \cos(\eta_B y) + \Phi_B \cosh(\xi y) & \text{if } |y| \leq \tfrac{1}{2}d, \\
e_A/\varepsilon_A U_A e^{-\eta_A y} + \Phi_A e^{-\xi y} & \text{if } y > \tfrac{1}{2}d.
\end{cases}
\tag{4-3}
$$

Substituting (3-1) and (3-4) into (4-2), we get the following expressions for the symmetric part of T and D:

$$
T_s = e^{i(\xi x - \omega t)}
\begin{cases}
U_A \bar{c}_A \eta_A e^{\eta_A y} + \Phi_A \xi e^{\xi y} & \text{if } y < -\tfrac{1}{2}d, \\
-U_B \bar{c}_B \eta_B \sin(\eta_B y) + \Phi_B e_B \xi \sinh(\xi y) & \text{if } |y| \leq \tfrac{1}{2}d, \\
-U_A \bar{c}_A \eta_A e^{-\eta_A y} - \Phi_A e_A \xi e^{-\xi y} & \text{if } y > \tfrac{1}{2}d,
\end{cases}
\tag{4-4}
$$

$$
D_s = e^{i(\xi x - \omega t)}
\begin{cases}
-\Phi_A \varepsilon_A \xi e^{\xi y} & \text{if } y < -\tfrac{1}{2}d, \\
-\Phi_B \varepsilon_B \xi \sinh(\xi y) & \text{if } |y| \leq \tfrac{1}{2}d, \\
\Phi_A \varepsilon_A \xi e^{-\xi y} & \text{if } y > \tfrac{1}{2}d.
\end{cases}
\tag{4-5}
$$

Analogously, we get the following expressions for the antisymmetric part of T and D:

$$T_{as} = e^{i(\xi x - \omega t)} \begin{cases} U_{A1}\bar{c}_A \eta_A e^{\eta_A y} + \Phi_{A1}\xi e^{\xi y} & \text{if } y < -\tfrac{1}{2}d, \\ U_{B1}\bar{c}_B \eta_B \cos(\eta_B y) + \Phi_{B1} e_B \xi \cosh(\xi y) & \text{if } |y| \le \tfrac{1}{2}d, \\ U_{A1}\bar{c}_A \eta_A e^{-\eta_A y} + \Phi_{A1} e_A \xi e^{-\xi y} & \text{if } y > \tfrac{1}{2}d, \end{cases} \tag{4-6}$$

$$D_{as} = e^{i(\xi x - \omega t)} \begin{cases} -\Phi_{A1}\varepsilon_A \xi e^{\xi y} & \text{if } y < -\tfrac{1}{2}d, \\ -\Phi_{B1}\varepsilon_B \xi \cosh(\xi y) & \text{if } |y| \le \tfrac{1}{2}d, \\ \Phi_{A1}\varepsilon_A \xi e^{-\xi y} & \text{if } y > \tfrac{1}{2}d. \end{cases} \tag{4-7}$$

4A. *The symmetric part.* Let us build the equations that satisfy the condition for the electro-mechanical imperfect contact at $y = -\tfrac{1}{2}d$ using the symmetric part of the solution. First,

$$T_A = k_u (u_A - u_B)$$

describes an elastic interface with spring constant material parameter $k_u > 0$. Then, we get

$$U_A(\bar{c}_A \eta_A - k_u)e^{-d\eta_A/2} + \Phi_A e_A \xi e^{-d\xi/2} + U_B k_u \cos\left(\tfrac{1}{2}d\eta_B\right) = 0, \tag{4-8}$$

with the second condition

$$T_B = k_u (u_A - u_B),$$

therefore we get

$$-U_A k_u e^{-d\eta_A/2} + U_B\left(\bar{c}_B \eta_B \sin\left(\tfrac{1}{2}d\eta_B\right) + k_u \cos\left(\tfrac{1}{2}d\eta_B\right)\right) - \Phi_B e_B \xi \sin\left(\tfrac{1}{2}d\xi\right) = 0. \tag{4-9}$$

The third condition,

$$D_A = k_\phi\left(\phi_A + \frac{e_A}{\varepsilon_A}u_A - \phi_B - \frac{e_B}{\varepsilon_B}u_B\right),$$

describes an electric interface with electric capacitor parameter $k_\varphi > 0$, i.e., if the electric potential at the interface is discontinuous, we get

$$-\frac{e_A}{\varepsilon_A}U_A k_\varphi e^{-d\eta_A/2} - \Phi_A(\varepsilon_A \xi + k_\varphi)e^{-d\xi/2} + \frac{e_B}{\varepsilon_B}U_B k_\varphi \cos\left(\tfrac{1}{2}d\eta_B\right) + \Phi_B k_\varphi \cos\left(\tfrac{1}{2}d\xi\right) = 0. \tag{4-10}$$

Using the fourth condition,

$$D_B = k_\varphi\left(\phi_A + \frac{e_A}{\varepsilon_A}u_A - \phi_B - \frac{e_B}{\varepsilon_B}u_B\right),$$

we obtain

$$-\frac{e_A}{\varepsilon_A}U_A k_\varphi e^{-d\eta_A/2} - \Phi_A k_\varphi e^{-d\xi/2} + \frac{e_B}{\varepsilon_B}U_B k_\varphi \cos\left(\tfrac{1}{2}d\eta_B\right)$$

$$+ \Phi_B\left(\varepsilon_B \xi \sinh\left(\tfrac{1}{2}d\xi\right) + k_\varphi \cosh\left(\tfrac{1}{2}d\xi\right)\right) = 0. \tag{4-11}$$

The set of equations (4-8)–(4-11) is a homogeneous system of linear algebraic equations for U_A, U_B, Φ_A, and Φ_B. In order to obtain nontrivial solutions, the determinant of the matrix formed by this system

of equations should be zero, and it can be simplified to

$$
\begin{vmatrix}
e_A\xi & 0 & \bar{c}_A\eta_A - k_u & k_u\cos\left(\frac{1}{2}\mathrm{d}\eta_B\right) \\
0 & -e_B\xi\sin\left(\frac{1}{2}\mathrm{d}\xi\right) & -k_u & \bar{c}_B\eta_B\sinh\left(\frac{1}{2}\mathrm{d}\eta_B\right) + k_u\cos\left(\frac{1}{2}\mathrm{d}\eta_B\right) \\
-\varepsilon_A\xi - k_\varphi & k_\varphi\cosh\left(\frac{1}{2}\mathrm{d}\xi\right) & -e_A/\varepsilon_A\, k_\varphi & e_B/\varepsilon_B\, k_\varphi\cos\left(\frac{1}{2}\mathrm{d}\eta_B\right) \\
-k_\varphi & \varepsilon_B\xi\sinh\left(\frac{1}{2}\mathrm{d}\xi\right) + k_\varphi\cosh\left(\frac{1}{2}\mathrm{d}\xi\right) & -e_A/\varepsilon_A\, k_\varphi & e_B/\varepsilon_B\, k_\varphi\cos\left(\frac{1}{2}\mathrm{d}\eta_B\right)
\end{vmatrix}.
$$

This determinant leads us to the following dispersion relations for the symmetric modes:

$$
P_A P_B - Q^2 + k_u(P_A + P_B + 2Q) = 0,
$$

where

$$
P_A = -\bar{c}_A\left(\eta_A - \xi\gamma_\phi\frac{M_A^2}{\varepsilon_A}\right), \quad P_B = \bar{c}_B\left(\eta_B\tan\left(\frac{1}{2}\mathrm{d}\eta_B\right) + \xi\gamma_\phi\frac{M_B^2}{\varepsilon_B}\right),
$$

$$
Q = -\xi\gamma_\phi\left(\frac{e_A e_B}{\varepsilon_A\varepsilon_B}\right), \qquad \gamma_\phi = \frac{k_\varphi}{\xi + k_\varphi\left(1/\varepsilon_A + 1/\varepsilon_B\coth\left(\frac{1}{2}\mathrm{d}\xi\right)\right)},
$$

$$
M_A^2 = \frac{e_A^2}{\bar{c}_A\varepsilon_A}, \qquad M_B^2 = \frac{e_B^2}{\bar{c}_B\varepsilon_A}.
$$

4B. *The antisymmetric part.* We now build the equations that satisfy the condition for the electromechanical imperfect contact at $y = -\frac{1}{2}d$ using the antisymmetric part of the solution.

The first condition,

$$
T_A = k_u(u_A - u_B),
$$

describes an elastic interface with spring constant material parameter $k_u > 0$. Then, we get

$$
U_{A1}(\bar{c}_A\eta_A - k_u)e^{-\mathrm{d}\eta_A/2} + \Phi_{A1}e_A\xi e^{-\mathrm{d}\xi/2} - U_{B1}k_u\sin\left(\frac{1}{2}\mathrm{d}\eta_B\right) = 0. \tag{4-12}
$$

With the second condition,

$$
T_B = k_u(u_A - u_B),
$$

we get

$$
-U_{A1}k_u e^{-\mathrm{d}\eta_A/2} + U_{B1}\left(\bar{c}_B\eta_B\cos\left(\frac{1}{2}\mathrm{d}\eta_B\right) - k_u\sin\left(\frac{1}{2}\mathrm{d}\eta_B\right)\right) + \Phi_{B1}e_B\xi\cosh\left(\frac{1}{2}\mathrm{d}\xi\right) = 0. \tag{4-13}
$$

The third condition,

$$
D_A = k_\varphi\left(\phi_A + \frac{e_A}{\varepsilon_A}u_A - \phi_B - \frac{e_B}{\varepsilon_B}u_B\right),
$$

describes an electric interface with an electric capacitor parameter $k_\varphi > 0$, i.e., the electric potential at the interface must be discontinuous, so we obtain

$$
-\frac{e_A}{\varepsilon_A}U_{A1}k_\varphi e^{-\mathrm{d}\eta_A/2} - \Phi_{A1}(\varepsilon_A\xi + k_\varphi)e^{-\mathrm{d}\xi/2} - \frac{e_B}{\varepsilon_B}U_{B1}k_\varphi\sin\left(\frac{1}{2}\mathrm{d}\eta_B\right) - \Phi_{B1}k_\varphi\sinh\left(\frac{1}{2}\mathrm{d}\xi\right) = 0. \tag{4-14}
$$

Using the fourth condition,

$$
D_B = k_\varphi\left(\phi_A + \frac{e_A}{\varepsilon_A}u_A - \phi_B - \frac{e_B}{\varepsilon_B}u_B\right),
$$

we obtain,

$$\frac{e_A}{\varepsilon_A} U_{A1} k_\varphi e^{-\mathrm{d}\eta_A/2} \Phi_{A1} k_\varphi e^{-\mathrm{d}\xi/2} + \frac{e_B}{\varepsilon_B} U_{B1} k_\varphi \sin\left(\tfrac{1}{2}\mathrm{d}\eta_B\right)$$
$$+ \Phi_{B1}\left(\varepsilon_B \xi \cosh\left(\tfrac{1}{2}\mathrm{d}\xi\right) + k_\varphi \sinh\left(\tfrac{1}{2}\mathrm{d}\xi\right)\right) = 0. \quad (4\text{-}15)$$

The set of equations (4-12)–(4-15) is a homogeneous system of linear algebraic equations for U_A, U_B, Φ_A, and Φ_B. In order to obtain nontrivial solutions, the determinant of the matrix formed by this system of equations should be zero, and it can be simplified to

$$\begin{vmatrix} e_A \xi & 0 & \bar{c}_A \eta_A - k_u & -k_u \sin\left(\tfrac{1}{2}\mathrm{d}\eta_B\right) \\ 0 & e_B \xi \cosh\left(\tfrac{1}{2}\mathrm{d}\xi\right) & -k_u & \bar{c}_B \eta_B \cos\left(\tfrac{1}{2}\mathrm{d}\eta_B\right) - k_u \sin\left(\tfrac{1}{2}\mathrm{d}\eta_B\right) \\ -\varepsilon_A \xi - k_\varphi & -k_\varphi \sinh\left(\tfrac{1}{2}\mathrm{d}\xi\right) & -e_A/\varepsilon_A k_\varphi & -e_B/\varepsilon_B k_\varphi \sin\left(\tfrac{1}{2}\mathrm{d}\eta_B\right) \\ -k_\varphi & -\varepsilon_B \xi \cosh\left(\tfrac{1}{2}\mathrm{d}\xi\right) - k_\varphi \sinh\left(\tfrac{1}{2}\mathrm{d}\xi\right) & -e_A/\varepsilon_A k_\varphi & -e_B/\varepsilon_B k_\varphi \sin\left(\tfrac{1}{2}\mathrm{d}\eta_B\right) \end{vmatrix}.$$

This determinant leads us to the following dispersion relations for the antisymmetric modes:

$$P_A P_B - Q^2 + k_u(P_A + P_B + 2Q) = 0,$$

where

$$P_A = -\bar{c}_A\left(\eta_A - \xi A\gamma_\phi \frac{M_A^2}{\varepsilon_A}\right), \qquad P_B = \bar{c}_B\left(\eta_B \tan\left(\tfrac{1}{2}\mathrm{d}\eta_B\right) + \xi A\gamma_\phi \frac{M_B^2}{\varepsilon_B}\right),$$

$$Q = -\xi A\gamma_\phi\left(\frac{e_A e_B}{\varepsilon_A \varepsilon_B}\right), \qquad A\gamma_\phi = \frac{k_\varphi}{\xi + k_\varphi\left(1/\varepsilon_A + 1/\varepsilon_B \tanh\left(\tfrac{1}{2}\mathrm{d}\xi\right)\right)},$$

$$M_A^2 = \frac{e_A^2}{\bar{c}_A \varepsilon_A}, \qquad M_B^2 = \frac{e_B^2}{\bar{c}_B \varepsilon_A}.$$

5. Limit cases

Let us consider the following limit cases for the symmetric part:

(1) The interface has partial electrical interaction but has no mechanical interaction:

$$k_u \to 0, \quad 0 < k_\varphi < \infty,$$

$$\sqrt{1 - v^2/\bar{v}_A^2}\sqrt{v^2/\bar{v}_B^2 - 1}\tan\left(\tfrac{1}{2}\mathrm{d}\xi\sqrt{v^2/\bar{v}_B^2 - 1}\right) + \gamma_\phi \frac{M_B^2}{\varepsilon_B}\sqrt{1 - v^2/\bar{v}_A^2}$$
$$- \gamma_\phi \frac{M_A^2}{\varepsilon_A}\sqrt{v^2/\bar{v}_B^2 - 1}\tan\left(\tfrac{1}{2}\mathrm{d}\xi\sqrt{v^2/\bar{v}_B^2 - 1}\right) = 0.$$

(2) The interface has perfect electrical interaction but has no mechanical interaction:

$$k_u \to 0, \quad k_\varphi \to \infty,$$

$$\sqrt{1 - v^2/\bar{v}_A^2}\sqrt{v^2/\bar{v}_B^2 - 1}\tan\left(\tfrac{1}{2}\mathrm{d}\xi\sqrt{v^2/\bar{v}_B^2 - 1}\right) + \frac{M_B^2}{\varepsilon_B/\varepsilon_A + \coth\left(\tfrac{1}{2}\mathrm{d}\xi\right)}\sqrt{1 - v^2/\bar{v}_A^2}$$
$$- \frac{M_A^2}{1 + \varepsilon_A/\varepsilon_B \coth\left(\tfrac{1}{2}\mathrm{d}\xi\right)}\sqrt{v^2/\bar{v}_B^2 - 1}\tan\left(\tfrac{1}{2}\mathrm{d}\xi\sqrt{v^2/\bar{v}_B^2 - 1}\right) = 0.$$

(3) The interface has neither mechanical nor electrical interaction:

$$k_u \to 0, \quad k_\varphi \to 0,$$

$$\sqrt{1 - v^2/\bar{v}_A^2}\sqrt{v^2/\bar{v}_B^2 - 1}\tan\left(\tfrac{1}{2}\mathrm{d}\xi\sqrt{v^2/\bar{v}_B^2 - 1}\right) = 0 \to \sin\left(\tfrac{1}{2}\mathrm{d}\xi\sqrt{v^2/\bar{v}_B^2 - 1}\right) = 0,$$

$$\tfrac{1}{4}\mathrm{d}^2\xi^2\left(v^2/\bar{v}_B^2 - 1\right) = n^2\pi^2; \quad n \in \mathbb{Z}.$$

(4) The interface has perfect mechanical interaction but partial electrical interaction:

$$k_u \to \infty, \quad 0 < k_\varphi < \infty,$$

$$\bar{c}_A\sqrt{1 - v^2/\bar{v}_A^2} - \bar{c}_B\sqrt{v^2/\bar{v}_B^2 - 1}\tan\left(\tfrac{1}{2}\mathrm{d}\xi\sqrt{v^2/\bar{v}_B^2 - 1}\right) = \gamma_\phi(e_A/\varepsilon_A - e_B/\varepsilon_B)^2.$$

(5) The interface has both perfect mechanical and electrical interactions:

$$k_u \to \infty, \quad k_\varphi \to \infty,$$

$$\bar{c}_A\sqrt{1 - v^2/\bar{v}_A^2} - \bar{c}_B\sqrt{v^2/\bar{v}_B^2 - 1}\tan\left(\tfrac{1}{2}\mathrm{d}\xi\sqrt{v^2/\bar{v}_B^2 - 1}\right) = \frac{(e_A/\varepsilon_A - e_B/\varepsilon_B)^2}{1/\varepsilon_A + 1/\varepsilon_B \coth\left(\tfrac{1}{2}\mathrm{d}\xi\right)}.$$

(6) The interface has perfect mechanical interaction but has no electrical interaction:

$$k_u \to \infty, \quad k_\varphi \to 0,$$

$$\bar{c}_A\sqrt{1 - v^2/\bar{v}_A^2} - \bar{c}_B\sqrt{v^2/\bar{v}_B^2 - 1}\tan\left(\tfrac{1}{2}\mathrm{d}\xi\sqrt{v^2/\bar{v}_B^2 - 1}\right) = 0.$$

Let us consider the following limit cases for the antisymmetric part:

(1) The interface has partial electrical interaction but has no mechanical interaction:

$$k_u \to 0, \quad 0 < k_\varphi < \infty,$$

$$\sqrt{1 - v^2/\bar{v}_A^2}\sqrt{v^2/\bar{v}_B^2 - 1}\cot\left(\tfrac{1}{2}\mathrm{d}\xi\sqrt{v^2/\bar{v}_B^2 - 1}\right) - A\gamma_\phi\frac{M_B^2}{\varepsilon_B}\sqrt{1 - v^2/\bar{v}_A^2}$$

$$- A\gamma_\phi\frac{M_A^2}{\varepsilon_A}\sqrt{v^2/\bar{v}_B^2 - 1}\cot\left(\tfrac{1}{2}\mathrm{d}\xi\sqrt{v^2/\bar{v}_B^2 - 1}\right) = 0.$$

(2) The interface has perfect electrical interaction but has no mechanical interaction:

$$k_u \to 0, \quad k_\varphi \to \infty,$$

$$\sqrt{1 - v^2/\bar{v}_A^2}\sqrt{v^2/\bar{v}_B^2 - 1}\cot\left(\tfrac{1}{2}\mathrm{d}\xi\sqrt{v^2/\bar{v}_B^2 - 1}\right) - \frac{M_B^2}{\varepsilon_B/\varepsilon_A + \coth\left(\tfrac{1}{2}\mathrm{d}\xi\right)}\sqrt{1 - v^2/\bar{v}_A^2}$$

$$- \frac{M_A^2}{1 + \varepsilon_A/\varepsilon_B \tanh\left(\tfrac{1}{2}\mathrm{d}\xi\right)}\sqrt{v^2/\bar{v}_B^2 - 1}\cot\left(\tfrac{1}{2}\mathrm{d}\xi\sqrt{v^2/\bar{v}_B^2 - 1}\right) = 0.$$

(3) The interface has neither mechanical nor electrical interaction:

$$k_u \to 0, \quad k_\varphi \to 0,$$

$$\sqrt{1 - v^2/\bar{v}_A^2}\sqrt{v^2/\bar{v}_B^2 - 1}\cot\left(\tfrac{1}{2}\mathrm{d}\xi\sqrt{v^2/\bar{v}_B^2 - 1}\right) = 0 \to \cos\left(\tfrac{1}{2}\mathrm{d}\xi\sqrt{v^2/\bar{v}_B^2 - 1}\right) = 0,$$

$$\mathrm{d}^2\xi^2(v^2/\bar{v}_B^2 - 1) = (2n + 1)^2\pi^2; \quad n \in \mathbb{Z}.$$

(4) The interface has perfect mechanical interaction but partial electrical interaction:

$$k_u \to \infty, \quad 0 < k_\varphi < \infty,$$

$$\bar{c}_A \sqrt{1 - v^2/\bar{v}_A^2} + \bar{c}_B \sqrt{v^2/\bar{v}_B^2 - 1} \cot\left(\tfrac{1}{2}d\xi \sqrt{v^2/\bar{v}_B^2 - 1}\right) = A\gamma_\phi (e_A/\varepsilon_A - e_B/\varepsilon_B)^2.$$

(5) The interface has both perfect mechanical and electrical interactions:

$$k_u \to \infty, \quad k_\varphi \to \infty,$$

$$\bar{c}_A \sqrt{1 - v^2/\bar{v}_A^2} - \bar{c}_B \sqrt{v^2/\bar{v}_B^2 - 1} \cot\left(\tfrac{1}{2}d\xi \sqrt{v^2/\bar{v}_B^2 - 1}\right) = \frac{(e_A/\varepsilon_A - e_B/\varepsilon_B)^2}{1/\varepsilon_A + 1/\varepsilon_B \tanh\left(\tfrac{1}{2}d\xi\right)}.$$

(6) The interface has perfect mechanical interaction but has no electrical interaction:

$$k_u \to \infty, \quad k_\varphi \to 0,$$

$$\bar{c}_A \sqrt{1 - v^2/\bar{v}_A^2} - \bar{c}_B \sqrt{v^2/\bar{v}_B^2 - 1} \cot\left(\tfrac{1}{2}d\xi \sqrt{v^2/\bar{v}_B^2 - 1}\right) = 0.$$

6. Numerical examples

In order to show the effects of the imperfections within the interfaces, we present some dispersion curves. We used two different piezoelectric materials: $BaTiO_3$ as the piezoelectric A and PZT4 as the piezoelectric B. The properties of the materials are summarized in Table 1.

In Figure 2, dispersion curves $v = f(\omega d)$ for the symmetric part for the fixed electrical imperfect parameter $k_\varphi = 0\,\text{F/m}^2$ and different values of the mechanical imperfect parameter k_u are shown. These curves are nonmonotonic for small values of k_u and strictly convex and decreasing for large values of k_u. As we can see, the dispersion curves are shifted to the right by increasing values of k_u. This behavior of the dispersion curves was shown by Otero et al. [2011, Figures 2(a) and 2(b)]. The value of k_u has a really strong influence on the dispersion curves and all the wave velocities tend to the wave velocity in phase B as ωd goes to infinity. Nevertheless, for high frequencies, the wave propagation is not affected. The wave velocities are between v_A and v_B, and both are shown in Figure 2.

In Figure 3, dispersion curves for the symmetric part for $k_\varphi = 5\,\text{F/m}^2$ and different values of the mechanical imperfect parameter k_u are shown. In Figure 4, dispersion curves for the symmetric part for $k_\varphi = 10^7\,\text{F/m}^2$ and different values of mechanical imperfect parameter k_u are shown.

The behavior in Figures 3 and 4 are quite similar for the case $k_\varphi = 0\,\text{F/m}^2$, but there is a slight difference, which is shown in Figure 5, if we compare the dispersion curves for $k_u = 0.3\,\text{GPa/m}$ in all cases. As we

properties	BaTiO$_3$	PZT4
c (GPa)	43	26
e (C/m^2)	11.6	10.5
ε (10^{-9} C^2/Nm^2)	11.2	7.124
ρ (10^3 kg/m^3)	5	7.5
$\bar{v}$ (10^3 m/s)	3.07981	2.35162

Table 1. Material properties.

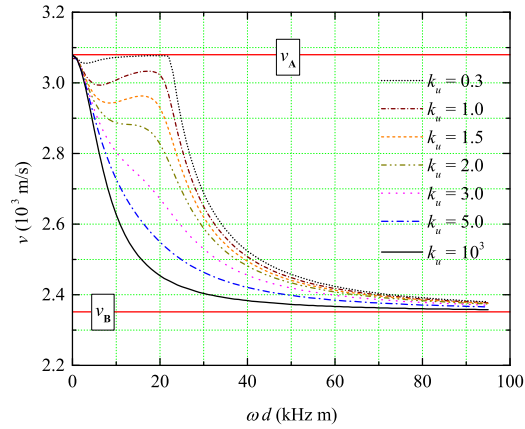M. A. REYES, J. A. OTERO AND R. PÉREZ-ÁLVAREZ

Figure 2. Dispersion curve for the symmetric part for $k_\varphi = 0$ F/m^2 and different values of k_u.
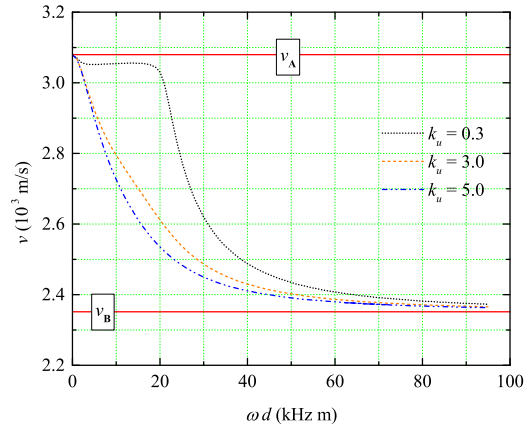

Figure 3. Dispersion curve for the symmetric part for $k_\varphi = 5$ F/m^2 and different values of k_u.
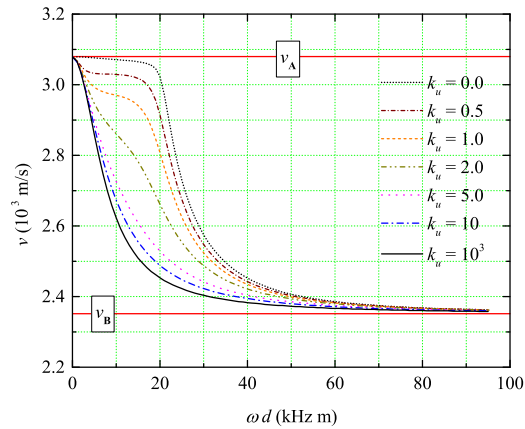

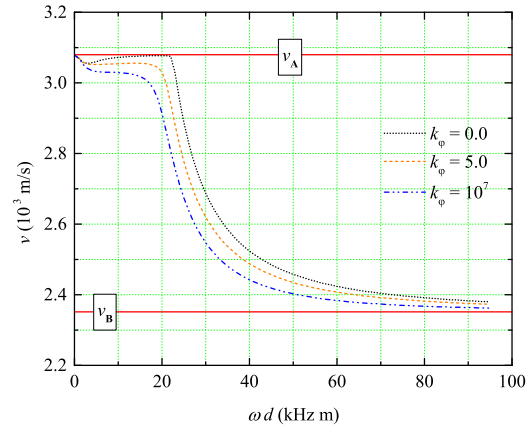**Figure 4.** Dispersion curves for the symmetric part for $k_\varphi = 10^7$ F/m^2 and different values of k_u.

Figure 5. Dispersion curve for the symmetric part for $k_u = 0.3\,\text{GPa/m}$ and different values of k_φ.
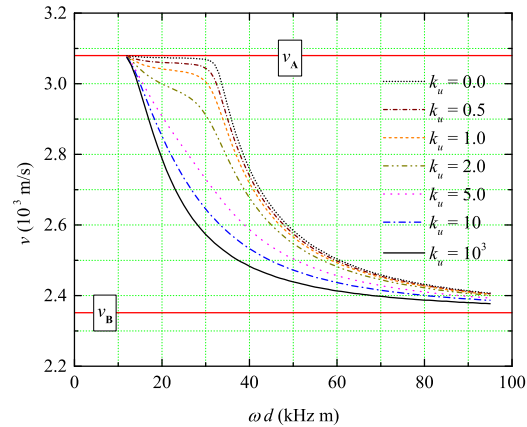
Figure 6. Dispersion curve for the antisymmetric part for $k_\varphi = 10\,\text{F/m}^2$ and different values of k_u.

can see in Figure 5, there is a notable displacement in both the frequency and the wave velocity axes. If k_φ is increased, the dispersion curves are shifted to the left and the wave velocity is decreased. This conclusion is really important because the dispersion curves are strongly dependent on the mechanical imperfect parameter (k_u) and depend weakly on the electrical parameter (k_φ).

In Figure 6, dispersion curves for the antisymmetric part for the fixed electrical imperfect parameter $k_\varphi = 10\,\text{F/m}^2$ and different values of mechanical imperfect parameter k_u are shown. These curves are strictly convex and have the same nonmonotonic behavior for small values for k_u and large values of k_u, similar to that of dispersion curves for the symmetric part. The visual difference between these curves and the symmetric ones is that dispersion curves for the antisymmetric part are shifted to the right. This behavior of the dispersion curves was shown in [Otero et al. 2011, Figures 8(a) and 8(b)]. The value of k_u has a really strong influence in the dispersion curves and all the wave velocities approach to the wave velocity in phase B as ωd goes to infinity. Nevertheless, for high frequencies, the wave propagation is not affected. The wave velocities are between v_A and v_B, and both are shown in Figure 6.
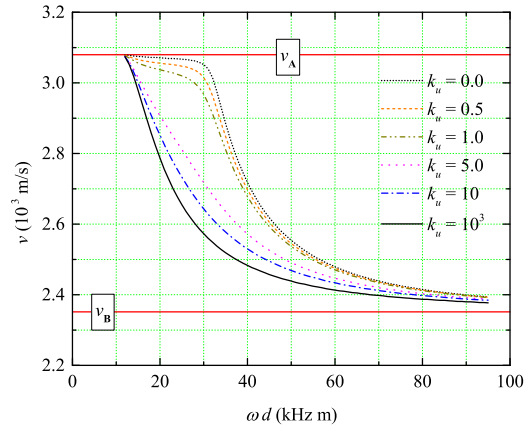
Figure 7. Dispersion curve for the antisymmetric part for $k_\varphi = 10^7$ F/m^2 and different values of k_u.
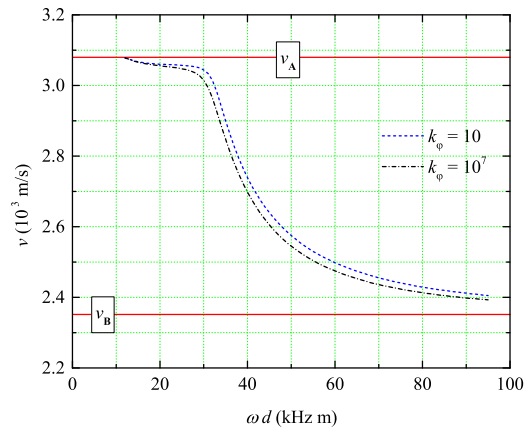

Figure 8. Dispersion curve for the antisymmetric part for $k_u = 0.5$ GPa/m and different values of k_φ.

In Figure 7, dispersion curves for the antisymmetric part for $k_\varphi = 10^7$ F/m^2 and different values of the mechanical imperfect parameter k_u are shown. The behavior in Figures 6 and 7 are quite similar, but there is a slight difference, which is shown in Figure 8, if we compare the dispersion curves for $k_u = 0.5$ GPa/m in both cases. As we can see in Figure 8, there is a notable displacement in both the frequency and wave velocity axes, which is the same behavior as in the symmetric part.

7. Conclusions

Dispersion relations for the propagation of an interfacial shear wave in an A/B/A piezoelectric structure for symmetric and antisymmetric parts have been studied by considering the existence of electrical and mechanical imperfections at the interfaces, which are modeled by means a capacitor and a spring, respectively. Analytical expressions for dispersion relations are obtained and different limit cases are studied, showing a good agreement with [Otero et al. 2011]. Numerical examples are presented by using two

piezoelectric materials (PZT4 and BaTiO$_3$), and dispersion curves for different values of the material parameters (k_u and k_φ) are shown. Some conclusions about dispersion curves have been obtained:

- they are confined within the velocity of media A and B for the symmetric and antisymmetric parts,

- they never intersect each other for the symmetric and antisymmetric parts,

- they go to v_B as ωd goes to infinity for all values of k_u, and possible values of k_ϕ,

- they are nonmonotonic for small values for k_u, strictly convex and decreasing for large values of k_u,

- the smaller the value of the imperfect bounding parameter (k_ϕ), the more shift to the right.

References

[Bleustein 1968] J. L. Bleustein, "A new surface wave in piezoelectric materials", *Appl. Phys. Lett.* **13**:12 (1968), 412–413.

[Chen et al. 2008] Z. G. Chen, Y. T. Hu, and J. S. Yang, "Shear horizontal piezoelectric waves in a piezoceramic plate imperfectly bonded to two piezoceramic half-spaces", *J. Mech.* **24**:3 (2008), 229–239.

[Fan et al. 2006a] H. Fan, J. Yang, and L. Xu, "Antiplane piezoelectric surface waves over a ceramic half-space with an imperfectly bonded layer", *IEEE Trans. Ultrason. Ferroelectr. Freq. Control* **53**:9 (2006), 1695–1698.

[Fan et al. 2006b] H. Fan, J. Yang, and L. Xu, "Piezoelectric waves near an imperfectly bonded interface between two half-spaces", *Appl. Phys. Lett.* **88**:20 (2006), 203509.

[Kakar 2015] R. Kakar, "SH-wave velocity in a fiber-reinforced anisotropic layer overlying a gravitational heterogeneous half-space", *Multi. Model. Mat. Struct.* **11**:3 (2015), 386–400.

[Kong et al. 2016] Y. Kong, J. Liu, and G. Nie, "Propagation characteristics of SH waves in a functionally graded piezomagnetic layer on PMN-0.29PT single crystal substrate", *Mech. Res. Commun.* **73** (2016), 107–112.

[Li and Jin 2015] P. Li and F. Jin, "Excitation and propagation of shear horizontal waves in a piezoelectric layer imperfectly bonded to a metal or elastic substrate", *Acta Mech.* **226**:2 (2015), 267–284.

[Li et al. 2013] P. Li, F. Jin, W. Chen, and J. Yang, "Effects of interface bonding on acoustic wave generation in an elastic body by surface-mounted piezoelectric transducers", *IEEE Trans. Ultrason. Ferroelectr. Freq. Control* **60**:9 (2013), 1957–1963.

[Li et al. 2015a] Y.-D. Li, T. Xiong, and Q.-G. Cai, "Coupled interfacial imperfections and their effects on the fracture behavior of a layered multiferroic cylinder", *Acta Mech.* **226**:4 (2015), 1183–1199.

[Li et al. 2015b] Y.-D. Li, T. Xiong, and L. Dong, "A new interfacial imperfection coupling model (IICM) and its effect on the facture behavior of a layered multiferroic composite: anti-plane case", *Eur. J. Mech. A Solids* **52** (2015), 26–36.

[Li et al. 2015c] Y.-D. Li, T. Xiong, and L. Dong, "Interfacial imperfection coupling model with application to the in-plane fracture problem of a multiferroic composite", *Int. J. Solids Struct.* **54** (2015), 31–41.

[Li et al. 2016a] Y.-D. Li, T. Xiong, and Y. Guan, "Effects of coupled interfacial imperfections on SH wave propagation in a layered multiferroic cylinder", *Ultrasonics* **66** (2016), 11–17.

[Li et al. 2016b] Y.-D. Li, K. Zhou, and T. Xiong, "Fracture analysis on a multiferroic cylindrical shell: effects of coupled interphase imperfections", *J. Intell. Mater. Syst. Struct.* **27**:2 (2016), 195–207.

[Liu et al. 2010] J. Liu, Y. Wang, and B. Wang, "Propagation of shear horizontal surface waves in a layered piezoelectric half-space with an imperfect interface", *IEEE Trans. Ultrason. Ferroelectr. Freq. Control* **57**:8 (2010), 1875–1879.

[Maerfeld and Tournois 1971] C. Maerfeld and P. Tournois, "Pure shear elastic surface wave guided by the interface of two semi-infinite media", *Appl. Phys. Lett.* **19**:4 (1971), 117–118.

[Otero et al. 2011] J. A. Otero, R. Rodriguez-Ramos, J. Bravo-Castillero, A. R. Aguiar, and G. Monsivais, "Dispersion relations for SH waves on a magnetoelectroelastic heteroestructure with imperfect interfaces", *J. Mech. Mater. Struct.* **6**:7–8 (2011), 969–993.

[Otero et al. 2012] J. A. Otero, R. Rodríguez-Ramos, J. Bravo-Castillero, and G. Monsivais, "Interfacial waves between two piezoelectric half-spaces with electro-mechanical imperfect interface", *Philos. Mag. Lett.* **92**:10 (2012), 534–540.

[Soh and Liu 2006] A. K. Soh and J. X. Liu, "Interfacial shear horizontal waves in a piezoelectric-piezomagnetic bi-material", *Philos. Mag. Lett.* **86**:1 (2006), 31–35.

[Sun et al. 2011] W.-H. Sun, G.-L. Ju, J.-W. Pan, and Y.-D. Li, "Effects of the imperfect interface and piezoelectric/piezomagnetic stiffening on the SH wave in a multiferroic composite", *Ultrasonics* **51**:7 (2011), 831–838.

[Xiong et al. 2015] T. Xiong, Y.-D. Li, and Z.-K. Song, "Interfacial sliding in a bi-layered multiferroic ceramics: localized sliding-prevention/promotion based mechanism of intra-layer fracture", *Int. J. Solids Struct.* **77** (2015), 15–27.

[Yang and Yang 2009] Z. Yang and J. Yang, "Effects of electric field gradient on the propagation of short piezoelectric interface waves", *Int. J. Appl. Electrom.* **29**:2 (2009), 101–108.

M. A. REYES: 777marcorey@gmail.com
Instituto Politécnico Nacional, UPIITA-IPN, Avenida Instituto Politécnico Nacional No. 2580, Col Barrio la Laguna Ticomán, 07340 Ciudad de México,, Mexico

J. A. OTERO: j.a.otero@itesm.mx
Campus Estado de México, Tecnológico de Monterrey, Carretera Lago de Guadalupe Km. 3.5, Atizapán de Zaragoza, 52926 Colonia Margarita Maza de Juárez,, Mexico

R. PÉREZ-ÁLVAREZ: rpa@uaem.mx
Centro de Investigacion en Ciencias, Instituto de Investigacion en Ciencias Basicas y Aplicadas, Universidad Autonoma del Estado de Morelos, Av. Universidad 1001, 62209 Cuernavaca,, Mexico

■msp

FULLY PERIODIC RVES FOR TECHNOLOGICAL RELEVANT COMPOSITES: NOT WORTH THE EFFORT!

KONRAD SCHNEIDER, BENJAMIN KLUSEMANN AND SWANTJE BARGMANN

The setup of a finite element model for homogenization featuring a fully periodic geometry and a fully periodic mesh topology in combination with a high quality discretization is a cumbersome task and might significantly reduce the overall efficiency in multiscale finite element simulations.

   In this work, we examine multiple methodologies of setting up finite element models for homogenization purposes that extenuate these difficulties. Approaches resulting in periodic and nonperiodic representative volume element topologies in the microstructural generation process are introduced. Furthermore, we review and analyze various types of boundary conditions that either enforce periodicity or do not require periodicity of the underlying discretization. Approximate periodic boundary conditions are discussed in detail.

   The benchmark study proves that a fully periodic topology and mesh discretization with periodic boundary conditions is not necessary in order to identify effective macroscopic material parameters for technologically relevant composites.

1. Introduction — numerical homogenization of heterogeneous solids

Advanced and complex materials often possess a distinctive microstructure at a certain length scale, which significantly influences the macroscopic material behavior. In composites, the combination of multiple material phases enhances mechanical properties over the single constituents, which in turn qualifies them as highly technologically relevant.

   In computational micromechanics, the state of the art approach only considers a small but representative part of the structure, namely a representative volume element (RVE), featuring all relevant characteristics of the materials microstructure [Böhm 1998; Geers et al. 2010; Klusemann et al. 2012; Kari et al. 2007; McBride et al. 2012; Saeb et al. 2016; Schröder and Hackl 2014; Yuan and Fish 2008; Suquet 1985]. Such a RVE should have a sufficiently large size to capture enough microstructural information while being significantly smaller than the macroscopic structure to hardly influence macroscopic gradients [Böhm 1998].

   One important issue to deal with is the application of appropriate boundary conditions. They have to be chosen carefully to fulfill the macrohomogeneity condition [Hill 1963] (also named the Hill–Mandel condition) for proper homogenization. At least five conditions obey this requirement: fully prescribed deformation over the entire domain, fully prescribed displacement on the boundary of the domain, periodic boundary conditions, fully prescribed stress vectors on the boundary of the domain and fully prescribed stresses over the entire domain.

Secondly, application of the finite element method (FEM) requires a discretization of the RVE. The type and accuracy of such discretizations significantly influence the quality of the results. As will be shown in this work, periodic RVEs with periodic boundary conditions are not necessarily worth the effort.

In the opinion of many researchers, a favorable FE model features a periodic topology with a large number of inhomogeneities as well as high quality discretizations suitable for the direct application of periodic boundary conditions [Böhm 1998; Torquato 2002; Yue and E 2007; Kanit et al. 2003; Perić et al. 2011; Miehe and Koch 2002; Glüge 2013; Gusev 1997; Böhm and Han 2001; Böhm et al. 2002; Gitman et al. 2007]. The construction of such models is either a very tedious and expensive task or even impossible to accomplish for certain microstructures [Dirrenberger et al. 2014; Fritzen et al. 2009; Fritzen and Böhlke 2011].

Tremendous effort might be necessary to gather microstructural information and transfer it to a discretized model. If periodicity in terms of geometry and boundary conditions is targeted, this effort is questionable for engineering applications. Various possibilities of relaxing these strict requirements are possible to ease the homogenization procedure. Discretizing geometrically complex microstructures (e.g., curved geometric entities) is typically realized by employing tetrahedralizations. To achieve trustworthy analyses, high quality meshes are required; however, their generation might become a very cumbersome and resource consuming task [Böhm et al. 2002; Fritzen et al. 2009; Schneider et al. 2016]. A viable solution is the utilization of voxel discretizations resulting in regular grid-like meshes [Glüge 2013; Kanit et al. 2003]. Regular voxel meshes naturally feature a periodic mesh topology, allowing a straightforward application of periodic boundary conditions.

As an alternative approach, approximate periodic boundary conditions and kinematic uniform stress vectors or displacement boundary conditions loosen the requirement of a periodic mesh topology. In fact, these methodologies allow completely nonperiodic RVEs.

The goal of this paper is a systematic evaluation of the influences of RVE topology, discretization and employed boundary conditions on the effective material response. A benchmark study is conducted for the example of composites consisting of a topologically interconnected matrix and nonoverlapping inclusions, so-called matrix inclusion composites.

2. Aspects of numerical homogenization in context of RVE topology, discretization and boundary conditions

Vital to a proper homogenization is the fulfillment of the macrohomogeneity condition suggested by Hill [1963]: the equality of the stress power deduced by the mean values (pure macroscopic quantities) and the stress power calculated by the actual volume integral of the microscopic quantities:[1]

$$\bar{\boldsymbol{P}} : \dot{\bar{\boldsymbol{F}}} = \frac{1}{V_0} \int_{\mathscr{B}_0} \boldsymbol{P} : \dot{\boldsymbol{F}} \, dV_0. \tag{1}$$

Here, V_0 is the volume in the reference configuration, $\boldsymbol{P}$ represents the first Piola–Kirchhoff stress tensor and $\boldsymbol{F}$ is the deformation gradient. The fulfillment is accomplished by the proper choice of boundary conditions.

---

[1]Quantities on the macroscopic scale are related to the microscopic scale via a volume average over the RVE domain $\mathscr{B}_0$ and are denoted by $\overline{(\dots)} = 1/V_0 \int_{\mathscr{B}_0} (\dots) \, dV_0$ in the following. Accordingly, the macroscopic deformation gradient is introduced via $\bar{\boldsymbol{F}} = 1/V_0 \int_{\mathscr{B}_0} F \, dV_0$.
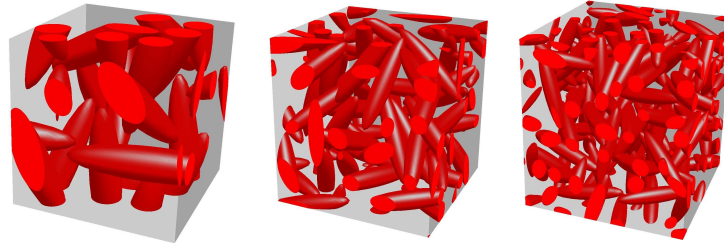
Figure 1. Example microstructures for an inclusion volume fraction of $f = 20\%$ featuring a periodic topology with (left) 10 inclusions, (center) 50 inclusions and (right) 100 inclusions.

2.1. *Microstructure generation.* In the following, the underlying RVE geometry is exemplarily based on matrix-inclusion microstructures.

The key idea of a RVE with an a priori periodic topology is approximating inhomogeneous materials by infinitely extended model materials with a periodic phase arrangement [Michel et al. 1999]. The constraint of generating a fully periodic geometry results in additional effort.

The generation process is based on our random sequential adsorption algorithm [Schneider et al. 2016]. Inclusions are modeled as nonoverlapping spheroids randomly oriented and located inside a cubic RVE as depicted in Figure 1. All investigated RVEs feature a target inclusion volume fraction of $f = 20\%$ with equally shaped, nonoverlapping spheroids incorporating an aspect ratio of $\gamma = \frac{1}{5}$ (ratio of minor to major spheroid axis).[2]

The size of the RVE is triggered by the ratio of the characteristic length of the microstructural components l (major axis of a spheroid) and the RVE edge length d. Three setups of 10, 50 and 100 inclusions along with their respective ratios, listed in Table 1, are considered.[3] [4]

target inclusion number n	10	50	100
major spheroid axis (*l*) / RVE length (*d*) *l/d*	0.49	0.28	0.23

Table 1. Ratios of characteristic lengths of microstructural components l (longest axis of the spheroid) and RVE dimension d for target inclusions numbers of 10, 50 and 100.

---

[2]Periodic RVEs always exhibit this intended inclusion volume fraction since a placed inclusion intersecting the RVE boundary has its periodic counterparts also inside the RVE. However, the actual volume fractions of inclusions intersecting with the RVE boundary cannot be determined exactly in advance due to the random nature of the placement procedure. Therefore, the inclusion volume fraction for nonperiodic cases are only approximate. The actual microstructure generation process for the nonperiodic case is terminated, if the inclusion volume fraction deviates less than 1% from target volume fraction.

[3] A RVE with a nonperiodic topology typically contains more inclusions than its periodic counterpart: randomly placed inclusions intersecting the RVEs boundary do not have periodic continuations and, thus, more inclusions are required to achieve the preassigned inclusion volume fraction.

[4]The expression l/d converges towards zero with an increasing inclusion number as the RVE length is set to $d = 1$ and remains constant. In the limit of infinitely many inclusions, $l \to 0$ and, thus, $l/d \to 0$.

2.2. *FE discretizations.* Two element types are employed for three-dimensional discretizations, namely tetrahedral or hexahedral elements. Tetrahedral elements are more versatile in terms of meshing complicated geometries, but typically exhibit increased computational costs compared to hexahedral elements [Benzley et al. 1995; Carl et al. 2006].

An alternative to avoid the tedious task of precisely resolving the geometry via a sophisticated mesh represents the utilization of fully structured grids, also known as voxel discretization. By assigning each element to material phases by means of the location of element midpoints or even Gauss points, it is possible to capture the geometric features to a certain extent. As a consequence, the mesh is easily generated, see Figures 2 and 3.
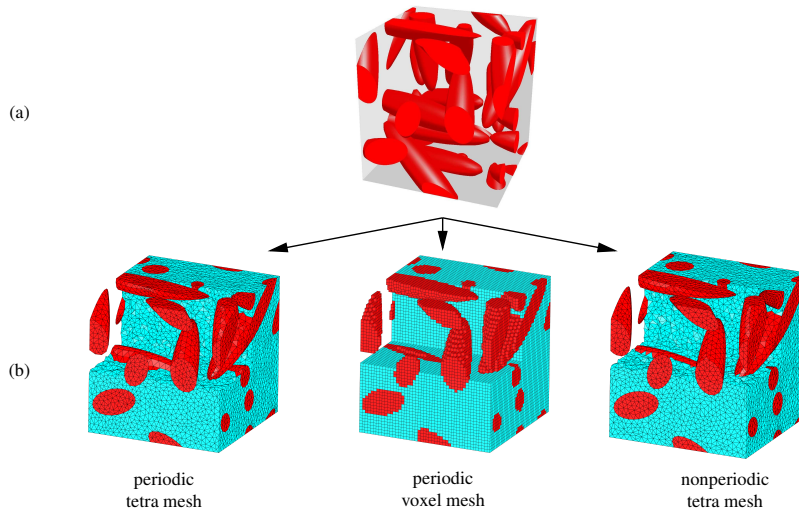
Figure 2. Periodic model setups considered in this study: (a) periodic topology and (b) tetrahedral and voxel discretizations.
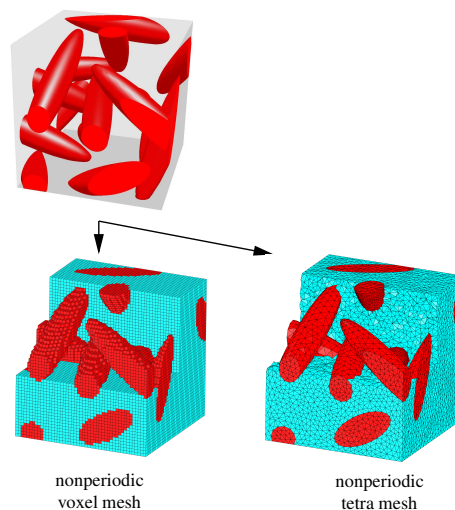
Figure 3. Nonperiodic model setups considered in this study: (a) nonperiodic topology and (b) tetrahedral and voxel discretizations.

We consider quadratic tetrahedral meshes as well as voxel discretizations featuring linear hexahedral elements. In this context, a tetrahedralization of the geometry generally provides higher geometric accuracy. However, due to the sharp curvature of the inclusions, the geometry cannot be perfectly captured. Following [Schneider et al. 2016], constrained triangulations and tetrahedralizations are utilized to generate high quality meshes which possess periodicity.

2.3. *Boundary conditions.* By applying boundary conditions to the RVE, macroscopic loadings are transferred to the microscale. Typically, the macroscopic deformation gradient $\bar{F}$ or the macroscopic first Piola–Kirchhoff stress tensor $\bar{P}$ are imposed on the microfield.

Kinematic uniform boundary conditions are formulated for the displacements u on the entire boundary $\partial \mathcal{B}_0$ of the RVE via

$$u = \bar{F} \cdot X \quad \forall X \in \partial \mathcal{B}_0. \tag{2}$$

Here, X denotes the position vector of a material point in the reference configuration of the RVE. Since the displacements are fully prescribed on the entire boundary, this boundary condition does not have any requirements on the mesh topology, making it operationally very easy to implement. Disadvantageously, the macroscopic response is predicted to be too stiff, resulting from strongly restricted degrees of freedom [Pecullan et al. 1999; Miehe and Koch 2002; Kanit et al. 2003].

Periodic boundary conditions relax these kinematic constraints. The boundary of the RVE is split into associated parts $\partial \mathcal{B}_0 = \partial \mathcal{B}_0^+ \cup \partial \mathcal{B}_0^-$ with associated material points X^+ and X^-. Displacements show a periodic behavior, whereas the tractions p are antiperiodic:

$$
\begin{aligned}
u(X^+) - u(X^-) &= [\bar{F} - 1] \cdot [X^+ - X^-] \text{ and} \\
p(X^+) + p(X^-) &= 0 \quad \forall X^+, X^- \in \partial \mathcal{B}_0^+, \partial \mathcal{B}_0^-.
\end{aligned}
\tag{3}
$$

Since the boundary is divided into opposing (periodic) counterparts, it is an inevitable requirement for the underlying discretization to possess a periodic mesh topology.

Furthermore, static uniform boundary conditions:

$$t = \bar{P} \cdot N \quad \forall N \in \partial \mathcal{B}_0 \tag{4}$$

are considered. Here, t represents the stress vector in the current configuration and N is the normal vector of the boundary in the reference configuration. Static uniform boundary conditions do not have any requirements on the mesh. Difficulties concerning the uniqueness of a solution resulting from the pure Neumann problem are overcome by employing *semi-Dirichlet boundary conditions* as suggested in [Javili et al. 2017; Saeb et al. 2016]. Rigid body motions are restricted by fixing one corner node in all three coordinate directions and applying *semi-Dirichlet boundary conditions* to the other corner nodes.[5]

2.3.1. *Approximate periodic boundary conditions (APBC).* If the underlying mesh topology is not periodic, there is no straightforward way to apply periodic boundary conditions. To circumvent the restriction on the mesh topology, some researchers weakly impose periodic boundary conditions on a nonperiodic mesh [Larsson et al. 2011; Nguyen et al. 2012; Xia et al. 2003]. However, these methods demand sophisticated programming and are hardly applicable to commercial software. A more practical approach

---

[5]Within the commercial FE software package Abaqus, static uniform boundary conditions are implemented via the DLOAD option.
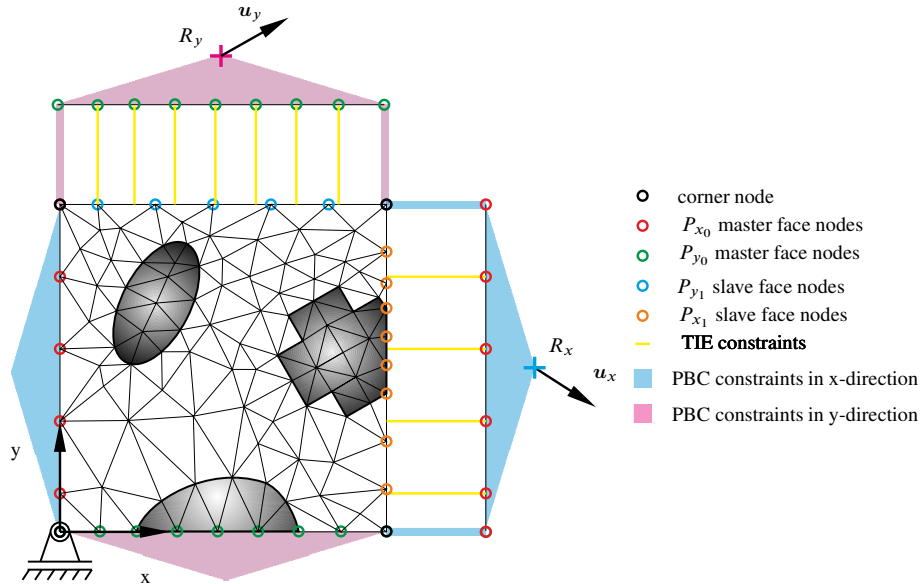
Figure 4. Sketch of approximate periodic boundary conditions using surface-to-surface constraints (e.g., TIE-constraints in Abaqus).

(suggested in [Yuan and Fish 2008; Kassem 2009]) is to apply approximate periodic boundary conditions via surface-to-surface constraints, available in commercial FE software packages, e.g., in Abaqus.

A schematic illustration of this method for the two-dimensional case is depicted in Figure 4. First, master faces $P_{x_0} : X = 0$ (red nodes) and $P_{y_0} : Y = 0$ (green nodes) are introduced. These faces are copied and, for better illustration purposes, translated to their opposing counterparts, namely $P_{x_1} : X = l_x$ (orange nodes) and $P_{y_1} : Y = l_y$ (blue nodes), with l_x and l_y being the dimensions of the RVE. The required constraints for the periodic boundary conditions are then formulated between reference points (R_x and R_y), copied faces and their source faces. Therefore, identical nodal distributions are maintained a priori, see the blue and violet area in Figure 4. Furthermore, the actual RVE boundaries P_{x_1} and P_{y_1} are coupled to the copied faces via surface-to-surface coupling, thus consequently equalizing their motion respectively and tying them together.[6] During this coupling, P_{x_1} and P_{y_1} act as slave surfaces implying the condensation of degrees of freedom of associated nodes.

In Abaqus, an element-based master-slave surface algorithm is employed. To every point on the master surface, the closest nodes on the slave surface are computed by a projection procedure. These quantities are then coupled via constraints which are generated using the element shape functions.

Special care must be taken to set up constraints for the corners (black nodes) and edges (in three dimensions) of copied surfaces to circumvent overconstraining. Edges and corner nodes are excluded in the coupling process and are processed via separate multipoint constraints. In particular, three master edges ($L_{x_0y_0} : x = y = 0$, $L_{y_0z_0} : y = z = 0$, $L_{x_0z_0} : x = z = 0$) have to be introduced and copied for

---

[6]As a consequence, all involved surfaces show the same motion during an analysis. In Abaqus, this coupling is conveniently established by utilizing the *TIE keyword.
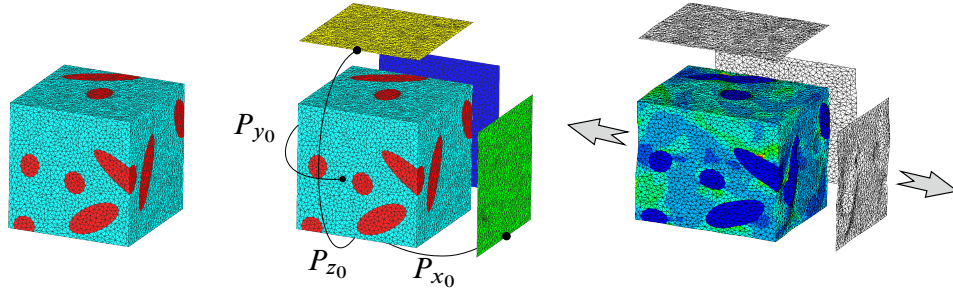
Figure 5. Model setup for a 3d nonperiodic mesh topology using TIE-constraints: virgin mesh (left), TIE-constraints with copied P_{x_0}, P_{y_0} and P_{z_0} faces (center) and conducted analysis for tensile loading (right).

coupling to each slave edge (analogously to the mentioned surfaces).[7] Since edges are one-dimensional, a coupling solely relying on nodal distributions is utilized.[8] The displacements are prescribed at the reference nodes before analysis.

Following the described approach, we are able to apply approximate periodic boundary conditions to nonperiodic three-dimensional meshes. Figure 5 exemplarily depicts a three-dimensional nonperiodic model. An additional investigation of the approximate periodic boundary conditions can be found in the Appendix.

3. Numerical examples

3.1. *Set-up of benchmark study.* All RVEs have a unit edge length d whereas the spheroid axis length l varies to trigger the RVE size. For each RVE, 20 randomized realizations are considered. A statistical study is given to support the results and extenuate artificial findings due to the randomness of the RVE generation process. To this end, a total of 3600 simulations are conducted for this study.[9] Two oppositional cases of matrix-inclusion materials are investigated:

(i) materials with soft inclusions and a stiff matrix, i.e., a low stiffness ratio $\alpha = E_{\mathrm{Inclusion}}/E_{\mathrm{Matrix}} = G_{\mathrm{Inclusion}}/G_{\mathrm{Matrix}}$ such as the polymer blend Acrylonitrile-Butadien-Styrene (ABS) [Michler 1992; Lombardo et al. 1994];

(ii) materials with a very high stiffness ratio such as glass-fiber or carbon-fiber reinforced composites.

Linear elastic material behavior is assumed with the corresponding material parameters documented in Table 2. Typically, the employed FE models exhibit a minimum element number of $n_{\mathrm{el}} = 10^5$, allowing for a sufficient resolution of geometric features. Furthermore, all meshes exhibit an average element shape factor of $\eta \leq 0.5$ to ensure reliable results. Additionally, plastic material behavior based on the von Mises yield criterion is considered for the matrix material. A yield stress of $\sigma_y = 60\,\mathrm{MPa}$ and a linear, isotropic hardening coefficient of $35\,\mathrm{MPa}$ are utilized to represent the deformation behavior of the

---

[7]A master edge possesses three slave edges, and thus three copies are necessary.

[8]In Abaqus, edge-coupling is realized by node-based surfaces tying.

[9]Three RVE sizes, two periodic and three nonperiodic topologies and discretizations, three types of boundary conditions, two loading cases, two stiffness ratios and 20 realizations.

E_{Matrix}	G_{Matrix}	$E_{\text{Inclusion}}$	$G_{\text{Inclusion}}$	α
3800	1300	38	13	$\frac{1}{100}$
3800	1300	38000	13000	100

Table 2. Material properties for the RVE constituents.

matrix material (SAN), see [Seelig and Van der Giessen 2009]. As load cases, tension as well as simple shear in the small strain context are considered. All results are normalized to the numerical reference solution, obtained by the full periodic RVE (periodic topology, mesh and boundary conditions) with 100 inclusions.

3.2. *Results and Discussion.*

3.2.1. *Influences of topology and mesh.* The effective macroscopic responses are seemingly independent of the chosen combinations of periodic and nonperiodic topologies and meshes. Figure 6 clearly demonstrates that for all cases, the five combinations predict a very similar material behavior: the markers in each group achieve the same normalized response, independent of the topology-mesh combination.[10]

This is true for the elastic as well as the plastic material behavior, tensile and shear loading, both stiffness ratios, all three RVE ratios and the various applied boundary conditions. The effort of the RVE construction strongly differs between the analyzed combinations. The simulation times when calculating the effective properties are in similar time ranges. Consequently, the high effort of constructing a fully periodic RVE, with periodic topology as well as a periodic mesh, does not pay off and simpler approaches should be used.

Remark. The averaged inclusion volume fractions emanating from varying topologies and discretizations are within a very small range for all combinations and are independent of the aspect ratio. The voxel mesh with a periodic topology naturally reaches the target volume fraction of 20%, whereas the others converge to a slightly smaller volume fraction (with a maximum underestimation of 1%). Moreover, voxel meshes feature linear hexahedral elements with an a priori perfect average element shape factor.

3.2.2. *Influence of boundary conditions.* With respect to elastic/plastic material behavior, topology/mesh combination, RVE ratios and load cases, the obtained differences are negligible.

However, with respect to the stiffness ratio α, the choice of boundary conditions may influence the results' quality to a large extent. In case of a low stiffness ratio $\alpha = 0.01$ (stiff matrix and soft inclusions), kinematic uniform boundary conditions and periodic boundary conditions predict very similar effective properties. In contrast, the static uniform boundary conditions reveal large discrepancies of 22.7% up to 55.3% for elastic material behavior and 18.0% up to 40.4% for von Mises plasticity.

If the composite under consideration possesses a high stiffness ratio, the situation drastically changes. In this case, the static uniform boundary conditions' performance enhances and the results are within the range of the periodic boundary conditions. The kinematic uniform boundary conditions, however, clearly overestimate the effective material properties to an unacceptable degree.

---

[10]Due to the meshing effect voxel meshes possess a slightly higher inclusion volume fraction, resulting in slight variations from the tetra meshes.
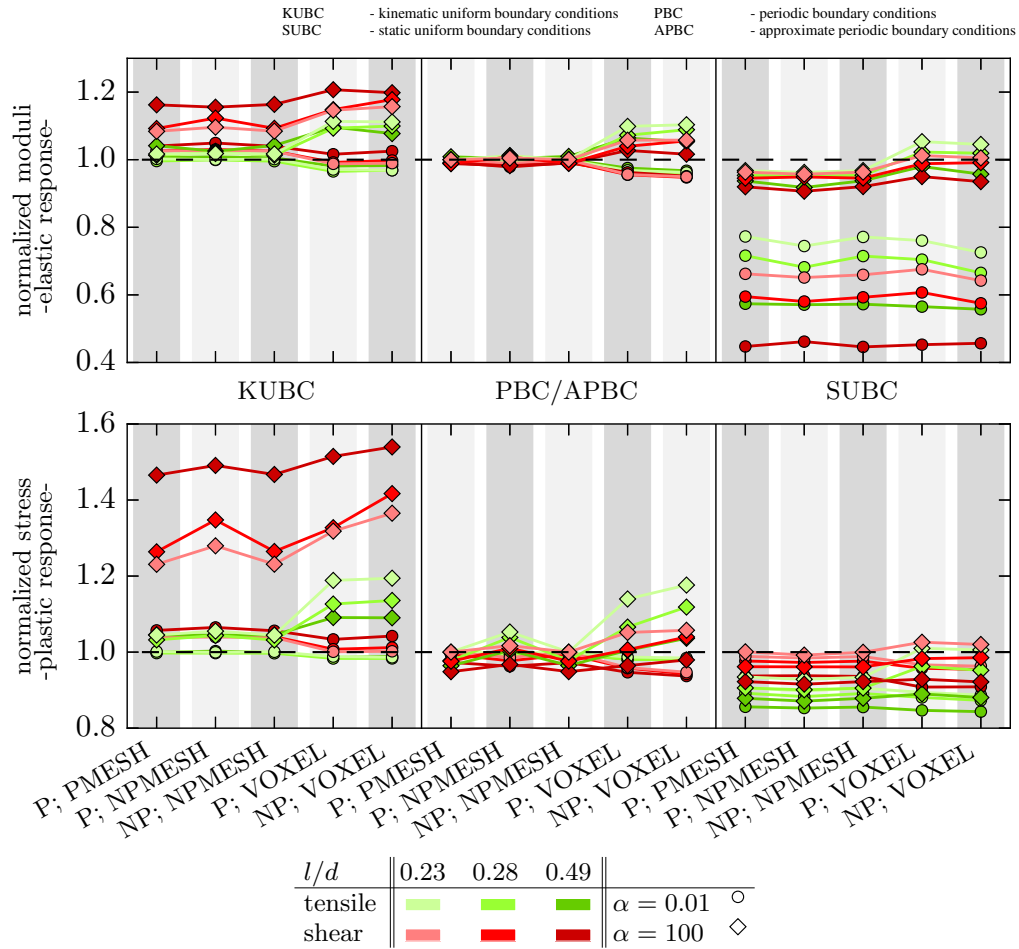
Figure 6. Normalized effective Young's and shear moduli and macroscopic stress responses (tensile: $\bar{\sigma}_{11}$, shear: $\bar{\sigma}_{12}$) at a state of deformation featuring a pronounced plastic deformation for all model variants, RVE sizes l/d and stiffness ratio α.

As discussed in Section 3.2.1, a fully periodic topology-mesh-RVE is not worth the construction effort and thus nonperiodic counterparts are strongly recommended. In this case, truly periodic boundary conditions must be replaced by approximate periodic boundary conditions, as described in Section 2.3.1. Advantageously, they are easily set up and their performance is by no means inferior to the truly periodic boundary conditions, see Figure 7. Disadvantageously, they necessitate slightly longer computational times.

If the finite element model is set up for one particular material or for one set of materials with similar stiffness ratios, either all high or all low, a short investigation of the different uniform boundary conditions might be well worth the effort to circumvent the fully periodic setup. If the model, however, is set up for materials with a strong deviation in the stiffness ratio, one needs to invest the effort of setting up periodic or approximate periodic boundary conditions in order to obtain meaningful numerical results for all simulations. In particular, the presented approximate boundary conditions ease the model generation effort.
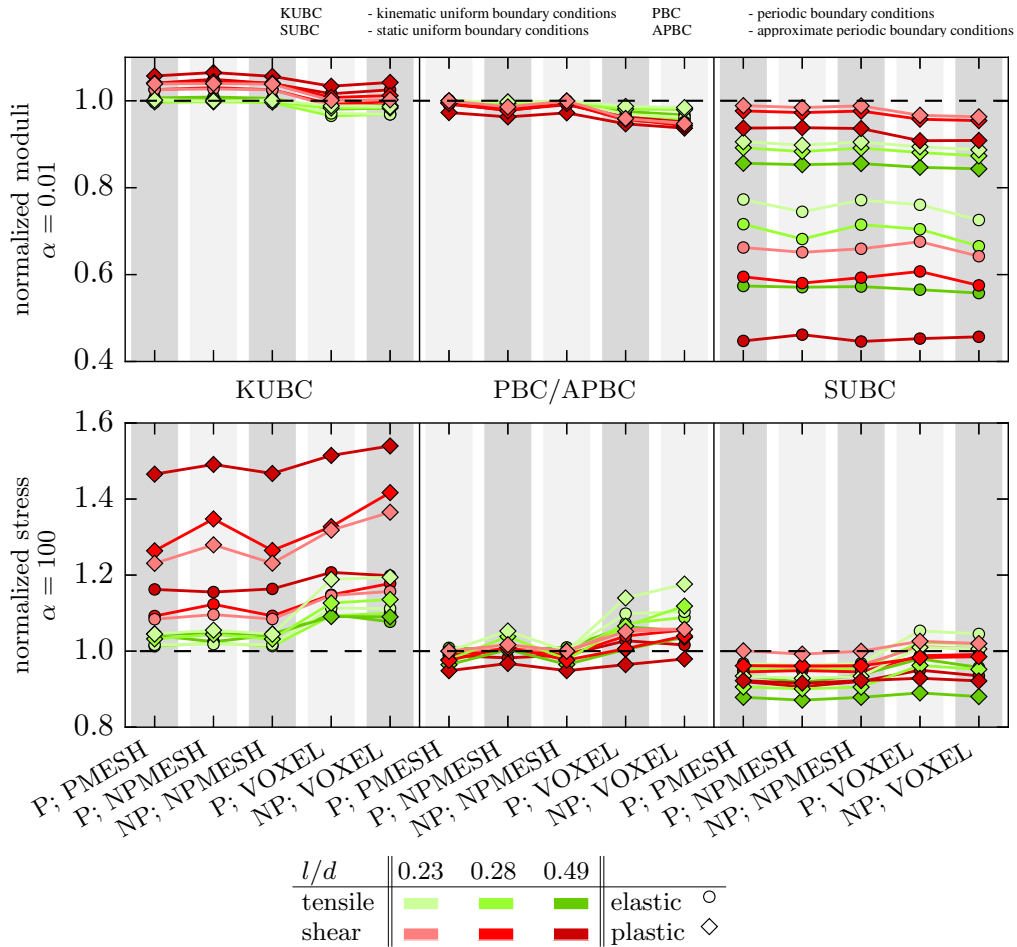
Figure 7. Normalized responses—effective Young's and shear moduli and macroscopic stress responses (tensile: $\bar{\sigma}_{11}$, shear: $\bar{\sigma}_{12}$) at a state of deformation ($\bar{\varepsilon}_{11} = \bar{\varepsilon}_{12} = 0.05$) featuring a pronounced plastic deformation for all model variants—for all model variants in the light of different and stiffness ratios α.

4. Conclusion

The current work presents a systematic study of different homogenization approaches. The RVEs of the matrix-inclusion composites were randomly generated and employed to compute effective material properties.

Within our benchmark study, we examined similar results for the simplest possible model setup (a nonperiodic RVE featuring a structured voxel discretization) and the most sophisticated approach of a fully periodic model setup.

For different stiffness ratios, nonperiodic and periodic microstructural topologies, periodic and nonperiodic tetrahedral meshes as well as structured voxel discretizations, kinematic and static uniform boundary conditions, approximate periodic boundary conditions and exact periodic boundary conditions

stiffness ratio	effective material parameters	inclusion positions		
		center	corner	side
$\alpha = \frac{1}{100}$	$\bar{E}_{11}$ [MPa]	3834.62	3833.99	3835.21
	$\bar{G}_{12}$ [MPa]	1310.01	1310.04	1310.12
$\alpha = 100$	$\bar{E}_{11}$ [MPa]	3765.93	3764.36	3766.65
	$\bar{G}_{12}$ [MPa]	1291.44	1291.39	1291.54

Table A1. Macroscopic material parameters for different single inclusion RVEs with approximate periodic boundary conditions.

were investigated. Subjected to macroscopic uniaxial tensile and simple shear loading cases, the effect of the individual model setups were analyzed. All simulations were conducted for linear elastic as well as nonlinear elastic-plastic material behavior.

As reported in the literature, kinematic uniform boundary conditions are a rougher choice in homogenization, leading to overly stiff responses, while static uniform boundary conditions show a softer response. Our studies show that kinematic uniform boundary conditions and static uniform boundary conditions are very sensitive with respect to the stiffness ratio. On the one hand, kinematic uniform boundary conditions show superior performance at low stiffness ratios, whereas static uniform boundary conditions are more suitable for high stiffness ratios.

Approximate periodic boundary conditions are very convenient to circumvent a cumbersome generation of periodic meshes. Thus, generation of truly periodic RVEs is not worth the effort.

Appendix: Performance study of approximate periodic boundary conditions

The following analysis indicates the effectiveness and feasibility of the approximated periodic boundary conditions introduced in Section 2.3.1. In compliance with Miehe [Miehe and Koch 2002], we investigate three different microstructures for a material with a periodic inclusion arrangement as shown in Figure A1:

(a) inclusion at RVE center;

(b) one eighth of the inclusion at each RVE corner;

(c) inclusion very close to one side of the RVE.

Due to the assumed periodic arrangement of the inclusion, all RVEs represent the same microstructure. The aspect ratio of the major spheroid axis (l) and the RVE length (d) is $l/d = 0.28$. The volume fraction of the single inclusion is 0.4%. We use a free meshing technique resulting in a nonperiodic mesh topology and apply approximate periodic boundary conditions. As in Section 3.1, we consider two stiffness ratios with the material properties given in Table 2. Tensile and shear loadings are applied. Table A1 lists the resulting macroscopic material parameters. The variations of the effective material parameters are negligible, i.e., the three different geometric setups yield almost identical results. Figure A1 exemplarily depicts contour plots of the von Mises stress distribution for tensile and shear loadings for a stiffness ratio of $\alpha = 100$. Regarding the stress distribution, similar patterns for the different variants are observable which indicates the conformity of the simulations. However, some artificial stress concentrations are
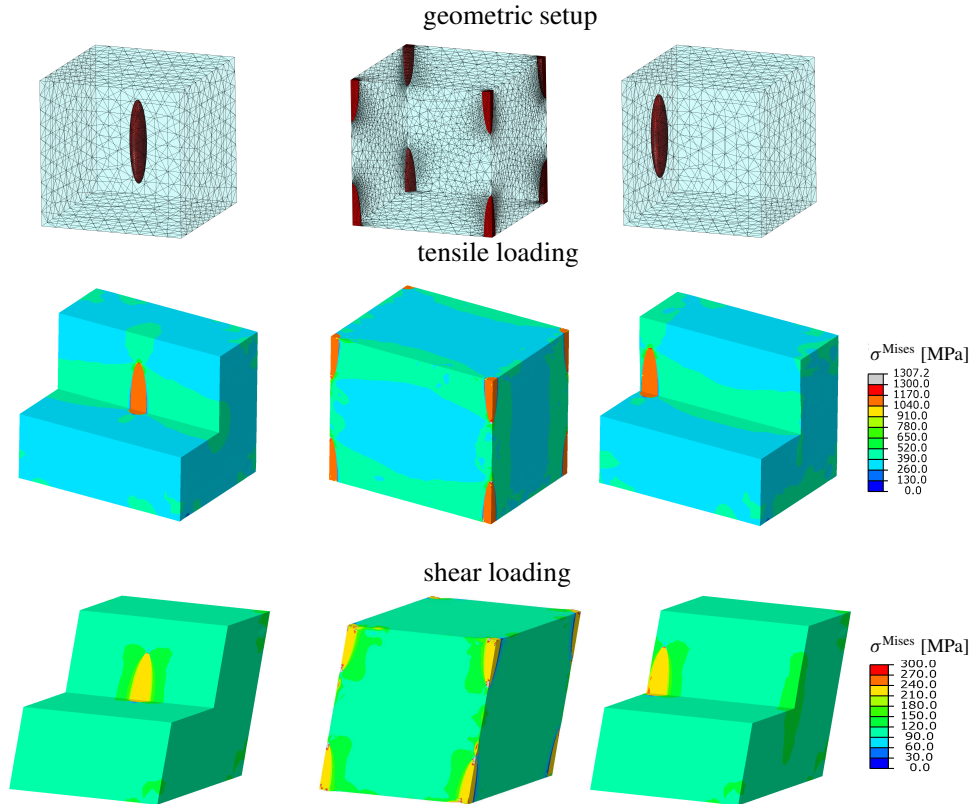
Figure A1. Geometric setup and von Mises stress distributions σ^v_{Mises} for tensile and shear loadings for a stiffness ratio of $\alpha = 100$: left, center inclusion; center, corner inclusion and, right, side inclusion.

present near the RVE edges due to the nonconformity of the mesh and the consequences of the approximations introduced by the approximate periodic boundary conditions. Nevertheless, the influences on the macroscopic properties are negligible. Thus, approximated periodic boundary conditions are feasible.

Acknowledgments

References

[Benzley et al. 1995] S. E. Benzley, E. Perry, K. Merkley, B. Clark, and G. Sjaardema, "A comparison of all hexagonal and all tetrahedral finite element meshes for elastic and elasto-plastic analysis", pp. 179–191 in *Proceedings of the 4th International Meshing Roundtable*, 1995.

[Böhm 1998] H. J. Böhm, "A short introduction to basic aspects of continuum micromechanics", Institute of Lightweight Design and Structural Biomechanics, 1998, available at https://www.ilsb.tuwien.ac.at/links/downloads/ilsbrep206.pdf.

[Böhm and Han 2001] H. J. Böhm and W. Han, "Comparisons between three-dimensional and two-dimensional multi-particle unit cell models for particle reinforced metal matrix composites", *Model. Simul. Mater. Sci. Eng.* **9**:2 (2001), 47–65.

[Böhm et al. 2002] H. J. Böhm, A. Eckschlager, and W. Han, "Multi-inclusion unit cell models for metal matrix composites with randomly oriented discontinuous reinforcements", *Comput. Mater. Sci.* **25**:1–2 (2002), 42–53.

[Carl et al. 2006] J. Carl, D. Müller-Hoeppe, and M. Meadows, "Comparison of tetrahedral and brick elements for linear elastic analysis", Term Project, University of Colorado at Boulder, 2006, available at http://www.colorado.edu/engineering/CAS/courses.d/AFEM.d/AFEM.projects.d/AFEM.projects.2006.d/AFEM.pr.06.CMM.d/CarlMullerMeadows.report.pdf.

[Dirrenberger et al. 2014] J. Dirrenberger, S. Forest, and D. Jeulin, "Towards gigantic RVE sizes for 3D stochastic fibrous networks", *Int. J. Solids Struct.* **51**:2 (2014), 359–376.

[Fritzen and Böhlke 2011] F. Fritzen and T. Böhlke, "Periodic three-dimensional mesh generation for particle reinforced composites with application to metal matrix composites", *Int. J. Solids Struct.* **48**:5 (2011), 706–718.

[Fritzen et al. 2009] F. Fritzen, T. Böhlke, and E. Schnack, "Periodic three-dimensional mesh generation for crystalline aggregates based on Voronoi tessellations", *Comput. Mech.* **43**:5 (2009), 701–713.

[Geers et al. 2010] M. G. D. Geers, V. Kouznetsova, and W. A. M. Brekelmans, "Multi-scale computational homogenization: trends and challenges", *J. Comput. Appl. Math.* **234**:7 (2010), 2175–2182.

[Gitman et al. 2007] I. M. Gitman, H. Askes, and L. J. Sluys, "Representative volume: existence and size determination", *Eng. Fract. Mech.* **74**:16 (2007), 2518–2534.

[Glüge 2013] R. Glüge, "Generalized boundary conditions on representative volume elements and their use in determining the effective material properties", *Comput. Mater. Sci.* **79** (2013), 408–416.

[Gusev 1997] A. A. Gusev, "Representative volume element size for elastic composites: a numerical study", *J. Mech. Phys. Solids* **45**:9 (1997), 1449–1459.

[Hill 1963] R. Hill, "Elastic properties of reinforced solids: some theoretical principles", *J. Mech. Phys. Solids* **11**:5 (1963), 357–372.

[Javili et al. 2017] A. Javili, S. Saeb, and P. Steinmann, "Aspects of implementing constant traction boundary conditions in computational homogenization via semi-Dirichlet boundary conditions", *Comput. Mech.* **59**:1 (2017), 21–35.

[Kanit et al. 2003] T. Kanit, S. Forest, I. Galliet, V. Mounoury, and D. Jeulin, "Determination of the size of the representative volume element for random composites: statistical and numerical approach", *Int. J. Solids Struct.* **40**:13–14 (2003), 3647–3679.

[Kari et al. 2007] S. Kari, H. Berger, R. Rodriguez-Ramos, and U. Gabbert, "Computational evaluation of effective material properties of composites reinforced by randomly distributed spherical particles", *Compos. Struct.* **77**:2 (2007), 223–231.

[Kassem 2009] G. A. Kassem, *Micromechanical material models for polymer composites through advanced numerical simulation techniques*, Ph.D. thesis, RWTH Aachen University, 2009, available at http://publications.rwth-aachen.de/record/51389.

[Klusemann et al. 2012] B. Klusemann, H. J. Böhm, and B. Svendsen, "Homogenization methods for multi-phase elastic composites with non-elliptical reinforcements: comparisons and benchmarks", *Eur. J. Mech. A Solids* **34** (2012), 21–37.

[Larsson et al. 2011] F. Larsson, K. Runesson, S. Saroukhani, and R. Vafadari, "Computational homogenization based on a weak format of micro-periodicity for RVE-problems", *Comput. Methods Appl. Mech. Eng.* **200**:1-4 (2011), 11–26.

[Lombardo et al. 1994] B. S. Lombardo, H. Keskkula, and D. R. Paul, "Influence of ABS type on morphology and mechanical properties of PC/ABS blends", *J. Appl. Polym. Sci.* **54**:11 (1994), 1697–1720.

[McBride et al. 2012] A. McBride, J. Mergheim, A. Javili, P. Steinmann, and S. Bargmann, "Micro-to-macro transitions for heterogeneous material layers accounting for in-plane stretch", *J. Mech. Phys. Solids* **60**:6 (2012), 1221–1239.

[Michel et al. 1999] J. C. Michel, H. Moulinec, and P. Suquet, "Effective properties of composite materials with periodic microstructure: a computational approach", *Comput. Methods Appl. Mech. Eng.* **172**:1–4 (1999), 109–143.

[Michler 1992] G. H. Michler, *Kunststoff-Mikromechanik: Morphologie, Deformations-und Bruchmechanismen*, 1992.

[Miehe and Koch 2002] C. Miehe and A. Koch, "Computational micro-to-macro transitions of discretized microstructures undergoing small strains", *Arch. Appl. Mech.* **72**:4 (2002), 300–317.

[Nguyen et al. 2012] V.-D. Nguyen, E. Béchet, C. Geuzaine, and L. Noels, "Imposing periodic boundary condition on arbitrary meshes by polynomial interpolation", *Comput. Mater. Sci.* **55** (2012), 390–406.

[Pecullan et al. 1999] S. Pecullan, L. V. Gibiansky, and S. Torquato, "Scale effects on the elastic behavior of periodic and hierarchical two-dimensional composites", *J. Mech. Phys. Solids* **47**:7 (1999), 1509–1542.

[Perić et al. 2011] D. Perić, E. A. de Souza Neto, R. A. Feijóo, M. Partovi, and A. J. C. Molina, "On micro-to-macro transitions for multi-scale analysis of non-linear heterogeneous materials: unified variational basis and finite element implementation", *Int. J. Numer. Methods Eng.* **87**:1–5 (2011), 149–170.

[Saeb et al. 2016] S. Saeb, P. Steinmann, and A. Javili, "Aspects of computational homogenization at finite deformations: a unifying review from Reuss' to Voigt's bound", *Appl. Mech. Rev. (ASME)* **68**:5 (2016), 050801–050801–33.

[Schneider et al. 2016] K. Schneider, B. Klusemann, and S. Bargmann, "Automatic three-dimensional geometry and mesh generation of periodic representative volume elements for matrix-inclusion composites", *Adv. Eng. Softw.* **99** (2016), 177–188.

[Schröder and Hackl 2014] J. Schröder and K. Hackl (editors), *Plasticity and beyond: microstructures, crystal-plasticity and phase transitions*, CISM International Centre for Mechanical Sciences. Courses and Lectures **550**, Springer, Vienna, 2014.

[Seelig and Van der Giessen 2009] T. Seelig and E. Van der Giessen, "A cell model study of crazing and matrix plasticity in rubber-toughened glassy polymers", *Comput. Mater. Sci.* **45**:3 (2009), 725–728.

[Suquet 1985] P. M. Suquet, "Local and global aspects in the mathematical theory of plasticity", pp. 279–310 in *Plasticity today: modelling, methods and applications*, vol. 198, edited by A. Sawczuk and G. Bianchi, Elsevier, London, 1985.

[Torquato 2002] S. Torquato, *Random heterogeneous materials: microstructure and macroscopic properties*, Interdisciplinary Applied Mathematics **16**, Springer, New York, 2002.

[Xia et al. 2003] Z. Xia, Y. Zhang, and F. Ellyin, "A unified periodical boundary conditions for representative volume elements of composites and applications", *Int. J. Solids Struct.* **40**:8 (2003), 1907–1921.

[Yuan and Fish 2008] Z. Yuan and J. Fish, "Toward realization of computational homogenization in practice", *Int. J. Numer. Methods Eng.* **73**:3 (2008), 361–380.

[Yue and E 2007] X. Yue and W. E, "The local microscale problem in the multiscale modeling of strongly heterogeneous media: effects of boundary conditions and cell size", *J. Comput. Phys.* **222**:2 (2007), 556–572.

KONRAD SCHNEIDER: Konrad.Schneider@tuhh.de
Institute of Continuum Mechanics and Material Mechanics, Hamburg University of Technology, D-22073 Hamburg, Germany

BENJAMIN KLUSEMANN: Benjamin.Klusemann@leuphana.de
Institute of Product and Process Innovation, Leuphana University of Lüneburg, D-21339 Lüneburg, Germany
and
Institute of Materials Research, Helmholtz-Zentrum Geesthacht, D-21502 Geesthacht, Germany

SWANTJE BARGMANN: bargmann@uni-wuppertal.de
Chair of Solid Mechanics, University of Wuppertal, D-42119 Wuppertal, Germany

■msp

HOMOGENIZATION OF A VIERENDEEL GIRDER WITH ELASTIC JOINTS INTO AN EQUIVALENT POLAR BEAM

ANTONIO GESUALDO, ANTONINO IANNUZZO, FRANCESCO PENTA AND GIOVANNI PIO PUCILLO

In this paper, a homogenization procedure of a Vierendeel girder with elastic joints is shown. The method is based on the Stephen transfer matrix analysis and employs (as a substitute continuum) a polar Timoshenko beam. The polar character of the equivalent beam arises quite naturally from the analysis of the pure bending eigenvector components of the girder force transfer matrix. Through the girder unit cell, two bending moments are transmitted: one is generated by the couple of axial forces acting on each nodal section of the beam, and the other is produced by the moments applied at the nodes of every section by the adjacent cells and is modeled as the resultant of the micropolar moments. Transfer force eigenvector analysis reveals that the unit cell bends while maintaining undeformed webs, a property that allows the evaluation of both the bending stiffnesses and the equivalent material micropolar scale parameter by means of straightforward equations.

The accuracy of the proposed method is verified by comparing the predictions of the homogenized model with literature data and with the results of the analysis of a series of girders carried out by the finite element method.

1. Introduction

Recently, in order to achieve simultaneously safety, sustainability and environmental compatibility, an increasing amount of attention has been paid to structural elements that are able to realize the optimal trade-off between strength and stiffness on one side, and lightness, economy and manufacturing times on the other.

A suitable example of a structural solution having these properties is the Vierendeel beam, which for this reason is often employed both in civil and industrial builds and in naval and aerospace constructions [Salmon et al. 2008; Tej and Tejová 2014; Nakayama 1985; Noor 1983; Cao et al. 2007]. The Vierendeel beam finds applications in railway structures as well. In fact, to design against the thermal track buckling phenomenon, rails, sleepers and fastenings are frequently modeled as a Vierendeel girder constrained to the ground by nonlinear springs, representative of the ballast actions [Kerr and Zarembski 1981; Pucillo 2016; De Iorio et al. 2014a; 2014b; 2014c].

The response of this kind of lattice beam to the service loads is usually analyzed in a CAE environment. The beam is reduced to a discrete system of finite elements and one of the solution methods for structural framework problems is then applied to it. If a great number of bays or unit cells composes the beam, it may be convenient to approximate its mechanical behavior by a continuum 1D model, whose properties are derived from those of the unit cell by a suitable homogenization method. In many cases, this kind

of approach offers the advantage of applying analytical solutions in closed form for the problem at hand. Moreover, the continuous approximation may be employed as a means of transition to a coarser discrete system with a smaller and more tractable set of kinematic and static unknowns.

However, the classical continuum theory does not provide an acceptable approximation and a micropolar theory has to be used in order to correctly analyze the in plane lattice bending. Several micropolar equivalent models have been reported in literature for the analysis of planar lattices [Noor 1988; Bazant and Christensen 1972; Kumar and McDowell 2004; Bakhvalov and Panasenko 1989; Hård af Segerstad et al. 2009; Wang and Stronge 1999; Warren and Byskov 2002; Onck 2002; Martinsson and Babuška 2007; Liu and Su 2009; Dos Reis and Ganghoffer 2012; Trovalusci et al. 2015; Bacigalupo and Gambarotta 2014; Hasanyan and Waas 2016]. However, studies on the micropolar models for analyzing beam-like lattices have not yet achieved the same advances. As far as the authors are aware, only two papers have specifically addressed this topic. In [Noor and Nemeth 1980], a rational approach was presented where stiffness parameters of the effective continuum model were obtained using energy equivalence concepts. Nodal displacements of the unit cell were obtained in an approximated way by a Taylor expansion of the kinematical model of the substitute continuum. Then, the equivalent stiffnesses were derived by equating the potential and kinetic energies of a unit cell of the lattice beam to those of the continuum. This approach leads to two questionable stiffness couplings: between the symmetric and antisymmetric components of the shear stresses and between the bending and couple stress moments. These make the solution of the equilibrium equations of the equivalent beam awkward for the simpler loading and constraining conditions. Furthermore, a key limitation of this research is that it does not take into account the girder joints elasticity.

More recently, Romanoff and Reddy [2014] used the modified couple stress Timoshenko beam theory [Ma et al. 2008; Reddy 2011] to analyze the transversal bending of web-core sandwich panels. The equivalent polar bending stiffness was determined by invoking the spring analogy criterion. According to this rule, along the substitute beam, the ratio of the couple stress moment to the total bending moment is given by the ratio of the chords' bending moments caused by the *thick face effect* to the moment of the couple of axial forces acting in the panels faces. As it will be shown, this assumption unfortunately leads to overestimates of the polar bending stiffness.

This article introduces an equivalent Timoshenko micropolar beam for the static analysis of Vierendeel girders with compliant joints. The adopted homogenization method is based on the force transfer matrix eigenanalysis presented in [Stephen and Wang 2000], where the homogenization of a truss made of hinged rods is also carried out as a numerical example. When this method is applied to the analysis of the girder, no approximations for the kinematical quantities nor subjective phenomenological assumptions on the inner moments are needed. The polar nature of the substitute beam is a direct consequence of the pure bending eigenvector structure of the force transfer matrix of the unit cell. Through the unit cell, two bending moments are transferred. The first one is generated by the axial forces acting on the nodal cross sections and corresponds to the Navier bending moment in the equivalent beam. The other one is due to the moments applied on the joints of the unit cell and is modeled by the polar moments. Furthermore, the ratio between the amplitudes of the two moments is such that the total moment is always transferred without deformations of the girder webs. On the basis of this property, equivalent bending stiffness and couple stress stiffness are expressed by means of a couple of surprisingly simple equations. These stiffnesses are also independent of the web properties, the cell length and the stiffness of web-chord
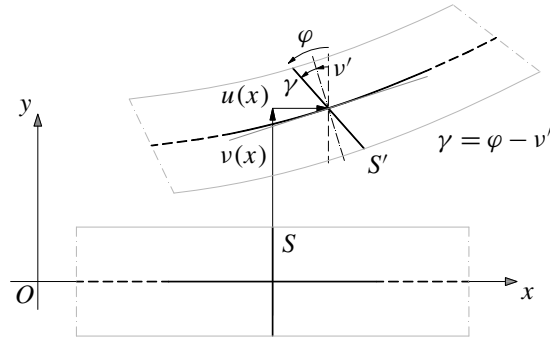
Figure 1. Kinematics of the Timoshenko beam.

joints, a result not yet reported in studies till now. Consequently, the polar material length scale ℓ is independent from the cell sizes and is a function only of the chords cross section geometry and material.

Finally, results from a validation study of the proposed model are also presented. The study has been carried out by means of both literature experimental data and the sensitivity analysis performed by finite element models.

2. The equivalent continuum

As an equivalent continuum, the modified polar Timoshenko beam is adopted [Ma et al. 2008; Reddy 2011]. The displacements (U, V) of a point $P(x, y)$ of the beam (see Figure 1) are given by

$$U = u(x) - y \cdot \varphi(x), \quad V = v(x),$$

where $u(x)$ and $v(x)$ denote respectively the longitudinal and transversal displacements of the beam axis and $\varphi(x)$ is the rotation of the cross section. The only nonzero strains at P are the normal strain in the x direction,

$$\varepsilon_x = \frac{\mathrm{d}u}{\mathrm{d}x} - y \frac{\mathrm{d}\varphi}{\mathrm{d}x},$$

the shear strain associated with the directions x and y,

$$\gamma_{xy} = \frac{\mathrm{d}v}{\mathrm{d}x} - \varphi(x),$$

and the curvature,

$$\chi_{xy} = \frac{1}{2} \frac{\mathrm{d}\omega}{\mathrm{d}x} = \frac{1}{4}\left(\frac{\mathrm{d}\varphi}{\mathrm{d}x} + \frac{\mathrm{d}^2 v}{\mathrm{d}x^2}\right),$$

where $\omega = \frac{1}{2}(\mathrm{d}v/\mathrm{d}x + \varphi)$ is the rotation of an elementary neighborhood of P in the x-y plane.

Denoting by $\delta(\cdot)$ the kinematically admissible variations of the strain components and by σ_x, τ_{xy} and m_{xy} respectively the normal, tangential and the couple stress acting on the beam cross section, the virtual

strain energy or internal work can be expressed as

$$\delta U = \int_l \int_A (\sigma_x \delta\varepsilon_x + \tau_{xy}\delta\gamma_{xy} + 2m_{xy}\delta\chi_{xy}) \, dA \, dx$$
$$= \int_l \left[N_x \frac{d\delta u}{dx} + M_x \frac{d\delta\varphi}{dx} + Q_x \left(\delta\varphi - \frac{d\delta v}{dx} \right) + \frac{1}{2} P_{xy} \left(\frac{d\delta\varphi}{dx} + \frac{d^2\delta v}{d^2 x} \right) \right] dx,$$

where l is the beam length and A is the area of its cross section,

$$N_x = \int_A \sigma_x \, dA, \quad Q_x = -\int_A \tau_{xy} \, dA, \tag{1}$$

are the beam axial and shear forces, while

$$M_x = -\int_A \sigma_x y \, dA \quad \text{and} \quad P_{xy} = \int_A m_{xy} \, dA \tag{2}$$

are the Navier and polar bending moments, respectively. It is worth nothing that the dual shear deformation of Q_x is

$$\gamma = -\gamma_{xy} = \varphi - \frac{dv}{dx}. \tag{3}$$

Under the assumption of homogeneous and isotropic linear elastic material, the stress-strain relationships are

$$\sigma_x = E\varepsilon_x, \quad \tau_{xy} = G\gamma_{xy}, \quad m_{xy} = 2G\ell^2\chi_{xy},$$

with E being the Young modulus, G the tangential elasticity modulus and ℓ the material length scale parameter. Substituting the previous constitutive relations into the expressions of the stress resultants (1) and (2) gives

$$N_x = A_{xx}\varepsilon_x, \qquad Q_x = D_Q\gamma,$$
$$M_x = D_{xx}\frac{d\varphi}{dX}, \quad P_{xy} = \tfrac{1}{2}S_{xy}\chi_{xy}, \tag{4}$$

where A_{xx} and D_Q are respectively the axial and shear beam stiffnesses, $D_{xx} = EI$ is the bending stiffness, with I the second order central moment of the beam cross section, and $S_{xy} = 4G\ell^2 A$ the couple stress bending stiffness.

The beam equilibrium equations can be derived by equating the virtual internal work δU to the virtual work of the external loads, integrating by parts and taking into account the beam boundary conditions. For the simpler loading and constraint conditions, approximate solutions for these equations can be obtained by the Fourier series method (see [Reddy 2011] for more details).

3. Girder transfer matrix analysis and homogenization

In this section, the equivalent beam properties are evaluated by employing the transfer matrix analysis of a unit cell. So far, the transfer matrix methods have been applied mostly for the dynamic analysis of repetitive or periodic structures [Mead 1970; Meirovitch and Engels 1977; Yong and Lin 1989; Zhong and Williams 1995; Langley 1996]. Only recently have they also been used for the elasto-static analysis of prismatic, curved and pretwisted repetitive beam-like lattices made of pin-jointed bars [Stephen and Zhang 2004; 2006; Stephen and Ghosh 2005].
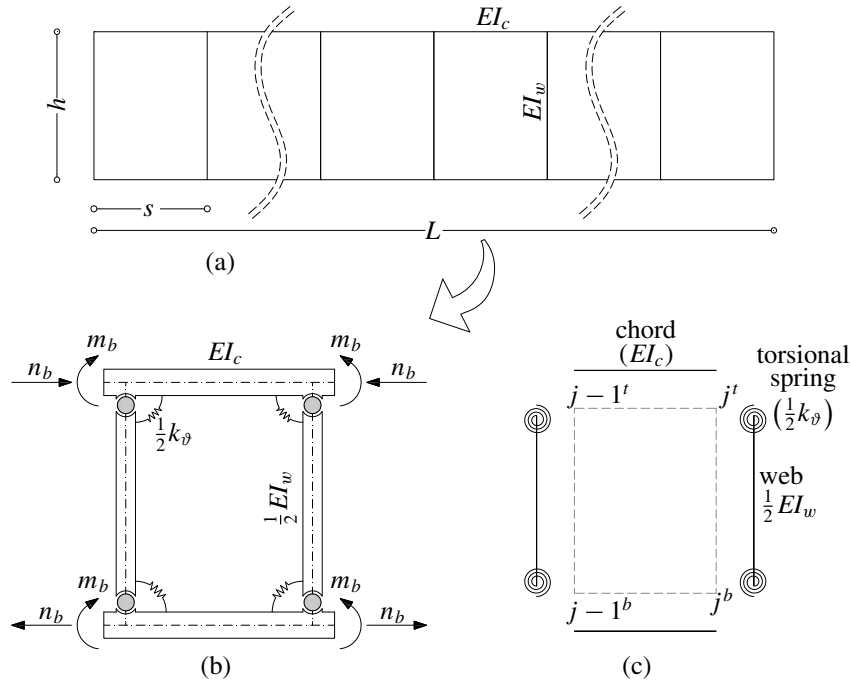
Figure 2. Vierendeel girder (a), unit cell (b) and exploded view of the elements composing the unit cell (c).

The main advantage of the method is that it allows evaluating both the Saint-Venant decay rates and the load transmission modes by carrying out an eigenanalysis of the transmission matrix G of the unit cell. Although it is conceptually simple, its practical implementation is problematic, since the G matrix is ill-conditioned and defective. Consequently, the Jordan block structure of G is very difficult to determine numerically. To overcome this problem, in this paper the force transfer matrix approach of Stephen and Wang [2000] is adopted. This method suppresses the redundant decay vectors and makes the assessment of the force transmission modes of the unit cell simpler.

In this study, the Vierendeel girder is modeled by assembling one-dimensional elements of Euler–Bernoulli type as represented in Figure 2. It consists of two straight parallel chords connected to the webs by means of torsional springs of stiffness k_ϑ. By these springs the elastic deformability of the web-chords' connections is taken into account. In Figure 2a the unit cell is depicted. Top and bottom chords have the same section, whose area and second order central moment are A_c and I_c, respectively. To respect the girder geometrical periodicity, cross sectional area and second order moment of the cell vertical beams are equal to the half part of the area A_w and second order moment I_w of the girder webs, while the stiffness of the unit cell torsional springs is $\frac{1}{2}k_\vartheta$.

In the following, we use the subscript j to identify any static or kinematic quantity concerning the nodal section j of the girder. Furthermore, to distinguish between the joints of a same section, we use superscripts t and b depending on whether the top or the bottom chords are involved. Coherently with this notation, the top and bottom joints of the section j are labeled $j^{(t)}$ and $j^{(b)}$.

For the sake of clarity, the nodal sections of the girder are numbered in such a way that sections $i - 1$
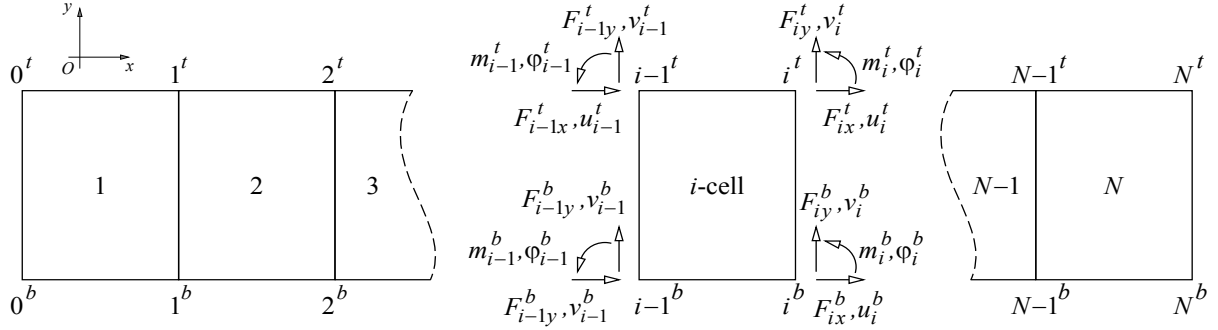
Figure 3. Unit cell nodes numbering with girder inner forces and nodal displacements.

and i bound the i-th cell respectively from the left and the right side, as shown in Figure 3. Therefore, the two extreme sections of a lattice beam of N cells are labeled correspondingly by 0 and N.

We denote with

$$s_j^t = [u_j^t, v_j^t, \varphi_j^t]^T \quad \text{and} \quad s_j^b = [u_j^b, v_j^b, \varphi_j^b]^T$$

the displacement vectors of the joints j^t and j^b, where $u_j^{(\cdot)}$ and $v_j^{(\cdot)}$ are the displacement components and $\varphi_j^{(\cdot)}$ the rotation of the joint $j^{(\cdot)}$. Therefore, the displacement vector of the nodal section j is $s_j = [s_j^{tT}, s_j^{bT}]^T$.

Similarly, the nodal forces applied on the joints j^t and j^b of the cell j are

$$p_j^t = \left[F_{jx}^t, F_{jy}^t, m_j^t\right]^T \quad \text{and} \quad p_j^b = \left[F_{jx}^b, F_{jy}^b, m_j^b\right]^T,$$

where $F_{jx}^{(\cdot)}$ and $F_{jy}^{(\cdot)}$ are respectively the axial and transversal components of the force and $m_j^{(\cdot)}$ the couple applied on the joint $j^{(\cdot)}$. Thus, the vector of the nodal forces acting on the section at the left side of the j-cell is

$$p_j = [\, p_j^{tT}, p_j^{bT}]^T.$$

In order to construct the displacement and force transfer matrix, we consider the couple of adjacent cells i and $i+1$ sharing the nodal cross section i. By equilibrium, in absence of external loads on the section, the nodal forces on the left sides of the cell $i+1$ are equal to $-p_i$.

The stiffness equations of the cells i and $i+1$ in partitioned form are thus given by

$$\begin{bmatrix} -p_{i-1} \\ p_i \end{bmatrix} = \begin{bmatrix} K_{LL} & K_{LR} \\ K_{RL} & K_{RR} \end{bmatrix} \cdot \begin{bmatrix} s_{j-1} \\ s_j \end{bmatrix}, \tag{5}$$

$$\begin{bmatrix} -p_i \\ p_{i+1} \end{bmatrix} = \begin{bmatrix} K_{LL} & K_{LR} \\ K_{RL} & K_{RR} \end{bmatrix} \cdot \begin{bmatrix} s_j \\ s_{j+1} \end{bmatrix}, \tag{6}$$

in which subscripts L and R adopted for the subpartitions of the stiffness matrix refer to the left and right side of the cell. For the problem at hand, the cell stiffness matrix has been obtained following the standard method adopted in the finite element analyses, that is by assembling the stiffness matrix of the chords and those of the elastic systems composed by a cell vertical beam and the couple of torsional springs constraining it to the chords (see Figure 2c).

Adding the second equation in (5) to the first equation within (6) eliminates the vector $\boldsymbol{p}_i$, since we obtain

$$0 = \boldsymbol{K}_{RL} \boldsymbol{s}_{i-1} + (\boldsymbol{K}_{RR} + \boldsymbol{K}_{LL}) \boldsymbol{s}_i + \boldsymbol{K}_{LR} \boldsymbol{s}_{i+1}. \tag{7}$$

From the previous equation written for the section $(N-1)$ of the girder, taking into account the boundary condition $\boldsymbol{s}_N = 0$, the following relationship between the displacement vector $\boldsymbol{s}_{N-1}$ and $\boldsymbol{s}_{N-2}$ is deduced:

$$\boldsymbol{s}_{N-1} = -\boldsymbol{S}_1^{-1} \boldsymbol{K}_{RL} \boldsymbol{s}_{N-2},$$

where $\boldsymbol{S}_1 = \boldsymbol{K}_{RR} + \boldsymbol{K}_{LL}$.

Substituting this result within relation (7) specialized to the case of section $(N-2)$, we have

$$\boldsymbol{s}_{N-2} = -\boldsymbol{S}_2^{-1} \boldsymbol{K}_{RL} \boldsymbol{s}_{N-3},$$

where $\boldsymbol{S}_2 = \boldsymbol{K}_{RR} + \boldsymbol{K}_{LL} - \boldsymbol{K}_{LR} \boldsymbol{S}_1^{-1} \boldsymbol{K}_{RL}$.

By iterating the previous algebraic operations until considering the section $j-1$, the displacement vector $\boldsymbol{s}_j$ of the inner section j can be expressed as function of the displacement vector $\boldsymbol{s}_{j-1}$ of the adjacent nodal section by means of the equation

$$\boldsymbol{s}_j = \boldsymbol{S}\, \boldsymbol{s}_{j-1},$$

where $\boldsymbol{S}$ is the j-cell displacement transfer matrix given by

$$\boldsymbol{S} = -\boldsymbol{S}_{N-j}^{-1} \boldsymbol{K}_{RL}, \tag{8}$$

with $\boldsymbol{S}_{N-j} = \boldsymbol{K}_{RR} + \boldsymbol{K}_{LL} - \boldsymbol{K}_{LR} \boldsymbol{S}_{(N-j+1)}^{-1} \boldsymbol{K}_{RL}$.

By expanding the stiffness matrix equation of the j-th cell and substituting in it the previous results, one obtains

$$\boldsymbol{p}_{j-1} = -\boldsymbol{K}_{LL} \boldsymbol{s}_{j-1} - \boldsymbol{K}_{LR} \boldsymbol{s}_j = -(\boldsymbol{K}_{LL} + \boldsymbol{K}_{LR} \boldsymbol{S}) \boldsymbol{s}_{j-1}, \tag{9a}$$

$$\boldsymbol{p}_j = \boldsymbol{K}_{RL} \boldsymbol{s}_{j-1} + \boldsymbol{K}_{RR} \boldsymbol{s}_j = (\boldsymbol{K}_{RL} + \boldsymbol{K}_{RR} \boldsymbol{S}) \boldsymbol{s}_{j-1}. \tag{9b}$$

Eliminating the displacement vector $\boldsymbol{s}_{j-1}$ in (9) gives

$$\boldsymbol{p}_j = \boldsymbol{M} \boldsymbol{p}_{j-1},$$

where $\boldsymbol{M} = -(\boldsymbol{K}_{RL} + \boldsymbol{K}_{RR} \boldsymbol{S})(\boldsymbol{K}_{LL} + \boldsymbol{K}_{LR} \boldsymbol{S})^{-1}$ is the force transfer matrix of the cell j.

Notice that the matrix $\boldsymbol{M}$ depends on the recurrence index j. It must have three unity eigenvalues corresponding to the force transmission modes and three nonunitary eigenvalues corresponding instead to the decay rates of self-equilibrated loadings [Stephen and Wang 2000]. However, when the j-index is not sufficiently high, numerical determination of the unitary eigenvector may be difficult or impossible. For the present analysis, a value of j equal to 100 has allowed the detection of the unit eigenvalues and the related eigenvectors with a precision of four decimal digits, at least.

Eigenspaces of $\boldsymbol{M}$ associated to unit eigenvalues have dimensions 1 and 2. The one-dimensional eigenspace is related to the transmission of the beam axial force. Pure bending eigenvectors $\boldsymbol{E}_b$ of the matrix $\boldsymbol{M}$ belong instead to the eigenspace of dimension 2, since they may be coupled with the shear
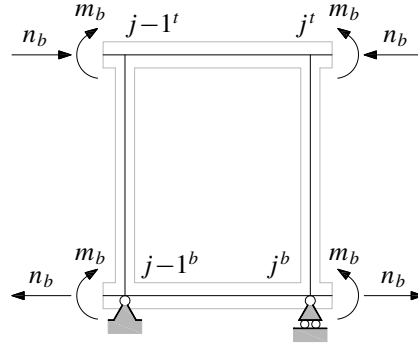
Figure 4. Unit cell under pure bending loading.

forces vector S_f. The latter is given by the chain rule defining the principal vector associated to the bending eigenvector E_b:

$$M \cdot E_b = E_b, \quad M \cdot S_f = E_b + S_f. \tag{10}$$

However, for the considered problem S_f can be obtained directly on the basis of very simple equilibrium considerations, without solving the algebraic problem defined by (10). In fact, it is worth noting that (9b) is the equilibrium relationship between the bending moments and the shear forces acting on a single cell.

The homogenized beam stiffnesses can be determined by averaging over the unit cell length s the cell responses under the load conditions defined by the unitary eigen- and principal vectors.

The eigenvector of the axial force E_a is

$$E_a = [n, 0, 0, n, 0, 0]^T.$$

Due to the symmetry of the cell, the two axial forces n are transmitted without bending; consequently only the chords deform with the axial elongations ns/EA_c. Thus, the equivalent axial stiffness of the homogenized beam is

$$A_{xx} = 2EA_c.$$

The pure bending eigenvector E_b has components

$$E_b = [-n_b, 0, m_b, +n_b, 0, m_b]^T,$$

where m and $\pm n_b$ are respectively the moments and the axial forces acting on the joints of the right side of the unit cell. The m moments correspond to the polar bending moment while the axial forces $\pm n_b$ generate the bending couple associated to the Navier moment in the Timoshenko polar beam.

To evaluate the equivalent bending stiffnesses, the cell displacements and rotations were calculated solving the elastic scheme of Figure 4. Denoting the upper and lower chords elongations respectively as $\Delta u_b = u_j^b - u_{j-1}^b$ and $\Delta u_t = u_j^t - u_{j-1}^t$, the mean curvature of the cell can be written in the form

$$\frac{1}{R} = \frac{\Delta u_b - \Delta u_t}{hs}.$$

Therefore, the equivalent bending stiffness D_{xx} is given by

$$D_{xx} = n_b h \cdot R = \frac{n_b h^2 s}{\Delta u_b - \Delta u_t}. \tag{11}$$

Polar bending stiffness can be evaluated by observing that when the shear force is zero, from (3) and (4) it follows that

$$\frac{d\varphi}{dX} = \frac{d^2 v}{dX^2}.$$

Hence, the polar and Navier moment of the homogenized beam make work by the same generalized strain, namely the beam curvature $d\varphi/dX$. For this reason, we evaluate the polar bending stiffness as

$$S_{xy} = 2m_b R = \frac{2m_b s h}{\Delta u_b - \Delta u_t}. \tag{12}$$

The principal vector of the shear forces is

$$S_f = \left[0, \ \tfrac{1}{2}T, \ 0, \ 0, \ \tfrac{1}{2}T, \ 0\right]^T,$$

where the shear resultant force T is obtained by the in plane rotation equilibrium of the unit cell

$$-Ts + n_b h + 2m_b = 0.$$

The equivalent shear stiffness is determined by analyzing the scheme in Figure 5. In it, the transversal load components of the principal vector S_f act on the left section of the unit cell, while on the right section, the axial forces vectors $\pm n_b$ and the moments m_b, given by the pure bending eigenvector E_b, are applied. Recalling the expression of the shear angle γ and denoting by

$$\hat{\varphi} = \tfrac{1}{4}(\varphi_{i-1}^{(t)} + \varphi_{i-1}^{(b)} + \varphi_i^{(t)} + \varphi_i^{(b)})$$

the average rotation angle of the cell and by

$$\frac{\Delta v}{s} = \frac{-v_{i-1}^{(t)} - v_{i-1}^{(b)}}{2s}$$

the mean slope of the cell center-line, the shear stiffness can be expressed as

$$D_Q = \frac{T}{\Delta v/s - \hat{\varphi}}. \tag{13}$$

Equations (11), (12) and (13) completely define the elastic behavior of the equivalent Timoshenko beam. The range of validity of these homogenized equations is analyzed in the next section on the basis of both literature experimental data and the numerical results of a sensitivity analysis.

4. Validation study

To verify the accuracy of the proposed micropolar beam, we use the experimental data from [Jutila and Romanoff 2007; Romanoff et al. 2007; 2009] as reported in [Romanoff and Reddy 2014]. They were obtained from specimens extracted from web-core sandwich panels. The specimens had unit cell length $s = 120\,\text{mm}$, web height $h_w = 40\,\text{mm}$, nominal web thickness $t_w = 4\,\text{mm}$ and were made of a steel
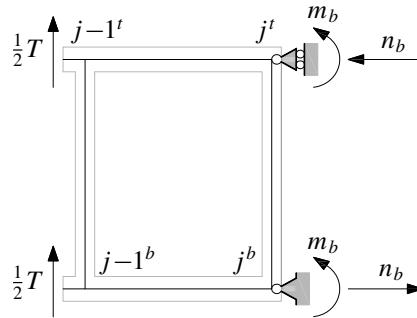
Figure 5. Unit cell under shear and bending loading.

having Young modulus $E = 200$–220 GPa and Poisson ratio $\nu = 0.3$. Top and bottom panels face plates had the same thickness $t = 2.5$–3 mm. A three point bending test was carried out on a beam of only 4 unit cells. Four point bending tests were executed on beams made of 9 and 15 unit cells. In these tests, the loads were applied at $\frac{1}{3}$ and at $\frac{2}{3}$ of the beam span L.

Only the deflection of the half-span section was measured for the 4 cell beam tested under the three points loading condition. For the 9 cell beam tested under the four points loading, the deflection was measured at the abscissas $X = 360$ mm. For the 15 cell beam having span $L = 1800$ mm, the deflections were instead measured at the abscissas $X = 200$ mm, $X = 400$ mm, $X = 600$ mm and $X = 1200$ mm. The measured deflections are listed in Table 1, together with the stiffnesses and the deflections obtained under the assumption of plane strain by both the theory of Reddy–Romanoff and the model we propose. As it can be seen, the deflections predicted by the latter are in good agreement with the experimental data. It is worth noting that the bending and shear stiffnesses from the Reddy–Romanoff theory are very close to those of our model while the Reddy–Romanoff polar stiffness results are at least four times greater than the results obtained by the present method.

To study the accuracy of the predictions from the equivalent beam defined in Section 3 in greater detail, it is essential to consider a wider data set than [Romanoff and Reddy 2014], including information on the effects of all the geometrical parameters influencing the girder response. To this end, a series of girder finite element models under the three points bending condition has been developed by assembling beam elements of Euler–Bernoulli type.

Given the properties of the chords and web cross-sections, as a first approximation the height h of the girder determines the relative importance of the two bending moments acting on its cross section. For this reason, in the first set of finite element analyses, the effects of different values of h for several values of the cell aspect ratio $\alpha = s/h$ and girder aspect ratio $\beta = L/h$ have been considered, under the assumption that the joints between chords and webs are rigid and that both chords and webs have the same cross section, specifically HEA100.

The results from these analysis are reported in Figure 5 where the joints vertical displacements v_i of the girder finite element models having $h = 300, 600, 1200$ mm, $\alpha = 0.5, 1, 2$ and $\beta = 6, 12, 24, 48$ are compared with the elastic curves $v(x)$ of the corresponding homogenized beams. Previous values of h, α and β as well as the cross section properties were chosen in order to obtain a girder geometry similar to those encountered in the practice of structural design. The stiffnesses of the homogenized beams of Figure 5 are listed in Table 2 together with the corresponding values of the following nondimensional

	Unit	4 unit cells specimen [Jutila and Romanoff 2007]	9 unit cells specimen [Romanoff et al. 2009]	15 unit cell specimen [Romanoff et al. 2007]			
F	[N/m]	2000	4000	1000			
E	[GPa]	212	221	221			
ν		−	−	0.3			
B	[mm]	50	50	1000			
s	[mm]	120	120	120			
α	−	2.79	2.82	2.8			
β	−	4	9	15			
A_c	[mm^2]	152	126	2860			
I_c	[mm^3]	117	66.7	1950			
I_w	[mm^3]	273	261	5210			
k_{J}	[kN]	107	113	107			
D_{xx}	[kN m]	657 / **656**	554 / **553**	613 / **612**			
D_Q	[kN/m]	388 / **500**	304 / **368**	355 / **447**			
S_{xy}	[kN m]	4.33 / **1.09**	2.57 / **0.648**	3.61 / **0.908**			
	$x/L =$	$\frac{1}{2}$	$\frac{1}{3}$	$\frac{1}{9}$	$\frac{2}{9}$	$\frac{1}{3}$	$\frac{1}{2}$
$v(x/L)$ [mm]		0.487	4.69	0.675	1.33	1.9	2.02
		0.439	**4.07**	**0.561**	**1.109**	**1.606**	**1.676**
		0.446	*4.14*	*0.750*	*1.37*	*1.88*	*2.02*

Table 1. Top: geometrical details of 4, 9 and 15 unit cell specimens. Middle: values of D_{xx}, D_Q and S_{xy} obtained from the Reddy–Romanoff theory (before the slash) and with the present model (bold, after the slash). Bottom: Values of v for various x/L, obtained from the Reddy–Romanoff theory (first of three rows of results), the present theory (middle row, bold), and experiment (bottom row, slanted). Experimental and Reddy–Romanoff data are from [Romanoff and Reddy 2014].

measure of the homogenization error:

$$e = \left\{ \frac{1}{\bar{n}} \cdot \sum_{i \in \bar{\mathbb{N}}} \left[\frac{v(x_i) - v_i}{v_i} \right]^2 \right\}^{1/2},$$

where $\bar{\mathbb{N}}$ is the set of $\bar{n}$ nodes belonging to the inner model cross section of the girder and x_i is the abscissas of these nodes.

For all the girder aspect ratio considered, the homogenization error quickly decreases as the cell aspect ratio decreases or equivalently as the number of cell per beam unit length increases. This behavior is expected since the adopted method of homogenization is asymptotically exact; that is, $e \to 0$ when $\alpha/\beta = s/L \to 0$. The highest values of the homogenization error in Table 2 are attained when the girder aspect ratio β is equal to 6, namely when the girder is very stout and its behavior can be approximated only roughly by any beam model. Instead, the homogenization errors in Table 2 are much smaller for the more slender girders.

	α [−]	D_Q [Nmm^{-1}]	S_{xy} [Nmm]	D_{xx} [Nmm]	e_{ave} [−]
$h = 300\,\mathrm{mm}$ $\beta = 24$	0.50	$1.579 \cdot 10^8$	$1.481 \cdot 10^{12}$	$2.026 \cdot 10^{13}$	$8.233 \cdot 10^{-3}$
	1.00	$6.580 \cdot 10^7$	”	”	$5.312 \cdot 10^{-3}$
	2.00	$2.468 \cdot 10^7$	”	”	$1.107 \cdot 10^{-2}$
$h = 600\,\mathrm{mm}$ $\beta = 12$	0.50	$3.948 \cdot 10^7$	$1.481 \cdot 10^{12}$	$8.105 \cdot 10^{13}$	$1.760 \cdot 10^{-2}$
	1.00	$1.645 \cdot 10^7$	”	”	$4.188 \cdot 10^{-2}$
	2.00	$6.169 \cdot 10^6$	”	”	$6.877 \cdot 10^{-2}$
$h = 1200\,\mathrm{mm}$ $\beta = 6$	0.50	$9.871 \cdot 10^6$	$1.481 \cdot 10^{12}$	$3.242 \cdot 10^{14}$	$9.880 \cdot 10^{-2}$
	1.00	$4.113 \cdot 10^6$	”	”	$1.532 \cdot 10^{-1}$
	2.00	$1.542 \cdot 10^6$	”	”	$3.350 \cdot 10^{-1}$

Table 2. Equivalent stiffnesses and homogenization errors for Vierendeel girders with various heights H (span $L = 7600\,\mathrm{mm}$, chords and web sections: HEA100).

	webs [−]	D_Q [Nmm^{-1}]	S_{xy} [Nmm]	D_{xx} [Nmm]	e_{ave} [−]
$h = 300\,\mathrm{mm}$ $\alpha = 0.5$ $\beta = 24$	HEA100	$3.131 \cdot 10^7$	$2.570 \cdot 10^{12}$	$2.417 \cdot 10^{13}$	$8.465 \cdot 10^{-3}$
	HEA120	$4.284 \cdot 10^7$	”	”	$1.739 \cdot 10^{-3}$
	HEA140	$5.399 \cdot 10^7$	”	”	$1.553 \cdot 10^{-3}$
	HEA160	$6.289 \cdot 10^7$	”	”	$2.283 \cdot 10^{-3}$
$h = 600\,\mathrm{mm}$ $\alpha = 1.0$ $\beta = 12$	HEA100	$1.955 \cdot 10^7$	$2.570 \cdot 10^{12}$	$9.670 \cdot 10^{13}$	$4.456 \cdot 10^{-2}$
	HEA120	$2.906 \cdot 10^7$	”	”	$3.145 \cdot 10^{-2}$
	HEA140	$3.997 \cdot 10^7$	”	”	$1.810 \cdot 10^{-2}$
	HEA160	$5.719 \cdot 10^7$	”	”	$2.623 \cdot 10^{-2}$

Table 3. Equivalent stiffnesses and homogenization errors for Vierendeel girders with webs of various cross section (span $L = 7600\,\mathrm{mm}$, chords' sections: HEA120).

In Figure 6 and in Table 3 the effects of the variations of the web bending stiffness on the accuracy of the proposed beam model are analyzed for two values of the girder aspect ratio β. It is evident that the homogenization error follows the same trend for both values of β, attaining the greater values when the webs have the lower shear stiffness. However, in both cases, the errors are negligible and are acceptable for engineering purposes, being less than or equal to 5%.

In Figure 6 the elastic lines of the homogenized beam models by Noor–Nemeth [1980] and Romanoff–Reddy [2014] are also reported for comparison purposes. As it can be seen, the Reddy–Romanoff theory in all the examined cases underestimates the finite element model's displacements while the predictions of the proposed approach are affected by an error of the same order of magnitude as the error of the Noor–Nemeth theory.

Also when the joints between webs and chords are elastically compliant, the predictions from our beam model are in excellent agreement with the finite element method results for a wide range of values of the joint compliance. This is evident from results reported in Figure 7, where the vertical displacements of a series of girder finite element models having various stiffnesses of the torsional springs are compared
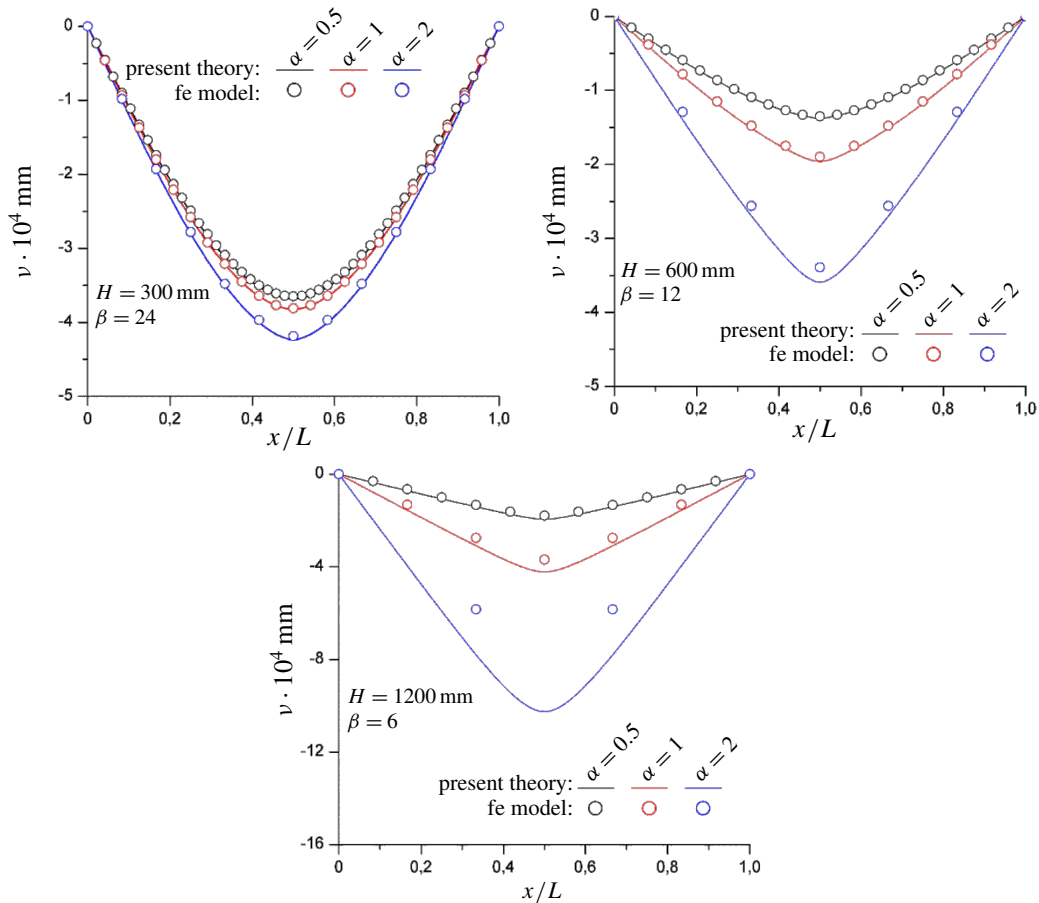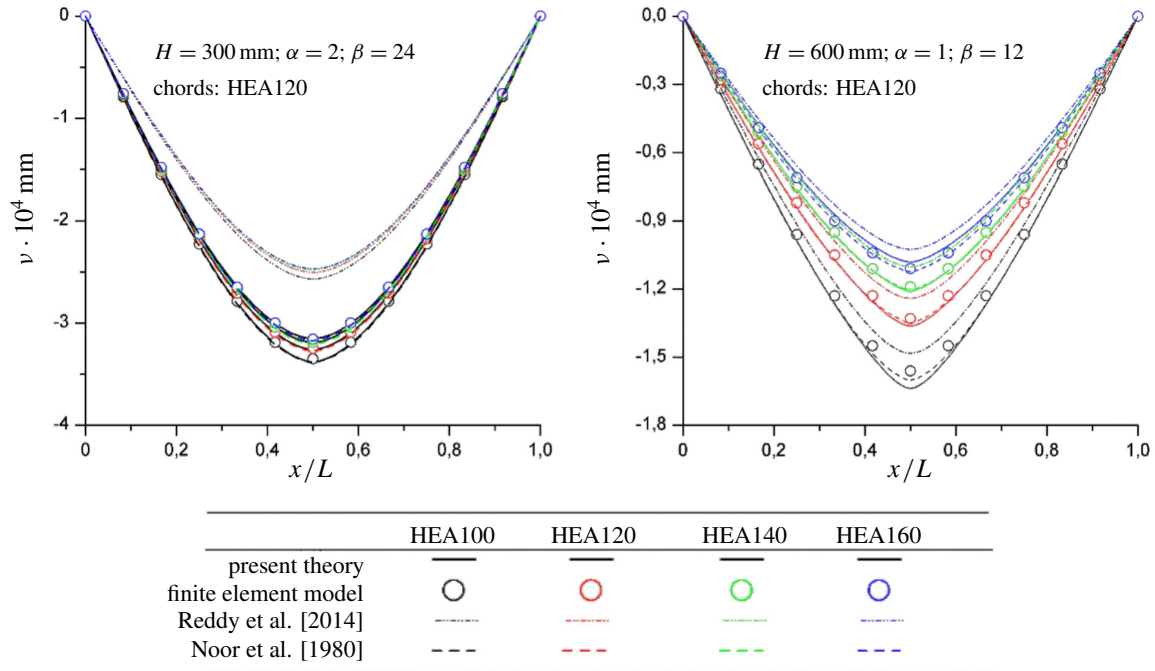
Figure 6. Vertical deflections of Vierendeel girders finite element models and elastic lines of the equivalent Timoshenko beams: effects of girder height H (span $L = 7600$ mm, chords and web sections HEA100).

with the elastic lines of the corresponding homogenized polar beam. The spring stiffness values of these girders have been chosen in order to realize, starting from the ideal case of perfectly rigid chord-webs joints, percent increments χ equal to 1, 5, 25, 50, 100, 400 and 2000 for the bending compliance of the elastic systems of Figure 2c. As schematically shown in Figure 7, the systems are composed by a web in series with the corresponding springs constraining it to the chords. In Table 4, the stiffnesses and the homogenization errors of the equivalent beam of Figure 7 are listed.

The influence that both web shear and joint stiffnesses have on the homogenization error can be explained as follows: recall that in a Vierendeel girder the bending constraint action that the chords exert on each other depends on these stiffnesses, being the Vierendeel effect directly proportional to them. In other words, for lower values of the web shear and joint stiffnesses, the jumps in the chords' axial forces at the girder joints become smaller; as a result, when either EI_w or k_ϑ decrease, the girder behavior tends toward an Euler–Bernoulli beam, having infinite shear stiffness and bending stiffness equal to the one

Figure 7. Vertical deflections of Vierendeel girders finite element models and elastic lines of the equivalent Timoshenko beams: effects of the girder webs cross sections.

	$\chi\%$ [−]	k_ϑ [Nmm]	D_Q [Nmm^{-1}]	S_{xy} [Nmm]	D_{xx} [Nmm]	e_{ave} [−]
$h = 300$ mm $\alpha = 2.0$ $\beta = 24$ chords = HEA100 webs = HEA100	1.0	$7.403 \cdot 10^{11}$	$2.530 \cdot 10^7$	$1.481 \cdot 10^{12}$	$2.026 \cdot 10^{13}$	$4.681 \cdot 10^{-3}$
	5.0	$1.481 \cdot 10^{11}$	$2.437 \cdot 10^7$	”	”	$5.925 \cdot 10^{-3}$
	25.0	$2.961 \cdot 10^{10}$	$2.058 \cdot 10^7$	”	”	$1.067 \cdot 10^{-2}$
	50.0	$1.481 \cdot 10^{10}$	$1.724 \cdot 10^7$	”	”	$1.360 \cdot 10^{-2}$
	100.0	$7.403 \cdot 10^9$	$1.300 \cdot 10^7$	”	”	$1.558 \cdot 10^{-2}$
	400.0	$1.851 \cdot 10^9$	$5.258 \cdot 10^6$	”	”	$5.639 \cdot 10^{-2}$
	2000.0	$3.702 \cdot 10^8$	$1.259 \cdot 10^6$	”	”	$1.881 \cdot 10^{-1}$
$h = 1200$ mm $\alpha = 0.5$ $\beta = 12$ chords = HEA160 webs = HEA160	1.0	$8.867 \cdot 10^{11}$	$4.655 \cdot 10^7$	$7.094 \cdot 10^{12}$	$5.918 \cdot 10^{14}$	$2.266 \cdot 10^{-2}$
	5.0	$1.773 \cdot 10^{11}$	$4.379 \cdot 10^7$	”	”	$2.317 \cdot 10^{-2}$
	25.0	$3.547 \cdot 10^{10}$	$3.378 \cdot 10^7$	”	”	$3.196 \cdot 10^{-2}$
	50.0	$1.773 \cdot 10^{10}$	$2.627 \cdot 10^7$	”	”	$4.158 \cdot 10^{-2}$
	100.0	$8.867 \cdot 10^9$	$1.819 \cdot 10^7$	”	”	$5.035 \cdot 10^{-2}$
	400.0	$2.217 \cdot 10^9$	$6.392 \cdot 10^6$	”	”	$9.207 \cdot 10^{-2}$
	2000.0	$4.433 \cdot 10^8$	$1.433 \cdot 10^6$	”	”	$2.144 \cdot 10^{-1}$

Table 4. Equivalent stiffnesses and homogenization errors for Vierendeel girders with elastic joints: effects of the joints stiffness (span $L = 7600$ mm).

of the two chords acting in parallel. However, when EI_w or k_ϑ become very small, the shear stiffness of the unit cell tends to the minimum value $3EI_c/s^3$ and consequently the Timoshenko beam model over-estimates the real displacements.

5. Analysis of results

Results listed in Tables 2, 3 and 4 clearly show that the bending and polar stiffnesses evaluated by the present method appear to be independent from the web bending stiffness and the stiffness k_ϑ of the torsional springs. For fixed values of the girder aspect ratio β, D_{xx} and S_{xy} are insensitive to any changes of the cell aspect ratio α. Moreover, given the girder span L, these stiffnesses do not change for changes in the ratio $\alpha/\beta = s/L$. This is in marked contrast to results of previous theories for homogenizing toward a polar beam, whose equivalent stiffnesses have the expressions reported in Table 5.

Indeed, the aforementioned property of D_{xx} and S_{xy} are a consequence of the deformation mode by which the cell transfers the bending moment to the neighboring cells. Actually, the cell bends while maintaining its webs in the straight configuration, a fact that allows the determination of the equivalent bending stiffnesses without executing the eigenanalysis of the transfer matrix M.

For this aim, we first observe that the unit cell is symmetric with respect to the vertical and horizontal centroidal axes; see Figure 2b. Under the loading condition defined by the pure bending eigenvector (see Figure 4), the bending moments at the ends of the chords and webs have the same amplitudes, respectively m_c and m_w. Hence, the corresponding cell equilibrium configuration (Figure 9) is defined by equilibrium equations of the joints having the form

$$m_b = m_c - m_w \tag{14}$$

and by the inner compatibility conditions

$$\varphi_{j(w)}^q = \varphi_{j(c)}^q, \text{ with } q = t, b, \tag{15}$$

where $\varphi_{j(w)}^q$ and $\varphi_{j(c)}^q$ are respectively the rotations of the web and chord end sections at the joint j^q. These rotations have expressions given by

$$\varphi_{j(c)}^{(q)} = \pm \frac{m_c s}{2EI_c}, \quad \varphi_{j(w)}^{(q)} = \pm \left(\psi - \frac{m_w s}{6EI_w} \right), \tag{16}$$

where the angles

$$\psi = \pm \frac{\Delta u_b - \Delta u_t}{2h} = \pm \frac{n_b s}{EA_c h} \tag{17}$$

	D_{xx}	S_{xy}	
Reddy–Romanoff theory [Romanoff and Reddy 2014]	$\frac{1}{2}EA_ch^2 + 2EI_c,$	$\frac{8(I_c D_{xx})}{\left(\frac{1}{2}EA_ch^2 + \delta EI_w\right)},$	$\delta = \left(\frac{I_w}{2I_c} + 12\frac{EI_w}{k_\vartheta s} + \frac{h}{s} \right)^{-1}$
Noor–Nemeth theory [Noor and Nemeth 1980]	$\frac{1}{2}EA_ch^2 + 3EI_w\frac{s}{h}$	$2EI_c + 3EI_w\frac{s}{h}$	

Table 5. Equivalent bending and polar stiffnesses of a Vierendeel girder.
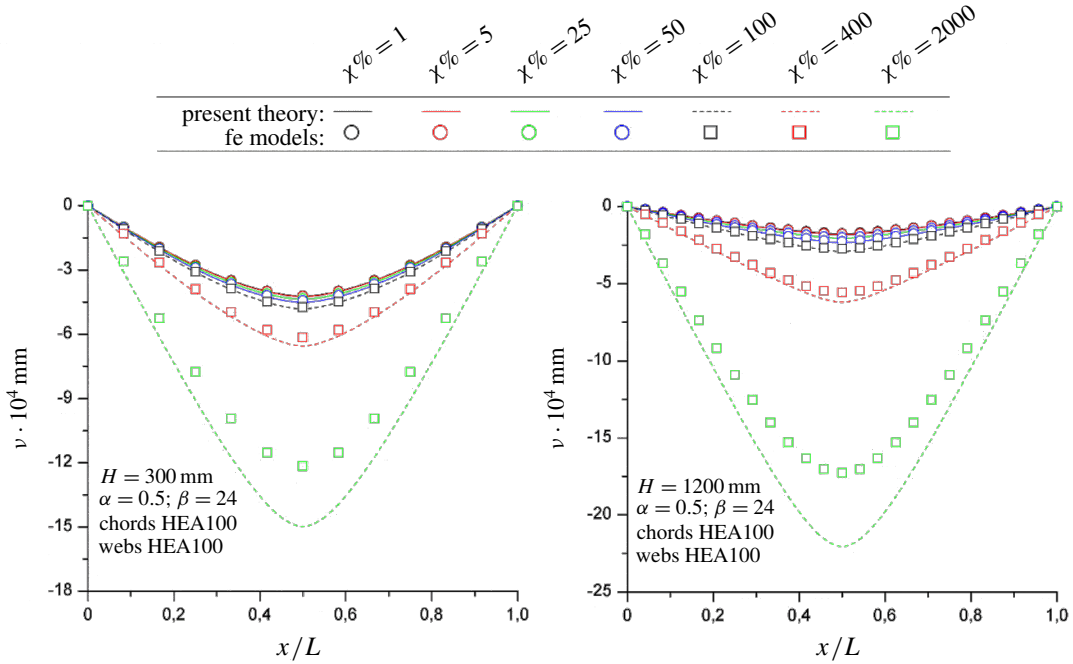
Figure 8. Vertical deflections of Vierendeel girders fe models and elastic lines of the equivalent Timoshenko beams: effects of joint elasticity.

are the web's rigid rotations that would occur as a consequence of the chords elongations if the webs were simply hinged to the chords. According to the sign convention of Figure 9, the choice of $+/-$ in the previous equations depends on whether joints on the right or on the left side of the cell are considered. Through (14)–(16), it can be recognized that the cell equilibrium can be attained without deformations of the webs, that is with $m_w = 0$, only if

$$\varphi^q_{j(w)} = \varphi^q_{j(c)} = \psi \quad \text{and} \quad m_b = m_c = \frac{2n_b I_c}{A_c h}. \tag{18}$$

When previous conditions are met, the curvature of the chords is given by

$$\frac{1}{R} = \frac{2\psi}{s} = \frac{2\,n_b}{E\,A_c\,h}.$$

Substituting this result into (11) and (12) and taking into account (18), we obtain the following expressions of the bending and polar stiffnesses of the equivalent beam:

$$\begin{aligned}
D_{xx} &= \frac{n_b hs}{2\psi} = \tfrac{1}{2} E A_c h^2, \\
S_{xy} &= \frac{2m_b s}{2\psi} = 2 E I_c.
\end{aligned} \tag{19}$$

The stiffnesses evaluated by previous formulas perfectly match those listed in Tables 1–4, which were obtained by the numerical procedure in Section 4.
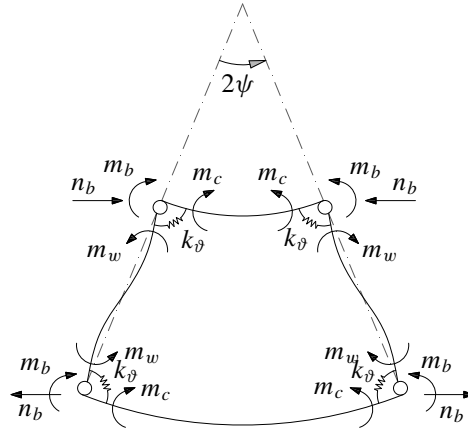
Figure 9. Unit cell deformed shape under pure bending loads.

Finally, equating the expression of S_{xy} given in (19) to the polar stiffness of a Timoshenko beam, the following expression for the material length scale ℓ is derived:

$$\ell = \rho_c \sqrt{1 + \nu},$$

where ρ_c is the central (inertial) radius of gyration of the chord cross section. According to this latter result, the severity of the polar effect in the equivalent Timoshenko beam appears to be totally independent from the cell sizes and is a function only of the chords cross section geometry and the girder material.

6. Conclusions

The homogenization of a Vierendeel girder having elastic joints has been performed by adopting a Timoshenko polar beam as substitute medium. The equivalent stiffnesses were determined by a numerical procedure based on the analysis of the eigen- and principal vectors of the force transfer matrix of the unit cell. While previous approaches proposed that the polar character of the beam is deduced by kinematical conjectures or is inspired by the microstructure, in the present study it is a direct consequence of the pattern of the inner forces acting in the lattice when the pure bending mode of the cell is active.

The method we proposed has been validated on the basis of some experimental data from literature and the results of a series of finite element models. In almost all the examined cases, the predictions of our model were in good agreement with numerical and experimental outcomes. Furthermore, from the validation study, we found that the bending and polar stiffnesses are independent from the web bending stiffness and do not change with either the unit cell length s or the stiffness k_ϑ of the torsional springs. In addition, the bending moment is transferred by the unit cell without deformation of the webs; during bending, the webs maintain their initial straight configuration. From this result, two simple formulas for the bending and polar stiffness were derived.

The presented beam model has great potential for analyzing the behavior of any beam-like repetitive structures with elastic or rigid joints. More specifically, it appears to be a serious candidate for analyzing the buckling and postbuckling response of infinitely long periodic beams, such as the railway track under thermal load. Its range of validity is bounded by the bending stiffness of the webs and the stiffness

of the web-chord connections. As these stiffnesses decrease, from the presented theory a family of Timoshenko beams having increasing shear flexibility are obtained. However, in real girders, the smaller these stiffnesses are, the weaker the Vierendeel effect results. As a consequence, the girder behavior tends toward an Euler–Bernoulli beam having bending stiffness equal to twice the chord bending stiffness. However, the extension of the proposed approach to girders with weak Vierendeel effects needs a deeper analysis and probably will be the object of future research.

Similarly, further research will be needed to apply the proposed model in the girder elasto-plastic range, where the response of the unit cell has to be analyzed by approximated methods, as presented in [Fraldi et al. 2010; 2014].

References

[Bacigalupo and Gambarotta 2014] A. Bacigalupo and L. Gambarotta, "Homogenization of periodic hexa- and tetrachiral cellular solids", *Compos. Struct.* **116** (2014), 461–476.

[Bakhvalov and Panasenko 1989] N. Bakhvalov and G. Panasenko, *Averaging processes in periodic media: mathematical problems in the mechanics of composite materials*, Mathematics and its Applications **36**, Kluwer Academic Publishers, Dordrecht, The Netherlands, 1989.

[Bazant and Christensen 1972] Z. Bazant and M. Christensen, "Analogy between micropolar continuum and grid frameworks under initial stress", *Int. J. Solids Struct.* **8** (1972), 327–346.

[Cao et al. 2007] J. Cao, J. L. Grenestedt, and W. J. Maroun, "Steel truss/composite skin hybrid ship hull, I: design and analysis", *Compos. A Appl. Sci. Manuf.* **38** (2007), 1755–1762.

[De Iorio et al. 2014a] A. De Iorio, M. Grasso, F. Penta, G. P. Pucillo, P. Pinto, S. Rossi, M. Testa, and G. Farneti, "Transverse strength of railway tracks, I: planning and experimental setup", *Frattura ed Integrità Strutturale* **30** (2014), 478–485.

[De Iorio et al. 2014b] A. De Iorio, M. Grasso, F. Penta, G. P. Pucillo, and V. Rosiello, "Transverse strength of railway tracks, II: test system for ballast resistance in line measurement", *Frattura ed Integrità Strutturale* **30** (2014), 578–592.

[De Iorio et al. 2014c] A. De Iorio, M. Grasso, F. Penta, G. P. Pucillo, V. Rosiello, S. Lisi, S. Rossi, and M. Testa, "Transverse strength of railway tracks, III: multiple scenarios test field", *Frattura ed Integrità Strutturale* **30** (2014c), 593–601.

[Dos Reis and Ganghoffer 2012] F. Dos Reis and J. F. Ganghoffer, "Construction of micropolar continua from the asymptotic homogenization of beam lattices", *Comput. Struct.* **112** (2012), 354–363.

[Fraldi et al. 2010] M. Fraldi, L. Nunziante, A. Gesualdo, and F. Guarracino, "On the bounding of limit multipliers for combined loading", *Proc. R. Soc. Lond. A* **466**:2114 (2010), 493–514.

[Fraldi et al. 2014] M. Fraldi, A. Gesualdo, and F. Guarracino, "Influence of actual plastic hinge placement on the behavior of ductile frames", *J. Zhejiang Univ. Sci. A* **15** (2014), 482–495.

[Hasanyan and Waas 2016] A. Hasanyan and A. Waas, "Micropolar constitutive relations for cellular solids", *J. Appl. Mech. (ASME)* **83** (2016), art. id. 041001, pp. 10.

[Jutila and Romanoff 2007] M. Jutila and J. Romanoff, *Laserhitsatun teräksisen kerroslevypalkin kolmipistetaivutus-kokeet*, master's thesis, Helsinki University of Technology, 2007.

[Kerr and Zarembski 1981] A. D. Kerr and A. M. Zarembski, "The response equations for a cross-tie track", *Acta Mech.* **40** (1981), 253–276.

[Kumar and McDowell 2004] R. S. Kumar and D. L. McDowell, "Generalized continuum modeling of 2-D periodic cellular solids", *Int. J. Solids Struct.* **41** (2004), 7399–7422.

[Langley 1996] R. S. Langley, "A transfer matrix analysis of the energetics of structural wave motion and harmonic vibration", *Proc. R. Soc. Lond. A* **452** (1996), 1631–1648.

[Liu and Su 2009] S. Liu and W. Su, "Effective couple-stress continuum model of cellular solids and size effects analysis", *Int. J. Solids Struct.* **46** (2009), 2787–2799.

[Ma et al. 2008] H. M. Ma, X.-L. Gao, and J. N. Reddy, "A microstructure-dependent Timoshenko beam model based on a modified couple stress theory", *J. Mech. Phys. Solids* **56**:12 (2008), 3379–3391.

[Martinsson and Babuška 2007] P.-G. Martinsson and I. Babuška, "Mechanics of materials with periodic truss or frame microstructures", *Arch. Ration. Mech. Anal.* **185**:2 (2007), 201–234.

[Mead 1970] D. J. Mead, "Free wave propagation in periodically-supported infinite beams", *J. Sound Vib.* **13** (1970), 181–197.

[Meirovitch and Engels 1977] L. Meirovitch and R. C. Engels, "Response of periodic structures by the *Z*-transform method", *AIAA J.* **15**:2 (1977), 167–174.

[Nakayama 1985] Y. Nakayama, "Aerodynamic stability of cable-stayed bridge with new Vierendeel-type girder", *Eng. Struct.* **7** (1985), 85–92.

[Noor 1983] A. K. Noor, "Assessment of current state of the art in modeling techniques and analysis methods for large space structures", pp. 5–32 in *NASA Conference Publication 2258* (Williamsburg, VA, 1982), edited by L. D. Pinson et al., 1983.

[Noor 1988] A. K. Noor, "Continuum modeling for repetitive lattice structures", *Appl. Mech. Rev. (ASME)* **41** (1988), 285–296.

[Noor and Nemeth 1980] A. K. Noor and M. P. Nemeth, "Micropolar beam models for lattice grids with rigid joints", *Comput. Methods Appl. Mech. Eng.* **21** (1980), 249–263.

[Onck 2002] P. R. Onck, "Cosserat modeling of cellular solids", *C. R. Mécanique* **330** (2002), 717–722.

[Pucillo 2016] G. P. Pucillo, "Thermal buckling and post-buckling behaviour of continuous welded rail track", *Veh. Syst. Dyn.* **54** (2016), 1785–1807.

[Reddy 2011] J. N. Reddy, "Microstructure-dependent couple stress theories of functionally graded beams", *J. Mech. Phys. Solids* **59**:11 (2011), 2382–2399.

[Romanoff and Reddy 2014] J. Romanoff and J. N. Reddy, "Experimental validation of the modified couple stress Timoshenko beam theory for web-core sandwich panels", *Compos. Struct.* **111** (2014), 130–137.

[Romanoff et al. 2007] J. Romanoff, H. Remes, G. Socha, M. Jutila, and P. Varsta, "The stiffness of laser stake welded T-joints in web-core sandwich structures", *Thin-Walled Struct.* **45** (2007), 453–462.

[Romanoff et al. 2009] J. Romanoff, A. Laakso, and P. Varsta, *Improving the shear properties of web-core sandwich structures using filling material: analysis and design of marine structures*, CRC Press, Leiden, The Netherlands, 2009.

[Salmon et al. 2008] G. C. Salmon, J. E. Johnson, and F. A. Malhas, *Steel structures: design and behavior*, 5th ed., Prentice Hall, 2008.

[Hård af Segerstad et al. 2009] P. Hård af Segerstad, S. Toll, and R. Larsson, "A micropolar theory for the finite elasticity of open-cell cellular solids", *Proc. R. Soc. Lond. A* **465** (2009), 843–865.

[Stephen and Ghosh 2005] N. G. Stephen and S. Ghosh, "Eigenanalysis and continuum modelling of a curved repetitive beam-like structure", *Int. J. Mech. Sci.* **47** (2005), 1854–1873.

[Stephen and Wang 2000] N. G. Stephen and P. J. Wang, "On transfer matrix eigenanalysis of pin-jointed frameworks", *Comput. Struct.* **78** (2000), 603–615.

[Stephen and Zhang 2004] N. G. Stephen and Y. Zhang, "Eigenanalysis and continuum modelling of an asymmetric beamlike repetitive structure", *Int. J. Mech. Sci.* **46** (2004), 1213–1231.

[Stephen and Zhang 2006] N. G. Stephen and Y. Zhang, "Eigenanalysis and continuum modeling of pre-twisted repetitive beam-like structures", *Int. J. Solids Struct.* **43** (2006), 3832–3855.

[Tej and Tejová 2014] P. Tej and A. Tejová, "Design of an experimental prestressed Vierendeel pedestrian bridge made of UHPC", *Appl. Mech. Mater.* **587** (2014), 1642–1645.

[Trovalusci et al. 2015] P. Trovalusci, M. Ostoja-Starzewski, M. L. De Bellis, and A. Murrali, "Scale-dependent homogenization of random composites as micropolar continua", *Eur. J. Mech. A Solid.* **49** (2015), 396–407.

[Wang and Stronge 1999] X. L. Wang and W. J. Stronge, "Micropolar theory for two-dimensional stresses in elastic honeycomb", *Proc. R. Soc. Lond. A* **455**:1986 (1999), 2091–2116.

[Warren and Byskov 2002] W. E. Warren and E. Byskov, "Three-fold symmetry restrictions on two-dimensional micropolar materials", *Eur. J. Mech. A Solids* **21**:5 (2002), 779–792.

[Yong and Lin 1989] Y. Yong and Y. K. Lin, "Dynamics of complex truss-type space structures", *AIAA J.* **28** (1989), 1250–1258.

[Zhong and Williams 1995] W. X. Zhong and F. W. Williams, "On the direct solution of wave propagation for repetitive structures", *J. Sound Vib.* **181** (1995), 485–501.

ANTONIO GESUALDO: gesualdo@unina.it
Department of Structures for Engineering and Architecture, University of Naples Federico II, Via Claudio 21, 80125 Naples, Italy

ANTONINO IANNUZZO: antoninoiannuzzo@libero.it
Department of Structures for Engineering and Architecture, University of Naples Federico II, Via Claudio 21, 80125 Naples, Italy

FRANCESCO PENTA: penta@unina.it
Department of Industrial Engineering, University of Naples Federico II, Piazzale Tecchio 80, 80125 Naples, Italy

GIOVANNI PIO PUCILLO: gpucillo@unina.it
Department of Industrial Engineering, University of Naples Federico II, Piazzale Tecchio 80, 80125 Naples, Italy

HIGHLY ACCURATE NONCOMPATIBLE GENERALIZED MIXED FINITE ELEMENT METHOD FOR 3D ELASTICITY PROBLEMS

GUANGHUI QING, JUNHUI MAO AND YANHONG LIU

Based on the generalized H–R mixed variational principle, the simple compatible and noncompatible generalized mixed elements (CGME, NCGME) for 3D linear elasticity problems were derived by the C_0 continuous polynomial shape functions used usually in the displacement methods. Two of main features of the generalized mixed finite element methods corresponding to the CGME and NCGME are that the coefficient matrix of system of equations are automatically symmetric and invertible. Without any extra techniques of the traditional mixed methods, the displacement and stress results can be obtained directly from the linear system of equations by introducing the stress and displacement boundary conditions simultaneously. The numerical examples show that the displacement and stress variables converge stably. The resulting stresses of NCGME have nearly the same accuracy as displacements and are certainly more accurate than the common noncompatible displacement finite element methods.

1. Introduction

It is well known that the finite element minimum potential energy principle leads, as its Euler–Lagrange (EL) equations, to not only equilibrium within the element but also interelement traction reciprocity. The equilibrium finite element methods are also straightforward applications of the minimum complementary energy principle. The finite element complementary energy principle leads, as its EL equations, to not only kinematic compatibility within each element but also interelement displacement compatibility.

The above requirements of interelement displacement continuity and traction reciprocity on the admissible displacement variables and stress variables (respectively) may not provide sufficient flexibility in the finite element solution of several problems in linear elasticity, such as plate bending, shells, multilayered composites, and problems with singularities found in fracture mechanics, among others [Pian 1964].

To gain this flexibility in application, one may relax the conditions of displacement continuity or traction reciprocity at interelement boundaries on the admissible displacement or stress fields, by introducing these as a posteriori constraints into the respective finite element variational principles. This is the underlying concept in the hybrid finite element methods [Pian 1964] (the hybrid methods, in essence, belong to the displacement methods [Tian and Pian 2011]) and the mixed finite element methods [Herrmann 1967; Dunham and Pister 1968]. The hybrid methods and mixed methods for the elasticity problem are mostly based on the mixed variational principle, which is a form of the Hellinger–Reissner (H–R) mixed variational principle [Reissner 1950]. Unlike the hybrid methods, where the element matrices are condensed into a stiffness matrix on the element level, in the mixed methods the element matrix is generally assembled to the global coefficient matrix by the usual superposition process. Consequently,

the mixed methods generally include two fields in the linear system of equations (e.g., displacement and stress fields for linear elasticity problems). The solution of resulting governing equations immediately also yields the static variables, which are of basic interest in the analysis and design of a structure.

It should be mentioned that the boundary nodal stresses obtained from the finite element analysis are inconsistent with the prescribed stresses in the displacement methods [Tian and Pian 2011]. The convergence rate of the displacement models for problems with large gradients of stresses is slow [Hoa and Feng 1998]. The equilibrium methods are rarely used in practical computation due to the difficulty of creating finite element spaces incorporating the necessary constraints. Thus the practical choice is usually between the displacement methods and the mixed methods.

The early and classical contributions for the mixed methods are reviewed in [Oden 1973; Atluri et al. 1983; Morley 1989; Arnold 1990]. More recent developments and extensions may be found in [Belytschko et al. 2013; Bonet and Wood 1997; Zienkiewicz and Taylor 2000; Arnold 2002; Arnold and Winther 2002; Adams and Cockburn 2005; Arnold et al. 2007; 2008; Gatica et al. 2008; Sinwel 2009; Qiu and Demkowicz 2010; 2011; Gopalakrishnan and Guzmán 2011; Hu et al. 2016].

One of the most prominent advantages of the mixed methods is the avoidance of using C_1 elements for plate bending and other fourth-order problems. This is because the mixed functional for plate bending involves no more than two derivatives in any term and hence, after a suitable integration by parts, may be evaluated on the finite element spaces with merely continuous elements. The primal variational principles, however, require the use of C_1 elements [Atluri et al. 1983; Arnold 1990]. Hence, the mixed methods are widely used in the linear and nonlinear applications of plate and shells for elasticity.

It is well known that for nearly incompressible and incompressible materials, finite element computations based on a standard displacement formulation fail due to the onset of the locking phenomenon. The traditional mixed formulations are a valid alternative to locking-affected methods, since they provide mathematical models capable of treating both compressible and incompressible linear elasticity problems under a unified framework [Atluri et al. 1983]. Of course, the mixed methods are also applied extensively for the numerical analysis of fluid mechanics problems.

The stability of the numerical results refers to the invertibility of the system matrix representing the discrete problem. Compared with the displacement methods, the mathematical properties of the mixed methods are not simple. If the same polynomial interpolation functions applied in the displacement methods are used to express the displacement and stress variables, the linear system of equations of mixed methods based on the H–R mixed variational principle is symmetric but possesses zeros on the diagonal. Thus, the coefficient matrix is usually indefinite and not invertible. The questions of convergence rate and stability of the traditional mixed models have attracted many mathematicians [Babuška et al. 1977; Oden and Reddy 1976; Talaslidis 1979].

Some representative researches on the mixed methods in recent years should be mentioned here. Arnold and Winther [2002] suggested some stable elements for a two-dimensional problem; the corresponding method in three-dimensional space was first characterized by Adams and Cockburn [2005]; and thorough analyses of the finite elements were provided in [Arnold et al. 2008]. The construction of these elements is not convenient for computer program, since they are of high polynomial order, which implies large costs even for the lowest-order scheme. A mixed finite element method was constructed by the tangential displacement-normal-normal-stress (TDNNS) formulation in [Sinwel 2009]. Thus, it is applicable for both nearly incompressible materials and the discretization of the thin structures using

flat elements. However, the mathematical theory and process on the basis of the TDNNS formulation are not simple and not suitable for engineers.

In a word, the above works show that it is not easy to construct a pair of finite elements for the displacement vector and the symmetric stress tensor which satisfy the stability Brezzi's conditions [1974]. There are still some open questions left in connection with the mixed methods for 2D and 3D problems.

2. Basic theory

2.1. *Governing equations.* Consider a body under static loading. The body occupies the volume V. S is the surface of body. $S = S_u \cup S_\sigma$, where S_u and S_σ are the segments of S where displacements and surface tractions are prescribed, respectively; the outward unit normal on S is denoted by $\boldsymbol{n} \equiv n_i$. Let ∇ be the gradient operator in the undeformed body which, under the assumption of infinitesimal deformation, is indistinguishable from the deformed body.

We define the following: stress $\boldsymbol{\sigma} \equiv \sigma_{ij}$ and strain $\boldsymbol{\varepsilon} \equiv \varepsilon_{ij}$; the surface traction $\boldsymbol{T} \equiv T_i$ and the prescribed surface traction $\overline{\boldsymbol{T}} \equiv \overline{T}_i$ on S_σ; the prescribed displacement $\bar{\boldsymbol{u}} \equiv \bar{u}_i$ on S_u; and $\bar{\boldsymbol{b}} \equiv \bar{b}_i$ is the body force in V. Thus, the boundary value problems in linear elasticity can be stated as:

- The constitutive relations:

$$\boldsymbol{\sigma} = \boldsymbol{C}\varepsilon \quad \text{or} \quad \sigma_{ij} = C_{ijkl}\varepsilon_{kl} \quad \text{or} \quad \boldsymbol{\varepsilon} = \boldsymbol{S}\boldsymbol{\sigma} \text{ in V}, \tag{1}$$

  where $\boldsymbol{C}$ is symmetric stiffness matrix of material and $\boldsymbol{S} = \boldsymbol{C}^{-1}$ is compliance matrix.

- The strain-displacement equations (the compatible equations):

$$\boldsymbol{\varepsilon} = \nabla\boldsymbol{u} \quad \text{or} \quad \varepsilon_{ij} = \tfrac{1}{2}(u_{i,j} + u_{j,i}) \text{ in V}. \tag{2}$$

- The equilibrium equations:

$$\nabla^{\mathrm{T}}\boldsymbol{\sigma} + \bar{\boldsymbol{b}} = 0 \quad \text{or} \quad \sigma_{ij,j} + \bar{b}_i = 0 \text{ in V}. \tag{3}$$

- The surface tractions boundary conditions:

$$\boldsymbol{n} \cdot \boldsymbol{\sigma} = \overline{\boldsymbol{T}} \quad \text{or} \quad \overline{T}_i = \sigma_{ij}n_j \text{ on } S_\sigma. \tag{4}$$

- The displacement boundary conditions:

$$\boldsymbol{u} = \bar{\boldsymbol{u}} \quad \text{or} \quad u_i = \bar{u}_i \text{ on } S_u. \tag{5}$$

2.2. *H–R mixed variational principle and generalized H–R mixed variational principle.* The H–R mixed variational principle contains the displacement field and stress field. Satisfying the displacement boundary conditions (5) a priori, such a principle takes the form

$$\Pi_{\mathrm{HR}} = \int_V \left(-\tfrac{1}{2}\boldsymbol{\sigma}^{\mathrm{T}}\boldsymbol{S}\boldsymbol{\sigma} + \boldsymbol{\sigma}^{\mathrm{T}}(\nabla\boldsymbol{u}) - \bar{\boldsymbol{b}}^{\mathrm{T}}\boldsymbol{u}\right) \mathrm{d}V - \int_{s_\sigma} \overline{\boldsymbol{T}}^{\mathrm{T}}\boldsymbol{u}\,\mathrm{d}S. \tag{6}$$

Like the H–R mixed variational principle, there are also both displacement and stress fields in the generalized H–R mixed variational principle [Chien 1983]. This principle can be expressed as

$$\Pi_{\mathrm{GHR}} = \Pi_{\mathrm{HR}} + \int_V \lambda\left(\tfrac{1}{2}\boldsymbol{\sigma}^{\mathrm{T}}\boldsymbol{S}\boldsymbol{\sigma} + \tfrac{1}{2}(\nabla\boldsymbol{u})^{\mathrm{T}}\boldsymbol{C}(\nabla\boldsymbol{u}) - \boldsymbol{\sigma}^{\mathrm{T}}(\nabla\boldsymbol{u})\right) \mathrm{d}V. \tag{7}$$

We should point out that Felippa [1989a; 1989b] constructed a one-parameter family of mixed variational principles for linear elasticity. This family includes the generalized H–R mixed and the minimum potential energy principles as special cases. We expect to take $0 \leq \lambda \leq 1$ in (7). If the parameter $\lambda < 0$ or $\lambda > 1$, there does not exist practical interest.

It is clear that, letting $\lambda = 0$, (7) is the H–R mixed variational principle, and letting $\lambda = 1$ yields the minimum potential energy principle.

Letting $\lambda = \frac{1}{2}$ leads to the simplest generalized H–R mixed variational principle:

$$\Pi_{\text{GHR}} = \int_V \left(-\tfrac{1}{4}\boldsymbol{\sigma}^{\text{T}}\boldsymbol{S}\boldsymbol{\sigma} + \tfrac{1}{2}\boldsymbol{\sigma}^{\text{T}}(\nabla \boldsymbol{u}) + \tfrac{1}{4}(\nabla \boldsymbol{u})^{\text{T}}\boldsymbol{C}(\nabla \boldsymbol{u}) - \bar{\boldsymbol{b}}^{\text{T}}\boldsymbol{u} \right) \mathrm{d}V - \int_{S_\sigma} \overline{\boldsymbol{T}}^{\text{T}}\boldsymbol{u} \, \mathrm{d}S. \qquad (8)$$

For principles (6)–(8), the only constraint conditions are given in (1), while the equilibrium equations (3) and the traction boundary conditions (4) are satisfied a posteriori.

We assume that all equations in the following sections are for the same finite element model. For clarity, the matrices or vectors with the same symbol in the following imply the identical expressions.

3. Compatible and noncompatible generalized mixed finite element formulations

3.1. *Mixed finite element formulations based on H–R mixed variable principle.* Without loss of generality, consider an n-node compatible linear element for 3D linear elasticity problems. Both displacement $\boldsymbol{u}$ and stress $\boldsymbol{\sigma}$ are expressed by the same shape functions:

$$\boldsymbol{u} = \boldsymbol{N}_{\text{q}}\boldsymbol{q}_{\text{e}}, \qquad (9)$$

$$\boldsymbol{\sigma} = \boldsymbol{N}_{\text{p}}\boldsymbol{p}_{\text{e}}. \qquad (10)$$

Here,

$$\text{Diag}(\boldsymbol{N}_q) = [\boldsymbol{N}_{\text{e}}, \boldsymbol{N}_{\text{e}}, \boldsymbol{N}_{\text{e}}]^{\text{T}}, \quad \boldsymbol{N}_{\text{e}} = [N_1, N_2, \dots, N_n], \quad \boldsymbol{q}_{\text{e}} = [\boldsymbol{u}_{\text{e}1}, \boldsymbol{u}_{\text{e}2}, \boldsymbol{u}_{\text{e}3}]^{\text{T}},$$

$$\text{Diag}(\boldsymbol{N}_p) = [\boldsymbol{N}_{\text{e}}, \boldsymbol{N}_{\text{e}}, \boldsymbol{N}_{\text{e}}, \boldsymbol{N}_{\text{e}}, \boldsymbol{N}_{\text{e}}, \boldsymbol{N}_{\text{e}}]^{\text{T}}, \quad \boldsymbol{p}_{\text{e}} = [\boldsymbol{\sigma}_{\text{e}13}, \boldsymbol{\sigma}_{\text{e}23}, \boldsymbol{\sigma}_{\text{e}33}, \boldsymbol{\sigma}_{\text{e}11}, \boldsymbol{\sigma}_{\text{e}22}, \boldsymbol{\sigma}_{\text{e}12}]^{\text{T}}.$$

Let $N_i = \frac{1}{8}(1 + \zeta_i\zeta)(1 + \eta_i\eta)(1 + \xi_i\xi)$, $i = 1, 2, 3, \dots, 8$, in (9) and (10); thus $\boldsymbol{N}_{\text{q}}$ and $\boldsymbol{N}_{\text{p}}$ are the 24 by 24 and 48 by 48 shape function matrices, respectively.

It is well known that by substituting (9) and (10) into (6) and performing the energy integration, one obtains the discrete functional

$$\Pi_{\text{HR}}(\boldsymbol{p}_{\text{e}}, \boldsymbol{q}_{\text{e}}) = \sum_{i=1}^{n} \left(-\tfrac{1}{2}\boldsymbol{p}_{\text{e}}^{\text{T}}\boldsymbol{K}_{\text{pp}}^{(i)}\boldsymbol{p}_{\text{e}} + \boldsymbol{p}_{\text{e}}^{\text{T}}\boldsymbol{K}_{\text{pq}}^{(i)}\boldsymbol{q}_{\text{e}} - (\boldsymbol{f}_{\text{q}}^{(i)})^{\text{T}}\boldsymbol{q}_{\text{e}} \right), \qquad (11)$$

in which $\sum$ implies summation with respect to all individual elements; $\boldsymbol{K}_{\text{pp}}^{(i)} = \int_{V_i} \boldsymbol{N}_{\text{p}}^{\text{T}}\boldsymbol{S}\boldsymbol{N}_{\text{p}} \, \mathrm{d}V$ is symmetric and positive definite matrix for each element; $\boldsymbol{K}_{\text{pq}}^{(i)} = \int_{V_i} \boldsymbol{N}_{\text{p}}^{\text{T}}(\nabla \boldsymbol{N}_{\text{q}}) \, \mathrm{d}V$ is a rectangular matrix; and $\boldsymbol{f}_{\text{q}}^{(i)} = \int_{V_i} \boldsymbol{N}_{\text{p}}^{\text{T}}\bar{\boldsymbol{b}} \, \mathrm{d}V + \int_{S_{\sigma i}} \boldsymbol{N}_{\text{q}}^{\text{T}}\overline{\boldsymbol{T}} \, \mathrm{d}S$ is the load vector of each element.

In the following, the superscript "(i)" of element submatrices will be dropped for clarity.

Consider p_e and q_e as independent variables. Using $\delta\Pi_{HR}(p_e, q_e) = 0$ yields the two Euler–Lagrange (EL) equations

$$-K_{pp}p_e + K_{pq}q_e = 0, \tag{12a}$$

$$K_{pq}^T p_e = f_q. \tag{12b}$$

The summation of (12a) and (12b) on all elements gives a linear system of equations with respect to both displacement and stress variables. It is well known as the mixed model:

$$\begin{bmatrix} -K_{11} & K_{12} \\ K_{12}^T & \mathbb{0} \end{bmatrix} \begin{Bmatrix} p \\ q \end{Bmatrix} = \begin{Bmatrix} \mathbb{0} \\ f \end{Bmatrix}. \tag{13}$$

Here, submatrices $K_{11} = \sum K_{pp}$, $K_{12} = \sum K_{pq}$; the vectors $p = \sum p_e$, $q = \sum q_e$; and the whole load vector $f = \sum f_q$.

The equation resulting from H–R mixed variational principles (6) of various physical problems is symmetric but possesses zeros on the diagonal. Indeed, it can be seen that the coefficient matrix of (13) is indefinite. For 2D or 3D problems, if the stable mixed element techniques [Adams and Cockburn 2005; Oden and Reddy 1976; Brezzi and Fortin 1991] are not employed, it is very difficult to obtain the stable and reliable solutions by (13).

3.2. *Compatible generalized mixed finite element formulations.* By the same way, using (9) and (10), the discrete form of the generalized H–R mixed variational principle is

$$\Pi_{GHR}(p_e, q_e) = \sum \left(-\tfrac{1}{4} p_e^T K_{pp} p_e + \tfrac{1}{2} p_e^T K_{pq} q_e + \tfrac{1}{4} q_e^T K_{qq} q_e - f_q^T q_e \right). \tag{14}$$

In (14), $K_{qq} = \int_{V_i} (\nabla N_q)^T C (\nabla N_q) \, dV$ is a full rank, symmetric, and positive definite matrix and undoubtedly it is equivalent to the expression derived from the minimum potential energy principle.

Similarly, the following 8-node compatible generalized mixed element (CGME) with 8 nodes for 3D problems can be derived from (14):

$$-K_{pp}p_e + K_{pq}q_e = 0, \tag{15a}$$

$$K_{pq}^T p_e + K_{qq}q_e = 2f_q. \tag{15b}$$

It is of interest to see that (15) can also be obtained by combining the EL equations of the finite element potential energy principle and the finite element H–R mixed variational principle.

The summation of (15) on all elements gives a novel algebraic system

$$\begin{bmatrix} -K_{11} & K_{12} \\ K_{12}^T & K_{22} \end{bmatrix} \begin{Bmatrix} p \\ q \end{Bmatrix} = \begin{Bmatrix} \mathbb{0} \\ 2f \end{Bmatrix}, \tag{16}$$

where K_{11} and K_{22} ($= \sum K_{qq}$) are symmetric and positive definite.

It is clear that the coefficient matrix of the above equation is indefinite because of submatrix $-K_{11}$. However, it is characterized by symmetry and all elements on the leading diagonal are nonzero.

Comparing (16) and (13), the main difference is the values of elements on the diagonal.

3.3. *Noncompatible generalized mixed finite element formulations.* On the basis of [Chen 1982; Taylor et al. 1976], for a noncompatible element weak discontinuity, the element displacements can be expressed as a sum of the compatible part $N_q q_e$ and the noncompatible part $N_r r_e$:

$$u = N_q q_e + N_r r_e. \tag{17}$$

Here, the expression of N_r can be found in [Chen 1982]; N_r are the shape functions with respect to points within elements; r_e is the displacement vector corresponding to points within elements.

In a similar way, by (17) and (10), the finite element functional of the generalized mixed variational principle is given by

$$\Pi_{\text{GHR}}(p_e, q_e, r_e) = \sum_{i=1}^{n} \left(-\tfrac{1}{4} p_e^T K_{pp} p_e + \tfrac{1}{2} p_e^T K_{pq} q_e + \tfrac{1}{2} p_e^T K_{pr} r_e + \tfrac{1}{4} q_e^T K_{qq} q_e \right.$$
$$\left. + \tfrac{1}{2} q_e^T K_{qr} r_e + \tfrac{1}{4} r_e^T K_{rr} r_e - f_q^T q_e - f_r^T r_e \right). \tag{18}$$

In (18),

$$K_{pr} = K_{rp}^T = \int_{V_i} N_p^T (\nabla N_r) \, dV, \qquad K_{qr} = K_{rq}^T = \int_{V_i} (\nabla N_q)^T C (\nabla N_r) \, dV,$$

$$K_{rr} = K_{rr}^T = \int_{V_i} (\nabla N_r)^T C (\nabla N_r) \, dV, \qquad f_r = \int_{V_i} N_r^T \bar{b} \, dV + \int_{S_{\sigma_i}} N_r^T \overline{T} \, dS.$$

Taking the variation of (18) with respect to r_e results in

$$K_{rr} r_e + K_{pr}^T p_e + K_{qr}^T q_e = 2 f_r. \tag{19}$$

K_{rr} in the above equations is identical to the corresponding expression obtained from the minimum potential energy principle for noncompatible displacement elements [Chen 1982; Taylor et al. 1976], and K_{rr} is an invertible matrix. Thus, one has

$$r_e = 2 K_{rr}^{-1} f_r - K_{rr}^{-1} K_{pr}^T p_e - K_{rr}^{-1} K_{qr}^T q_e. \tag{20}$$

Finding the extrema of (18) with respect to p_e and q_e leads to two EL equations:

$$-K_{pp} p_e + K_{pq} q_e + K_{pr} r_e = 0, \tag{21}$$

$$K_{pq}^T p_e + K_{qq} q_e + K_{pr}^T r_e = 2 f_q. \tag{22}$$

On substituting (20) into (21) and (22), one obtains

$$-\mathcal{K}_{pp} p_e + \mathcal{K}_{pq} q_e = -2 K_{pr} K_{rr}^{-1} f_r, \tag{23a}$$

$$\mathcal{K}_{pq}^T p_e + \mathcal{K}_{qq} q_e = 2 f_q - 2 K_{qr} K_{rr}^{-1} f_r, \tag{23b}$$

in which

$$\mathcal{K}_{pp} = K_{pp} + K_{pr} K_{rr}^{-1} K_{pr}^T, \quad \mathcal{K}_{pq} = K_{pq} - K_{pr} K_{rr}^{-1} K_{qr}^T, \quad \mathcal{K}_{qq} = K_{qq} - K_{qr} K_{rr}^{-1} K_{qr}^T.$$

Note that, for general numerical examples, if the body force is ignored, the vectors $2 K_{pr} K_{rr}^{-1} f_r$ and $2 K_{qr} K_{rr}^{-1} f_r$ on the right-hand side of (21) are close to zero. Such a property is the same as the noncompatible displacement element formulations [Tian and Pian 2011]. Therefore, the following 8-node

noncompatible generalized mixed element (NCGME) problems is of the form

$$\begin{bmatrix} -\mathcal{K}_{\text{pp}} & \mathcal{K}_{\text{pq}} \\ \mathcal{K}_{\text{pq}}^{\text{T}} & \mathcal{K}_{\text{qq}} \end{bmatrix} \begin{Bmatrix} p_{\text{e}} \\ q_{\text{e}} \end{Bmatrix} = \begin{Bmatrix} \mathbb{0} \\ 2f_{\text{q}} \end{Bmatrix}. \tag{24}$$

Similarly, the noncompatible generalized mixed model corresponding to (24) is as follows:

$$\begin{bmatrix} -\mathcal{K}_{11} & \mathcal{K}_{12} \\ \mathcal{K}_{12}^{\text{T}} & \mathcal{K}_{22} \end{bmatrix} \begin{Bmatrix} p \\ q \end{Bmatrix} = \begin{Bmatrix} \mathbb{0} \\ 2f \end{Bmatrix}, \tag{25}$$

where submatrices $\mathcal{K}_{11} = \sum \mathcal{K}_{\text{pp}}$, $\mathcal{K}_{12} = \sum \mathcal{K}_{\text{pq}}$, $\mathcal{K}_{22} = \sum \mathcal{K}_{\text{qq}}$; the vectors $p = \sum p_{\text{e}}$, $q = \sum q_{\text{e}}$, and the whole load vector $f = \sum f_{\text{q}}$.

It is obvious that the main difference between (25) and (16) is their coefficient matrices.

3.4. *A unified approach for imposing stress and displacement boundary conditions.* Assume that symbol a refers to the known value vector with respect to nodes on the surface or edges, whose values are determined by the prescribed surface traction $\overline{T}$ on S_σ and the prescribed displacement $\bar{u}$ on S_u.

Interchanging the rows and columns of (25), it can be recast into the form

$$\begin{bmatrix} -\hat{\mathcal{K}}_{11} & \hat{\mathcal{K}}_{12} & \hat{\mathcal{K}}_{13} \\ \hat{\mathcal{K}}_{12}^{\text{T}} & \hat{\mathcal{K}}_{22} & \hat{\mathcal{K}}_{23} \\ \hat{\mathcal{K}}_{13}^{\text{T}} & \hat{\mathcal{K}}_{23}^{\text{T}} & \hat{\mathcal{K}}_{33} \end{bmatrix} \begin{Bmatrix} \hat{p} \\ \hat{q} \\ a \end{Bmatrix} = \begin{Bmatrix} f_1 \\ f_2 \\ f_3 \end{Bmatrix}, \tag{26}$$

where $\hat{p}$ and $\hat{q}$ are the unknown parameter vectors of the nodal stresses and displacements, respectively.

Therefore,

$$-\hat{\mathcal{K}}_{11}\hat{p} + \hat{\mathcal{K}}_{12}\hat{q} = f_1 - \hat{\mathcal{K}}_{13}a, \tag{27a}$$

$$\hat{\mathcal{K}}_{12}^{\text{T}}\hat{p} + \hat{\mathcal{K}}_{22}\hat{q} = f_2 - \hat{\mathcal{K}}_{23}a, \tag{27b}$$

$$\hat{\mathcal{K}}_{13}^{\text{T}}\hat{p} + \hat{\mathcal{K}}_{23}^{\text{T}}\hat{q} = f_3 - \hat{\mathcal{K}}_{33}a. \tag{27c}$$

Of course, (27c) is redundant. Consequently, the final system of equations for the finite element solutions is

$$\begin{bmatrix} -\hat{\mathcal{K}}_{11} & \hat{\mathcal{K}}_{12} \\ \hat{\mathcal{K}}_{12}^{\text{T}} & \hat{\mathcal{K}}_{22} \end{bmatrix} \begin{Bmatrix} \hat{p} \\ \hat{q} \end{Bmatrix} = \begin{Bmatrix} f_1 - \hat{\mathcal{K}}_{13}a \\ f_2 - \hat{\mathcal{K}}_{23}a \end{Bmatrix}. \tag{28}$$

The above unified approach for imposing stress and displacement boundary conditions is employed in our program. In the next section, one of the numerical examples indicates that boundary nodal stresses are consistent with the prescribed stresses.

4. Numerical examples and discussions

4.1. *A thick rectangular plate with simply supported edges.* As shown in Figure 1, consider a thick rectangular plate with in-plane dimensions $a = b = 1.0$ and thickness $h = 0.10$. The material properties are $E_{11} = 10E_{22} = 10E_{33}$, $G_{12} = G_{13} = 0.6E_{33}$, $G_{23} = 0.5E_{33}$, and $\nu_{12} = \nu_{13} = \nu_{23} = 0.25$. The boundary conditions are $\sigma_{11} = u_2 = u_3 = 0$ on $x_1 = 0$ and $x_1 = a$; and $\sigma_{22} = u_1 = u_3 = 0$ on $x_2 = 0$ and $x_2 = b$. The uniform normal load 0.1 is on the upper surface of the plate [Fan 1996].
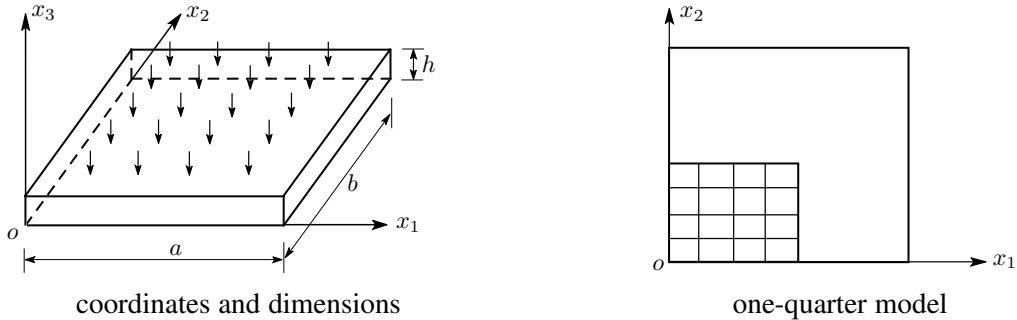
Figure 1. Coordinates and dimensions of a thick rectangular plate.

Using the symmetry about the x_1 and x_2-axes, only one-quarter of plate (see Figure 1, right) is analyzed with uniform meshes. The convergence rate and accuracy of displacements and stresses at special locations are depicted in Figures 2–12. The notation $l \times m \times n$ mesh denotes l subdivisions along the x_1-axis and m subdivisions along the x_2-axis with the same type of elements, while n denotes the element number in the x_3 direction. The nodal stresses of the 8-node noncompatible displacement element (NCDE) for 3D problems in the commercially available software ABAQUS are obtained from the stresses of Gauss quadrature points by the extrapolation method. On the basis of the results of the $12 \times 12 \times 4$ mesh, errors, which are illustrated in the legends in Figures 2–10, are computed by the formulation

$$\frac{\text{exact solution} - \text{solution of element}}{\text{exact solution}} \times 100\%.$$

In our computer program, two Gauss quadrature points in each direction are used for both CGME and NCGME.

As far as displacements $u_1\left(\frac{1}{8}a, \frac{1}{2}b, h\right)$, $u_2\left(\frac{1}{2}a, \frac{1}{8}b, h\right)$ and $u_3\left(\frac{1}{2}a, \frac{1}{2}b, \frac{1}{2}h\right)$ are concerned (see Figures 2, 3, and 4), there is no significant difference between NCGME and NCDE for the convergence rate and accuracy. Certainly, it is clear that when the element mesh is relatively fine, the results of NCGME and NCDE are more accurate than those of CGME.

Figures 5 and 6 show that the results $\sigma_{13}\left(\frac{1}{8}a, \frac{1}{2}b, \frac{1}{2}h\right)$ and $\sigma_{23}\left(\frac{1}{2}a, \frac{1}{8}b, \frac{1}{2}h\right)$ of NCGME are in good agreement with the exact solution for even coarse meshes. It can also be observed that the accuracy of the $\sigma_{13}\left(\frac{1}{8}a, \frac{1}{2}b, \frac{1}{2}h\right)$ and $\sigma_{23}\left(\frac{1}{2}a, \frac{1}{8}b, \frac{1}{2}h\right)$ of the compatible element CGME are greatly superior to NCDE.
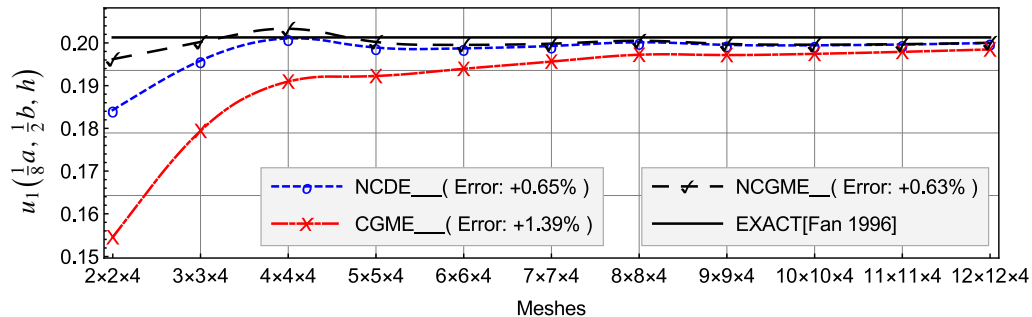

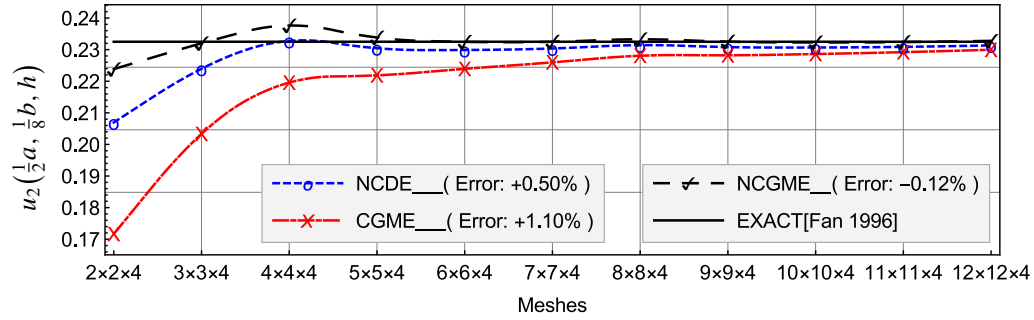**Figure 2.** Comparison of displacement $u_1\left(\frac{1}{8}a, \frac{1}{2}b, h\right)$.

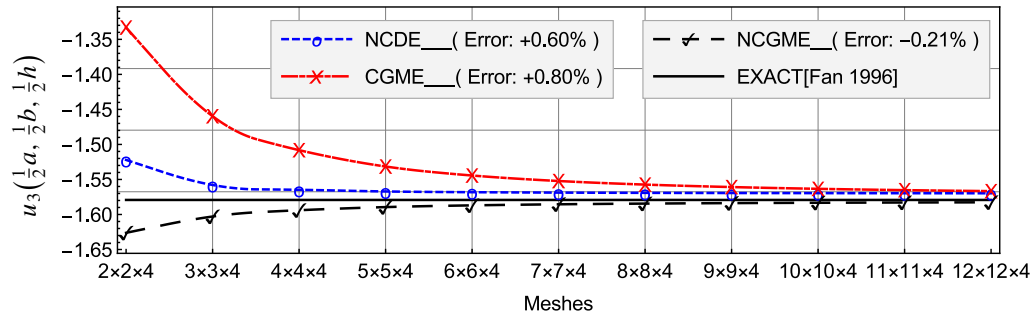**Figure 3.** Comparison of displacement $u_2\left(\frac{1}{2}a, \frac{1}{8}b, h\right)$.

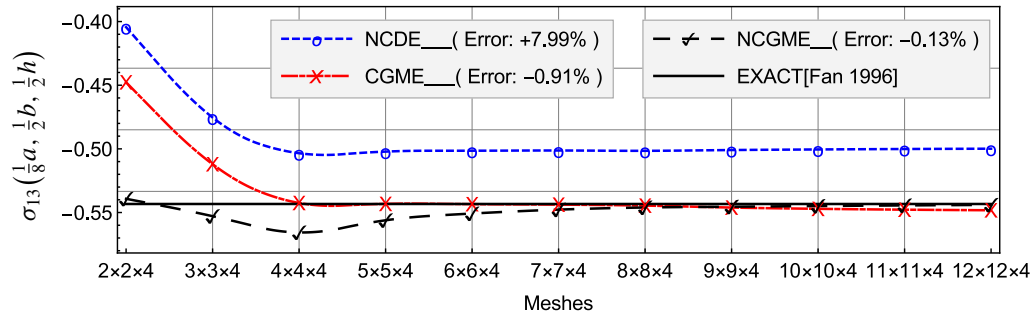**Figure 4.** Comparison of displacement $u_3\left(\frac{1}{2}a, \frac{1}{2}b, \frac{1}{2}h\right)$.

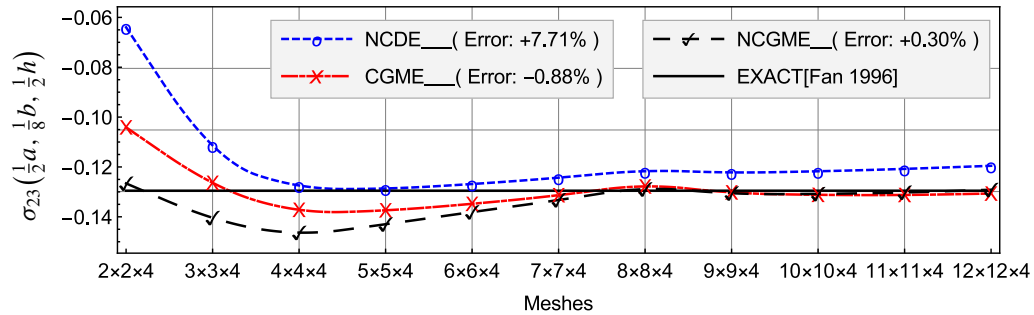**Figure 5.** Comparison of stress $\sigma_{13}\left(\frac{1}{8}a, \frac{1}{2}b, \frac{1}{2}h\right)$.

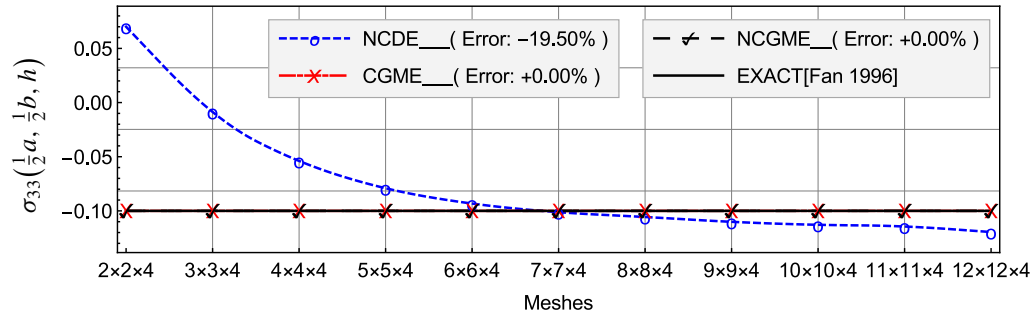**Figure 6.** Comparison of stress $\sigma_{23}\left(\frac{1}{2}a, \frac{1}{8}b, \frac{1}{2}h\right)$.

Figure 7. Comparison of stress $\sigma_{33}\left(\frac{1}{2}a, \frac{1}{2}b, h\right)$.
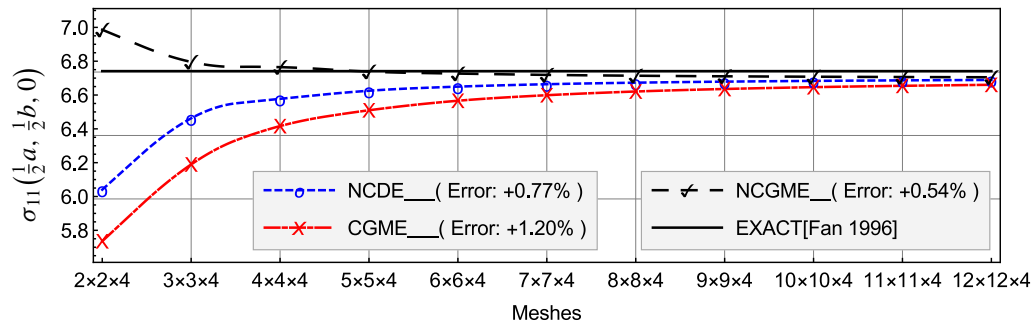
Figure 8. Comparison of stress $\sigma_{11}\left(\frac{1}{2}a, \frac{1}{2}b, 0\right)$.
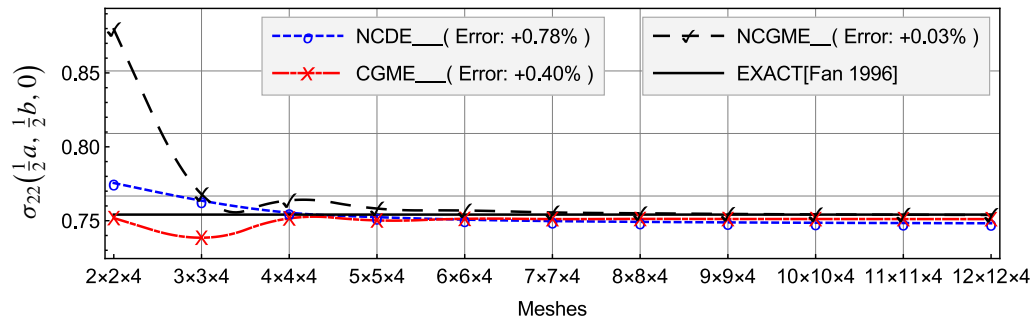
Figure 9. Comparison of stress $\sigma_{22}\left(\frac{1}{2}a, \frac{1}{2}b, 0\right)$.
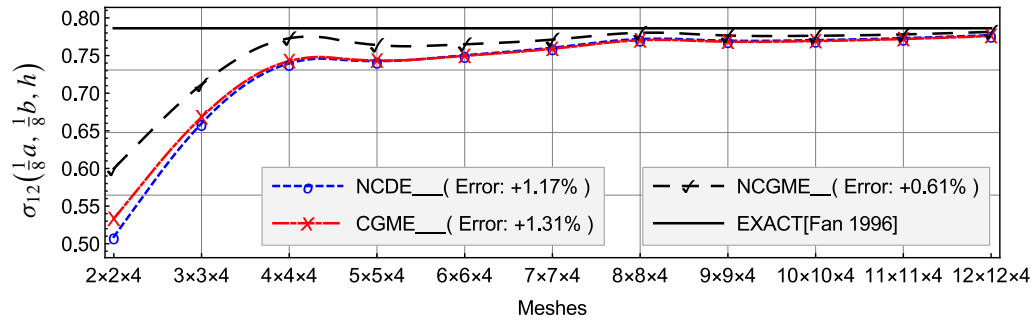
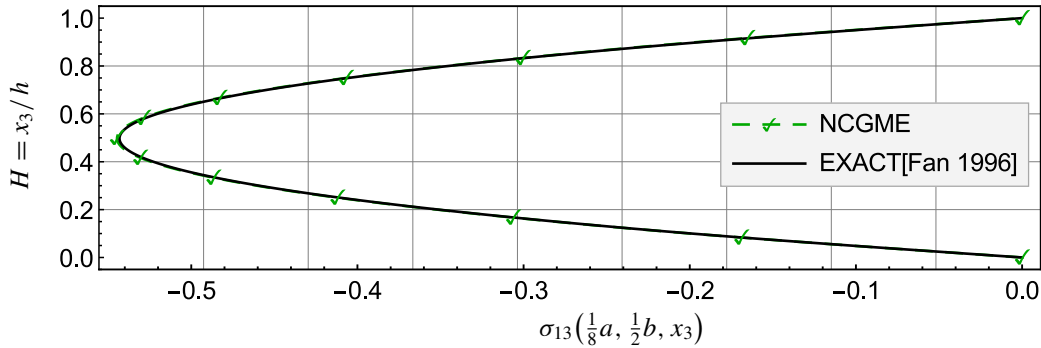**Figure 10.** Comparison of stress $\sigma_{12}\left(\frac{1}{8}a, \frac{1}{8}b, h\right)$.

Figure 11. Comparison of stress $\sigma_{13}\left(\frac{1}{8}a, \frac{1}{2}b, x_3\right)$ distribution along thickness of NCGME.
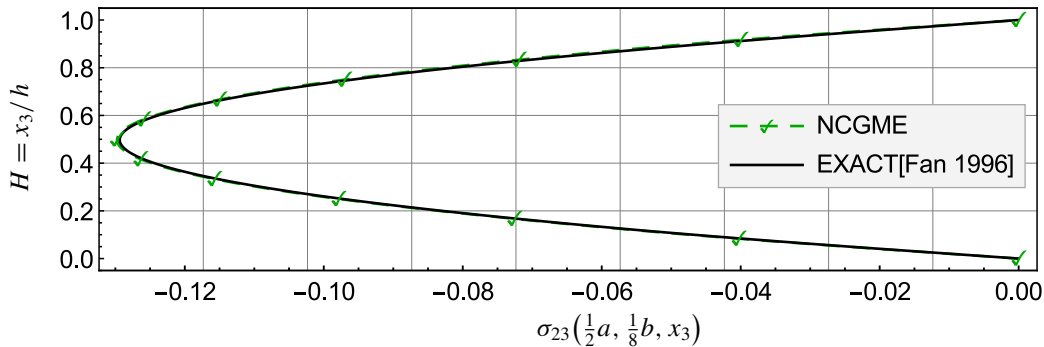

Figure 12. Comparison of stress $\sigma_{23}\left(\frac{1}{2}a, \frac{1}{8}b, x_3\right)$ distribution along thickness of NCGME.

In this example, NCDE can not predict accurately the transversal stresses with respect to the geometrical neutral plane of plate, since the distribution of σ_{13} and σ_{23} along the thickness is nonlinear (see Figures 11 and 12), and the maximum or minimum values on the neutral plane is near to the neutral plane.

Figure 7 indicates that the accuracy of $\sigma_{33}\left(\frac{1}{2}a, \frac{1}{2}b, h\right)$ of NCDE is very poor. As mentioned above, it is difficult to introduce the traction boundary conditions when the stress variables are computed by the constitutive relations (1) on the element level. Hence, the stress results of NCDE on the boundary are inconsistent with the prescribed stresses. However, the stress results of CGMCE8 and NCGMCE8 on the boundary are fully consistent with the prescribed stresses.

The in-plane stress $\sigma_{22}\left(\frac{1}{2}a, \frac{1}{2}b, 0\right)$ of NCGME is characterized by rapid convergence. The accuracy of $\sigma_{11}\left(\frac{1}{2}a, \frac{1}{2}b, 0\right)$, $\sigma_{22}\left(\frac{1}{2}a, \frac{1}{2}b, 0\right)$ and $\sigma_{12}\left(\frac{1}{8}a, \frac{1}{8}b, h\right)$ of NCGME is slightly better than NCDE (see Figures 8–10).

On the basis of the mesh $12 \times 12 \times 4$, the distribution of both $\sigma_{13}\left(\frac{1}{8}a, \frac{1}{2}b, x_3\right)$ and $\sigma_{23}\left(\frac{1}{2}a, \frac{1}{8}b, x_3\right)$ along the thickness of NCGME are depicted by Figures 11 and 12, respectively. They indicate further that the σ_{13} and σ_{23} can approximate to the exact solutions.

4.2. *A classical cantilever beam problem.* The effect of element geometric distortions on the accuracy of CGME and NCGME are investigated in this example.
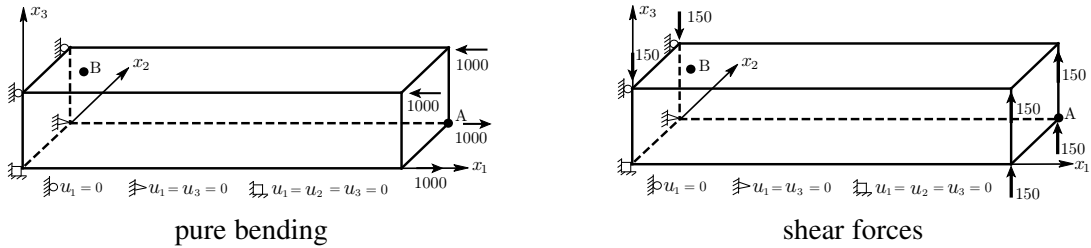
Figure 13. A cantilever beam under pure bending or acted upon by shear forces at the tip [Cheung and Chen 1988].
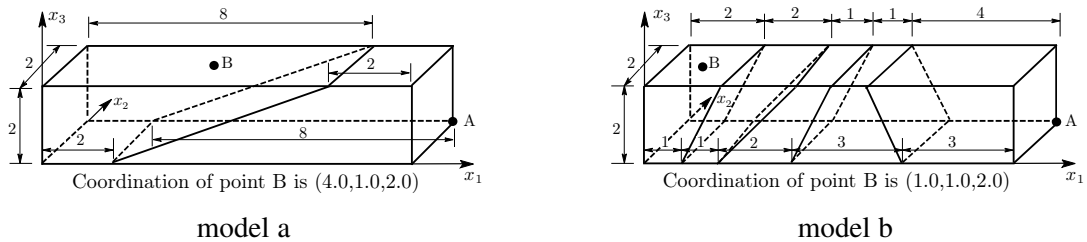

Figure 14. Models of element geometric distortion.

load cases	$Q_{S_{11-1}}$	$Q_{S_{11-2}}$	CGME	NCGME	exact
pure bending	31.2	37.5	15.0	75.1	100.0
shear forces	37.4	45.1	22.6	81.8	102.6

Table 1. Vertical displacements u_3 at point A of model a.

load cases	$Q_{S_{11-1}}$	$Q_{S_{11-2}}$	CGME	NCGME	exact
pure bending	−1162.4	−1350.9	−423.8	−2549.1	−3000.0
shear forces	−1623.2	−1953.6	−573.3	−2642.9	−2700.0

Table 2. The stresses σ_{11} at point B(4.0,1.0,2.0) of model a

Consider a cantilever beam [Cheung and Chen 1988] under pure bending or acted upon by shear forces at the tip (see Figure 13). The geometry dimensions are $2 \times 2 \times 10$, and the material properties are $E = 1500$ and $\nu = 0.25$. The vertical displacements at point A and the bending stress σ_{11} at point B for two finite element models (as shown in Figure 14) are presented in Tables 1–4, and they are compared with $Q_{S_{11-1}}$ [Cheung and Chen 1988], $Q_{S_{11-2}}$ [Cheung and Chen 1988] and the exact solutions.

From the results listed in Tables 1–4, it can be concluded that:

(1) The displacement and stress results of NCGME appear to be more accurate than those of the hybrid stress elements $Q_{S_{11-1}}$ and $Q_{S_{11-2}}$.

load cases	$Q_{S_{11-1}}$	$Q_{S_{11-2}}$	CGME	NCGME	exact
pure bending	92.2	92.9	22.7	99.6	100.0
shear forces	94.05	94.9	67.6	103.6	102.6

Table 3. Vertical displacements u_3 at point A of model b.

load cases	$Q_{S_{11-1}}$	$Q_{S_{11-2}}$	CGME	NCGME	exact
pure bending	−3006.6	−3015.1	−2294.9	−2996.5	−3000.0
shear forces	−4125.3	−4138.2	−3155.8	−4076.2	−4050.0

Table 4. The stresses σ_{11} at point B(1.0,1.0,2.0) of model b.

(2) Obviously, NCGME is less sensitive to geometric distortions (see Figure 14) in cases where elements are distorted. It is also observed that the accuracy of u_3 and σ_{11} from CGME is very poor due to the geometric distortions of elements.

5. Conclusions

For the generalized mixed finite elements presented in this work, both conditions of displacement continuity and traction reciprocity at interelement boundaries are relaxed by including them in the generalized mixed variational principle itself. Hence, the generalized H–R mixed variational principle is crucial to ensure that the generalized mixed elements are effective in obtaining the displacements and stresses directly in the mixed finite element computations. As mentioned in Section 3, two of the most prominent advantages of the compatible and noncompatible generalized mixed elements are that the symmetry with respect to both displacement and stress variables are guaranteed, and the coefficient matrix is invertible. The generalized mixed models seem to be preferable for introducing the displacement and traction boundary conditions simultaneously. The numerical results of the compatible and noncompatible generalized mixed elements are stable and the displacement and stress results of noncompatible generalized mixed elements are characterized by high-precision.

Certainly, like in the traditional mixed methods, a drawback of the generalized mixed methods is a larger number of unknown parameters in the linear system of equations for the finite element analysis. The added number of stress variables means that generally larger size algebraic problems have to be handled. But with the present computer technologies, it is not a problem. In fact, the power of the present computers will always be suitable for a large-scale finite element system. We emphasize that conveniently obtaining stable and highly accurate numerical results is the first priority for the design of engineering structures.

We believe the generalized mixed methods are simple and will be useful, especially as the methods are developed further. For wide engineering structures, some important applications of the noncompatible generalized mixed method should be extended, such as the treatment of the combination with other structural members, the evolution of the possible advantages in stress singularity problems, and nonlinear applications which may result from special structures. The pertinent theories of the generalized mixed elements should also be explored deeply; for instance, investigations of the local error bounds or practical

estimates for the variables should be done. On the other hand, the stresses and the displacements are interpolated with the same interpolation order in this work. Does this choice of interpolation order satisfy the inf-sup Ladyzhenskaya–Babuška–Breezi (LBB) condition? This work should be discussed in the next paper.

The task of developing high-performance finite element methods for complex engineering problems never seems to be completed.

Acknowledgments

References

[Adams and Cockburn 2005] S. Adams and B. Cockburn, "A mixed finite element method for elasticity in three dimensions", *J. Sci. Comput.* **25**:3 (2005), 515–521.

[Arnold 1990] D. N. Arnold, "Mixed finite element methods for elliptic problems", *Comput. Methods Appl. Mech. Eng.* **82**:1-3 (1990), 281–300.

[Arnold 2002] D. N. Arnold, "Differential complexes and numerical stability", pp. 137–157 in *Proceedings of the international congress of mathematicians (ICM 2002), I: Plenary lectures and ceremonies* (Beijing, 2002), Higher Education Press, Beijing, 2002.

[Arnold and Winther 2002] D. N. Arnold and R. Winther, "Mixed finite elements for elasticity", *Numer. Math.* **92**:3 (2002), 401–419.

[Arnold et al. 2007] D. N. Arnold, R. S. Falk, and R. Winther, "Mixed finite element methods for linear elasticity with weakly imposed symmetry", *Math. Comput.* **76**:260 (2007), 1699–1723.

[Arnold et al. 2008] D. N. Arnold, G. Awanou, and R. Winther, "Finite elements for symmetric tensors in three dimensions", *Math. Comput.* **77**:263 (2008), 1229–1251.

[Atluri et al. 1983] S. N. Atluri, R. H. Gallagher, and O. C. Zienkiewicz, *Hybrid and mixed finite element methods*, Wiley, Chichester, England, 1983.

[Babuška et al. 1977] I. Babuška, J. T. Oden, and J. K. Lee, "Mixed-hybrid finite element approximations of second-order elliptic boundary-value problems", *Comput. Methods Appl. Mech. Eng.* **11**:2 (1977), 175–206.

[Belytschko et al. 2013] T. Belytschko, W. K. Liu, and B. Moran, *Nonlinear finite elements for continua and structures*, 2nd ed., Wiley, Chichester, England, 2013.

[Bonet and Wood 1997] J. Bonet and R. D. Wood, *Nonlinear continuum mechanics for finite element analysis*, Cambridge University Press, 1997.

[Brezzi 1974] F. Brezzi, "On the existence, uniqueness and approximation of saddle-point problems arising from Lagrangian multipliers", *Rev. Française Automat. Informat. Recherche Opérationnelle Sér. Rouge* **8**:R-2 (1974), 129–151.

[Brezzi and Fortin 1991] F. Brezzi and M. Fortin, *Mixed and hybrid finite element methods*, Springer Series in Computational Mathematics **15**, Springer, New York, 1991.

[Chen 1982] W. J. Chen, "A high precision eight-node hexahedron element", *Chin. J. Theor. Appl. Mech.* **3**:26 (1982), 262–271.

[Cheung and Chen 1988] Y. K. Cheung and W. Chen, "Isoparametric hybrid hexahedral elements for three dimensional stress analysis", *Int. J. Numer. Methods Eng.* **26**:3 (1988), 677–693.

[Chien 1983] W. Z. Chien, "Method of high-order Lagrange multiplier and generalized variational principles of elasticity with more general forms of functionals", *Appl. Math. Mech.* **4**:2 (1983), 143–157.

[Dunham and Pister 1968] R. S. Dunham and K. S. Pister, "A finite element application of the Hellinger–Reissner variational theorem", DTIC Document, 1968, http://oai.dtic.mil/oai/oai?verb=getRecord&metadataPrefix=html&identifier=ADA446774.

[Fan 1996] J. R. Fan, *Exact theory of laminated thick plates and shells*, Science Press, Beijing, 1996. In Chinese.

[Felippa 1989a] C. A. Felippa, "Parametrized multifield variational principles in elasticity, I: Mixed functionals", *Comm. Appl. Numer. Methods* **5**:2 (1989), 79–88.

[Felippa 1989b] C. A. Felippa, "Parametrized multifield variational principles in elasticity, II: Hybrid functionals and the free formulation", *Comm. Appl. Numer. Methods* **5**:2 (1989), 89–98.

[Gatica et al. 2008] G. N. Gatica, A. Márquez, and S. Meddahi, "A new dual-mixed finite element method for the plane linear elasticity problem with pure traction boundary conditions", *Comput. Methods Appl. Mech. Eng.* **197**:9-12 (2008), 1115–1130.

[Gopalakrishnan and Guzmán 2011] J. Gopalakrishnan and J. Guzmán, "Symmetric nonconforming mixed finite elements for linear elasticity", *SIAM J. Numer. Anal.* **49**:4 (2011), 1504–1520.

[Herrmann 1967] L. R. Herrmann, "Finite element bending analysis for plates", *J. Eng. Mech. Div.* (*ASCE*) **93**:5 (1967), 13–26.

[Hoa and Feng 1998] S. V. Hoa and W. Feng, *Hybrid finite element method for stress analysis of laminated composites*, Kluwer Academic Publishers, Boston, 1998.

[Hu et al. 2016] J. Hu, H. Man, J. Wang, and S. Zhang, "The simplest nonconforming mixed finite element method for linear elasticity in the symmetric formulation on n-rectangular grids", *Comput. Math. Appl.* **71**:7 (2016), 1317–1336.

[Morley 1989] M. E. Morley, "A family of mixed finite elements for linear elasticity", *Numer. Math.* **55**:6 (1989), 633–666.

[Oden 1973] J. T. Oden, "Some contributions to the mathematical theory of mixed finite element approximations", pp. 3–23 in *Theory and practice in finite element structural anaylysis: proceedings of the 1973 Tokyo seminar on finite element analysis*, 1973.

[Oden and Reddy 1976] J. T. Oden and J. N. Reddy, "On mixed finite element approximations", *SIAM J. Numer. Anal.* **13**:3 (1976), 393–404.

[Pian 1964] T. H. Pian, "Derivation of element stiffness matrices by assumed stress distributions", *AIAA J.* **2**:7 (1964), 1333–1336.

[Qiu and Demkowicz 2010] W. Qiu and L. Demkowicz, "Variable Order Mixed H-Finite Element Method for Linear Elasticity with Weakly Imposed Symmetry. Ii. Affine and Curvilinear Elements in 2D", preprint, 2010. arXiv

[Qiu and Demkowicz 2011] W. Qiu and L. Demkowicz, "Mixed variable order h-finite element method for linear elasticity with weakly imposed symmetry: curvilinear elements in 2D", *Comput. Methods Appl. Math.* **11**:4 (2011), 510–539.

[Reissner 1950] E. Reissner, "On a variational theorem in elasticity", *J. Math. Physics* **29** (1950), 90–95.

[Sinwel 2009] A. Sinwel, *A new family of mixed finite elements for elasticity*, Ph.D. Thesis, Johannes Kepler University, 2009, http://www.uni-linz.ac.at.

[Talaslidis 1979] D. Talaslidis, "On the convergence of a mixed finite element approximation for cylindrical shells", *Z. Angew. Math. Mech.* **59**:9 (1979), 431–436.

[Taylor et al. 1976] R. L. Taylor, P. J. Beresford, and E. L. Wilson, "A non-conforming element for stress analysis", *Int. J. Numer. Methods Eng.* **10**:6 (1976), 1211–1219.

[Tian and Pian 2011] S. Z. Tian and T. H. Pian, *Variational principles with multi-variables and finite element methods with multi-variables*, Science Press, Beijing, 2011. In Chinese.

[Zienkiewicz and Taylor 2000] O. C. Zienkiewicz and R. L. Taylor, *The finite element method, II: Solid mechanics*, 5th ed., Butterworth-Heinemann, Oxford, 2000.

GUANGHUI QING: qingluke@126.com
College of Aeronautical Engineering, Civil Aviation University of China, Jinbei Road 2898, Tianjin, 300300, China

JUNHUI MAO: maojunhui@outlook.com
College of Aeronautical Engineering, Civil Aviation University of China, Jinbei Road 2898, Tianjin, 300300, China

YANHONG LIU: lyhqzh@126.com
College of Aeronautical Engineering, Civil Aviation University of China, Jinbei Road 2898, Tianjin, 300300, China

msp

▪msp

THICKNESS EFFECTS IN THE FREE VIBRATION OF LAMINATED MAGNETOELECTROELASTIC PLATES

CHAO JIANG AND PAUL R. HEYLIGER

A semianalytical discrete-layer approach is used to evaluate thickness effects in the free vibration of laminated magneto-electro-elastic (MEE) plates under various lateral boundary conditions. To match the primary physical phenomenon and simplify the study, piecewise continuous approximations are used through the thickness direction and either continuous global polynomial or trigonometric functions are used to simulate the deflection in axial or planar displacement fields. Thin plate models can be recovered to predict frequency estimation for various boundary conditions and compared with continuum-based theories using more complex approximations. Based on symmetry, the natural vibratory modes can be grouped to optimize computation. Numerical examples are used to show the thickness effects, with nondimensional frequencies computed for multiple plates under six lateral boundary conditions: simply supported, clamped, and four different combinations of free and clamped/simply supported edges. Along with the influence of electroelastic and magnetoelastic coupling, the results of these analyses clearly illustrate the limits of thin-plate approximations.

Introduction

Kirchhoff's plate theory yields many exact solutions that can predict the behavior of elastic deformations and stresses near or across the interface of material layers under static and dynamic loading, but usually only when the planar dimensions are much larger than the thickness. These methods can also be used for solving more complicated situations for multilayered composites that are more complex than for homogeneous elastic materials. An example of this is a plate formed with materials that combine elastic, electric, and magnetic effects. These are typically referred to as magneto-electro-elastic (MEE) solids, and have behavior that is significantly different than the purely elastic case.

The free vibration of purely elastic laminated plates has a very rich history with numerous contributions, with one of the most significant being the early work of Srinivas et al. [1970]. The development of representative theories and solutions for laminates where the elastic fields are coupled with both magnetic and electric fields are much more recent. The free vibration of MEE plates has been investigated by several researchers. By expanding the general boundary conditions in series form, Vel and Batra [2000] solved the static deformation of multilayered piezoelectric plates using a three-dimensional solution. The corresponding bending vibration problem has been studied by Vel et al. [2004]. For a simply supported multilayered MEE plate, the exact free vibration behavior using an exact closed-form solution has been derived using the pseudo-Stroh formulation by Pan and Heyliger [2002]. The state-space formulation is another method that has been used to analyze the static and dynamic behavior of MEE multilayered plates [Wang et al. 2003; Chen et al. 2007]. This methodology was also used by Chen [Chen et al.

2005] in the study of the free vibration of a nonhomogeneous isotropic MEE plate. Kondaiah, Shankar, and Ganesan [Kondaiah et al. 2012] used the finite element method to investigate beams made of MEE-thermo materials with different volume fractions under uniform temperature increase and clamped-free boundary conditions. The discrete-layer (DL) and domain-discretization methods have also been widely used in the analysis of anisotropic elastic and MEE plates and shells. The free vibration of an anisotropic and MEE plate was worked out by Chen, Heyliger and Pan [Chen et al. 2014] corresponding to different lateral boundary conditions.

The studies of many computational schemes for the solution of the equations of motion are based on the early work of Demarest [1971] and Eer Nisse [1967] through algorithms for elastic and piezoelectric parallelepipeds. However, if there is no existing closed-form solution, by expanding the displacements in terms of reasonable approximations, Hamilton's principle can be used to solve the weak form of the equations of motion. Furthermore, at an interface made of different materials, such as elastic, piezoelectric, and piezomagnetic properties, additional considerations may apply. Between two dissimilar materials, interface conditions include continuous stress, normal electric displacement, and normal magnetic induction. At a region of discontinuous material properties, these cause a discontinuity in the slope of the displacement and potential fields. The use of piecewise linear functions through the thickness with continuous global polynomial or trigonometric functions in the plane parallel to the interface allows a relatively accurate solution to be achieved. Via a semianalytical discrete-layer model, Heyliger [2000] developed the governing equations of layered elastic and piezoelectric parallelepipeds and obtained frequencies for a number of geometries and material combinations using this sort of approach.

Kirchhoff's classical theory of thin plates can often give sufficiently accurate results instead of carrying out a full three-dimensional stress analysis. But accuracy usually decreases with increasing thickness of the plate. Many authors qualify the value of the thickness relative to the larger plate dimensions as being "small" [Rao 2007], "much smaller" [Whitney 1987], or "significantly smaller" [Hjelmstad 1997]. Several authors have suggested limits with numbers attached: the thickness is "less than 1/20" [Ugural and Fenster 1995] of the lateral dimensions or that the lateral dimensions are "at least ten times" the thickness [Szilard 1974]. There has always been significant latitude assumed in applying these limits, since they are clearly influenced by plate geometry, the nature of the loading, and the material constitution. Such an inherent limitation of classical plate theory for the moderately thick plates necessitated the development of more refined theories in order to obtain reliable results for the behavior of these new materials. By plotting the frequencies as a function of the length-to-thickness ratio a/h, the present results indicate the level of errors influenced by thickness effects. The errors even within prior recommendations of a/h ratios can be significant.

The objective of this study is to use Hamilton's principle and appropriate approximations to make the link between the thin plate theory and more accurate continuum models to determine at what a/h ratios thin plate theory may be adequate for plates of laminated MEE material.

Theory

Governing equations.   A plate is a structural element that is typically flat and thin. The lateral dimension is larger than the thickness by a factor that will be directly considered in this work. The plates considered in this study are formed by multiple anisotropic layers and all constitutive relations are linear. A
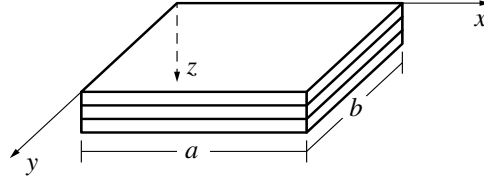
Figure 1. The geometry and coordinate system of the laminated plate.

rectangular Cartesian coordinate is used to formulate the governing equations with the origin as shown in Figure 1.

Of primary interest in this work are the thickness effects in laminated plate vibration for plates composed of MEE materials. Square laminates with lateral dimensions $a = b$ and a total thickness h are considered in this study. Each layer is homogeneous and each interface is perfectly bonded; therefore, the compatibility of displacements and the potentials are enforced. Even though the elastic displacements, electric and magnetic potentials, elastic traction, and the z-components of the electric displacement and magnetic induction are continuous, there is a discontinuity in the z-direction gradient of the displacement components, the electrostatic potential, and magnetostatic potential at the interface of two layers.

In a linear, isotropic MEE solid, the coupled constitutive law for each lamina can be expressed as

$$\sigma_{ij} = C_{ijkl} S_{kl} - e_{kij} E_k - q_{kij} H_k, \tag{1}$$

$$D_m = e_{mkl} S_{kl} + \epsilon_{mk} E_k + d_{mk} H_k, \tag{2}$$

$$B_m = q_{mkl} S_{kl} + d_{mk} E_k + \mu_{mk} H_k. \tag{3}$$

Here σ_{ij}, D_m, and B_m are respectively the components of stress, electric displacement, and magnetic induction; S_{kl}, E_k, and H_k represent the components of strain, electric field and magnetic field; C_{ijkl}, ϵ_{mk}, and μ_{mk} indicate the elastic, dielectric, and magnetic permeability coefficients; and e_{kij}, q_{kij}, and d_{mk} are the piezoelectric, piezomagnetic, and magnetoelectric coefficients. Moreover, by setting the values e_{mkl} or q_{mkl} equal to zero, the results for either purely piezoelectric, piezomagnetic, or elastic material can be achieved.

The relationship between the strain and displacement, electric (magnetic) field and its potential can be written as

$$S_{ij} = \frac{1}{2} \left(\frac{\partial u_i}{\partial x_j} + \frac{\partial u_j}{\partial x_i} \right), \tag{4}$$

$$E_k = -\frac{\partial \phi}{\partial x_k}, \tag{5}$$

$$H_k = -\frac{\partial \psi}{\partial x_k}. \tag{6}$$

Here, u_i are the infinitesimal displacement components and ϕ and ψ are the electric and magnetic potentials, respectively. The components x_k are related to the x, y and z in the rectangular Cartesian coordinates for $k = 1, 2, 3$.

The weak form of the equations of motion, the charge equation and the electromagnetic equation for a MEE medium within Hamilton's principle can be expressed as [Tiersten 1969]

$$\delta \int_{t_0}^{t} \mathrm{d}t \int_V \left[\tfrac{1}{2}\rho \dot{u}_j \dot{u}_j - H(S_{kl}, E_k, H_k) \right] \mathrm{d}V + \int_{t_0}^{t} \mathrm{d}t \int_S (T_k \delta u_k - \sigma \delta\phi - I \delta\psi) \, \mathrm{d}S = 0. \qquad (7)$$

Here, t_0 and t are two specified times, V is the volume of the plate, S is the surface that bounds V, and δ is the variational operator. The $\cdot$ superscript represents differentiation with respect to time, and T, σ, and I are surface tractions, surface charge, and surface current. H is the system enthalpy and can be written as

$$H = \tfrac{1}{2}C_{ijkl}S_{ij}S_{kl} - e_{ijk}E_i S_{jk} - \tfrac{1}{2}\epsilon_{ij}E_i E_j - q_{ijk}H_i S_{jk} - \tfrac{1}{2}\mu_{ij}H_i H_j - \mathrm{d}_{ik}E_i H_k. \qquad (8)$$

Based on the specific material properties used in this study, and setting $x_1 = x$, $x_2 = y$, and $x_3 = z$, with the corresponding displacement field as u, v, w, the weak form can be expanded as

$$\begin{aligned}
\int_{t_0}^{t} \mathrm{d}t \int_V \Big\{ & \rho(\dot{u}\delta\dot{u} + \dot{v}\delta\dot{v} + \dot{w}\delta\dot{w}) \\
& -\Big[C_{11}\frac{\partial u}{\partial x}\frac{\partial \delta u}{\partial x} + C_{12}\frac{\partial u}{\partial x}\frac{\partial \delta v}{\partial y} + C_{12}\frac{\partial \delta u}{\partial x}\frac{\partial v}{\partial y} + C_{13}\frac{\partial u}{\partial x}\frac{\partial \delta w}{\partial z} \\
& + C_{13}\frac{\partial \delta u}{\partial x}\frac{\partial w}{\partial z} + C_{22}\frac{\partial v}{\partial y}\frac{\partial \delta v}{\partial y} + C_{23}\frac{\partial v}{\partial y}\frac{\partial \delta w}{\partial z} + C_{23}\frac{\partial \delta v}{\partial y}\frac{\partial w}{\partial z} + C_{33}\frac{\partial w}{\partial z}\frac{\partial \delta w}{\partial z} \\
& + C_{16}\frac{\partial u}{\partial x}\Big(\frac{\partial \delta u}{\partial y} + \frac{\partial \delta v}{\partial x}\Big) + C_{16}\frac{\partial \delta u}{\partial x}\Big(\frac{\partial u}{\partial y} + \frac{\partial v}{\partial x}\Big) + C_{26}\frac{\partial v}{\partial y}\Big(\frac{\partial \delta u}{\partial y} + \frac{\partial \delta v}{\partial x}\Big) \\
& + C_{26}\frac{\partial \delta v}{\partial y}\Big(\frac{\partial u}{\partial y} + \frac{\partial v}{\partial x}\Big) + C_{36}\frac{\partial w}{\partial z}\Big(\frac{\partial \delta u}{\partial y} + \frac{\partial \delta v}{\partial x}\Big) + C_{36}\frac{\partial \delta w}{\partial z}\Big(\frac{\partial u}{\partial y} + \frac{\partial v}{\partial x}\Big) \\
& + C_{44}\Big(\frac{\partial v}{\partial z} + \frac{\partial w}{\partial x}\Big)\Big(\frac{\partial \delta v}{\partial z} + \frac{\partial \delta w}{\partial x}\Big) + C_{55}\Big(\frac{\partial u}{\partial z} + \frac{\partial w}{\partial y}\Big)\Big(\frac{\partial \delta u}{\partial z} + \frac{\partial \delta w}{\partial y}\Big) \\
& + C_{66}\Big(\frac{\partial u}{\partial y} + \frac{\partial v}{\partial x}\Big)\Big(\frac{\partial \delta u}{\partial y} + \frac{\partial \delta v}{\partial x}\Big) + C_{45}\Big(\frac{\partial v}{\partial z} + \frac{\partial w}{\partial x}\Big)\Big(\frac{\partial \delta u}{\partial z} + \frac{\partial \delta w}{\partial y}\Big) \\
& + C_{45}\Big(\frac{\partial \delta v}{\partial z} + \frac{\partial \delta w}{\partial x}\Big)\Big(\frac{\partial u}{\partial z} + \frac{\partial w}{\partial y}\Big) - e_{15}\delta E_1\Big(\frac{\partial u}{\partial z} + \frac{\partial w}{\partial x}\Big) - e_{15}E_1\Big(\frac{\partial \delta u}{\partial z} + \frac{\partial \delta w}{\partial x}\Big) \\
& - e_{24}\delta E_2\Big(\frac{\partial v}{\partial z} + \frac{\partial w}{\partial y}\Big) - e_{24}E_2\Big(\frac{\partial \delta v}{\partial z} + \frac{\partial \delta w}{\partial y}\Big) - e_{31}\delta E_3\frac{\partial u}{\partial x} - e_{31}E_3\frac{\partial \delta u}{\partial x} \\
& - e_{32}\delta E_3\frac{\partial v}{\partial y} - e_{32}E_3\frac{\partial \delta v}{\partial y} - e_{33}\delta E_3\frac{\partial w}{\partial z} - e_{33}E_3\frac{\partial \delta w}{\partial z} - q_{15}\delta H_1\Big(\frac{\partial u}{\partial z} + \frac{\partial w}{\partial x}\Big) \\
& - q_{15}H_1\Big(\frac{\partial \delta u}{\partial z} + \frac{\partial \delta w}{\partial x}\Big) - q_{24}\delta H_2\Big(\frac{\partial v}{\partial z} + \frac{\partial w}{\partial y}\Big) - q_{24}H_2\Big(\frac{\partial \delta v}{\partial z} + \frac{\partial \delta w}{\partial y}\Big) \\
& - q_{31}\delta H_3\frac{\partial u}{\partial x} - q_{31}H_3\frac{\partial \delta u}{\partial x} - q_{32}\delta H_3\frac{\partial v}{\partial y} - q_{32}H_3\frac{\partial \delta v}{\partial y} - q_{33}\delta H_3\frac{\partial w}{\partial z} - q_{33}H_3\frac{\partial \delta w}{\partial z} \\
& - \epsilon_{11}E_1\delta E_1 - \epsilon_{22}E_2\delta E_2 - \epsilon_{33}E_3\delta E_3 - \mu_{11}H_1\delta H_1 - \mu_{22}H_2\delta H_2 - \mu_{33}H_3\delta H_3 \Big] \Big\} \mathrm{d}V \\
& + \int_{t_0}^{t} \mathrm{d}t \int_S (T_k \delta u_k - \sigma\delta\phi - I\delta\psi)\,\mathrm{d}S = 0. \quad (9)
\end{aligned}$$

It is possible to integrate the weak form by parts and collect the coefficients with respect to δu, δv, δw, $\delta\phi$, and $\delta\psi$. Since we use the Ritz method, there is no need for this step. Here the focus is on the

quasistatic state, which means there is no electric charge or current densities across the surface. Body forces are also assumed to be zero in the results that follow.

Ritz approximations. The five primary field variables (u, v, w, ϕ, and ψ) can be approximated with x, y, z, and t as follows:

$$u(x, y, z, t) = \sum_{j=1}^{n} U_j(x, y, t)\overline{\Psi}_j^u(z) = \sum_{i=1}^{m}\sum_{j=1}^{n} U_{ji}(t)\Psi_i^u(x, y)\overline{\Psi}_j^u(z),$$

$$v(x, y, z, t) = \sum_{j=1}^{n} V_j(x, y, t)\overline{\Psi}_j^v(z) = \sum_{i=1}^{m}\sum_{j=1}^{n} V_{ji}(t)\Psi_i^v(x, y)\overline{\Psi}_j^v(z),$$

$$w(x, y, z, t) = \sum_{j=1}^{n} W_j(x, y, t)\overline{\Psi}_j^w(z) = \sum_{i=1}^{m}\sum_{j=1}^{n} W_{ji}(t)\Psi_i^w(x, y)\overline{\Psi}_j^w(z), \qquad (10)$$

$$\phi(x, y, z, t) = \sum_{j=1}^{n} \Phi_j(x, y, t)\overline{\Psi}_j^v(z) = \sum_{i=1}^{m}\sum_{j=1}^{n} \Phi_{ji}(t)\Psi_i^\phi(x, y)\overline{\Psi}_j^\phi(z),$$

$$\psi(x, y, z, t) = \sum_{j=1}^{n} \Psi_j(x, y, t)\overline{\Psi}_j^v(z) = \sum_{i=1}^{m}\sum_{j=1}^{n} \Psi_{ji}(t)\Psi_i^\psi(x, y)\overline{\Psi}_j^\psi(z).$$

Here, U_{ji}, V_{ji}, W_{ji}, Φ_{ji}, and Ψ_{ji} are unknown constants. $\Psi_i(x, y)$ are the in-plane approximation functions, while $\overline{\Psi}_j$ are the one-dimensional Lagrangian interpolation polynomials in the thickness direction with respect to each variable.

The corresponding virtual fields can be expressed as

$$\delta u = \Psi_i^u(x, y)\overline{\Psi}_j^u(z), \quad \delta v = \Psi_i^v(x, y)\overline{\Psi}_j^v(z), \quad \delta w = \Psi_i^w(x, y)\overline{\Psi}_j^w(z),$$
$$\delta\phi = \Psi_i^\phi(x, y)\overline{\Psi}_j^\phi(z), \quad \delta\psi = \Psi_i^\psi(x, y)\overline{\Psi}_j^\psi(z). \qquad (11)$$

By assuming periodic motion, substituting these approximations into the weak form, and collecting the coefficients of the variations of the displacements and placing the results in matrix form, the system can be written as

$$\begin{bmatrix} [M^{11}] & [0] & [0] & [0] & [0] \\ [0] & [M^{22}] & [0] & [0] & [0] \\ [0] & [0] & [M^{33}] & [0] & [0] \\ [0] & [0] & [0] & [0] & [0] \\ [0] & [0] & [0] & [0] & [0] \end{bmatrix} \begin{Bmatrix} \{U\} \\ \{V\} \\ \{W\} \\ \{\Phi\} \\ \{\Psi\} \end{Bmatrix} \rho\omega^2 = \begin{bmatrix} [K^{11}] & [K^{12}] & [K^{13}] & [K^{14}] & [K^{15}] \\ [K^{21}] & [K^{22}] & [K^{23}] & [K^{24}] & [K^{25}] \\ [K^{31}] & [K^{32}] & [K^{33}] & [K^{34}] & [K^{35}] \\ [K^{41}] & [K^{42}] & [K^{43}] & [K^{44}] & [K^{45}] \\ [K^{51}] & [K^{52}] & [K^{53}] & [K^{54}] & [K^{55}] \end{bmatrix} \begin{Bmatrix} \{U\} \\ \{V\} \\ \{W\} \\ \{\Phi\} \\ \{\Psi\} \end{Bmatrix}. \qquad (12)$$

The submatrices here are related to the materials' characteristics, which include the elastic stiffnesses, piezoelectric coefficients, piezomagnetic coefficients, and shape functions. These matrices are given in the Appendix.

The DL model is based on separating the field variables in the thickness direction and within the plane of the plate. This can effectively reduce the computational effort. One-dimensional Lagrangian polynomials are sufficient to describe these displacements in the thickness direction. The in-plane functions are generated depending on the various lateral boundary conditions. These are described below.

Boundary Conditions. The following classes of boundary conditions are discussed.

SSSS: simply supported around all edges. Srinivas [Srinivas et al. 1970] solved this problem using an exact method. The in-plane approximation functions are treated as harmonic functions, as per Heyliger [2000], to determine the fundamental in-plane modes.

For the simply supported condition,

$$w = \sigma_{xx} = \sigma_{xy} = \phi = \psi = 0 \quad \text{at} \quad x = 0, a, \tag{13}$$

$$w = \sigma_{xy} = \sigma_{yy} = \phi = \psi = 0 \quad \text{at} \quad y = 0, b. \tag{14}$$

To satisfy the essential boundary conditions on w, ϕ, and ψ, the in-plane approximations are

$$\Psi_i^u(x, y) = \cos \frac{m\pi x}{a} \sin \frac{n\pi y}{b}, \quad \Psi_i^v(x, y) = \sin \frac{m\pi x}{a} \cos \frac{n\pi y}{b}, \quad \Psi_i^w(x, y) = \sin \frac{m\pi x}{a} \sin \frac{n\pi y}{b}.$$

Here, ϕ and ψ have the same expression as w, and each individual pair of (m, n) contains a different value of i.

CCCC: clamped around all edges. The boundary conditions for this case are

$$u = v = w = \phi = \psi = 0 \quad \text{at} \quad x = 0, a \quad \text{and at} \quad y = 0, b. \tag{15}$$

Since displacements are zero at the domain endpoints, it is convenient to give the approximations along the (x, y) directions written in the "parent" domain (ξ, η), which allows computations in terms of coordinate origins. Chen et al. [2014] used this approximation for all the clamped conditions and compared their results with frequencies from a FEM approach. The coordinates ξ and η are introduced as $\xi = 2x/a$ and $\eta = 2y/b$ and varying from -1 to 1, with ξ_i and η_i being the equally spaced locations within $(-1, 1)$. For example, within the ξ domain, the displacements are expressed as following:

$$\text{when } i = 1, \ f_x = (1 - \xi)(1 + \xi);$$

$$\text{when } i = 2, \ f_x = (1 - \xi)\xi(1 + \xi);$$

$$\text{when } i = 3, \ f_x = (1 - \xi)\left(\tfrac{1}{3} - \xi\right)\left(\tfrac{1}{3} + \xi\right)(1 + \xi).$$

FCFC: free-clamped-free-clamped. Here two opposite sides of the plate are "free" (in that all components of the stress-traction vector are 0, as are the electric displacement and normal flux), and the others are clamped. In this case it is assumed that the plate is clamped along the x direction, while the y direction is free. Therefore, the appropriate boundary conditions are

$$u = v = w = \phi = \psi = 0 \qquad \text{at} \quad x = 0, a, \tag{16}$$

$$\sigma_{yy} = \sigma_{xy} = \sigma_{yz} = D_y = B_y = 0 \quad \text{at} \quad y = 0, b. \tag{17}$$

Demarest [1971] showed that group theory can be used to simplify vibration analysis in the case of traction-free surfaces using Legendre polynomials. The approximations are given in even/odd forms for these functions. The lowest three terms in the even group are 1, $(3x^2 - 1)/2$, and $(35x^4 - 30x^2 + 3)/8$, while for the odd functions are shown as x, $(5x^3 - 3x)/2$, and $(63x^5 - 70x^3 + 15x)/8$ [Abromowitz and Stegun 1966].

CFFF: clamped-free-free-free. Here, only one edge is clamped; the others are free. This is also known as the cantilever plate; boundary conditions are as follows:

$$u = v = w = \phi = \psi = 0 \qquad \text{at} \quad x = 0, \tag{18}$$

$$\sigma_{xx} = \sigma_{xy} = \sigma_{xz} = D_x = B_x = 0 \quad \text{at} \quad x = a, \tag{19}$$

$$\sigma_{yy} = \sigma_{xy} = \sigma_{yz} = D_y = B_y = 0 \quad \text{at} \quad y = 0, b. \tag{20}$$

Here, to match the displacements at $x = 0$, we use power series of at least first order along the x direction and maintain the Legendre polynomials in the y direction.

CCFF: clamped-clamped-free-free. Here two adjacent edges are clamped, while the others are free; boundary conditions are as follows:

$$u = v = w = \phi = \psi = 0 \qquad \text{at} \quad x = 0, \ y = 0, \tag{21}$$

$$\sigma_{xx} = \sigma_{xy} = \sigma_{xz} = D_x = B_x = 0 \quad \text{at} \quad x = a, \tag{22}$$

$$\sigma_{yy} = \sigma_{xy} = \sigma_{yz} = D_y = B_y = 0 \quad \text{at} \quad y = b. \tag{23}$$

The displacements and potential along the x and y directions are extended as power series in a manner similar to the cantilever plate.

SFSF: simple-free-simple-free. In this condition, two opposite sides are simply supported and the others are free; boundary conditions are as follows:

$$w = \sigma_{xx} = \sigma_{xy} = \phi = \psi = 0 \qquad \text{at} \quad x = 0, a, \tag{24}$$

$$\sigma_{yy} = \sigma_{xy} = \sigma_{yz} = D_y = B_y = 0 \quad \text{at} \quad y = 0, b. \tag{25}$$

Fourier series are used in the x direction. The only difference is specified terms for the approximate function, as m and n are either $2i + 1$ or $2i$. The approximation functions in u and v are coupled with the displacement in w, and the modes are separated into two groups (odd and even) according to these groupings. For example, the first terms in odd group are: $\Psi_1^u(x, y) = \cos(\pi x/a) \sin(\pi y/b)$, $\Psi_1^v(x, y) = \sin(\pi x/a) \cos(\pi y/b)$, and $\Psi_1^w(x, y) = \sin(\pi x/a) \sin(\pi y/b)$. The first terms in the even group are: $\Psi_2^u(x, y) = \cos(2\pi x/a) \sin(2\pi y/b)$, $\Psi_2^v(x, y) = \sin(2\pi x/a) \cos(2\pi y/b)$, and $\Psi_2^w(x, y) = \sin(2\pi x/a) \sin(2\pi y/b)$. For all clamped-clamped and clamped-free conditions, symmetry can be used to exploit the nature of the eigenvalue problem. By grouping the approximations according to symmetry groups as introduced by Ohno [1976], the original complete problem can be reduced into four smaller problems with the same result but at a lower computational cost.

Results

Isotropic plates. Several problems are first considered for the homogeneous isotropic plate to demonstrate the accuracy of the DL model. This type of plate has a number of solutions with which to compare.

Simply supported condition. The convergence of the semianalytical discrete layer model has been explored using the natural frequencies of a square isotropic plate. For the simply supported condition, the Navier solution gives an exact result for Kirchhoff's plate theory. The in-plane variations in transverse displacement are given as a single term in the sine or cosine components of the expansion. Fixing $a/b = 1$,
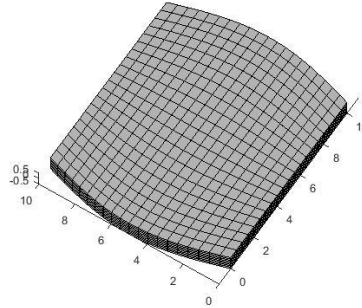
Figure 2. The first in-plane mode of the SSSS isotropic plate (mode 7).

$a/h = 10$, and $\nu = 0.3$, the natural frequencies are compared with Srinivas's elasticity theory and Reddy's higher-order shear deformation theory (HSDPT) [Reddy and Phan 1985].

Equal thicknesses of each discrete layer were used. The results are presented in terms of the nondimensional parameter $\bar{\omega} = \omega(\rho h^2/G)^{1/2}$. Each frequency was computed using 36 in-plane terms and eight sublayers, which gave values of sufficient accuracy such that little change was observed in increasing the numbers beyond these limits. The results are shown in Table 1. The highlights in bold indicate the in-plane modes for which the transverse displacement is zero. The mode shapes for the bending modes are well known and are not repeated here. The seventh mode, which is purely in-plane and is not included or computed by Srinivas or Reddy, is shown in Figure 2 and is an example of the usefulness of continuum theories that provide all modes rather than just those related to bending.

All-clamped condition. The natural frequencies of an all clamped isotropic ($\nu = 0.3$) plate have been computed by Liew et al. [1993] using the Rayleigh–Ritz procedure to solve the energy function derived from Mindlin's plate theory. The frequency parameter was given as $\bar{\omega} = (\omega a^2/\pi^2)\sqrt{\rho h/D}$, where $D = Eh^3/[12(1-\nu^2)]$ and h is the total thickness. Using 36 in-plane terms with eight layers, results are shown in Table 2. Once again, the present model captures in-plane modes (listed in bold face) that were not considered by the previous authors. It is clear that as the thickness increases, the in-plane frequencies are reduced and approach the lowest bending frequency given by simpler theories.

frequency number	[Srinivas et al. 1970]	HSDPT [Reddy and Phan 1985]	present solution		
			$N=4$	$N=8$	$N=16$
1	0.0932	0.0931	0.0939	0.0933	0.0932
2, 3	0.226	0.2222	0.2245	0.2231	0.2227
4	0.3421	0.3411	0.3452	0.3429	0.3423
5, 6	0.4171	0.4158	0.4211	0.4182	0.4174
7	–	–	**0.4443**	**0.4443**	**0.4443**
8, 9	0.5239	0.5221	0.5292	0.5253	0.5243
10	–	0.6545	0.6642	0.6589	0.6575

Table 1. The first ten nondimensional frequencies of an isotropic square plate under the simply supported boundary condition (SSSS) with $\nu = 0.3$ and $a/h = 10$, normalized by $\bar{\omega} = \omega(\rho h^2/G)^{1/2}$.

frequency number	$a/h = 10$		$a/h = 5$	
	[Liew et al. 1993]	present	[Liew et al. 1993]	present
1	3.2954	3.3297	2.6875	2.7370
2	6.2858	6.3633	4.6907	4.7940
3	6.2858	6.3633	4.6907	4.7940
4	8.8098	8.9295	–	**6.2751**
5	10.3788	10.5316	–	**6.2751**
6	10.4778	10.6316	6.2985	6.4484
7	–	**12.5221**	7.1767	7.3598
8	–	**12.5221**	–	**7.4371**
9	12.5529	12.7474	7.2759	7.4621
10	12.5529	12.7474	8.5155	8.7416

Table 2. The first ten nondimensional frequencies of an isotropic square plate under the CCCC boundary condition with $\nu = 0.3$, normalized by $\bar{\omega} = (\omega a^2/\pi^2)\sqrt{\rho h/D}$.

frequency number	$a/h = 10$		$a/h = 5$	
	[Liew et al. 1993]	present	[Liew et al. 1993]	present
1	2.0904	2.1094	1.7772	1.8061
2	2.4342	2.4533	2.0151	2.0429
3	3.9055	3.9312	–	**2.9771**
4	5.3392	5.3996	3.1652	3.2004
5	5.7811	5.8408	4.0413	4.1242
6	–	**5.9501**	4.3472	4.4262
7	6.9368	6.9834	–	**5.3326**
8	7.3046	7.3757	–	**5.4493**
9	9.6241	9.7567	5.3813	5.4827
10	9.9989	10.0960	5.3813	5.4831

Table 3. The first ten nondimensional frequencies of an isotropic square plate under the FCFC boundary condition with $\nu = 0.3$, normalized by $\bar{\omega} = (\omega a^2/\pi^2)\sqrt{\rho h/D}$.

FCFC condition. Table 3 lists the first ten nondimensional natural frequencies of isotropic square plates for the FCFC condition. This case was also considered by Liew et al. [1993] and the DL results provide frequency predictions that are close to but slightly above those numbers.

CFFF condition. The cantilever plate is an extremely important case that has numerous practical applications. Liew et al. [1993] gave results without showing the mode shapes. Frequencies are given in Table 4. The present model again consistently gives bending and torsional frequencies that are slightly larger than those of the Mindlin results compared to the previous work. The in-plane frequencies are normally smaller.

CCFF Condition. Results for this case are computed using four terms in both x and y directions together with four layers through the thickness. Comparison of frequencies is demonstrated in Table 5 and indicate

frequency number	$a/h = 10$		$a/h = 5$	
	[Liew et al. 1993]	present	[Liew et al. 1993]	present
1	0.3476	0.3573	0.3384	0.3471
2	0.8168	0.8401	0.7445	0.7637
3	2.0356	2.1111	–	**1.1181**
4	2.5836	**2.2349**	1.7806	1.8451
5	2.8620	2.9795	2.2765	2.5154
6	4.8162	3.0007	2.4205	2.5742
7	5.4834	**5.3357**	3.8851	**2.6689**
8	5.7769	5.4769	4.3168	**2.9809**
9	6.2381	**5.9619**	4.5996	4.3811
10	7.9181	7.9682	4.8966	**4.8979**

Table 4. The first ten nondimensional frequencies of an isotropic square plate under the CFFF boundary condition with $v = 0.3$, normalized by $\bar{\omega} = (\omega a^2/\pi^2)\sqrt{\rho h/D}$.

frequency number	$a/h = 10$		$a/h = 5$	
	[Liew et al. 1993]	present	[Liew et al. 1993]	present
1	0.6762	0.6946	0.6328	0.6489
2	2.2438	2.3246	1.9221	1.9856
3	2.5049	2.6055	2.1499	2.2313
4	4.2557	4.5059	–	**2.6032**
5	5.5633	**5.2043**	–	**3.3287**
6	5.8188	**6.6564**	3.4217	3.5729
7	7.2399	7.9353	4.3468	**3.9720**
8	7.5055	**7.9449**	4.5533	5.3123
9	9.9651	8.6372	5.4276	5.6800
10	10.1661	9.5767	5.6539	**6.1263**

Table 5. The first ten nondimensional frequencies of an isotropic square plate under the CCFF boundary condition with $v = 0.3$, normalized by $\bar{\omega} = (\omega a^2/\pi^2)\sqrt{\rho h/D}$.

slightly larger discrepancies that those of prior predictions. Some of this may be differences in actual bending frequencies, but other gaps may exist because the model of Liew et al. [1993] may not capture some of the nonbending modes, especially as the plate becomes thick.

SFSF condition. Table 6 shows the comparison with Liew et al.'s results [1993]. It again appears that the model of the previous authors captures only the bending frequencies under the SFSF condition. Hence at a minimum, the lower modes can be directly compared.

Composite MEE plates. There are three primary features associated with the results in this section. The first is a direct comparison with one of the few models of laminated MEE plates to ensure accuracy of the results that follow. The second is a collection of results for laminated MEE plates under a variety of

frequency number	$a/h = 10$		$a/h = 5$	
	[Liew et al. 1993]	present	[Liew et al. 1993]	present
1	0.9565	0.9593	0.9102	0.9139
2	1.5593	1.5670	1.4280	1.4342
3	3.4307	3.4808	–	**2.4697**
4	3.6838	3.7036	2.9521	2.9845
5	4.3358	4.3634	3.1684	3.1994
6	–	**4.9400**	3.6435	3.6777
7	6.2971	6.4010	–	**4.6127**
8	6.7071	6.9051	5.0216	5.0994
9	7.7648	7.8291	5.3173	5.4507
10	8.3513	8.4230	–	**5.6993**

Table 6. The first ten nondimensional frequencies of an isotropic square plate under SFSF boundary condition with $\nu = 0.3$, normalized by $\bar{\omega} = (\omega a^2/\pi^2)\sqrt{\rho h/D}$.

CCCC	[Chen et al. 2014]	present	FCFC	[Chen et al. 2014]	present
1	0.3332	0.3332	1	0.2193	0.2193
2	0.5987	0.5987	2	0.2572	0.2572
3	0.5987	0.5987	3	0.3798	0.3798
4	0.7459	0.7459	4	0.3967	0.3967
5	0.7459	0.7459	5	0.5182	0.5182
6	0.8138	0.8138	6	0.5656	0.5656

Table 7. The first six nondimensional frequencies of an elastic square plate with hexagonal materials under CCCC and FCFC conditions, normalized by $\bar{\omega} = \omega h \sqrt{\rho/C_{11}}$.

lamination schemes and boundary conditions. Finally, the influence of the a/h ratio on the frequencies for these plates are explored.

Comparison with existing results. The free vibration of composite MEE plates under CCCC and FCFC conditions has been extensively studied by Chen, Heyliger and Pan [Chen et al. 2014] for a fixed a/h ratio. These simulations all used properties for either a purely elastic hexagonal material, the piezoelectric material barium titanate ($BaTiO_3$), denoted in this work by the letter B, and the magnetostrictive material cobalt ferrite ($CoFe_2O_4$), denoted in this study by the letter F. All plates are assumed to have three layers of equal thickness. In the case of homogeneous MEE materials, either BBB or FFF are used to denote the differing materials. Composites use FBF or BFB to indicate the lamination scheme. The material properties are given in [Chen et al. 2014]. These results were repeated here to ensure accuracy for MEE media and are summarized in Table 7. Excellent agreement was found for all cases.

For the remaining examples, the nondimensional frequencies are calculated by $\bar{\omega} = \omega h \sqrt{\rho_{max}/c_{max}}$ and are typically plotted using the parameter $\Omega = \bar{\omega}(a^2/h)\sqrt{\rho_{max}/c_{max}}$. Here ρ_{max} is the largest value of material density in the laminate and c_{max} is the largest component of the elastic stiffness tensor in the laminate.
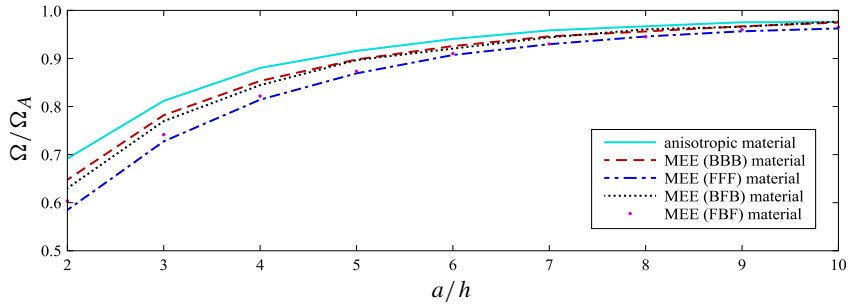
Figure 3. The relative differences of fundamental frequencies of the SSSS plate compared to the thin plate limit for the five different material combinations as a function of a/h.

SSSS condition. The influence of a/h for very thick plates was first studied for the five basic lamination schemes (hexagonal, BBB, FFF, FBF, and BFB). In this case, all frequencies were normalized by their respective values for the thin plate, taken as the frequency computed at $a/h = 30$. Beyond this point there was very little change in the dimensionless frequency for all plates considered. The results of this analysis are shown in Figure 3 for the fundamental frequency and show that the level of difference with thin plate limits are ordered as FFF > FBF > BFB > BBB > hex. Hence the purely magnetostrictive plate has stronger thickness effects than the purely elastic hexagonal plate.

Figure 4 displays the influence of slenderness for the first six frequencies of a hexagonal material along with the corresponding mode shapes. It appears that there are only four curves, but this is because

dimensionless frequency variation
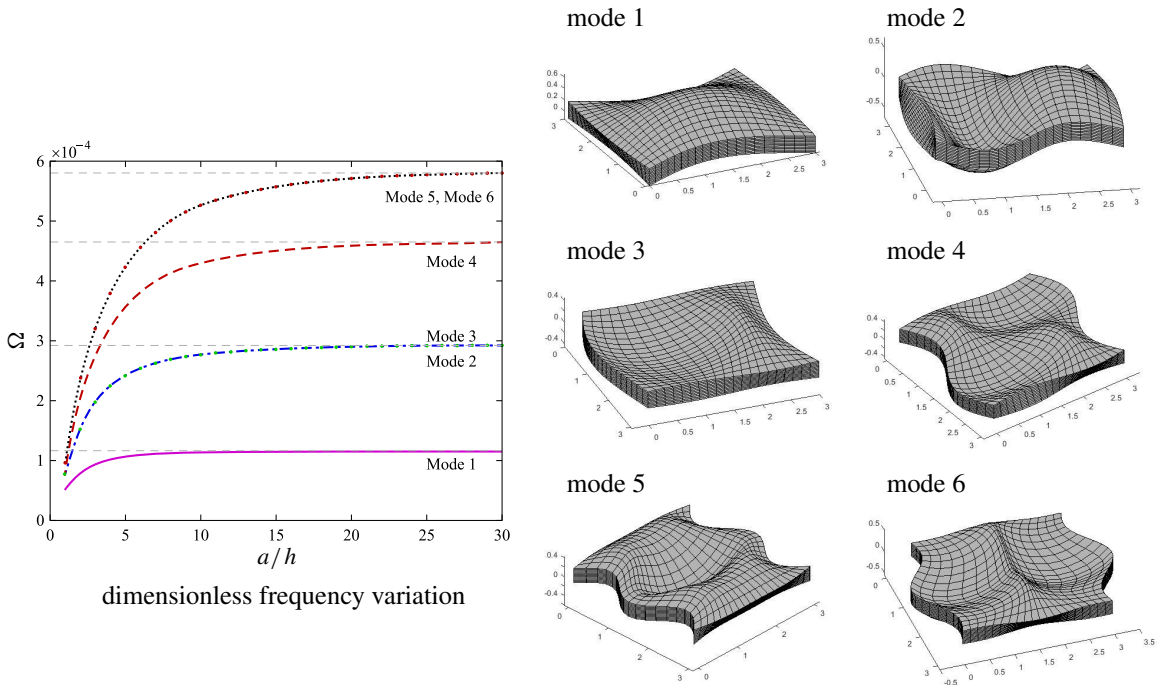
Figure 4. Frequency variation as a function of a/h and the first six mode shapes ($a/h = 10$) for the anisotropic elastic square SSSS plate.
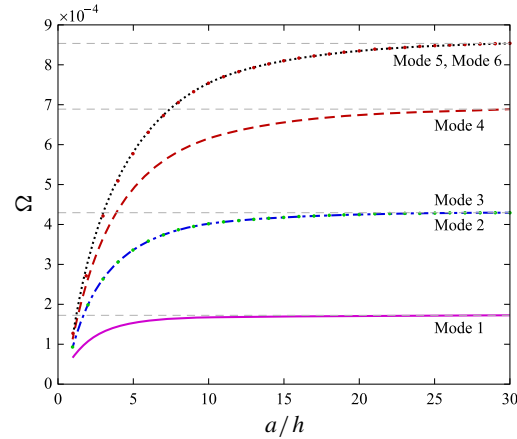
Figure 5. Dimensionless frequency variation as a function of a/h for the SSSS square BFB plate.

frequencies	B material		F material	
	[Chen et al. 2014]	present	[Chen et al. 2014]	present
1	1.7817	1.7817	1.3667	1.3667
2	2.9486	2.9486	2.2311	2.2311
3	2.9486	2.9486	2.2311	2.2311
4	3.2195	3.2195	2.7905	2.7905
5	3.2195	3.2195	2.2311	2.2311
6	3.7120	3.7120	2.9345	2.9345

Table 8. The first six nondimensional frequencies of square plates composed of BBB and FFF materials under the CCCC condition, normalized by $\bar{\omega} = \omega a \sqrt{\rho_{\max}/C_{\max}}$.

several of the modes for this boundary condition are repeated. The horizontal dashed lines indicate the asymptote of each frequency which is again chosen using the value at $a/h = 30$. Figure 5 shows the frequency arrangement of BFB materials. The arrangements are similar for other stacking sequences. The character of all of the curves are very similar in nature, with slight differences in value and mode order sometimes occurring. Table 9 lists the first six frequencies at a/h ratios of 30 for reference since these values are used for all plots and can be used as thin plate predictions using other models. As was the case for the very thick plates, an increased amount of F material results in larger differences in the thin plate limits. Yet for an a/h ratio larger than 20, the differences are within 3 percent.

CCCC condition. The differences of the first frequency with respect to a/h for the five stacking sequences are shown in Figure 6. The differences between the thin-plate limits are all slightly higher than those of the SSSS condition, with differences of about 10 percent when $a/h = 10$. Figure 7 gives the first six frequencies of the hexagonal plate as a function of a/h ratio and the corresponding mode shapes. It is clear that as the slenderness increases, the fifth and the sixth frequencies are identical.

bending mode	hex	BBB	FFF	BFB	FBF
1	$1.17 \cdot 10^{-4}$	$2.92 \cdot 10^{-4}$	$1.83 \cdot 10^{-4}$	$1.73 \cdot 10^{-4}$	$1.97 \cdot 10^{-4}$
2	$2.92 \cdot 10^{-4}$	$7.24 \cdot 10^{-4}$	$4.55 \cdot 10^{-4}$	$4.31 \cdot 10^{-4}$	$4.88 \cdot 10^{-4}$
3	$2.92 \cdot 10^{-4}$	$7.24 \cdot 10^{-4}$	$4.55 \cdot 10^{-4}$	$4.31 \cdot 10^{-4}$	$4.88 \cdot 10^{-4}$
4	$4.65 \cdot 10^{-4}$	$1.16 \cdot 10^{-3}$	$7.24 \cdot 10^{-4}$	$6.88 \cdot 10^{-4}$	$7.79 \cdot 10^{-4}$
5	$5.79 \cdot 10^{-4}$	$1.44 \cdot 10^{-3}$	$9.01 \cdot 10^{-4}$	$8.52 \cdot 10^{-4}$	$9.68 \cdot 10^{-4}$
6	$5.79 \cdot 10^{-4}$	$1.44 \cdot 10^{-3}$	$9.01 \cdot 10^{-4}$	$8.52 \cdot 10^{-4}$	$9.68 \cdot 10^{-4}$

Table 9. Frequencies for homogeneous plates composed of five stacking sequences under the SSSS condition at $a/h = 30$.
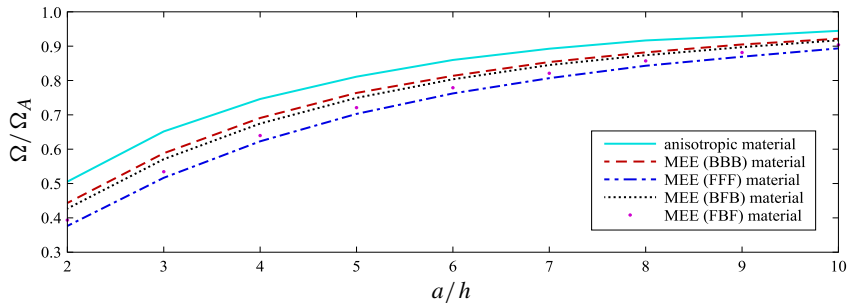
Figure 6. The relative differences of fundamental frequencies of the CCCC plate compared to the thin plate limit for the five different material combinations as a function of a/h.

dimensionless frequency variation
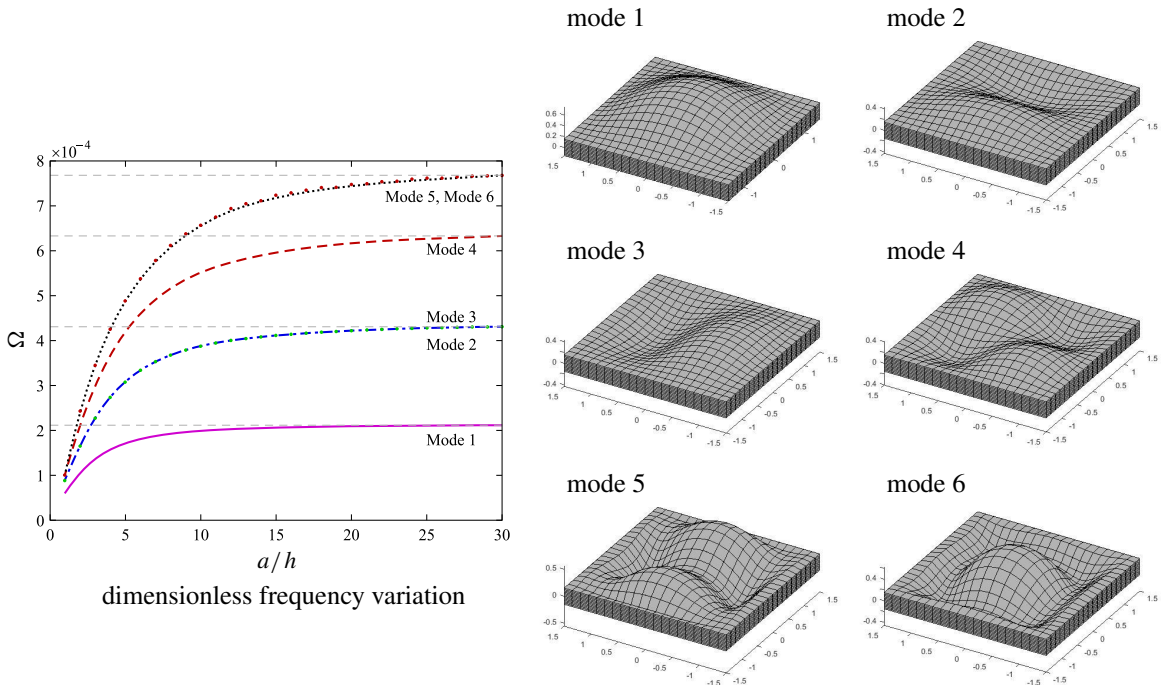
Figure 7. Frequency variation as a function of a/h and the first six mode shapes ($a/h = 10$) for the anisotropic elastic square CCCC plate.
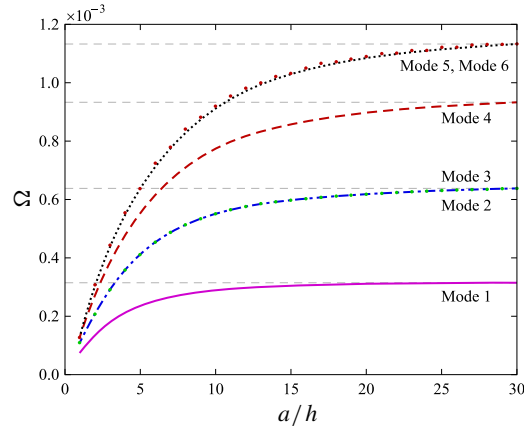
Figure 8. Dimensionless frequency variation as a function of a/h for the CCCC square BFB plate.

bending mode	hex	BBB	FFF	BFB	FBF
1	$2.12 \cdot 10^{-4}$	$5.32 \cdot 10^{-4}$	$3.37 \cdot 10^{-4}$	$3.16 \cdot 10^{-4}$	$3.61 \cdot 10^{-4}$
2	$4.31 \cdot 10^{-4}$	$1.07 \cdot 10^{-3}$	$6.76 \cdot 10^{-4}$	$6.39 \cdot 10^{-4}$	$7.24 \cdot 10^{-4}$
3	$4.31 \cdot 10^{-4}$	$1.07 \cdot 10^{-3}$	$6.76 \cdot 10^{-4}$	$6.39 \cdot 10^{-4}$	$7.24 \cdot 10^{-4}$
4	$6.33 \cdot 10^{-4}$	$1.57 \cdot 10^{-3}$	$9.86 \cdot 10^{-4}$	$9.31 \cdot 10^{-4}$	$1.06 \cdot 10^{-3}$
5	$7.67 \cdot 10^{-4}$	$1.90 \cdot 10^{-3}$	$1.19 \cdot 10^{-3}$	$1.13 \cdot 10^{-3}$	$1.28 \cdot 10^{-3}$
6	$7.67 \cdot 10^{-4}$	$1.92 \cdot 10^{-3}$	$1.20 \cdot 10^{-3}$	$1.13 \cdot 10^{-3}$	$1.29 \cdot 10^{-3}$

Table 10. Frequencies for homogeneous plates composed of five stacking sequences under the CCCC condition at $a/h = 30$.

Figure 8 shows the effect of the length-to-thickness ratio for the first six frequencies for BFB plates under all-clamped conditions. The levels of difference with the thin-plate limits are similar to those of the fully simply supported condition. Frequencies are repeated and lines are coincident for modes 2 and 3. Table 10 lists the first six frequencies of the five stacking sequences under the all-clamped condition with a/h equal to 30.

FCFC condition. Figure 9 shows the frequency response for the five stacking sequences under the FCFC condition. Figure 10 shows the influence of a/h ratio for the hexagonal material along with the lowest six mode shapes. Figure 11 gives the slenderness effects for BFB materials. Table 11 gives the values of the first seven frequencies according to five stacking sequences at slenderness of $a/h = 30$. Reductions are smaller for the piezoelectric and piezomagnetic plates in the sixth frequency. This is apparent from the different curvature of each frequency lines. As a/h ratios approach 20, the percentage differences are within 5 percent.

CFFF condition. Figure 12 shows the difference of the five stacking sequences with respect to the fundamental frequency. Reductions are less variable under this condition than several other support conditions. Even with $a/h = 10$, the BFB plate still maintains a 5 percent reduction from the thin-plate estimates.
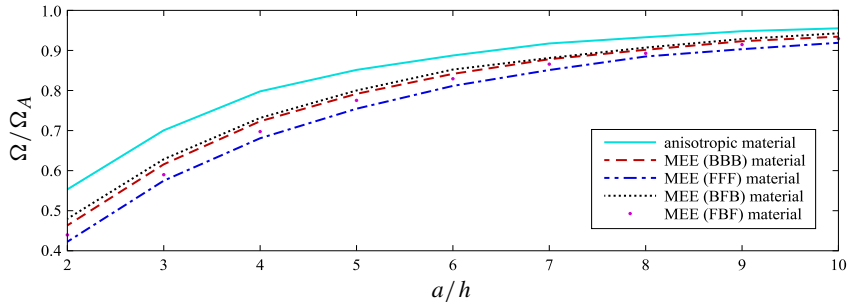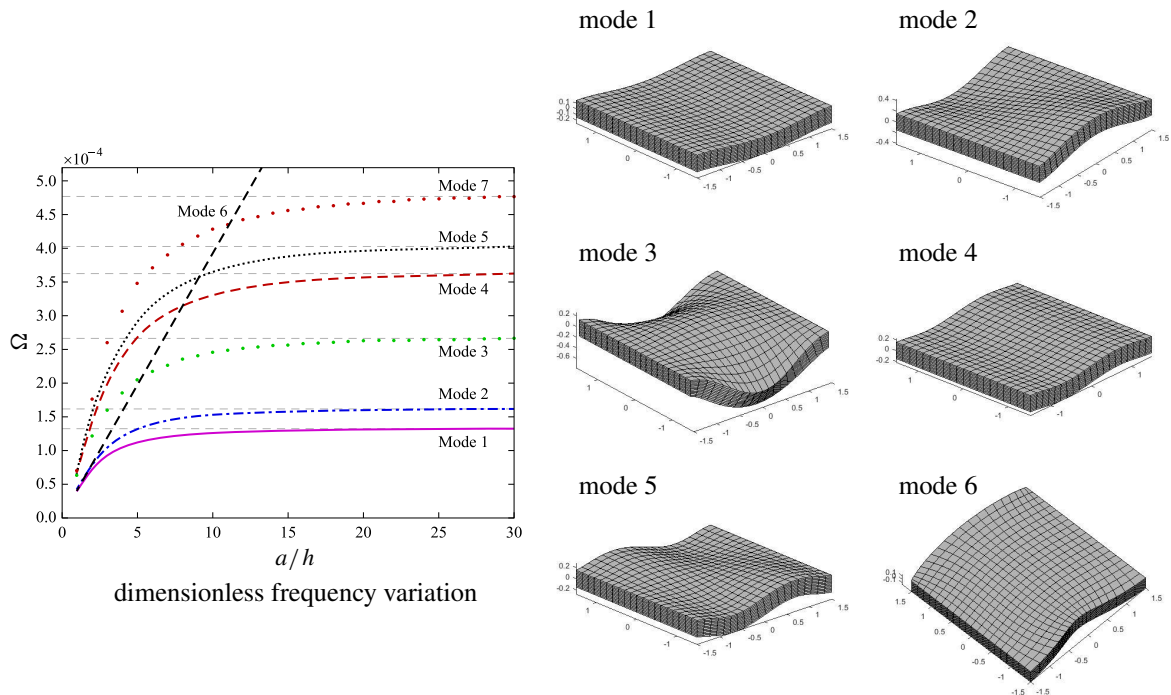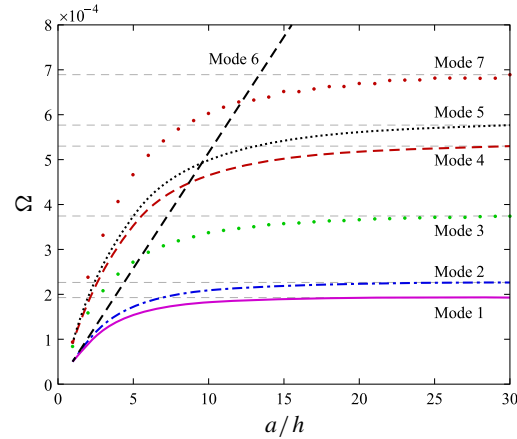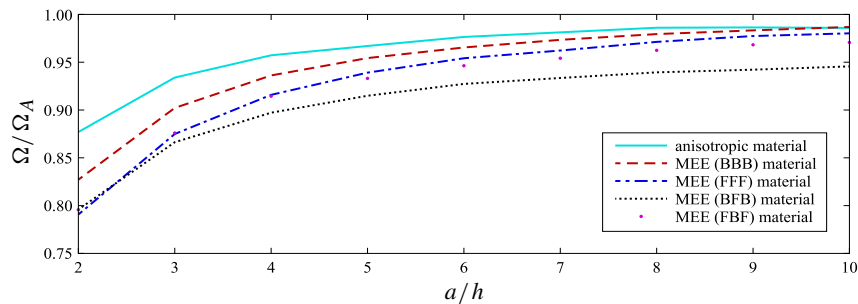
Figure 9. The relative differences of fundamental frequencies of the FCFC plate compared to the thin plate limit for the five different material combinations as a function of a/h.

dimensionless frequency variation

Figure 10. Frequency variation as a function of a/h and the first six mode shapes ($a/h = 10$) for the anisotropic elastic square FCFC plate.

bending mode	hex	BBB	FFF	BFB	FBF
1	$1.33 \cdot 10^{-4}$	$3.20 \cdot 10^{-4}$	$2.07 \cdot 10^{-4}$	$1.94 \cdot 10^{-4}$	$2.22 \cdot 10^{-4}$
2	$1.62 \cdot 10^{-4}$	$3.77 \cdot 10^{-4}$	$2.42 \cdot 10^{-4}$	$2.28 \cdot 10^{-4}$	$2.59 \cdot 10^{-4}$
3	$2.67 \cdot 10^{-4}$	$6.21 \cdot 10^{-4}$	$3.96 \cdot 10^{-4}$	$3.74 \cdot 10^{-4}$	$4.25 \cdot 10^{-4}$
4	$3.63 \cdot 10^{-4}$	$8.70 \cdot 10^{-4}$	$5.62 \cdot 10^{-4}$	$5.30 \cdot 10^{-4}$	$6.04 \cdot 10^{-4}$
5	$4.03 \cdot 10^{-4}$	$9.49 \cdot 10^{-4}$	$6.09 \cdot 10^{-4}$	$5.76 \cdot 10^{-4}$	$6.57 \cdot 10^{-4}$
6	$4.77 \cdot 10^{-4}$	$1.13 \cdot 10^{-3}$	$7.24 \cdot 10^{-4}$	$6.88 \cdot 10^{-4}$	$7.79 \cdot 10^{-4}$

Table 11. Frequencies for homogeneous plates composed of five stacking sequences under the FCFC condition at $a/h = 30$.

Figure 11. Dimensionless frequency variation as a function of a/h for the FCFC square BFB plate.

Figure 12. The relative differences of fundamental frequencies of the CFFF plate compared to the thin plate limit for the five different material combinations as a function of a/h.

Figure 13 displays the first eight frequencies as a function of a/h ratio and the first six mode shapes under CFFF condition. Once again the straight dashed lines represent the in-plane modes. The mode shapes are almost the same as isotropic plates under this boundary condition. Figure 14 gives the configuration of frequencies of the BFB stacking sequence. Table 12 lists the frequency values of the first six bending modes at $a/h = 30$. The differences are quite small for this condition, with the percent difference being below 10 percent even up to the fifth frequency with $a/h = 10$. When the length-to-thickness ratio is 20, the sixth frequency reductions are nearly 2 percent.

CCFF condition. Figure 15 demonstrates the reduction for the lowest frequency for various a/h ratios. At a/h of 6, percent differences are within 10 percent for each material. Figure 16 shows the first nine frequencies and the first six mode shapes of the plates made of anisotropic materials under CCFF condition. More in-plane modes appear within these bending frequencies than for prior conditions, indicating increased stiffening in bending. Figure 17 gives the influence of slenderness for the first nine frequencies for the plate composed with BFB materials. Even as a/h is equal to 20, the reductions are still over 5 percent. Table 13 gives the first six modes at $a/h = 30$ for reference.

SFSF condition. Figure 18 shows the differences of the fundamental frequency for the five cases. This
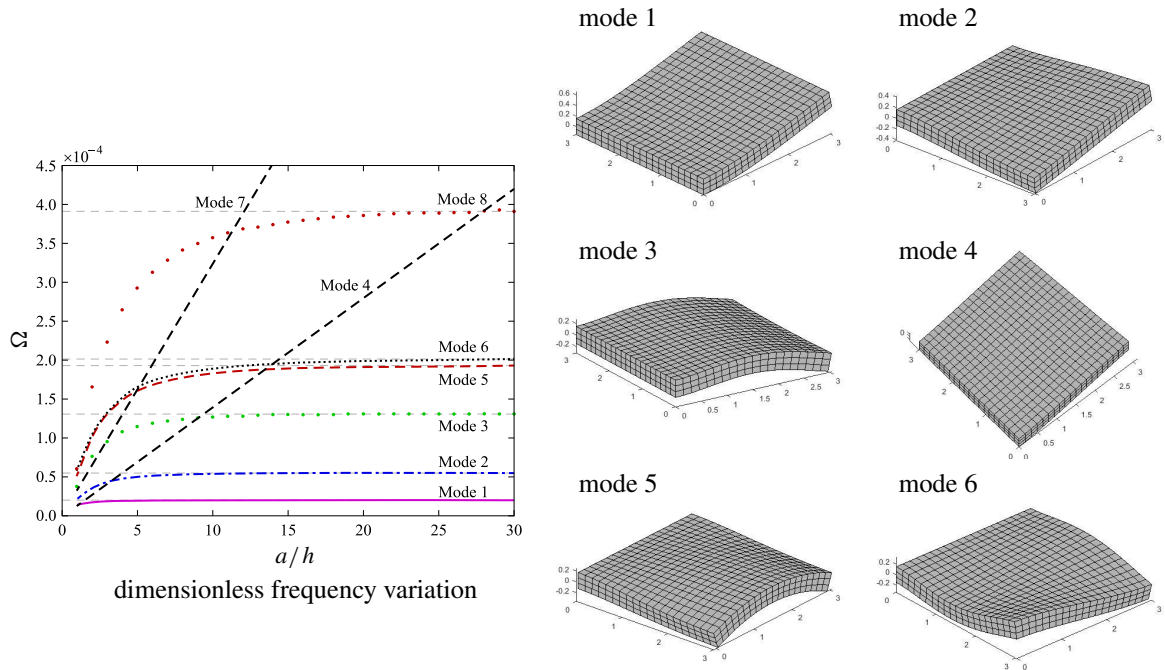
Figure 13. Frequency variation as a function of a/h and the first six mode shapes ($a/h = 10$) for the anisotropic elastic square CFFF plate.
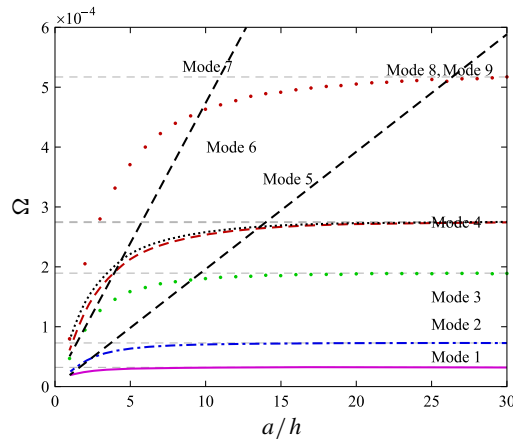

Figure 14. Dimensionless frequency variation as a function of a/h for the CFFF square BFB plate.

configuration is similar to the all simply supported condition; however, reductions are slightly smaller for the same a/h conditions. Figure 19 demonstrates the configuration of the first seven frequencies and the first six modes of anisotropic materials under SFSF condition. The straight dashed line corresponds to the in-plane mode 6. Figure 20 shows frequency variation as a function of a/h. These are almost the same as those for anisotropic plates except that the difference between the third and fourth bending frequencies, which are the bending modes along simply supported edges and the bending mode along

bending mode	hex	BBB	FFF	BFB	FBF
1	$2.09 \cdot 10^{-5}$	$5.19 \cdot 10^{-5}$	$3.45 \cdot 10^{-5}$	$3.29 \cdot 10^{-5}$	$3.72 \cdot 10^{-5}$
2	$5.57 \cdot 10^{-5}$	$1.22 \cdot 10^{-4}$	$7.85 \cdot 10^{-5}$	$7.30 \cdot 10^{-5}$	$8.40 \cdot 10^{-5}$
3	$1.31 \cdot 10^{-4}$	$3.15 \cdot 10^{-4}$	$2.08 \cdot 10^{-4}$	$1.90 \cdot 10^{-4}$	$2.22 \cdot 10^{-4}$
4	$1.93 \cdot 10^{-4}$	$4.58 \cdot 10^{-4}$	$2.96 \cdot 10^{-4}$	$2.74 \cdot 10^{-4}$	$3.17 \cdot 10^{-4}$
5	$2.01 \cdot 10^{-4}$	$4.53 \cdot 10^{-4}$	$2.95 \cdot 10^{-4}$	$2.75 \cdot 10^{-4}$	$3.13 \cdot 10^{-4}$
6	$3.91 \cdot 10^{-4}$	$8.58 \cdot 10^{-4}$	$5.48 \cdot 10^{-4}$	$5.17 \cdot 10^{-4}$	$5.87 \cdot 10^{-4}$

Table 12. Frequencies for homogeneous plates composed of five stacking sequences under the CFFF condition at $a/h = 30$.
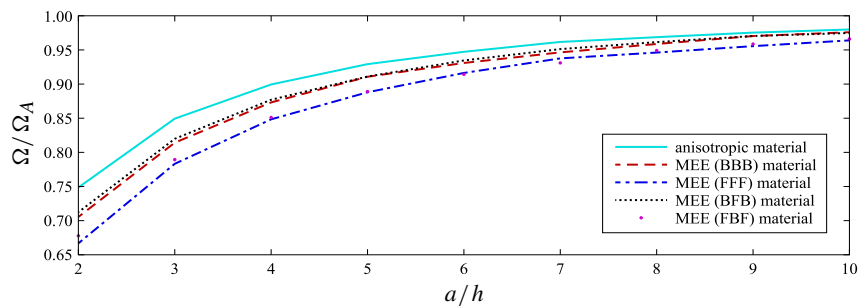
Figure 15. The relative differences of fundamental frequency of the CCFF plate compared to the thin plate limit for the five different material combinations as a function of a/h.
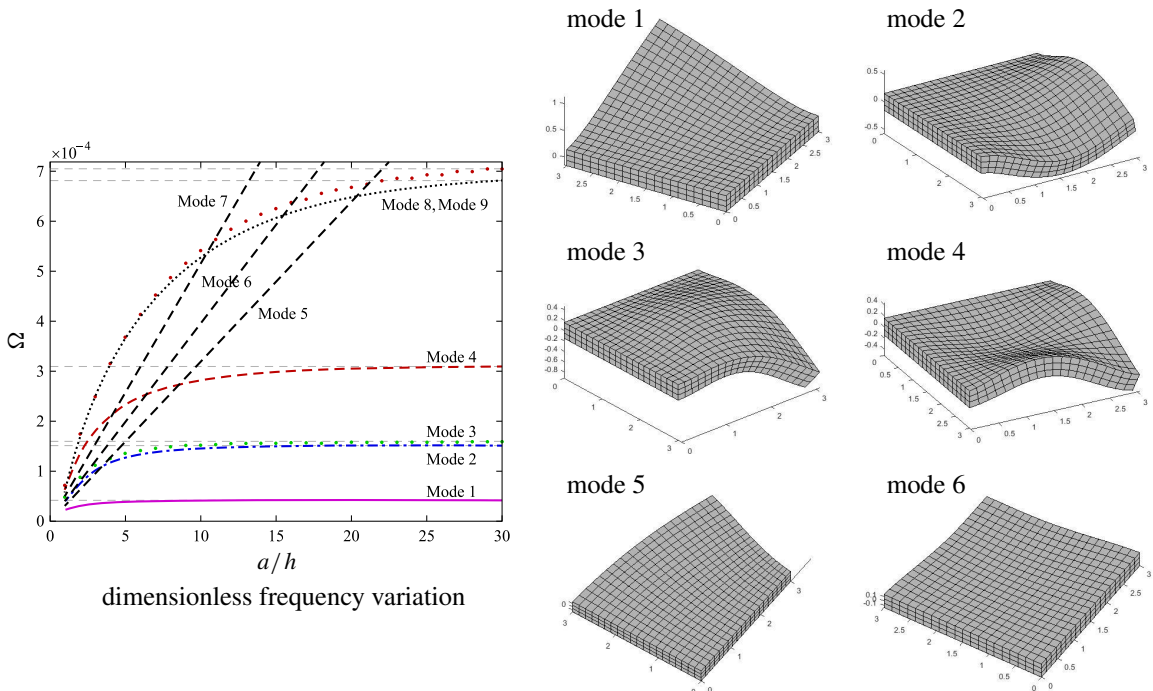

Figure 16. Frequency variation as a function of a/h and the first six mode shapes ($a/h = 10$) for the anisotropic elastic square CCFF plate.
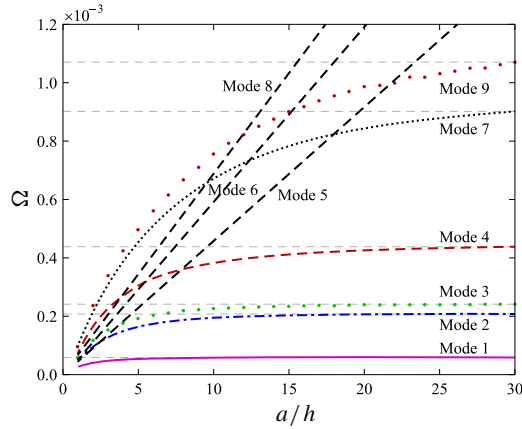
Figure 17. Dimensionless frequency variation as a function of a/h for the CCFF square BFB plate.

bending mode	hex	BBB	FFF	BFB	FBF
1	$4.36 \cdot 10^{-5}$	$1.01 \cdot 10^{-4}$	$6.63 \cdot 10^{-5}$	$6.08 \cdot 10^{-5}$	$7.12 \cdot 10^{-5}$
2	$1.53 \cdot 10^{-4}$	$3.50 \cdot 10^{-4}$	$2.28 \cdot 10^{-4}$	$2.10 \cdot 10^{-4}$	$2.44 \cdot 10^{-4}$
3	$1.60 \cdot 10^{-4}$	$3.99 \cdot 10^{-4}$	$2.64 \cdot 10^{-4}$	$2.42 \cdot 10^{-4}$	$2.82 \cdot 10^{-4}$
4	$3.11 \cdot 10^{-4}$	$7.24 \cdot 10^{-4}$	$4.67 \cdot 10^{-4}$	$4.38 \cdot 10^{-4}$	$5.00 \cdot 10^{-4}$
5	$6.82 \cdot 10^{-4}$	$1.50 \cdot 10^{-3}$	$9.43 \cdot 10^{-4}$	$9.01 \cdot 10^{-4}$	$1.02 \cdot 10^{-3}$
6	$7.06 \cdot 10^{-4}$	$1.73 \cdot 10^{-3}$	$1.12 \cdot 10^{-3}$	$1.07 \cdot 10^{-3}$	$1.20 \cdot 10^{-3}$

Table 13. Frequencies for homogeneous plates composed of five stacking sequences under CCFF condition at $a/h = 30$.
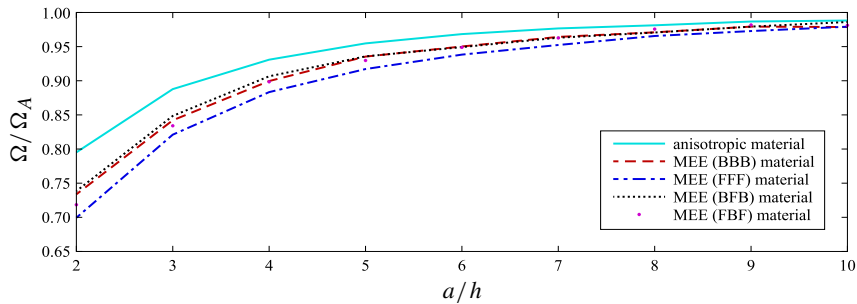
Figure 18. The relative differences of fundamental frequencies of the SFSF plate compared to the thin plate limit for the five different material combinations as a function of a/h.

free edges, are much smaller. With $a/h = 10$, the differences are within 10 percent. At $a/h = 20$, the percent differences are smaller than 2 percent. Table 14 gives the first six modes at $a/h = 30$.
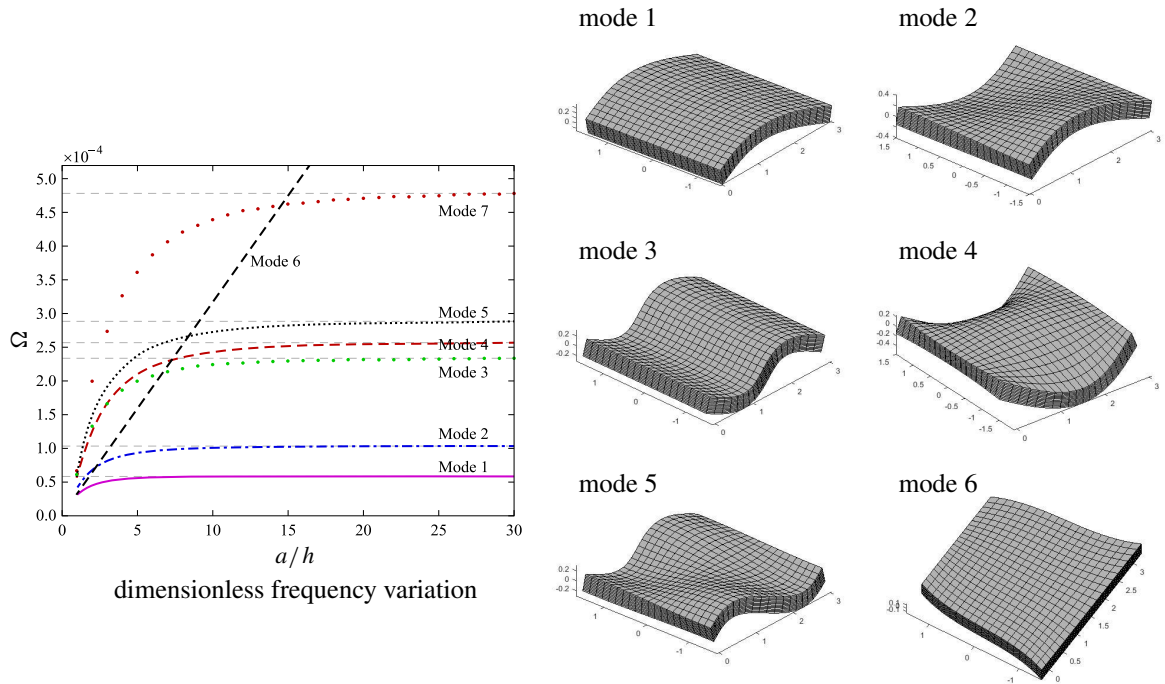
Figure 19. Frequency variation as a function of a/h and the first six mode shapes $(a/h = 10)$ for the anisotropic elastic square SFSF plate.
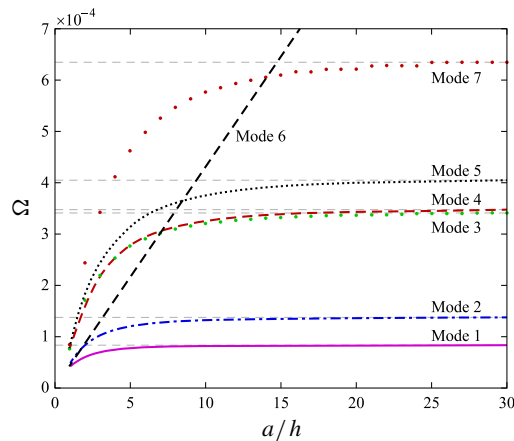

Figure 20. Dimensionless frequency variation as a function of a/h for the SFSF square BFB plate.

Conclusions

A discrete-layer model was used to approximate the natural frequencies of laminated isotropic and MEE plates under various boundary conditions. There are three primary conclusions related to this work:

 (1) The current DL model gives excellent agreement with most existing solutions for both isotropic and layered MEE plates. The main discrepancies arise for specific combinations of boundary conditions that have seen very little study in the literature.

bending mode	hex	BBB	FFF	BFB	FBF
1	$5.86 \cdot 10^{-5}$	$1.39 \cdot 10^{-4}$	$8.89 \cdot 10^{-5}$	$8.40 \cdot 10^{-5}$	$9.49 \cdot 10^{-5}$
2	$1.04 \cdot 10^{-4}$	$2.30 \cdot 10^{-4}$	$1.45 \cdot 10^{-4}$	$1.38 \cdot 10^{-4}$	$1.56 \cdot 10^{-4}$
3	$2.34 \cdot 10^{-4}$	$5.61 \cdot 10^{-4}$	$3.60 \cdot 10^{-4}$	$3.41 \cdot 10^{-4}$	$3.86 \cdot 10^{-4}$
4	$2.57 \cdot 10^{-4}$	$5.76 \cdot 10^{-4}$	$3.66 \cdot 10^{-4}$	$3.47 \cdot 10^{-4}$	$3.93 \cdot 10^{-4}$
5	$2.88 \cdot 10^{-4}$	$6.69 \cdot 10^{-4}$	$4.27 \cdot 10^{-4}$	$4.05 \cdot 10^{-4}$	$4.58 \cdot 10^{-4}$
6	$4.78 \cdot 10^{-4}$	$1.05 \cdot 10^{-3}$	$6.69 \cdot 10^{-4}$	$6.33 \cdot 10^{-4}$	$7.18 \cdot 10^{-4}$

Table 14. Frequencies for homogeneous plates composed of five stacking sequences under the SFSF condition at $a/h = 30$.

(2) From all results and all cases considered in this study, the thin-plate limit of $a/h = 10$ does not give sufficient accuracy for a wide enough range of lamination schemes and boundary conditions. An a/h ratio of 20 gives a far better limit for using any thin-plate kinematic assumption.

(3) The results contained herein for all boundary conditions can be used for purposes of comparison using other simplified theories of MEE plate behavior.

Appendix

$$K_{ij}^{11} = \int_V \left[C_{11} \frac{\partial \Psi_i^u}{\partial x} \frac{\partial \Psi_j^u}{\partial x} + C_{16} \left(\frac{\partial \Psi_i^u}{\partial x} \frac{\partial \Psi_j^u}{\partial y} + \frac{\partial \Psi_i^u}{\partial y} \frac{\partial \Psi_j^u}{\partial x} \right) + C_{55} \frac{\partial \Psi_i^u}{\partial z} \frac{\partial \Psi_j^u}{\partial z} + C_{66} \frac{\partial \Psi_i^u}{\partial y} \frac{\partial \Psi_j^u}{\partial y} \right] dV \quad (26)$$

$$K_{ij}^{12} = \int_V \left[C_{12} \frac{\partial \Psi_i^u}{\partial x} \frac{\partial \Psi_j^v}{\partial y} + C_{16} \frac{\partial \Psi_i^u}{\partial x} \frac{\partial \Psi_j^v}{\partial x} + C_{45} \frac{\partial \Psi_i^u}{\partial z} \frac{\partial \Psi_j^v}{\partial z} + C_{26} \frac{\partial \Psi_i^u}{\partial y} \frac{\partial \Psi_j^v}{\partial y} + C_{66} \frac{\partial \Psi_i^u}{\partial y} \frac{\partial \Psi_j^v}{\partial x} \right] dV \quad (27)$$

$$K_{ij}^{13} = \int_V \left[C_{13} \frac{\partial \Psi_i^u}{\partial x} \frac{\partial \Psi_j^w}{\partial z} + C_{45} \frac{\partial \Psi_i^u}{\partial z} \frac{\partial \Psi_j^w}{\partial y} + C_{55} \frac{\partial \Psi_i^u}{\partial z} \frac{\partial \Psi_j^w}{\partial x} + C_{36} \frac{\partial \Psi_i^u}{\partial y} \frac{\partial \Psi_j^w}{\partial z} \right] dV \quad (28)$$

$$K_{ij}^{14} = \int_V \left[e_{11} \frac{\partial \Psi_i^u}{\partial x} \frac{\partial \Psi_j^\phi}{\partial x} + e_{21} \frac{\partial \Psi_i^u}{\partial x} \frac{\partial \Psi_j^\phi}{\partial y} + e_{31} \frac{\partial \Psi_i^u}{\partial x} \frac{\partial \Psi_j^\phi}{\partial z} + e_{15} \frac{\partial \Psi_i^u}{\partial z} \frac{\partial \Psi_j^\phi}{\partial x} + e_{25} \frac{\partial \Psi_i^u}{\partial z} \frac{\partial \Psi_j^\phi}{\partial y} \right.$$
$$\left. + e_{35} \frac{\partial \Psi_i^u}{\partial z} \frac{\partial \Psi_j^\phi}{\partial z} + e_{16} \frac{\partial \Psi_i^u}{\partial y} \frac{\partial \Psi_j^\phi}{\partial x} + e_{26} \frac{\partial \Psi_i^u}{\partial y} \frac{\partial \Psi_j^\phi}{\partial y} + e_{36} \frac{\partial \Psi_i^u}{\partial y} \frac{\partial \Psi_j^\phi}{\partial z} \right] dV \quad (29)$$

$$K_{ij}^{15} = \int_V \left[q_{11} \frac{\partial \Psi_i^u}{\partial x} \frac{\partial \Psi_j^\psi}{\partial x} + q_{21} \frac{\partial \Psi_i^u}{\partial x} \frac{\partial \Psi_j^\psi}{\partial y} + q_{31} \frac{\partial \Psi_i^u}{\partial x} \frac{\partial \Psi_j^\psi}{\partial z} + q_{15} \frac{\partial \Psi_i^u}{\partial z} \frac{\partial \Psi_j^\psi}{\partial x} + q_{25} \frac{\partial \Psi_i^u}{\partial z} \frac{\partial \Psi_j^\psi}{\partial y} \right.$$
$$\left. + q_{35} \frac{\partial \Psi_i^u}{\partial z} \frac{\partial \Psi_j^\psi}{\partial z} + q_{16} \frac{\partial \Psi_i^u}{\partial y} \frac{\partial \Psi_j^\psi}{\partial x} + q_{26} \frac{\partial \Psi_i^u}{\partial y} \frac{\partial \Psi_j^\psi}{\partial y} + q_{36} \frac{\partial \Psi_i^u}{\partial y} \frac{\partial \Psi_j^\psi}{\partial z} \right] dV \quad (30)$$

$$K_{ij}^{22} = \int_V \left[C_{22} \frac{\partial \Psi_i^v}{\partial y} \frac{\partial \Psi_j^v}{\partial y} + C_{26} \left(\frac{\partial \Psi_i^v}{\partial y} \frac{\partial \Psi_j^v}{\partial x} + \frac{\partial \Psi_i^v}{\partial x} \frac{\partial \Psi_j^v}{\partial y} \right) + C_{44} \frac{\partial \Psi_i^v}{\partial z} \frac{\partial \Psi_j^v}{\partial z} + C_{66} \frac{\partial \Psi_i^v}{\partial x} \frac{\partial \Psi_j^v}{\partial x} \right] dV \quad (31)$$

$$K_{ij}^{23} = \int_V \left[C_{23} \frac{\partial \Psi_i^v}{\partial y} \frac{\partial \Psi_j^w}{\partial z} + C_{44} \frac{\partial \Psi_i^v}{\partial z} \frac{\partial \Psi_j^w}{\partial y} + C_{45} \frac{\partial \Psi_i^v}{\partial z} \frac{\partial \Psi_j^w}{\partial x} + C_{36} \frac{\partial \Psi_i^v}{\partial x} \frac{\partial \Psi_j^w}{\partial z} \right] dV \tag{32}$$

$$K_{ij}^{24} = \int_V \left[e_{12} \frac{\partial \Psi_i^v}{\partial y} \frac{\partial \Psi_j^\phi}{\partial x} + e_{22} \frac{\partial \Psi_i^v}{\partial y} \frac{\partial \Psi_j^\phi}{\partial y} + e_{32} \frac{\partial \Psi_i^v}{\partial y} \frac{\partial \Psi_j^\phi}{\partial z} + e_{14} \frac{\partial \Psi_i^v}{\partial z} \frac{\partial \Psi_j^\phi}{\partial x} + e_{24} \frac{\partial \Psi_i^v}{\partial z} \frac{\partial \Psi_j^\phi}{\partial y} \right.$$
$$\left. + e_{34} \frac{\partial \Psi_i^v}{\partial z} \frac{\partial \Psi_j^\phi}{\partial z} + e_{16} \frac{\partial \Psi_i^v}{\partial x} \frac{\partial \Psi_j^\phi}{\partial x} + e_{26} \frac{\partial \Psi_i^v}{\partial x} \frac{\partial \Psi_j^\phi}{\partial y} + e_{36} \frac{\partial \Psi_i^v}{\partial x} \frac{\partial \Psi_j^\phi}{\partial z} \right] dV \tag{33}$$

$$K_{ij}^{25} = \int_V \left[q_{12} \frac{\partial \Psi_i^v}{\partial y} \frac{\partial \Psi_j^\psi}{\partial x} + q_{22} \frac{\partial \Psi_i^v}{\partial y} \frac{\partial \Psi_j^\psi}{\partial y} + q_{32} \frac{\partial \Psi_i^v}{\partial y} \frac{\partial \Psi_j^\psi}{\partial z} + q_{14} \frac{\partial \Psi_i^v}{\partial z} \frac{\partial \Psi_j^\psi}{\partial x} + q_{24} \frac{\partial \Psi_i^v}{\partial z} \frac{\partial \Psi_j^\psi}{\partial y} \right.$$
$$\left. + q_{34} \frac{\partial \Psi_i^v}{\partial z} \frac{\partial \Psi_j^\psi}{\partial z} + q_{16} \frac{\partial \Psi_i^v}{\partial x} \frac{\partial \Psi_j^\psi}{\partial x} + q_{26} \frac{\partial \Psi_i^v}{\partial x} \frac{\partial \Psi_j^\psi}{\partial y} + q_{36} \frac{\partial \Psi_i^v}{\partial x} \frac{\partial \Psi_j^\psi}{\partial z} \right] dV \tag{34}$$

$$K_{ij}^{33} = \int_V \left[C_{33} \frac{\partial \Psi_i^w}{\partial z} \frac{\partial \Psi_j^w}{\partial z} + C_{44} \frac{\partial \Psi_i^w}{\partial y} \frac{\partial \Psi_j^w}{\partial y} \right.$$
$$\left. + C_{45} \frac{\partial \Psi_i^w}{\partial y} \frac{\partial \Psi_j^w}{\partial x} + C_{45} \frac{\partial \Psi_i^w}{\partial x} \frac{\partial \Psi_j^w}{\partial y} + C_{55} \frac{\partial \Psi_i^w}{\partial x} \frac{\partial \Psi_j^w}{\partial x} \right] dV \tag{35}$$

$$K_{ij}^{34} = \int_V \left[e_{13} \frac{\partial \Psi_i^w}{\partial z} \frac{\partial \Psi_j^\phi}{\partial x} + e_{23} \frac{\partial \Psi_i^w}{\partial z} \frac{\partial \Psi_j^\phi}{\partial y} + e_{33} \frac{\partial \Psi_i^w}{\partial z} \frac{\partial \Psi_j^\phi}{\partial z} + e_{14} \frac{\partial \Psi_i^w}{\partial y} \frac{\partial \Psi_j^\phi}{\partial x} + e_{24} \frac{\partial \Psi_i^w}{\partial y} \frac{\partial \Psi_j^\phi}{\partial y} \right.$$
$$\left. + e_{34} \frac{\partial \Psi_i^w}{\partial y} \frac{\partial \Psi_j^\phi}{\partial z} + e_{15} \frac{\partial \Psi_i^w}{\partial x} \frac{\partial \Psi_j^\phi}{\partial x} + e_{25} \frac{\partial \Psi_i^w}{\partial x} \frac{\partial \Psi_j^\phi}{\partial y} + e_{35} \frac{\partial \Psi_i^w}{\partial x} \frac{\partial \Psi_j^\phi}{\partial z} \right] dV \tag{36}$$

$$K_{ij}^{44} = \int_V \left[-\epsilon_{11} \frac{\partial \Psi_i^\phi}{\partial x} \frac{\partial \Psi_j^\phi}{\partial x} - \epsilon_{22} \frac{\partial \Psi_i^\phi}{\partial y} \frac{\partial \Psi_j^\phi}{\partial y} - \epsilon_{33} \frac{\partial \Psi_i^\phi}{\partial z} \frac{\partial \Psi_j^\phi}{\partial z} \right] dV \tag{37}$$

$$K_{ij}^{55} = \int_V \left[-\mu_{11} \frac{\partial \Psi_i^\psi}{\partial x} \frac{\partial \Psi_j^\psi}{\partial x} - \mu_{22} \frac{\partial \Psi_i^\psi}{\partial y} \frac{\partial \Psi_j^\psi}{\partial y} - \mu_{33} \frac{\partial \Psi_i^\psi}{\partial z} \frac{\partial \Psi_j^\psi}{\partial z} \right] dV \tag{38}$$

References

[Abromowitz and Stegun 1966] M. Abromowitz and I. A. Stegun (editors), *Handbook of mathematical functions, with formulas, graphs, and mathematical tables*, Dover, New York, 1966.

[Chen et al. 2005] W. Q. Chen, K. Y. Lee, and H. J. Ding, "On free vibration of non-homogeneous transversely isotropic magneto-electro-elastic plates", *J. Sound Vib.* **279**:1 (2005), 237–251.

[Chen et al. 2007] J. Chen, H. Chen, E. Pan, and P. R. Heyliger, "Modal analysis of magneto-electro-elastic plates using the state-vector approach", *J. Sound Vib.* **304**:3 (2007), 722–734.

[Chen et al. 2014] J. Y. Chen, P. R. Heyliger, and E. Pan, "Free vibration of three-dimensional multilayered magneto-electro-elastic plates under combined clamped/free boundary conditions", *J. Sound Vib.* **333**:17 (2014), 4017–4029.

[Demarest 1971] H. H. Demarest, Jr., "Cube-resonance method to determine the elastic constants of solids", *J. Acoust. Soc. Am.* **49**:3B (1971), 768–775.

[Eer Nisse 1967] E. P. Eer Nisse, "Variational method for electroelastic vibration analysis", *IEEE Transactions on Sonics and Ultrasonics* **14**:4 (1967), 153–159.

[Heyliger 2000] P. Heyliger, "Traction-free vibration of layered elastic and piezoelectric rectangular parallelepipeds", *J. Acoust. Soc. Am.* **107**:3 (2000), 1235–1245.

[Hjelmstad 1997] K. D. Hjelmstad, *Fundamentals of structural mechanics*, 1st ed., Prentice Hall, Upper Saddle River, NJ, 1997.

[Kondaiah et al. 2012] P. Kondaiah, K. Shankar, and N. Ganesan, "Studies on magneto-electro-elastic cantilever beam under thermal environment", *Coupled systems mechanics* **1**:2 (2012), 205–217.

[Liew et al. 1993] K. M. Liew, Y. Xiang, and S. Kitipornchai, "Transverse vibration of thick rectangular plates, I: comprehensive sets of boundary conditions", *Comput. Struct.* **49**:1 (1993), 1–29.

[Ohno 1976] I. Ohno, "Free vibration of a rectangular parallelepiped crystal and its application to determination of elastic constants of orthorhombic crystals", *J. Phys. Earth* **24**:4 (1976), 355–379.

[Pan and Heyliger 2002] E. Pan and P. R. Heyliger, "Free vibrations of simply supported and multilayered magneto-electro-elastic plates", *J. Sound Vib.* **252**:3 (2002), 429–442.

[Rao 2007] S. S. Rao, *Vibration of continuous systems*, Wiley, 2007.

[Reddy and Phan 1985] J. Reddy and N. Phan, "Stability and vibration of isotropic, orthotropic and laminated plates according to a higher-order shear deformation theory", *J. Sound Vib.* **98**:2 (1985), 157–170.

[Srinivas et al. 1970] S. Srinivas, C. V. Joga Rao, and A. K. Rao, "Some results from an exact analysis of thick laminates in vibration and buckling", *J. Appl. Mech.* (*ASME*) **37** (1970), 868–870.

[Szilard 1974] R. Szilard, *Theory and analysis of plates*, Prentice-Hall, Englewood Cliffs, N.J., 1974.

[Tiersten 1969] H. F. Tiersten, *Linear piezoelectric plate vibrations*, Springer, New York, 1969.

[Ugural and Fenster 1995] A. C. Ugural and S. K. Fenster, *Advanced strength and applied elasticity*, 3rd ed., Prentice-Hall, Englewood Cliffs, NJ, 1995.

[Vel and Batra 2000] S. S. Vel and R. C. Batra, "Three-dimensional analytical solution for hybrid multilayered piezoelectric plates", *J. Appl. Mech.* (*ASME*) **67**:3 (2000), 558–567.

[Vel et al. 2004] S. S. Vel, R. Mewer, and R. Batra, "Analytical solution for the cylindrical bending vibration of piezoelectric composite plates", *Int. J. Solids Struct.* **41**:5-6 (2004), 1625–1643.

[Wang et al. 2003] J. Wang, L. Chen, and S. Fang, "State vector approach to analysis of multilayered magneto-electro-elastic plates", *Int. J. Solids Struct.* **40**:7 (2003), 1669–1680.

[Whitney 1987] J. M. Whitney, *Structural analysis of laminated composite plates*, CRC Press, 1987.

CHAO JIANG: chao@rams.colostate.edu
Department of Civil and Environmental Engineering, Colorado State University, Fort Collins, CO, United States

PAUL R. HEYLIGER: prh@engr.colostate.edu
Department of Civil and Environmental Engineering, Colorado State University, Fort Collins, CO, United States

msp

LOCALIZED BULGING OF ROTATING ELASTIC CYLINDERS AND TUBES

JUAN WANG, ALI ALTHOBAITI AND YIBIN FU

We investigate axially symmetric localized bulging of an incompressible hyperelastic circular solid cylinder or tube that is rotating about its axis of symmetry with angular velocity ω. For such a solid cylinder, the homogeneous primary deformation is completely determined by the axial stretch λ_z, and it is shown that the bifurcation condition is simply given by $d\omega/d\lambda_z = 0$ if the resultant axial force F is fixed. For a tube that is shrink-fitted to a rigid circular cylindrical spindle, the azimuthal stretch λ_a on the inner surface of the tube is specified and the deformation is again completely determined by the axial stretch λ_z although the deformation is now inhomogeneous. For this case it is shown that with F fixed the bifurcation condition is also given by $d\omega/d\lambda_z = 0$. When the spindle is absent (the case of unconstrained rotation), we also allow for the possibility that the tube is additionally subjected to an internal pressure P. It is shown that with P fixed, and ω and F both viewed as functions of λ_a and λ_z, the bifurcation condition for localized bulging is that the Jacobian of ω and F should vanish. Alternatively, the same bifurcation condition can be derived by fixing ω and setting the Jacobian of P and F to zero. Illustrative numerical results are presented using the Ogden and Gent material models.

1. Introduction

In a series of classic papers by Haughton and Ogden [1979a; 1979b; 1980a; 1980b; 1980c] on the periodic buckling of hyperelastic circular solid cylinders or cylindrical tubes described by a general strain-energy function, two types of loading were considered separately. The first type consists of an internal pressure and an end thrust, and the second type consists of rotation about the axis of symmetry and an end thrust. The first situation has recently been reexamined with a view to characterize axially symmetric localized bulging, motivated by the fact that in some loading regimes localized bulging is usually observed first but had previously not been fully understood. The second situation is now reexamined in the current paper, motivated by similar considerations.

Deformation of a rotating hyperelastic cylinder or tube is one of the first problems solved using the continuum mechanics theory [Green and Zerna 1957] with results used to test the validity of constitutive assumptions. For instance, when the neo-Hookean material model is used, the resulting axial stretch λ_z in a solid cylinder rotating with angular velocity ω is given by

$$\rho\omega^2 = \frac{4\mu}{A^2}(1 - \lambda_z^3), \tag{1-1}$$

where μ, ρ, and A are the ground state shear modulus, material density, and undeformed radius, respectively. The above result predicts that when $\rho\omega^2$ approaches the finite value $4\mu/A^2$, the stretch tends to zero, which is clearly unphysical, thus showing the inadequacy of the neo-Hookean material model in the large deformation regime. The question of the existence of a unique homogeneous (shape-preserving) solution valid for all values of ω was then examined by Chadwick et al. [1977] using the newly proposed Ogden material model at that time. In a parallel study, the question of an axisymmetric bifurcation for a rotating cylinder was studied by Patterson and Hill [1977] using the neo-Hookean material model. They showed that such a bifurcation would take place before ω reaches the value corresponding to $\lambda = 0$. The bifurcation condition has an explicit expression and was derived in a similar manner to that used by Wilkes [1955] for studying the buckling of a cylinder or tube under end thrust. A significant generalization was subsequently made by Haughton and Ogden [1980a; 1980b; 1980c], who considered all the possible periodic buckling modes (prismatic, axisymmetric, or asymmetric) for a rotating cylinder or tube without restricting the material model in their general formulation although numerical results were presented only for the Ogden material model. In the last three studies, it was observed that the rotation speed, when viewed as a function of a stretch measure, may reach a maximum beyond which the primary deformation no longer exists. This is similar to the so-called limiting point instability which was receiving a lot of attention around the same period; see, e.g., [Kanner and Horgan 2007] and the references therein. However, in both situations the connection between the limiting point instability and localized bulging bifurcation was not fully understood at that time. It is shown in the present paper that under a certain loading condition the existence of such an angular speed maximum is closely associated with axisymmetric bulging localized in the axial direction, a phenomenon rather similar to localized bulging in circular cylindrical tubes that are inflated by an internal pressure.

We follow the same strategy as in [Fu et al. 2016]. After formulating the problem and summarizing the expressions for the angular speed ω, the internal pressure P, and the resultant axial force F associated with the primary shape-preserving deformation in the next section, we first derive the bifurcation condition in Section 3, and then conjecture and verify that the bifurcation condition in each case can be written simply in terms of the derivatives of ω, F, and/or P with respect to the stretches as stated in the abstract. In Section 4 the bifurcation condition is solved and numerical results are presented when both the Gent and Ogden material models are used. Section 5 concludes the paper with a summary of our main results and a discussion of whether localized bulging under rotation could be observed experimentally.

2. Primary deformation

We first write down the solution for the primary shape-preserving deformation associated with an incompressible circular cylindrical tube that is rotating about its axis of symmetry with angular velocity ω. The corresponding results for a solid cylinder will be obtained by specialization. The tube is assumed to have inner radius A and outer radius B in the undeformed configuration, and these dimensions take the values a and b in the deformed configuration. The outer surface of the tube is traction-free, but its inner surface may in general be subjected to a hydrostatic pressure P or shrink-fitted to a rigid circular cylindrical spindle with a radius larger than A. It is also assumed that each plane end face of the tube is subject to a resultant axial force F (e.g., $F = 0$, in which case the end faces are traction-free). In terms

of cylindrical polar coordinates, the primary shape-preserving deformation is given by

$$r = \sqrt{\lambda_z^{-1}(R^2 - A^2) + a^2}, \qquad \theta = \Theta + \omega t, \qquad z = \lambda_z Z, \tag{2-1}$$

where (R, Θ, Z) and (r, θ, z) are the cylindrical polar coordinates in the undeformed and deformed configurations, respectively, t denotes time, and λ_z is a constant. The associated principal stretches are

$$\lambda_1 = \frac{r}{R} \equiv \lambda, \qquad \lambda_2 = \lambda_z, \qquad \lambda_3 = \frac{dr}{dR} = 1/(\lambda\lambda_z). \tag{2-2}$$

We assume that the constitutive behavior of the tube is described by a strain-energy function $W(\lambda_1, \lambda_2, \lambda_3)$. By integrating the only equilibrium equation in the r-direction, it can be shown that various quantities can be expressed in terms of the reduced strain-energy function w, and its derivatives w_1 and w_2, defined by

$$w(\lambda, \lambda_z) = W(\lambda, \lambda_z, \lambda^{-1}\lambda_z^{-1}), \qquad w_1 = \frac{\partial w}{\partial \lambda}, \qquad w_2 = \frac{\partial w}{\partial \lambda_z} \tag{2-3}$$

[Haughton and Ogden 1980c]. For instance, the normal stress on the inner surface is given by

$$\sigma_{33}(a) = \tfrac{1}{2}\rho\omega^2\lambda_z^{-1}(B^2 - A^2) - \int_{\lambda_b}^{\lambda_a} \frac{w_1}{\lambda^2\lambda_z - 1}\, d\lambda, \tag{2-4}$$

where ρ is the material density and the two limits λ_a and λ_b are defined by

$$\lambda_a = \frac{a}{A}, \qquad \lambda_b = \frac{b}{B},$$

and are related to each other, through incompressibility, by

$$\lambda_a^2\lambda_z - 1 = \frac{B^2}{A^2}(\lambda_b^2\lambda_z - 1). \tag{2-5}$$

We observe that with λ_b eliminated using the above relation, the deformation is completely determined by the two stretches λ_a and λ_z.

The expression (2-4) suggests the introduction of a nondimensional quantity Γ defined by

$$\Gamma = \rho\omega^2 B^2/\mu, \tag{2-6}$$

where μ denotes the ground-state shear modulus. In the rest of this paper, we shall assume that the strain-energy function, stress components, and pressure have all been scaled by μ, forces by μB^2, and the radii A, a, and b by B. As a result of nondimensionalization, (2-4) is now replaced by

$$\sigma_{33}(a) = \tfrac{1}{2}\Gamma\lambda_z^{-1}(1 - A^2) - \int_{\lambda_b}^{\lambda_a} \frac{w_1}{\lambda^2\lambda_z - 1}\, d\lambda, \tag{2-7}$$

and the resultant of σ_{22} at any cross section is given by

$$\widetilde{F}_0(\lambda_a, \lambda_z, \Gamma) \equiv 2\pi \int_a^b \sigma_{22} r\, dr = \tfrac{1}{4}\pi\Gamma\lambda_z^{-2}(1 - A^2)^2 + \pi a^2 \int_{\lambda_b}^{\lambda_a} \frac{w_1}{\lambda^2\lambda_z - 1}\, d\lambda$$

$$+ \pi A^2(\lambda_a^2\lambda_z - 1)\int_{\lambda_b}^{\lambda_a} \frac{2\lambda_z w_2 - \lambda w_1}{(\lambda^2\lambda_z - 1)^2}\lambda\, d\lambda, \tag{2-8}$$

where the first equation serves to define the function $\widetilde{F}_0$. Finally, the normal stress component σ_{33} in the r-direction is given by

$$\sigma_{33}(r) = \tfrac{1}{2}\Gamma(b^2 - r^2) - \int_{\lambda_b}^{\lambda} \frac{w_1}{\lambda^2 \lambda_z - 1}\, d\lambda. \tag{2-9}$$

This expression recovers (2-7) on evaluation at $r = a$ followed by the use of the identity $(b^2 - a^2)\lambda_z = B^2 - A^2$. We can now specialize the above formulae to three different loading and geometry conditions.

Firstly, consider a tube under the combined action of an internal pressure, rotation, and an end thrust (referred to hereafter as the unconstrained case). Denoting the internal pressure by P, we have $\sigma_{33}(a) = -P$, and (2-7) then becomes

$$P = \widetilde{P}(\lambda_a, \lambda_z) \equiv -\tfrac{1}{2}\Gamma\lambda_z^{-1}(1 - A^2) + \int_{\lambda_b}^{\lambda_a} \frac{w_1}{\lambda^2 \lambda_z - 1}\, d\lambda \tag{2-10}$$

or equivalently

$$\Gamma = \widetilde{\Gamma}(\lambda_a, \lambda_z) \equiv \frac{2\lambda_z}{1 - A^2} \int_{\lambda_b}^{\lambda_a} \frac{w_1}{\lambda^2 \lambda_z - 1}\, d\lambda - \frac{2\lambda_z P}{1 - A^2}, \tag{2-11}$$

where the second expression in each equation defines the functions $\widetilde{P}$ and $\widetilde{\Gamma}$, respectively. To simplify notation, we have not shown explicitly the dependence of $\widetilde{P}$ on Γ or $\widetilde{\Gamma}$ on P.

The resultant axial force at any cross section, that is to be balanced by the net force F applied at each plane end face, is given by

$$F = \widetilde{F}(\lambda_a, \lambda_z) \equiv 2\pi \int_a^b \sigma_{22} r\, dr - \pi a^2 P$$
$$= \tfrac{1}{4}\pi \Gamma \lambda_z^{-1}(a^2 + b^2)(1 - A^2) + \pi A^2(\lambda_a^2 \lambda_z - 1) \int_{\lambda_b}^{\lambda_a} \frac{2\lambda_z w_2 - \lambda w_1}{(\lambda^2 \lambda_z - 1)^2} \lambda\, d\lambda, \tag{2-12}$$

where $\equiv$ defines the function $\widetilde{F}$, which should be compared with the $\widetilde{F}_0$ defined by (2-8). We note that the Γ in the expression for $\widetilde{F}$ could be eliminated in favor of P with the use of (2-11). Thus, whenever $\widetilde{F}$ is partially differentiated, it can be either Γ or P that is fixed. This will always be indicated explicitly.

Once the geometry of the tube is specified, either P or Γ can be assumed to take a dominant role together with F. If, for instance, P is specified and is assumed to take a passive role (by being sufficiently small), then Γ and F can be viewed as functions of the two stretches λ_a and λ_z, and we expect the following Jacobian to play a role in the characterization of localized bulging:

$$\Omega_u(\lambda_a, \lambda_z) \equiv J(\widetilde{\Gamma}, \widetilde{F}) = \frac{\partial \widetilde{\Gamma}}{\partial \lambda_a} \frac{\partial \widetilde{F}}{\partial \lambda_z} - \frac{\partial \widetilde{\Gamma}}{\partial \lambda_z} \frac{\partial \widetilde{F}}{\partial \lambda_a}, \tag{2-13}$$

where the first equation defines the function $\Omega_u(\lambda_a, \lambda_z)$ with the subscript u signifying "unconstrained". Similarly, if Γ is assumed to take a passive role, then the Jacobian $J(\widetilde{P}, \widetilde{F})$ can be defined. However, it can be shown that this Jacobian is a nonzero multiple of $J(\widetilde{\Gamma}, \widetilde{F})$ when the connection (2-10) is used.

The case previously studied by [Fu et al. 2016] can now be viewed as a special case, corresponding to $\Gamma \equiv 0$, of the current more general formulation. The observations made in that paper about $J(\widetilde{P}, \widetilde{F})$ can be extended to the case when Γ is nonzero but is held fixed. In particular, it can be shown that when F and Γ are both fixed, the pressure will reach a maximum precisely when $J(\widetilde{P}, \widetilde{F}) = 0$. In a similar

manner, we note that if both P and F are held fixed when Γ is increased gradually, $\widetilde{F}(\lambda_a, \lambda_z) = F$ would define λ_z as a function of λ_a, and we then have

$$\frac{\partial \widetilde{F}}{\partial \lambda_a} + \frac{\partial \widetilde{F}}{\partial \lambda_z} \frac{d\lambda_z}{d\lambda_a} = 0,$$

and

$$\frac{d\widetilde{\Gamma}}{d\lambda_a} = \frac{\partial \widetilde{\Gamma}}{\partial \lambda_a} + \frac{\partial \widetilde{\Gamma}}{\partial \lambda_z} \frac{d\lambda_z}{d\lambda_a} = \left(\frac{\partial \widetilde{F}}{\partial \lambda_z}\right)^{-1} J(\widetilde{\Gamma}, \widetilde{F}).$$

Thus, Γ reaches a maximum when the Jacobian $J(\widetilde{\Gamma}, \widetilde{F})$ vanishes. We emphasize that this correspondence is lost when, for instance, it is the λ_z that is held fixed in rotating the tube. Drawing upon the results of [Fu et al. 2016], we may then further conjecture that when the inner surface is traction-free or subjected to a hydrostatic pressure P the bifurcation condition for localized bulging is simply $J(\widetilde{\Gamma}, \widetilde{F}) = 0$, whether it is the F or λ_z that is fixed in rotating the tube. We shall verify in the next section that this is indeed the case.

Next, consider the case when a tube is mounted on a rigid circular cylindrical spindle with a radius larger than A, which is the shrink-fit case discussed in [Chadwick et al. 1977]. We assume that the contact is smooth so that at the inner surface the stretch λ_a is specified and the shear stress components are negligible. When such a tube is rotated, the expression (2-4) can be used to compute the contact pressure, and the resultant $\widetilde{F}_0(\lambda_a, \lambda_z, \Gamma)$ of σ_{22} given by (2-8) is now a function of the only variable stretch λ_z. It will be shown in the next section that the bifurcation condition for localized bulging is simply

$$\Omega_c(\lambda_a, \lambda_z, \Gamma) \equiv \frac{\partial \widetilde{F}_0}{\partial \lambda_z} = 0, \tag{2-14}$$

where the first equation defines the function $\Omega_c(\lambda_a, \lambda_z, \Gamma)$ with the subscript c signifying "constrained". Suppose that the equation $\widetilde{F}_0(\lambda_a, \lambda_z, \Gamma) = F$, with $\widetilde{F}_0$ given by (2-8), is solved for Γ and the result is denoted by $\Gamma = \widetilde{\Gamma}_0(\lambda_a, \lambda_z, F)$. Then it can also be shown that the above bifurcation condition is equivalent to $\partial \widetilde{\Gamma}_0 / \partial \lambda_z = 0$.

Finally, in the special case of a solid cylinder ($A = a = 0$), the three principal stretches given by (2-2) reduce to

$$\lambda_1 = \lambda_z^{-1/2}, \qquad \lambda_2 = \lambda_z, \qquad \lambda_3 = \lambda_z^{-1/2}, \tag{2-15}$$

which are all independent of r. Then in terms of the reduced strain-energy function $\widehat{w}$ defined by

$$\widehat{w}(\lambda_z) = W(\lambda_z^{-1/2}, \lambda_z, \lambda_z^{-1/2}), \tag{2-16}$$

the principal stretch λ_z is determined by

$$\Gamma = 4\lambda_z^2 \left(\frac{F}{\pi} - \widehat{w}'\right), \tag{2-17}$$

where the prime denotes differentiation with respect to the argument λ_z. If F is fixed, then setting $d\Gamma/\lambda_z = 0$ would yield, after F has been eliminated with the use of (2-17), the condition

$$\Omega_s(\lambda_z) \equiv 2\lambda_z^3 \widehat{w}'' - \Gamma = 0, \tag{2-18}$$

where the first relation defines the function $\Omega_s(\lambda_z)$ with the subscript s signifying "solid". On the other hand, if Γ is fixed instead, then setting $dF/\lambda_z = 0$ would again yield the same condition (2-18). It will be shown in the next section that this is in fact the bifurcation condition for localized bulging.

3. Bifurcation conditions for localized bulging

To investigate the axisymmetric localized bulging of the finitely deformed configurations determined in the previous section, we consider an incremental displacement field $\dot{x}$ given by

$$\dot{x} = u(r, z)e_r + v(r, z)e_z, \tag{3-1}$$

where $u(r, z)$ and $v(r, z)$ are the incremental displacements in the r- and z-directions, respectively. The incremental equation of motion takes the form

$$\operatorname{div} \chi^T = -\Gamma u e_r, \tag{3-2}$$

where the incremental stress tensor χ is defined by the following components relative to the orthonormal basis $\{e_\theta, e_z, e_r\}$:

$$\chi_{ij} = \mathcal{B}_{jilk}\eta_{kl} + \bar{p}\eta_{ji} - p^*\delta_{ji}. \tag{3-3}$$

In the above expression, the $\mathcal{B}_{jilk}$ are the incremental elastic moduli whose expression in terms of the principal stretches can be found in [Haughton and Ogden 1979a], $\bar{p}$ and p^* are, respectively, the primary and incremental pressures associated with the constraint of incompressibility, and the tensor η is given by

$$\eta = \begin{bmatrix} u/r & 0 & 0 \\ 0 & v_z & v_r \\ 0 & u_z & u_r \end{bmatrix} \quad \text{with } v_z \equiv \frac{\partial v}{\partial z}, \, v_r \equiv \frac{\partial v}{\partial r}, \text{ etc.} \tag{3-4}$$

The equation of motion is to be supplemented by the incompressibility condition

$$\operatorname{tr} \eta = u_r + v_z + \frac{u}{r} = 0, \tag{3-5}$$

and is to be solved subject to appropriate boundary conditions on $r = a, b$. On the outer boundary $r = b$, we impose the traction-free boundary condition

$$\chi n = 0 \quad \text{on } r = b \tag{3-6}$$

for all three cases under consideration, where n denotes the unit normal to the surface. For a solid cylinder, this boundary condition is supplemented by the condition that the solution must be bounded at $r = 0$. For the case when a tube is subjected to an internal (hydrostatic) pressure P, the boundary condition on $r = a$ is given by

$$\chi n = P\eta^T n \quad \text{on } r = a. \tag{3-7}$$

Finally, for the shrink-fit case, the boundary condition on $r = a$ is given by

$$\chi_{23} = 0, \quad u = 0 \quad \text{on } r = a. \tag{3-8}$$

As explained in [Fu et al. 2016], the bifurcation condition can be derived by first looking for a solution of the form

$$u = f(r)e^{\alpha z}, \qquad v = g(r)e^{\alpha z}, \qquad p^* = h(r)e^{\alpha z}. \tag{3-9}$$

On substituting these expressions into the incremental equilibrium equations and then eliminating $g(r)$ and $h(r)$ in favor of $f(r)$, we find that $f(r)$ satisfies the single fourth-order ordinary differential equation

$$\begin{aligned}
r^4 \{r^{-1}[r^{-1}\mathcal{B}_{3232}(r^2 f'' + rf' - f)]'\}' + \alpha^2 r^2 \big\{ r[r(\mathcal{B}_{2222} + \mathcal{B}_{3333} - 2\mathcal{B}_{2233} - 2\mathcal{B}_{3223})f']' \\
+ \big(r^2 \sigma_{33}'' - r^2 \mathcal{B}_{3232}'' + r\mathcal{B}_{2222}' + r\mathcal{B}_{1133}' - r\mathcal{B}_{1122}' - r\mathcal{B}_{2233}' - r\mathcal{B}_{3223}' \\
+ 2\mathcal{B}_{1122} + 2\mathcal{B}_{3223} - \mathcal{B}_{1111} - \mathcal{B}_{2222} + r^2 \Gamma \big) f \big\} + \alpha^4 r^4 \mathcal{B}_{2323} f = 0. \tag{3-10}
\end{aligned}$$

This corresponds to [Haughton and Ogden 1980c, (49)] with α replaced by $i\alpha$. In a similar manner, the two boundary conditions (3-6) and (3-7) yield

$$r^2 f'' + rf' - (\alpha^2 r^2 + 1)f = 0 \quad \text{on } r = a, b, \tag{3-11}$$

and

$$\begin{aligned}
r^2 [r^{-1}\mathcal{B}_{3232}(r^2 f'' + rf' - f)]' + \alpha^2 r^3 (\mathcal{B}_{2222} + \mathcal{B}_{3333} - 2\mathcal{B}_{2233} - 2\mathcal{B}_{3223} + \mathcal{B}_{3232})f' \\
- \alpha^2 r^2 (r\sigma_{33}' - r\mathcal{B}_{3232}' + \mathcal{B}_{2222} + \mathcal{B}_{1133} - \mathcal{B}_{1122} - \mathcal{B}_{2233} - \mathcal{B}_{3223})f = 0 \quad \text{on } r = a, b. \tag{3-12}
\end{aligned}$$

The last boundary condition (3-12) on $r = a$ corresponds to (3-7) applied in the normal direction. For the shrink-fitting case, this is replaced by

$$f(a) = 0, \tag{3-13}$$

and as a result the boundary condition (3-11), which corresponds to $\chi_{23} = 0$, reduces to

$$af''(a) + f'(a) = 0. \tag{3-14}$$

Because of the translational invariance in terms of z, $\alpha = 0$ is always an eigenvalue of the above eigenvalue problem. For sufficiently small values of Γ, P, and F, none of the other eigenvalues can be pure imaginary since such eigenvalues give rise to bifurcation modes that are sinusoidal in the z-direction, and we only expect such modes to appear for sufficiently large values of Γ, P, and F. We note that Haughton and Ogden's [1980a; 1980b; 1980c] analysis is concerned with the conditions under which such bifurcation modes would appear. Since our current analysis is concerned with a bifurcation mode that is localized in the axial direction, as a first attempt we may assume that the tube or solid cylinder is infinitely long so that boundary conditions at the two end faces need not be considered. This is essentially the "perfect" bifurcation case (i.e., bifurcation in the absence of any imperfections). Effects of finite length as well as material inhomogeneity and/or nonuniform wall thickness can all be considered as imperfections. Since localized bulging is in general a subcritical bifurcation, it is expected that in the presence of imperfections, the critical value of angular speed will be significantly lower than the value determined in the current paper. For an illustration of the effect of imperfections, we refer to [Fu and Xie 2012].

For the problem under consideration, there exist two *real* eigenvalues of the form $\alpha = \pm\alpha_1$ that are closest to $\alpha = 0$ when Γ, P, and F are sufficiently small. These two eigenvalues would move along the real axis towards the origin as Γ and/or P is increased gradually. According to the dynamical systems theory, a necessary condition for a localized bulging bifurcation to take place is when α_1 vanishes, making

zero a triple eigenvalue; see, e.g., [Kirchgässner 1982] or [Haragus and Iooss 2011]. This necessary condition is now derived for the three different cases defined earlier.

Solid cylinder. For the case of a solid cylinder, all the elastic moduli are constants and the reduced eigenvalue problem can be solved analytically. Adapting Haughton and Ogden's [1980a] results slightly, we obtain the following equation satisfied by all the eigenvalues of α:

$$K_1 - K_2 = 0, \tag{3-15}$$

where K_1 and K_2 are defined by

$$\nu_\beta(\nu_\beta^2 + 1)I_1(\nu_\beta\alpha b)K_\beta = \alpha b(\nu_\beta^2 \mathcal{B}_{1212} + \mathcal{B}_{2121})I_0(\nu_\beta\alpha b) - \nu_\beta(2\mathcal{B}_{1313} + \Gamma b^2)I_1(\nu_\beta\alpha b), \tag{3-16}$$

with ν_1 and ν_2 denoting the two positive roots of the biquadratic equation

$$\nu^4 \mathcal{B}_{1212} - \nu^2(\mathcal{B}_{1111} + \mathcal{B}_{2222} - 2\mathcal{B}_{1122} - 2\mathcal{B}_{1221}) + \mathcal{B}_{2121} = 0. \tag{3-17}$$

The condition for zero to become a triple eigenvalue can be obtained by expanding (3-15) in terms of α and then setting the leading term to zero. The result is

$$(2\mathcal{B}_{1313} - 2\mathcal{B}_{1212} + \Gamma b^2)\nu_1^2\nu_2^2 - 2\mathcal{B}_{2121}(\nu_1^2 + \nu_2^2) - 2\mathcal{B}_{2121} = 0,$$

which, on using (3-17), can be reduced to

$$\Gamma b^2 - 2\mathcal{B}_{1111} + 4\mathcal{B}_{1122} - 4\mathcal{B}_{1212} + 4\mathcal{B}_{1221} + 2\mathcal{B}_{1313} - 2\mathcal{B}_{2222} = 0. \tag{3-18}$$

With the use of the expressions for the elastic moduli given by [Haughton and Ogden 1979a], we have verified that (3-18) can be reduced to (2-18). Thus, we conclude that for a rotating solid cylinder, a localized bulge will be initiated when the rotation speed ω or the axial force given by (2-17) reaches a maximum.

Unconstrained tube. We next consider the case of an unconstrained tube that is subjected to the combined action of rotation, internal inflation, and an axial force. An inspection of the associated eigenvalue problem governed by (3-10), (3-11), and (3-12) shows that it can be obtained from the case with $\Gamma = 0$ by the simple substitution

$$\mathcal{B}_{1111} \to \mathcal{B}_{1111} - \Gamma r^2. \tag{3-19}$$

As a result, the exact bifurcation condition can be derived following the same procedure as in [Fu et al. 2016]. Guided by the results in that paper, we may further conjecture that with the above substitution, the new bifurcation condition should be equivalent to $\Omega_u(\lambda_a, \lambda_z) = 0$, where $\Omega_u(\lambda_a, \lambda_z)$ is defined by (2-13). We have checked to verify that this is indeed the case. Furthermore, in the thin-wall limit, with the aid of an expansion procedure adapted from [Fu et al. 2016], we find that the exact bifurcation condition to leading order reduces to

$$\lambda_m(w_1 - \lambda_z w_{12})^2 + \lambda_z^2 w_{22}(w_1 - \lambda_1 w_{11}) + \lambda_m^3\Gamma^2 + 2\lambda_m^2(\lambda_z w_{12} - w_1)\Gamma = 0, \tag{3-20}$$

where λ_m denotes the azimuthal stretch in the mid-surface, and all the partial derivatives are now evaluated at $\lambda = \lambda_m$. The associated leading-order expressions for Γ and F take the form

$$\Gamma = w_1/\lambda_m - \lambda_z P_0, \qquad F = \pi(2w_2 - P_0\lambda_m^2), \tag{3-21}$$

where $P_0 = P/\epsilon$, ϵ being the wall thickness scaled by the averaged radius. If $(3\text{-}21)_1$ is used to eliminate Γ in (3-20), we obtain the alternative bifurcation condition

$$\lambda_m(w_{11}w_{22} - w_{12}^2) - w_1 w_{22} + P_0 \lambda_m^2 (2w_{12} - \lambda_m P_0) = 0, \tag{3-22}$$

which is valid if P_0 is held fixed in rotating the tube. As a useful check, this leading-order bifurcation condition can also be obtained from $J(\Gamma, F) = 0$ when the leading-order expressions (3-21) are used.

As expected, when $\Gamma = 0$, (3-20) reduces to its counterpart for the pure inflation case given in [Fu et al. 2008], and it is known that this reduced bifurcation condition has a solution that defines λ_z as a function of λ_m for most of the commonly used strain-energy functions. In contrast, if we set $P_0 = 0$ in (3-22), the existence of a solution of the reduced bifurcation condition depends very much on the material model used: it again has a solution when the Ogden material model is used, but it does not have a solution when the Gent material model is used. This difference carries over even when finite wall thickness is considered, which will be discussed further in the next section. We also observe that (3-22) with $P_0 = 0$ is the same as [Haughton and Ogden 1980c, (63)] which emerged as the limit of the condition of bifurcation into axially symmetric periodic modes in an infinitely long tube. This equation reappeared as (71) in the same paper, where it was observed as characterizing the turning point of ω when the axial force F is held fixed.

Constrained tube. Finally, we consider the shrink-fit case for which the applicable boundary conditions at $r = a, b$ are (3-13)–(3-14) and (3-11)–(3-12), respectively. Again, the bifurcation condition is the condition under which zero becomes a triple eigenvalue. To derive this condition, we expand the stretches as

$$\lambda_a = \lambda_a^{(0)} + \alpha^2 \lambda_a^{(1)} + \cdots, \qquad \lambda_z = \lambda_z^{(0)} + \alpha^2 \lambda_z^{(1)} + \cdots \tag{3-23}$$

and look for a regular perturbation solution of the form

$$f(r) = f^{(0)}(r) + \alpha^2 f^{(1)}(r) + \cdots, \tag{3-24}$$

where the constants $\lambda_a^{(i)}$ and $\lambda_z^{(i)}$ $(i = 0, 1, \ldots)$ and functions $f^{(i)}(r)$ $(i = 0, 1, \ldots)$ are to be determined. We are basically assuming that there is a small real eigenvalue α and then determining the required values of the stretches that support such a small eigenvalue. If such a nontrivial solution can be found, then the leading-order values $\lambda_a^{(0)}$ and $\lambda_z^{(0)}$ are the stretch values at which zero becomes a triple eigenvalue.

On substituting (3-24) into (3-10) and equating the coefficients of α^0 and α^2, we obtain a homogeneous equation for $f^{(0)}(r)$ and an inhomogeneous equation for $f^{(1)}(r)$. These equations are the same as their counterparts derived in [Fu et al. 2016] except for the substitution (3-19). We thus have

$$f^{(0)}(r) = c_1 r + c_2 \frac{1}{r} + c_3 \kappa_1(r) + c_4 \kappa_2(r), \tag{3-25}$$

and

$$f^{(1)}(r) = d_1 r + d_2 \frac{1}{r} + d_3 \kappa_1(r) + d_4 \kappa_2(r) + c_1 \kappa_3(r) + c_2 \kappa_4(r) + c_3 \kappa_5(r) + c_4 \kappa_6(r), \tag{3-26}$$

where c_i and d_i $(i = 1, 2, 3, 4)$ are constants and the expressions for $\kappa_i(r)$ $(i = 1, \ldots, 6)$ are not written out here for the sake of brevity. We observe that the last four terms in (3-26) are simply particular integrals. The boundary conditions can similarly be expanded. On substituting (3-24) together with (3-25) and (3-26) into the leading- and second-order boundary conditions, we find that $c_3 = c_4 = 0$, $c_2 = -ac_1$, and

$d_2 = -ad_1$, and that the three constants c_1, d_3, and d_4 satisfy three homogeneous linear equations. For a nontrivial solution, we set the determinant of its coefficient matrix to zero, thus obtaining the condition

$$\Omega(\lambda_a^{(0)}, \lambda_z^{(0)}) = 0, \tag{3-27}$$

where

$$
\begin{aligned}
\Omega(\lambda_a, \lambda_z) =\ & (a^2b^2 - b^4)F_1 + (a^2b^4 - a^4b^2)F_2 + 2b^2 F_3 - 2a^2b^2 F_4 + (a^4 - b^4)\sigma_3(b) \\
& + b^4\big(\mathscr{B}_{1122}(b) - \mathscr{B}_{1133}(b) - 2\mathscr{B}_{2222}(b) + 3\mathscr{B}_{2233}(b) + 2\mathscr{B}_{3223}(b) - 2\mathscr{B}_{3232}(b) - \mathscr{B}_{3333}(b)\big) \\
& + a^2b^2\big(2\mathscr{B}_{1133}(b) + 2\mathscr{B}_{2222}(b) + 2\mathscr{B}_{3232}(b) - 2\mathscr{B}_{1122}(b) - 2\mathscr{B}_{2233}(b) - 2\mathscr{B}_{3223}(b)\big) \\
& + b(a^2 - b^2)^2(\mathscr{B}'_{3223}(b) + \bar{p}'(b)) + a^4(\mathscr{B}_{1122}(b) - \mathscr{B}_{1133}(b) - \mathscr{B}_{2233}(b) + \mathscr{B}_{3333}(b)).
\end{aligned}
$$

In the last expression, the constants $F_1, \ldots, F_4$ are given by

$$F_1 = \int_a^b \omega_1(t)\, dt, \qquad F_3 = \int_a^b t\left(\int_a^t \omega_1(s)\, ds\right) dt,$$

$$F_2 = \int_a^b \omega_2(t)\, dt, \qquad F_4 = \int_a^b t\left(\int_a^t \omega_2(s)\, ds\right) dt,$$

$$
\begin{aligned}
\omega_1(r) =\ & \mathscr{B}'_{1122} - \mathscr{B}'_{1133} + 3\mathscr{B}'_{2233} - 2\mathscr{B}'_{2222} - \mathscr{B}'_{3333} + 3\mathscr{B}'_{3223} + r(\mathscr{B}''_{3223} + \bar{p}'') \\
& + \frac{1}{r}(\mathscr{B}_{1111} - \Gamma r^2 - 2\mathscr{B}_{1122} + 2\mathscr{B}_{2233} - \mathscr{B}_{3333}),
\end{aligned}
$$

$$
\begin{aligned}
\omega_2(r) =\ & \frac{1}{r}(\mathscr{B}''_{3223} + \bar{p}'') + \frac{1}{r^2}(\mathscr{B}'_{1122} - \mathscr{B}'_{1133} - \mathscr{B}'_{2233} - \mathscr{B}'_{3333} - \mathscr{B}'_{3223}) \\
& + \frac{1}{r^3}(\mathscr{B}_{1111} - \Gamma r^2 - 2\mathscr{B}_{1122} + 2\mathscr{B}_{2233} - \mathscr{B}_{3333}).
\end{aligned}
$$

We may conjecture that the bifurcation condition (3-27) is equivalent to (2-14). This is verified numerically to indeed be the case.

4. Numerical results

We present some representative numerical results by considering two commonly used material models for rubber-like materials, the Ogden [1972] and Gent [1996] material models. The associated strain-energy function is given by

$$W = \mu \sum_{r=1}^{3} \mu_r^*(\lambda_1^{\alpha_r} + \lambda_2^{\alpha_r} + \lambda_3^{\alpha_r} - 3)/\alpha_r \tag{4-1}$$

or

$$W = -\frac{\mu}{2} J_m \ln\left(1 - \frac{J_1}{J_m}\right), \quad J_1 = \lambda_1^2 + \lambda_2^2 + \lambda_3^2 - 3, \tag{4-2}$$

respectively, where μ is the ground state shear modulus,

$$\alpha_1 = 1.3, \qquad \alpha_2 = 5.0, \qquad \alpha_3 = -2.0, \qquad \mu_1^* = 1.491, \qquad \mu_2^* = 0.003, \qquad \mu_3^* = -0.023,$$
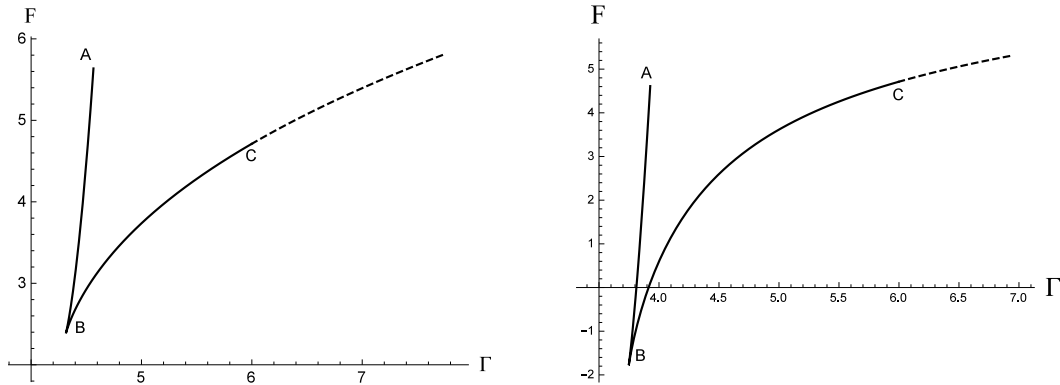
Figure 1. Relation between Γ and F when localized bulging takes place. The solid and dashed parts on each curve correspond to $\lambda_z < 1$ and $\lambda_z > 1$, respectively. Left: Gent material. Right: Ogden material.
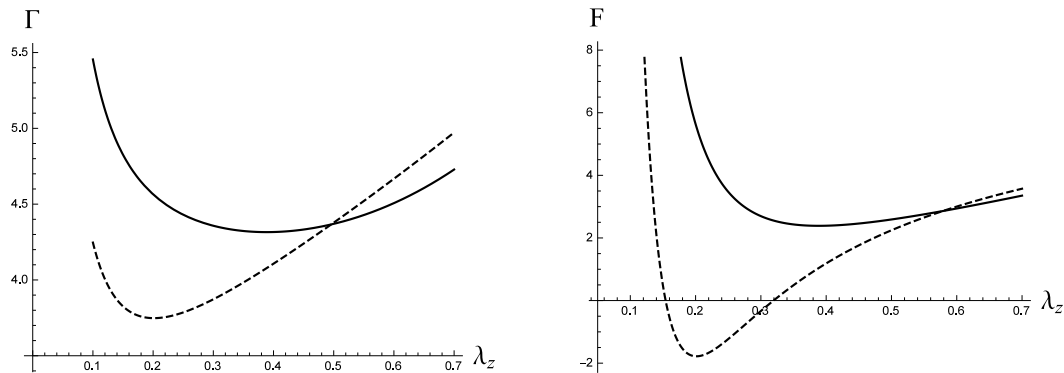

Figure 2. Dependence of Γ and F on λ_z when localized bulging takes place. Solid and dashed lines correspond to the Gent and Ogden material models, respectively.

and J_m is a material constant which we shall take to be 97.2 following [Gent 1996]. All our numerical computations were carried out using Mathematica version 10.2.0.0.

Solid cylinder. We assume that a net axial force F is specified and we wish to determine the value of Γ at which localized bulging may take place. In Figure 1, we have shown the relation between Γ and F when the bifurcation condition (2-18) is satisfied. The relation is obtained by varying λ_z continuously from 0.2 to 1.2 and computing the associated Γ and F using (2-17) and (3-15). It is seen that both curves contain a cusp point, corresponding to the fact that the Γ given by $\Gamma = 2\lambda_z^3 \widehat{w}''$, defined by the bifurcation condition (2-18), attains a minimum at $\lambda_z = 0.39$ for the Gent material, and $\lambda_z = 0.20$ for the Ogden material; see Figure 2, left. In Figure 2, right, is shown the dependence of F on λ_z when localized bulging occurs. It is seen that there is a major difference between the predictions between the two material models: whereas the Ogden model predicts that localized bulging may take place when $F = 0$ and the associated critical value of $\Gamma = 3.81$ is attained at $\lambda_z = 0.15$, the Gent material model predicts that localized bulging can never take place when $F = 0$.
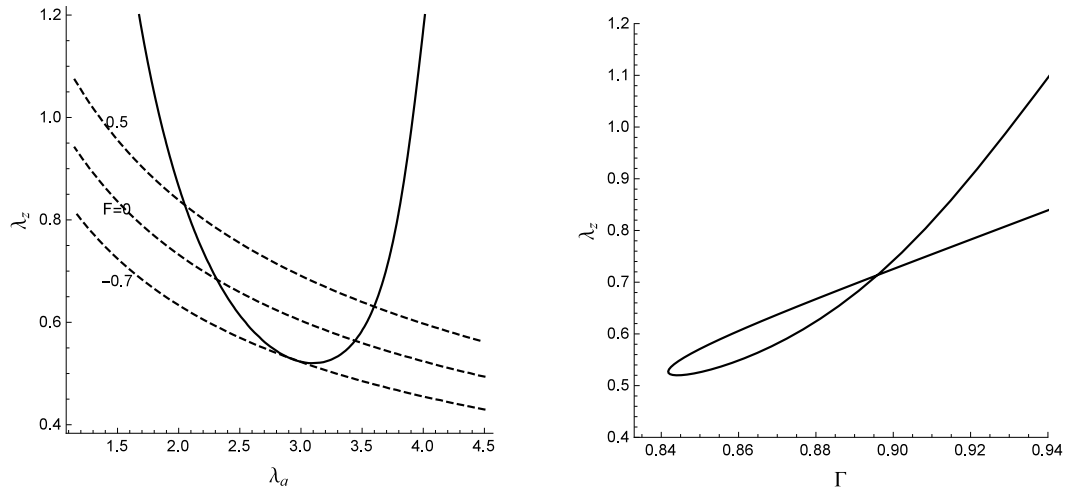
Figure 3. Solution of the bifurcation condition $\Omega_u(\lambda_a, \lambda_z) = 0$, when the Ogden material is used, for a rotating tube with $A = 0.8$ and $P = 0$ in terms of (λ_a, λ_z) (left) and (Γ, λ_z) (right). The dashed lines represent the loading paths with $F = 0, 0.5, -0.7$.

Unconstrained tube. We first consider the simplest case when $P = 0$, and we determine the critical value of Γ at which localized bulging may occur. We have in mind two possible types of end conditions: either F or λ_z is fixed when Γ is increased. We note, however, that the solution of the bifurcation condition $\Omega_u(\lambda_a, \lambda_z) = 0$ is independent of the end conditions. It is found that when the Gent material model is used, this bifurcation condition does not have a solution, and so localized bulging can never occur however large the rotation speed is. This fact was already noted in the previous section in the thin-wall limit. In contrast, when the Ogden material model is used, $\Omega_u(\lambda_a, \lambda_z) = 0$ has a solution giving λ_z as a function of λ_a; see the solid line in Figure 3, left, where we have also shown a typical loading curve defined by $\widetilde{F}(\lambda_a, \lambda_z) = 0$. As Γ is increased gradually from zero, loading starts from the point where $(\lambda_a, \lambda_z) = (1, 1)$ and traces down the loading curve $\widetilde{F}(\lambda_a, \lambda_z) = 0$. Localized bulging would occur when this curve intersects the bifurcation curve $\Omega_u(\lambda_a, \lambda_z) = 0$ at

$$(\lambda_a, \lambda_z) = (2.313, 0.683),$$

with the associated value of Γ equal to 0.885.

As a comparison, we have also shown in Figure 3, left, the loading paths associated with $F = 0.5, -0.7$. It is seen that as F is increased from zero, the loading path is shifted upwards, whereas as F is decreased from zero, the loading path is shifted downwards, eventually losing the intersections with the bifurcation curve when F is approximately equal to -0.7. This means that when $P = 0$, localized bulging is always possible when a stretching force is applied axially in addition to the rotation but becomes impossible when a compressive force exceeding 0.7 in magnitude is applied.

To offer a different perspective on the bifurcation, we have shown in Figure 3, right, the critical value of λ_z as a function of Γ. This curve is obtained as follows. For each value of λ_z, the bifurcation condition $\Omega_u(\lambda_a, \lambda_z) = 0$ is solved to find the corresponding values of λ_a (there are zero, one, or two such values, as can be seen from Figure 3, left), and hence the values of Γ. This alternative plot of the bifurcation

A/B	0.43	0.5	0.6	0.7	0.8	0.9	0.99
λ_a	3.4779	2.9635	2.6486	2.4518	2.3128	2.2085	2.1346
λ_z	0.6291	0.6591	0.6729	0.6797	0.6834	0.6851	0.6956
Γ	1.4446	1.2984	1.1304	0.9958	0.8855	0.7935	0.7230
$\Gamma \approx$	(1.3641)	(1.2397)	(1.0896)	(0.9907)	(0.8837)	(0.7931)	(0.7230)

Table 1. Critical values of Γ in free rotation ($F = 0$).
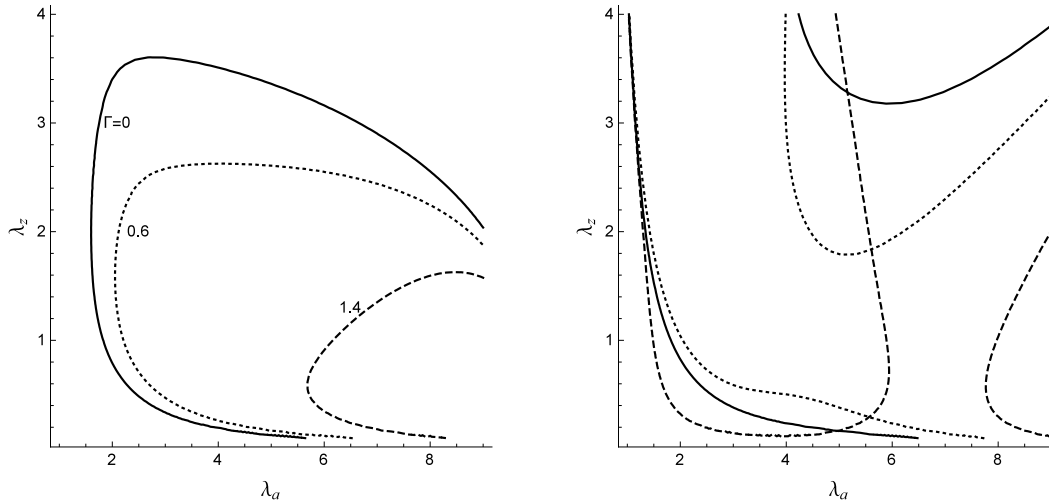
Figure 4. Solution of the bifurcation condition $J(\widetilde{P}, \widetilde{F}) = 0$ for the different values of Γ indicated. The solid, dotted, and dashed lines correspond to $\Gamma = 0, 0.2, 0.5$, respectively. Left: Gent material. Right: Ogden material.

condition is particularly useful when it is the axial stretch that is fixed as the rotation speed is increased gradually. For each such axial stretch, λ_{z0} say, the corresponding critical value of Γ can simply be obtained from the leftmost intersection of the horizontal line $\lambda_z = \lambda_{z0}$ in this plot with the bifurcation curve. For instance, when λ_z is fixed at unity so that the tube is not allowed to contract axially as the rotation speed is increased, the associated critical value of Γ is equal to 0.997. It is seen that the critical value of Γ is an increasing function of λ_z.

We have also carried out calculations to find out how the results in Figure 3 depend on A. It is found that as A decreases (so that the wall thickness increases), the curve corresponding to $F = 0$ would shift downwards relative to the curve of $\Omega_u(\lambda_a, \lambda_z) = 0$. When A reaches 0.428 approximately, the two curves would no longer intersect, implying that localized bulging becomes impossible below this threshold value. In Table 1, we have listed the critical values of Γ for a selection of values of A. Since the wall thickness is a decreasing function of A/B, it can be seen that the larger the wall thickness, the larger the critical value of Γ. The numbers in parentheses in the last row are the corresponding results based on the thin-wall approximation (3-21) and (3-22) and is seen to provide a good approximation, with a relative error of less than 5%, for values of A as small as 0.5.

We next consider the effect of allowing for a nonzero internal pressure. There are now two subcases. The first subcase is when the unconstrained tube is mainly subjected to the action of internal inflation
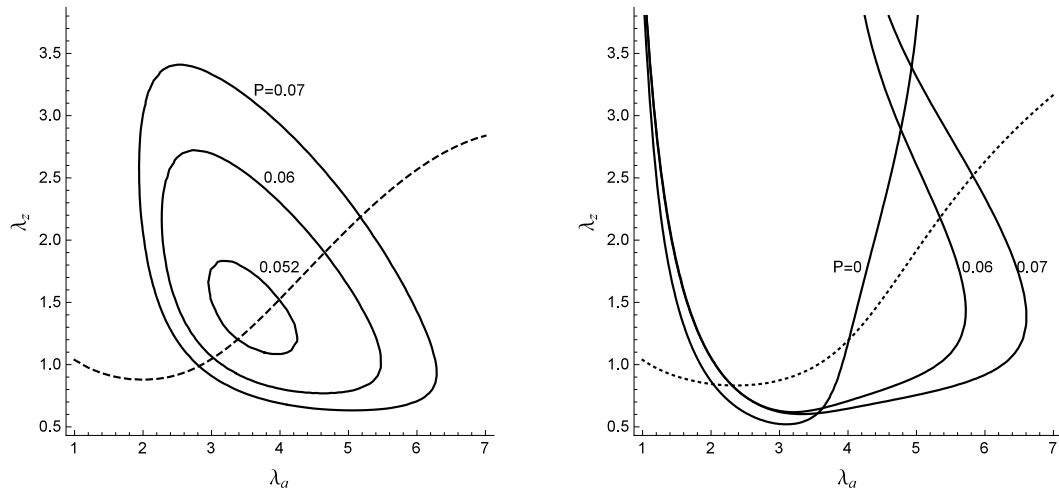
Figure 5. Solution of the bifurcation condition $\Omega_u(\lambda_a, \lambda_z) = 0$ for the three different values of P indicated. The dashed line corresponds to the solution of $\widetilde{F}(\lambda_a, \lambda_z) = 0$ when $P = 0.06$ and is the loading path when there is no net axial force applied at the plane end faces. Its intersection with the solid curve associated with $P = 0.06$ gives the values of the two stretches when localized bulging takes place. Left: Gent material. Right: Ogden material.

and an axial force, with rotation being small and playing a minor role. This subcase covers the case of zero rotation which has previously been investigated in [Fu et al. 2016]. In Figure 4 we have shown the solution of the bifurcation condition $\Omega_u(\lambda_a, \lambda_z) = 0$ for three representative values of Γ and the common value of $A = 0.8$. We note that when Γ is nonzero, the solution again has two branches when the Ogden material model is used. We shall focus our discussion on the parameter regime near $\lambda_a = \lambda_z = 1$. It is seen that adding a rotation to the tube delays the onset of localized bulging when the Gent material is used, but when the Ogden material is used the rotation has a delaying effect when the rotation speed is small, but has an opposite effect when the rotation speed is large enough.

Finally, we assume that the internal pressure P is zero or small, and it is the rotation and axial force F that play a dominant role. In Figure 5 we have shown the solution of $\Omega_u(\lambda_a, \lambda_z) = 0$ for three representative values of P. There is here a big difference between the predictions of the two material models. When $P = 0$ and the Gent material model is used, the condition $\Omega_u(\lambda_a, \lambda_z) = 0$ does not have a solution at all, which means that localized bulging is impossible now matter how large the rotation speed is. Localized bulging first becomes possible when P is increased to the value of 0.051. In contrast, according to the Ogden material model, localized bulging is possible even if P is zero. The dotted line in each figure represents the loading path, the solution of $\widetilde{F}(\lambda_a, \lambda_z) = 0$, when $P = 0.06$ and the net axial force is zero.

The shrink-fit case. In this case the stretches must satisfy $\widetilde{F}_0(\lambda_a, \lambda_z, \Gamma) = F$. This equation may also be solved to express Γ in terms of F. The bifurcation condition (2-14) then depends on F as well as λ_a and λ_z. For each specified F, this condition defines a curve in the (λ_a, λ_z) plane. A typical solution with $F = 2$ is shown in Figure 6, where the solution of $\sigma_{33}(a) = 0$ is also shown with a dashed line. It is seen that although localized bulging is possible, the contact force at $r = a$ must necessarily be tensile. This
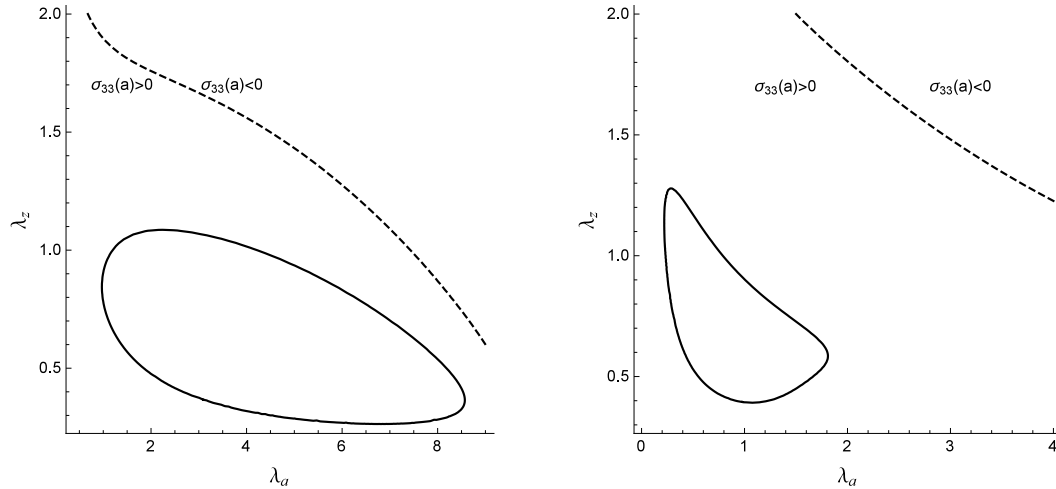
Figure 6. Solution of the bifurcation condition (2-14). The result corresponds to $F = 2$ and is shown with a solid line. The dashed line in each plot represents the solution of $\sigma_{33}(a) = 0$. Left: Gent material. Right: Ogden material.

means that no matter how tight the initial fitting is, localized bulging will not occur before the tube loses contact with the rigid spindle. It is also found that as F is gradually reduced, the closed curve shrinks in size and eventually disappears at $F = 1.29$ when the Gent material model is used and at $F = 1.66$ when the Ogden material model is used. Thus, in particular, when the plane ends of the tube are traction-free, localized bulging will not occur no matter how large λ_a or Γ is.

5. Conclusion

In this paper we have studied the bifurcation condition for localized bulging of a circular solid cylinder or cylindrical tube which rotates about its axis of symmetry. Additional external forces may include a nonzero net axial force and/or internal pressure. In each case, the bifurcation condition is derived with the aid of the dynamical systems theory and found to have simple interpretations in terms of physical quantities such as the rotation speed, axial force, and internal pressure. For instance, when the axial force and internal pressure are both fixed, the bifurcation condition simply corresponds to the angular velocity reaching a maximum when viewed as a function of λ_a for a tube or λ_z for a solid cylinder. However, this correspondence is lost when for instance it is the axial stretch λ_z that is fixed in rotating the tube. Although we have only presented numerical results for $A = 0.8$ and two typical strain-energy functions, our simple representation of the bifurcation condition can be used to evaluate the effects of wall thickness and dependence on the material model in a straightforward manner if required.

The simplest case is perhaps the case of free rotation when both F and P are zero. Our illustrative calculations show that the Ogden material model would predict that localized bulging may occur but the Gent material model would predict that localized bulging can never occur. According to the Gent material model, localized bulging could occur only if a sufficiently large internal pressure is added. Also, according to both models, localized bulging will not occur in the shrink-fit case before contact with the rigid spindle is lost.

It would be of interest to ask whether the localized bulging discussed in the current study could be realized for realistic material parameters and angular speeds in free rotation. As a rough estimate, we take

$$\rho = 0.91 \, \text{kg/m}^3, \qquad \mu = 667 \, \text{kPa},$$

which are typical values for natural rubber. If $B = 0.1$ m, the critical value of $\Gamma = 3.81$ predicted by the Ogden model for a solid cylinder would correspond to an angular velocity $\omega = 528/\text{s}$, which translates to a rotation frequency of 5046 rpm (revolutions per minute). For a cylindrical tube with $B = 0.1$ m, $A/B = 0.8$, the critical value of $\Gamma = 0.885$ predicted by the Ogden model for an unconstrained tube corresponds to an angular velocity $\omega = 270/\text{s}$, which is about 2582 rpm. This is within the achievable rotor speed of 3000 rpm. The required speed for the solid cylinder is higher, but it can be brought down by choosing a softer material since the rotation frequency is proportional to the square root of μ. For instance, for a typical gelatin, the shear modulus can be as small as 30 kPa [Markidou et al. 2005], for which the critical rotation frequency would be 1070 rpm. Thus, we may conclude that localized bulging should be easily observable in soft materials.

In the current study, we have assumed that the solid cylinder or tube is made of an isotropic elastic material. Our study can be easily extended to the case when the tube is helically reinforced by two families of identical fibres. The symmetry of the fibres ensures that axisymmetric deformations are again possible, and as far as such deformations are concerned, the tube would behave effectively like an isotropic material. However, as demonstrated in a recent study for the pure inflation case [Wang and Fu 2017], it is expected that the fibres will have a drastic effect on localized bulging. To be more precise, using fibre reinforcement can be a very effective method to construct nonbulging tubes.

Finally, we remark that the bifurcation condition derived in the present paper is only a necessary condition for localized bulging to occur. Strictly speaking, whether localized bulging can actually take place at the critical value of rotation can only be established by a weakly nonlinear analysis. However, from our experience with the pure inflation case for which both analytical and experimental results are available, we expect that the existence of localized bulging configurations should be the norm rather than the exception.

References

[Chadwick et al. 1977] P. Chadwick, C. F. M. Creasy, and V. G. Hart, "The deformation of rubber cylinders and tubes by rotation", *J. Austral. Math. Soc. B* **20**:1 (1977), 62–96.

[Fu and Xie 2012] Y. B. Fu and Y. X. Xie, "Effects of imperfections on localized bulging in inflated membranes tubes", *Philos. Trans. Roy. Soc. Lond. A* **370**:1965 (2012), 1896–1911.

[Fu et al. 2008] Y. B. Fu, S. P. Pearce, and K. K. Liu, "Post-bifurcation analysis of a thin-walled hyperelastic tube under inflation", *Int. J. Non-lin. Mech.* **43**:8 (2008), 697–706.

[Fu et al. 2016] Y. B. Fu, J. L. Liu, and G. S. Francisco, "Localized bulging in an inflated cylindrical tube of arbitrary thickness: the effect of bending stiffness", *J. Mech. Phys. Solids* **90** (2016), 45–60.

[Gent 1996] A. N. Gent, "A new constitutive relation for rubber", *Rubber Chem. Technol.* **69**:1 (1996), 59–61.

[Green and Zerna 1957] A. E. Green and W. Zerna, *Theoretical elasticity*, 1st ed., Clarendon, Oxford, 1957.

[Haragus and Iooss 2011] M. Haragus and G. Iooss, *Local bifurcations, center manifolds, and normal forms in infinite-dimensional dynamical systems*, Springer, London, 2011.

[Haughton and Ogden 1979a] D. M. Haughton and R. W. Ogden, "Bifurcation of inflated circular cylinders of elastic material under axial loading, I: Membrane theory for thin-walled tubes", *J. Mech. Phys. Solids* **27**:3 (1979), 179–212.

[Haughton and Ogden 1979b] D. M. Haughton and R. W. Ogden, "Bifurcation of inflated circular cylinders of elastic material under axial loading, II: Exact theory for thick-walled tubes", *J. Mech. Phys. Solids* **27**:5–6 (1979), 489–512.

[Haughton and Ogden 1980a] D. M. Haughton and R. W. Ogden, "Bifurcation of finitely deformed rotating elastic cylinders", *Quart. J. Mech. Appl. Math.* **33**:3 (1980), 251–265.

[Haughton and Ogden 1980b] D. M. Haughton and R. W. Ogden, "Bifurcation of rotating circular cylindrical elastic membranes", *Math. Proc. Cambridge Philos. Soc.* **87**:2 (1980), 357–376.

[Haughton and Ogden 1980c] D. M. Haughton and R. W. Ogden, "Bifurcation of rotating thick-walled elastic tubes", *J. Mech. Phys. Solids* **28**:1 (1980), 59–74.

[Kanner and Horgan 2007] L. M. Kanner and C. O. Horgan, "Elastic instabilities for strain-stiffening rubber-like spherical and cylindrical thin shells under inflation", *Int. J. Non-lin. Mech.* **42**:2 (2007), 204–215.

[Kirchgässner 1982] K. Kirchgässner, "Wave-solutions of reversible systems and applications", *J. Differential Equations* **45**:1 (1982), 113–127.

[Markidou et al. 2005] A. Markidou, W. Y. Shih, and W.-H. Shih, "Soft-materials elastic and shear moduli measurement using piezoelectric cantilevers", *Rev. Sci. Instrum.* **76**:6 (2005), 064302.

[Ogden 1972] R. W. Ogden, "Large deformation isotropic elasticity: on the correlation of theory and experiment for incompressible rubberlike solids", *P. Roy. Soc. A* **326**:1567 (1972), 565–584.

[Patterson and Hill 1977] J. C. Patterson and J. M. Hill, "The stability of a solid rotating neo-Hookean cylinder", *Mech. Res. Commun.* **4**:1 (1977), 69–74.

[Wang and Fu 2017] J. Wang and Y. B. Fu, "Effect of double-fibre reinforcement on localized bulging of an inflated cylindrical tube of arbitrary thickness", *J. Eng. Math.* (online publication March 2017).

[Wilkes 1955] E. W. Wilkes, "On the stability of a circular tube under end thrust", *Quart. J. Mech. Appl. Math.* **8**:1 (1955), 88–100.

JUAN WANG: jwang@usst.edu.cn
College of Science, University of Shanghai for Science and Technology, Shanghai 200093, China

ALI ALTHOBAITI: a.a.k.althobaiti@keele.ac.uk
School of Computing and Mathematics, Keele University, Staffordshire ST5 5BG, United Kingdom

YIBIN FU: y.fu@keele.ac.uk
School of Computing and Mathematics, Keele University, Staffordshire, ST5 5BG, United Kingdom

SUBMISSION GUIDELINES

ORIGINALITY

Authors may submit manuscripts in PDF format online at the Submissions page. Submission of a manuscript acknowledges that the manuscript is original and has neither previously, nor simultaneously, in whole or in part, been submitted elsewhere. Information regarding the preparation of manuscripts is provided below. Correspondence by email is requested for convenience and speed. For further information, write to contact@msp.org.

LANGUAGE

Manuscripts must be in English. A brief abstract of about 150 words or less must be included. The abstract should be self-contained and not make any reference to the bibliography. Also required are keywords and subject classification for the article, and, for each author, postal address, affiliation (if appropriate), and email address if available. A home-page URL is optional.

FORMAT

Authors can use their preferred manuscript-preparation software, including for example Microsoft Word or any variant of TeX. The journal itself is produced in LaTeX, so accepted articles prepared using other software will be converted to LaTeX at production time. Authors wishing to prepare their document in LaTeX can follow the example file at www.jomms.net (but the use of other class files is acceptable). At submission time only a PDF file is required. After acceptance, authors must submit all source material (see especially Figures below).

REFERENCES

Bibliographical references should be complete, including article titles and page ranges. All references in the bibliography should be cited in the text. The use of BibTeX is preferred but not required. Tags will be converted to the house format (see a current issue for examples); however, for submission you may use the format of your choice. Links will be provided to all literature with known web locations; authors can supply their own links in addition to those provided by the editorial process.

FIGURES

Figures must be of publication quality. After acceptance, you will need to submit the original source files in vector format for all diagrams and graphs in your manuscript: vector EPS or vector PDF files are the most useful. (EPS stands for Encapsulated PostScript.)

Most drawing and graphing packages—Mathematica, Adobe Illustrator, Corel Draw, MATLAB, etc.—allow the user to save files in one of these formats. Make sure that what you're saving is vector graphics and not a bitmap. If you need help, please write to graphics@msp.org with as many details as you can about how your graphics were generated.

Please also include the original data for any plots. This is particularly important if you are unable to save Excel-generated plots in vector format. Saving them as bitmaps is not useful; please send the Excel (.xls) spreadsheets instead. Bundle your figure files into a single archive (using zip, tar, rar or other format of your choice) and upload on the link you been given at acceptance time.

Each figure should be captioned and numbered so that it can float. Small figures occupying no more than three lines of vertical space can be kept in the text ("the curve looks like this:"). It is acceptable to submit a manuscript with all figures at the end, if their placement is specified in the text by means of comments such as "Place Figure 1 here". The same considerations apply to tables.

WHITE SPACE

Forced line breaks or page breaks should not be inserted in the document. There is no point in your trying to optimize line and page breaks in the original manuscript. The manuscript will be reformatted to use the journal's preferred fonts and layout.

PROOFS

Page proofs will be made available to authors (or to the designated corresponding author) at a Web site in PDF format. Failure to acknowledge the receipt of proofs or to return corrections within the requested deadline may cause publication to be postponed.